# STRATIGRAPHIC ARCHITECTURE OF SLOPE DEPOSITS ASSOCIATED WITH PROGRADING MARGINS, SOBRARBE FORMATION: AINSA BASIN, SPAIN

**by**

**Henri Sahat Mian Parulian Silalahi**

A thesis submitted to the Faculty and the Board of Trustees of the Colorado School of Mines in partial fulfillment of the requirements for the degree of Master of Science (Geology).

Golden, Colorado

Date _____

Sign: _____
Henri Sahat Mian Parulian Silalahi

Approved: _____
Dr. David R. Pyles
Thesis Advisor

Golden, Colorado

Date 2/19/09

Sign: _____
Dr. John D. Humphrey
Professor and Head
Department of Geology and Geological Engineering

## ABSTRACT

An improve knowledge of the relationship between delta and slope deposition has important applications to petroleum exploration and reservoir development. Few studies have addressed reservoir-scale stratigraphic architecture along the depositional profile of prograding systems. The Eocene Sobrarbe Formation contains 5.5 km of continuous outcrop exposure from the shelf-edge delta to the distal slope. The Sobrarbe Formation records a prograding system deposited during the final phases of the Ainsa Basin fill succession. This study, conducted on one fourth-order parasequence of the Sobrarbe Formation (maximum thickness 120 m), utilizes stratigraphic columns, photopanels, paleocurrent measurements, and mapped geologic boundaries to document change in stratigraphic architecture from the proximal to distal slope.

Several proximal to distal slope changes in stratigraphic architecture are documented in the parasequence. First, architectural elements change from proximal to distal slope. Proximal slope strata contain a large proportion of mouth bar elements that are directly associated with channel elements and mudstone sheets. Medial slope strata contain mouth bar elements, channel elements, overbank elements and mudstone sheet elements. Distal slope strata contain a large proportion of mudstone sheet elements and channel elements and overbank elements. Second, paleoflow direction change from proximal to distal slope. The proximal slope has a low paleocurrent diversity. The medial slope has high paleocurrent diversity. The distal slope has high paleocurrent diversity. Area with high paleocurrent diversity are interpreted to reflect area of high channel sinuosity. Third, channel types are uniquely distributed across slope profile. Proximal slope channels are highly erosional, contain sigmoid-shape bars, and stack vertically to build channel complexes. Medial slope channels are less erosional than proximal slope channels. They display distinctive axis to margin changes of grainsize and do not contain sigmoid-shaped bars. The channel stack both vertically and laterally to build channel complexes. Distal slope channel do not contain axis to margin change in grain size and they primarily stack laterally to build channel complexes. Fourth, channel geometry changes down the profile. Channel increase in thickness, width and aspect ratio basinward. Channel asymmetries remain constant across slope profile. Fifth, facies

diversity changes down the profile. Intra and extra channel facies diversity decreases basin ward. Sixth, overall grain size and net-to-gross ratio decrease from proximal to distal slope.

The observations above reveal some key stratigraphic concepts related to prograding slope system. First, deepwater channels are related to deltaic processes. This association suggests that initiation of slope channels correspond to avulsion of distributary channels. Second, the timing of deepwater deposition in the parasequence most likely occurred during sea level highstand. Third, the properties of sediment gravity flows changed down the profile. The sediment gravity flow were largely depletive and lost turbulent kinetic energy and competency resulting in on sediment portioning, decreasing in facies diversity from proximal to distal slope. Fourth, channel element sinuosity is controlled by a combination of gradient and the lithology of the substrate.

The results of this study can be use to decrease uncertainty in reservoir prediction and modeling, and they help better understand reservoir connectivity within deepwater prograding systems such as West Siberia Basin, Northwest Slope Australia and Sahakalin Island.

## TABLE OF CONTENTS

## LIST OF FIGURES

## LIST OF TABLES

## ACKNOWLEDGMENTS

I would like to express my sincere gratitude to my advisor, Dr. David R. Pyles for his patience, support, encouragement, and time during this research and my graduate education. Thank you to my committee members: Dr. Renaud Bouroullec, Dr. Donna Anderson, Dr. Julian Clark, and Dr. Stephen A. Sonnenberg for all their technical advice and support. To Drs. Pyles, Bouroullec, and Clark, special thanks for their creative ideas and continuous support during the thesis writing process. I appreciate their friendship, tutoring, and example during fieldwork in Ainsa, Spain. My thanks to Drs. Anderson, Sonnenberg, Carr, and Plink-Bjorklund for their willingness to help me on the path to resolving my research questions.

Many thanks to PT. Chevron Pacific Indonesia and the Chevron Center of Research Excellence (CoRE), that provided financial and logistical support for my graduate program and research. Thank you to Robert N. Ryan, Jr., Cary Mrozowski, Mark Koelmel, Nigel Middleton, Terry Young and John Humphrey that have given continuous support as DRB member of this research program. I am also thankful to Charlie Rourke, CoRE Program Manager, for her continuous support, patience, understanding, and advice through my program. I also want to thank to Vennesa Carroll and David Pyles whom willingly helping me through out all my writing challenges during this research.

My fellow graduate students have been so helpful to me during this process. Thank you, Olumide, Cheryl,and Maria. A special thank you to my teammates in CoRE, Prianto Setiawan, Jeremiah Moody, Amy Moss-Russell, and Matt Hoffman. Their friendship, discussions, and English tutoring contributed so much to accomplishing my goals. Each of you has been contribute to accomplishment of this research in many ways.

Last, but certainly not least, I am thankful to my small family. I could not have done this without their encouragement, patience, understanding, and sacrifice.

I dedicate this manuscript to my father and my mother,
Muller Silalahi and Senti Ompusunggu,
and to my lovely wife, daughter and son,
Roma Simbolon, Sandrina and Abhyudita Silalahi
who gave unconditional support and tolerated my interminable absence.

# CHAPTER 1
# RESEARCH BACKGROUND, OBJECTIVES AND DATA

## 1.1 Research Background and Scientific Problem

Linked, prograding shelf-slope-basin depositional systems form significant oil and gas reservoirs around the world such as in the Western Siberia Basin, Northwest Slope of Australia, on the North Slope of Alaska, Sakhalin Basin, Russia, and the Lewis Shale of Wyoming. Numerous studies have been carried out on linked shelf-slope-basin depositional systems, most of which use subsurface data including seismic and log data which nicely reveal regional stratigraphic patterns. Examples include the Northwest slope of Australia (Erskine and Vail, 1988 and Donovan, 2003) (Figure 1.1) and the West Siberia Basin (Pinous *et al*., 2001) (Figure 1.2). Subsurface data has many advantages and weaknesses. Seismic data has excellent lateral resolution, however, vertical resolution is limited (Figure 1.1). Conversely, log and core data have excellent vertical resolution, but they are limited in terms of lateral resolution (Figure 1.2). Although seismic, log and core data were utilized together in these studies, due to limited data resolution, the studies still lack reservoir-scale information such facies and stratigraphic architecture. For this reason there remains uncertainty regarding reservoir sedimentary architecture in these systems for petroleum exploration and development purposes. Outcrop data can complement these earlier findings by providing added information of how facies and stratigraphic architectural change down the physiographic profile of prograding systems.

Linked-prograding shelf-slope-basin depositional systems are common; however, few outcrop analogs of these types of systems are known to exist. Examples include the Lewis Shale in Wyoming (Pyles and Slatt, 2006), clinoforms of Spitsbergen (Plink-Bjorklund *et al*., 2005), and the Sobrarbe Formation of Ainsa Basin (Dreyer *et al.*, 1999). Of these three, the Sobrarbe Formation provides the most complete exposure of shelf edge to proximal basin floor strata. Slope channels can be traced in the landward direction to their coeval deltas and in the basinward direction to their coeval fans. The Sobrarbe Formation is also the least studied of these formations. For these reasons, the Sobrarbe Formation is the ideal outcrop to study in order to improve our understanding of

how stratigraphic architecture changes from the shelf edge to the basin floor in prograding systems. The lessons learned are beneficial in reducing uncertainty on reservoir architecture of prograding shelf-slope systems.

### 1.2. Research Objectives

This research is driven by a growing interest in detailed stratigraphic information of linked shelf-slope-basin systems. This study has three objectives:

1. To document changes in stratigraphic architecture from the shelf edge to the basin floor of one parasequence in the Sobrarbe Formation. The parasequence is about 120 meters thick, and crops out over a down-current distance of 10 km.
2. To describe the stratigraphic architecture of proximal, medial and distal slope strata for one parasequence in order to clarify differences in slope channel reservoirs.
3. To test existing hypotheses regarding the timing of slope and basin floor deposition. For example, are slope channels and basin floor fans strictly associated with sea level lowstand, or can they be associated with highstand deposition?

### 1.3. Data

This study documents one parasequence of the Sobrarbe Formation. The study area is 12 km (N-S) by 4 km (E-W) totaling 48 $km^2$. Data collected in this study include parasequence boundaries, strike and dips, measured sections, regional and local photopanels, and geologic map, and channel geometry and paleo current data. These data were used to construct stratigraphic cross-sections to calculate net-to-gross and channel geometry.

A. Parasequence Boundaries

The upper and lower boundaries of the parasequence are plotted on a topographic map. The top and base of the parasequence appear as the finest grain and darkest color interval within the parasequence.

B. Strike and Dips

Strike and dip of bedding data are collected at various locations throughout the field area including the top and base of the parasequence. A total of 100 measurements were collected.

C. Measured Sections

Measured sections collected in this study record vertical change in lithology, grain size, sedimentary structures and bed thickness at the centimeter scale. A total of 967 meters of measured sections were collected in scale 1 cm equal to 1 m. It is consist of six full regional measured sections, four partial regional measured section and 18 channel measured section.

D. Regional and Local Photopanels and Geologic Mapping

Photopanels record a continuous visual record of the outcrop. This research utilizes four regional photo panels that collectively document the continuous outcrop from the shelf edge to basin floor for Parasequence 2. These data are used to record the distribution, temporal and spatial relationship and the number of architectural elements from the shelf edge to basin floor. Five high-resolution photopanels are used to constrain the geometry, internal surfaces and facies of architectural elements at various positions from shelf edge to basin floor. Observations from photopanels are further recorded on the geological map.

E. Channel Geometry

This data set captures channel thickness, the position of channel margins (GPS), position of channel axes (GPS), channel outcrop orientations. The accuracy of position measurement is within 5 meters. This study recorded 64 channel margins, 32 channel axes, and 32 channel thicknesses from a total of 32 channels.

F. Paleo-current Data

Paleo-current direction measured from flutes and grooves at the base of each channel body. This study recorded 487 paleo-currents across slope profile.

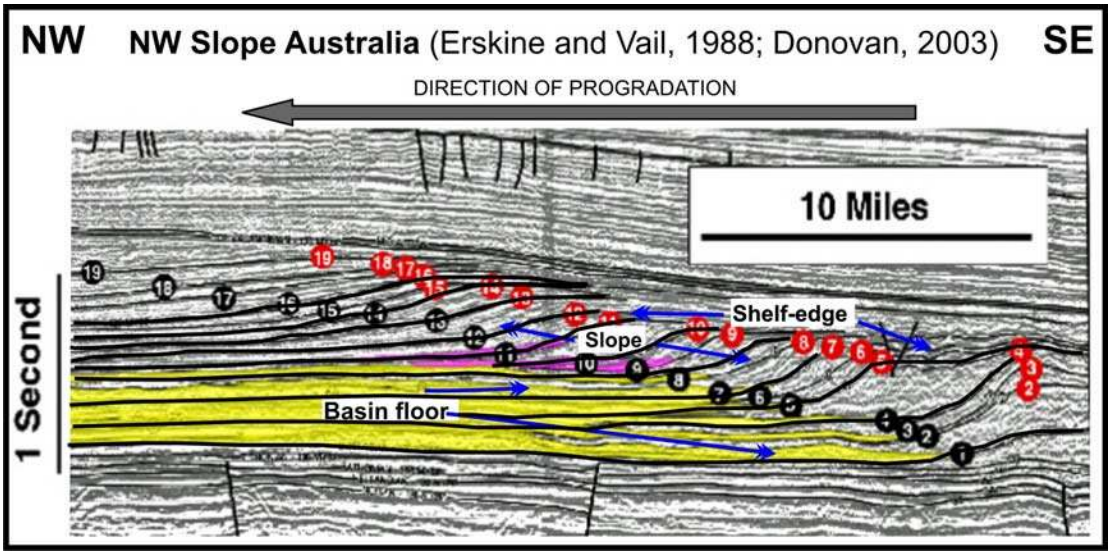


Figure 1.1 Seismic section of NW Slope of Australia showing progradational stacking patterns composed of a linked shelf-slope-basin system (Erskine and Vail, 1988 and Donovan, 2003). Seismic data have good lateral continuity of reflection that define the clinoforms but does not reveal reservoir-scale stratigraphy, including facies and architectural elements.

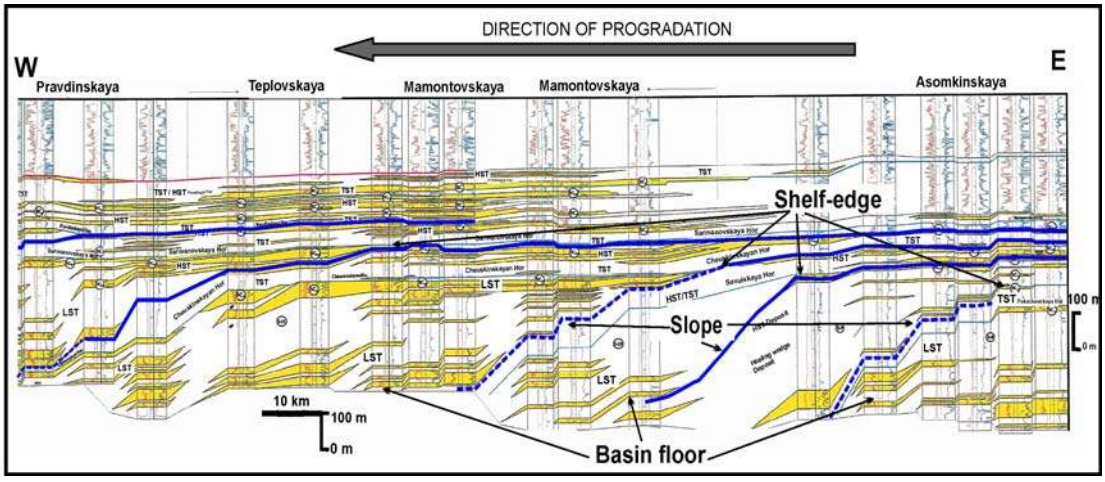


Figure 1.2 Regional cross section from the West Siberian Basin illustrating a linked prograding shelf-slope-basin system (Pinous *et al*., 2001). The cross section is constrained by well logs and reveals the regional stratigraphic pattern, but it does not reveal lateral distribution of reservoir-scale stratigraphic facies and architectural elements.

# CHAPTER 2
# GEOLOGICAL SETTING OF RESEARCH AREA

This chapter reviews the regional geology setting of the research area as published in established studies. This chapter also introduces a new geological map that is based on data collected from recent mapping.

## 2.1 Location

This study focuses on one parasequence of the Sobrarbe Formation in the Ainsa Basin of the Spanish Pyrenees. The outcrops are located in the Huesca Province, 280 km northwest of Barcelona (Figure 2.1). This research focuses on continuous outcrops that reveal coeval strata exposed from Mondot to Urriales (Figure 2.2). The researched area is 12 km (NS) by 4 km (EW).

## 2.2 Regional Tectonic Setting

The formation of the Ainsa Basin is linked to the Pyrenean orogeny which occurred from upper Cretaceous to Oligocene time as a result of continental collision between the Iberian micro-plate and the Eurasian plate (Figure 2.3) (Puigdefabregas *et al.*, 1986). The Pyrenean orogeny was divided into two phases. The earlier phase is ended in the early Cretaceous and is dominated by sinistral strike-slip movement in response to Iberian anticlockwise rotation relative to France (Le Pichon *et al.*, 1970; Fischer 1984 in Farrell *et al.*, 1987). The later phase was active from Paleocene to Oligocene and was dominated by north to south contractional deformation with approximately 100 km of shortening on a southward-propagating thrust system (William & Fischer 1994; William 1985 in Farrell *et al.*, 1987). This tectonic activity created a southward-directed thrust system (Munoz *et al.*, 1986), which indicates more shortening in the southern part of the Pyrenees than the northern part. The floor thrust of the imbricated thrust system also acts as a sole thrust for the Pyrenean Orogeny and is interpreted to be caused by subduction of the Iberian micro-plate below the Eurasian plate (Puigdefabregas and Souquet, 1986).

The Southern Pyrenean thrust system is divided into upper, middle, and lower thrust sheets (Puigdefabregas *et al.*, 1986). The upper thrust sheet, such as the central

south Pyrenean thrust sheet (Pedraforca and Montgri-nappes) developed during early Eocene time and involved Mesozoic cover (Figure 2.3). The middle thrust sheet involved cover sediments and the Hercynian basement (such as Gavarnie and Cadi nappes composed of mostly post-Silurian deposits). The covers sediment consists of Mesozoic and overlaying Paleogene foreland basin sediment. The middle thrust emplaced below the upper thrust sheet (Figure 2.3). The lower thrust involves the pre-Silurian basement and a very reduced Mesozoic cover and is active during late Eocene to Oligocene (Puigdefabregas *et al.*, 1986). Overall, the southward directed fold-thrust system created a series of foreland basins at the southern part of the Pyrenees (Puigdefabregas *et al.*, 1986; Farrell *et al*., 1987).

Two models have been proposed that link the Ainsa Basin to the large South Pyrenean Foreland Basin. Puigdefabregas *et al.* (1986) describe the Ainsa Basin as having formed on top of the Gavarnie Thrust System (middle thrust sheet of Figure 2.3). In contrast, Farrell *et al*. (1987) proposed that the Ainsa Basin was formed by the younger Montsect-Segre Thrust Sheet (early Eocene) (Figure 2.4). The latest regional studies by Choukroune (1992); Soto *et al*. (2002) and Fernandez *et al*. (2004), describe the Ainsa Basin as having occured on top of the lower and younger South Pyrenean Frontal Thrust System (or Barbastro-Balaguer Thrust System by Soto *et al*., 2002; or Garvanie-Siereas Exteriores Thrust system by Fernandez *et al*., 2004) (Figure 2.5). These recent studies similar with Puigdefabregas *et al.* (1986) study result.

**2.3 Ainsa Basin Structure**

The Ainsa Basin was formed by a complex folded-thrust system in the South Pyrenean Foreland Basin (Farrell *et al*., 1987 and Fernandez *et al*., 2004). This basin is dominated by northwest trending imbricated thrust systems and related folds (Farrell *et al*., 1987). The basin is bounded to the west by the Boltana Anticline, to the east by Mediano Anticline, and to the north by Anisclo Anticline (Figure 2.6). The present-day axis of the basin is defined by the Buil Syncline which extends from south to north and opens to form the Buerba and San Vicente Synclines around the Anisclo Anticline (Fernandez *et al*., 2004).

The formation of the anticlines within the Ainsa Basin is not conclusively defined. Previous studies that focus on this subject express very different opinions regarding how the anticlines formed. Farrell *et al*. (1987) describe the Mediano anticline as having been formed in response to the southward moving Montsec Thrust Sheet System. They interpret the west and east parts of the Montsec Thrust System as propagating west and east, respectively (Figure 2.4). These authors interpret the younger thrust sheet to have propagated in the same direction and to have merged with the Montsec Thrust System to create the Boltana Anticline. The latest studies by Fernandez *et al*. (2004) argue that all anticlines are created by propagation of the Gavarnies Thrust Sheet. They further argue that Mediano anticline is formed by east-verging detachment fold, Anisclo anticline by a west-verging fault-propagation fold and the Boltana Anticline also formed by a west-verging fault-propagation fold with sub horizontal axis that extend to north and south of Ainsa Basin (Figure 2.6).

**2.4 Ainsa Basin Stratigraphic Succession**

The stratigraphy of the Ainsa Basin is linked to the South Pyrenean Foreland Basin (SPFB) filling succession. SPFB stratigraphy was deposited during the tectonic events that formed the basin. Puigdefabregas (1986) introduces four divisions to the Pyrenean orogeny that closely related to Ainsa Basin fill succession:

1. Extensional basin rift (Upper Santonian-Maastrichtian).
2. Initiation of tectonic inversion / wrench tectonics (Uppermost Maastrichtian-Paleocene); sedimentation dominated by flexural subsidence rather than thrust loading.
3. Continuing tectonic inversion due to Iberian subduction which created sudden subsidence (Lower to Middle Eocene) with sedimentation mainly occurring within the flexural part due to thrust sheet and loading.
4. High inversion tectonics due to plate convergence (upper Eocene Oligocene); sedimentation affected by reduced basin subsidence.

Stratigraphically, the Ainsa Basin is divided into six major unconformity-bounded formations referred to as the Hecho Group (Mutti *et al*., 1988). More recent studies by Pickering and Corregidor (2005) and Fernandez *et al*. (2004) divide the Hecho group into

seven formations which are, from oldest to youngest (Figure 2.7): 1) Posado 2) Arro-Charo, 3) Gerbe, 4) Banaston, 5) Ainsa, 6) Morillo, and 7) Guaso. Each formation is greater than 100-200 m thick. Internally they are muddy formations that have isolated sand bodies, typically tens of meters thick. The depocenters of each succession formation step progressively to the southwest (Figure 2.7). The Sobrarbe Formation overlies the Hecho Group.

Several studies have focused on determining the ages for strata in the Ainsa Basin fill succession. Berggren *et al.* (1995) used planktonic foraminifera zonation and recently, by using the same methods, Gradstein and Ogg. (2004) published a new time scale to date the Ainsa Basin fill succession from early to middle Eocene (Cusian-Ypresian and Lutetian Stages) (Figure 2.7). Using these dates, they conclude that the deep-marine strata of Ainsa Basin records 10-12 million years of deposition. The latest study by Labourdette *et al*. (2008), adds fluvio-deltaic of Sobrarbe and Escanilla Formation into Ainsa Basin strata which overlying Guaso Formations (Figure 2.8a). The Sobrarbe Formation is placed in the Lower TSU-5 (Middle Eocene, Upper Lutetian) (Figure 2.8b).

**2.5 Sobrarbe Formation**

The Sobrarbre Formation records the final depositional phase of the Ainsa Basin. It was deposited as part of a prograding deltaic system during the evolution of a lateral thrust ramp represented by the intrabasinal Boltana growth anticline (from middle to upper Eocene) within the Ainsa Basin (Dreyer *et al*., 1999). This formation is part of the large sediment dispersal system of the South Pyrenees Foreland Basin. It is underlain by marls and turbidite sandstones of the Hecho Group, which Dreyer *et al.* (1999) referred to as the San Vicente Formation, and is overlain by and laterally interfingers with the Escanilla Formation. The Sobrarbe Formation is deposited within a linked fluvial, deltaic, deepwater slope depositional setting (Figures 2.9 and 2.10). Overall, the sediment packages are interpreted as regressive deposits (Dreyer *et al*., 1999).

The Sobrarbre Formation is characterized by cyclical alternation between muddy delta slope, delta front sandstone, collapsed complexes, carbonate and mudstone-dominated delta plain deposits. This formation is stratigraphically divided into four

major composite sequences (CS) (Figure 2.10) (Dreyer *et al*., 1999). Each consists of minor lowstand, transgressive and highstand components (Dreyer *et al*., 1999). The four composite sequences are Comaron CS, Las Gorgas CS, Barranco el Solano CS and Buil CS. The Comaron CS is characterized by a WNW-prograding deltaic system and consists of six minor sequences (Figure 2.10). The Las Gorgas CS is characterized by a dominant regressive sandstone wedge of syngrowth strata (Figure 2.10). This composite sequence was strongly influenced by the growth of the Boltana Anticline and intrabasinal Arcusa Anticline. The transition of upper Las Gorgas CS to Baranco el Solano CS is characterized the deposition of large collapse delta front deposits. Barranco el Solano form a dominantly carbonate deposits, overlain by a progradational mix of clastic carbonate such as nummulites bank, shoreface marl and sandstone. The Buil composite sequence is characterized by coarse sediment deposits that are the results of coastal plain erosion during uplift of Ainsa Basin. This composite sequence records a change from marine to fully continental (fluvial) depositional environment (Dreyer *et al*., 1999). More recent un-published work by Pyles and Clark (2007) divide the Comaron Sequence into three flooding surface bounded parasequences. This study focuses on Parasequence 2 of Pyles and Clark (2007), which is the best exposed parasequence in the Comaron CS (Figure 2.10 and 2.11). Outcrops of Parasequence 2 show strata deposited contemporaneously along the fluvial, delta, slope and toe of slope profile. This study focuses on the upper slope to base-of-slope strata of Parasequence 2.

## 2.6 Geologic Map of Research Area

This research focuses on reservoir-scale architecture of slope strata in Parasequence 2. Geologic mapping defined the upper and lower bounding surface of Parasequence 2 as wells as the lower contact of the Sobrarbe Formation (Figure 2.12). The map reveals that some structures influenced the outcrop's exposures such as slump structure, the Boltana anticline and a large monocline. The slump structures are observed in the northern part of the research area, from Arcusa to Rio Enya area. The slump feature is shown as an unconformity surface on the top of Parasequence 2 (Figure 2.12 and 2.13) in Arcusa. The slump removes the distal-most basinal strata of parasequence. The other indication of these slump structures are slided shallow water

sediment blocks located directly above deep marine sediment at outcrops close to Rio Enya (Figure 2.12 and 2.14). Both monocline and Boltana Anticline located in the northern part of the field area (Figure 2.12), creates a drastic change of bedding dips within the study area.

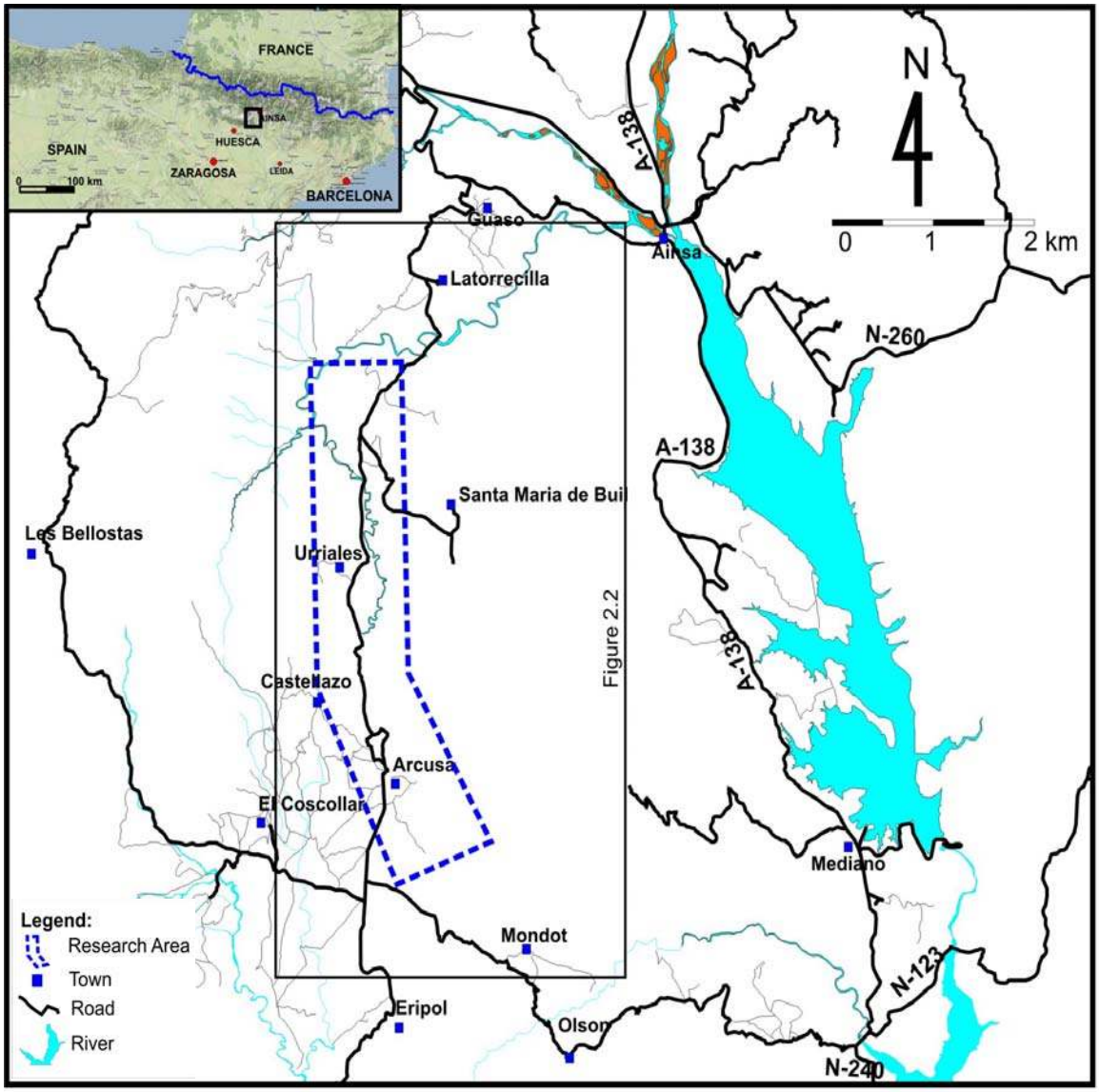


Figure 2.1 Regional map showing the location of the study area near Ainsa, Spain about 180 km northwest of Barcelona.

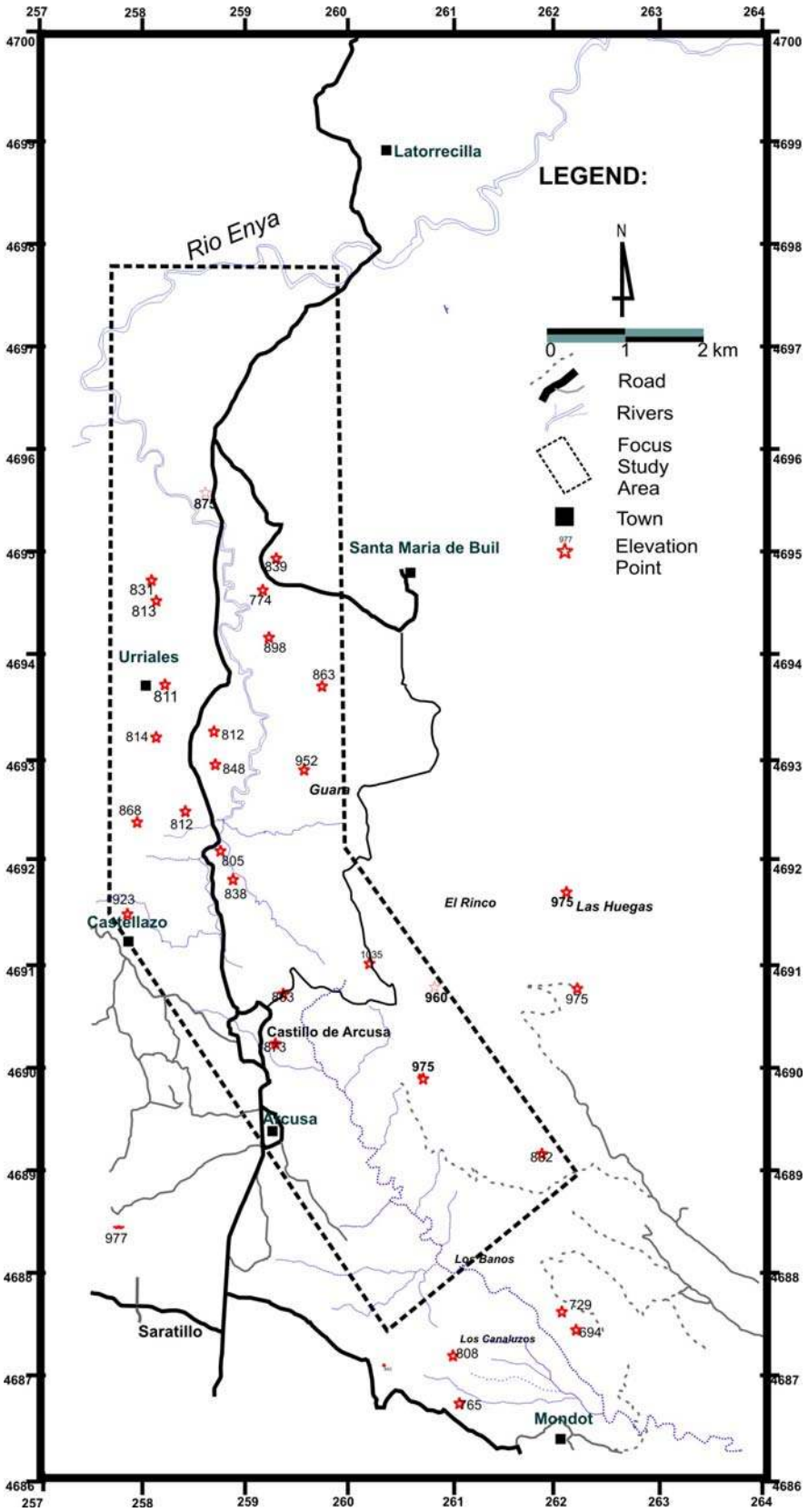


Figure 2.2 Simplified geographic map of the study area (location shown in Figure 2.1).

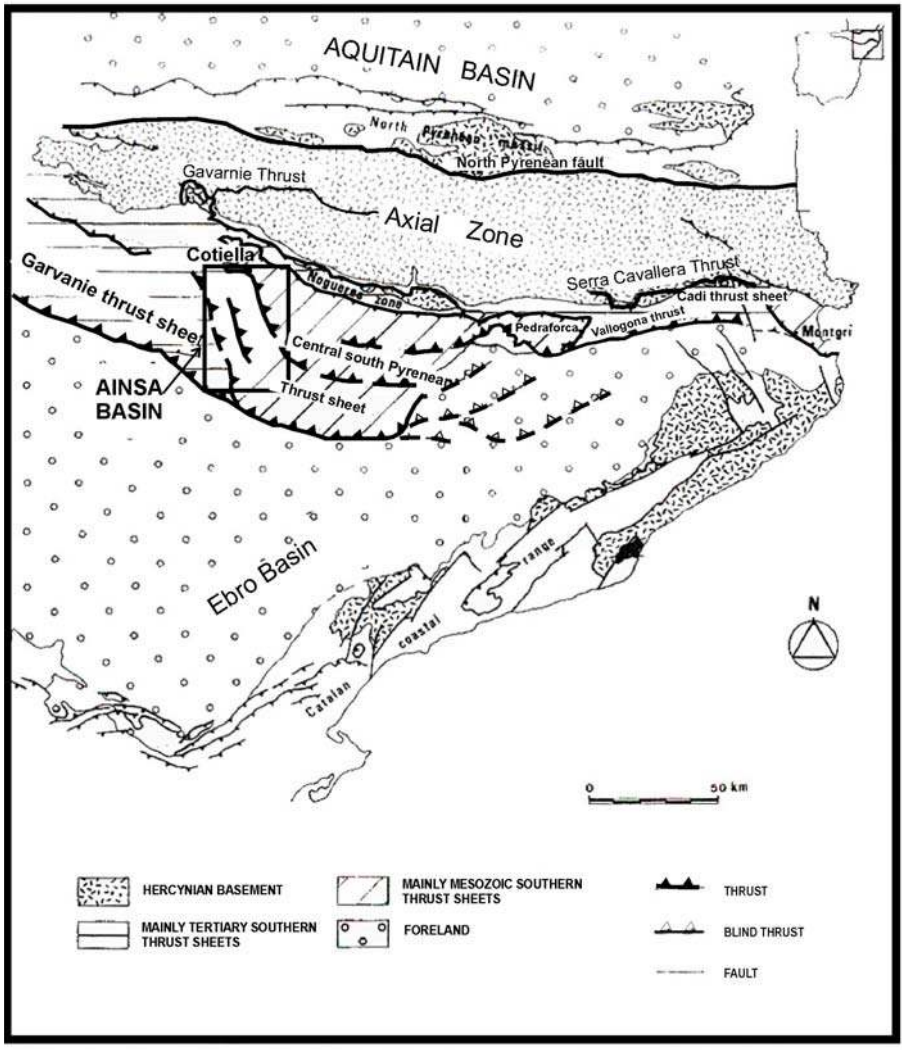


Figure 2.3 Structural map of the eastern part of the Pyreneans. This map shows the Pyrenean Foreland Basin by Puigdefabregas *et al.* (1986). The Ainsa Basin is located on top of the Gavarnie Thrust Sheet and is bounded to the east by Cotiella Thrust System.

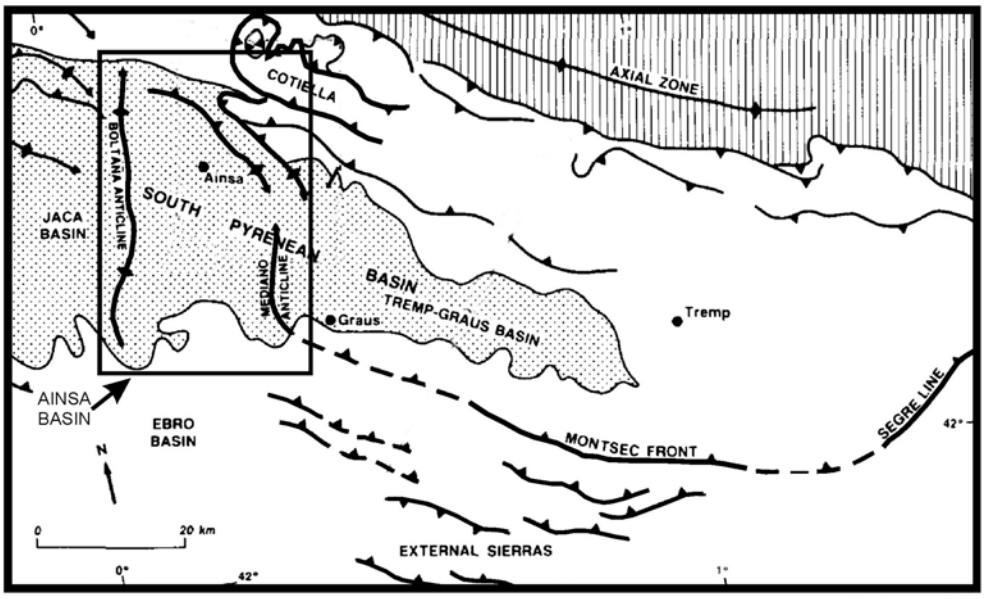


Figure 2.4 Structural map showing regional thrust sheet system within the South Pyrenean Foreland Basin by Farrell *et al*. (1987). The Ainsa Basin was interpreted to have been emplaced above the Montsec-Segre Thrust Sheet. This basin is bounded by the Cotiella Thrust System (north-northwest), Mediano Anticline (east) and Boltana Anticline (west). Farrell *et al*. (1987) interpreted the Mediano and Boltana Anticline as part of the Montsec Thrust System.

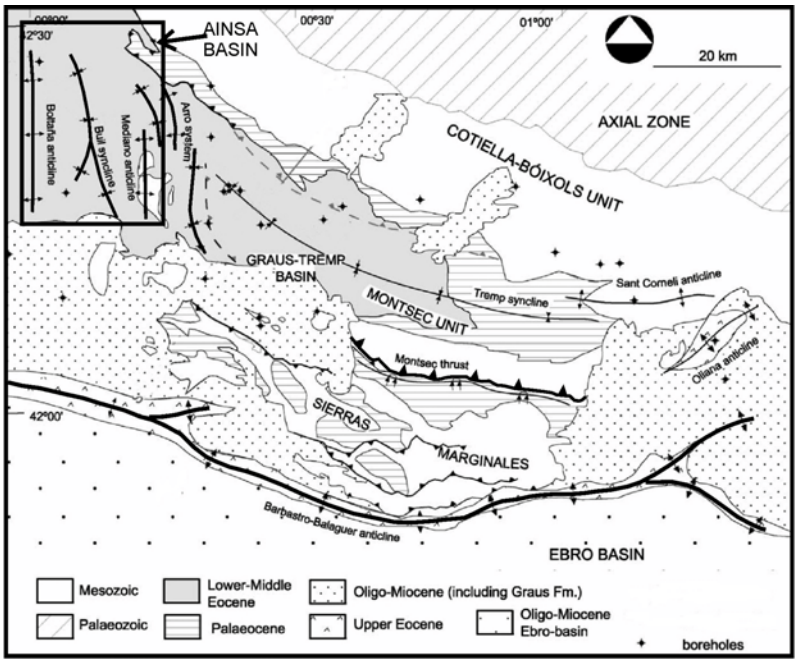


Figure 2.5 Structural map showing the regional thrust sheet system of the South Pyrenean Foreland Basin by Soto *et al*. (2002). The Ainsa Basin is located on top of the younger Barbastro-Balaguer Thrust Sheet (similar to South Pyrenean Frontal Thrust System by Choukroune, 1992).

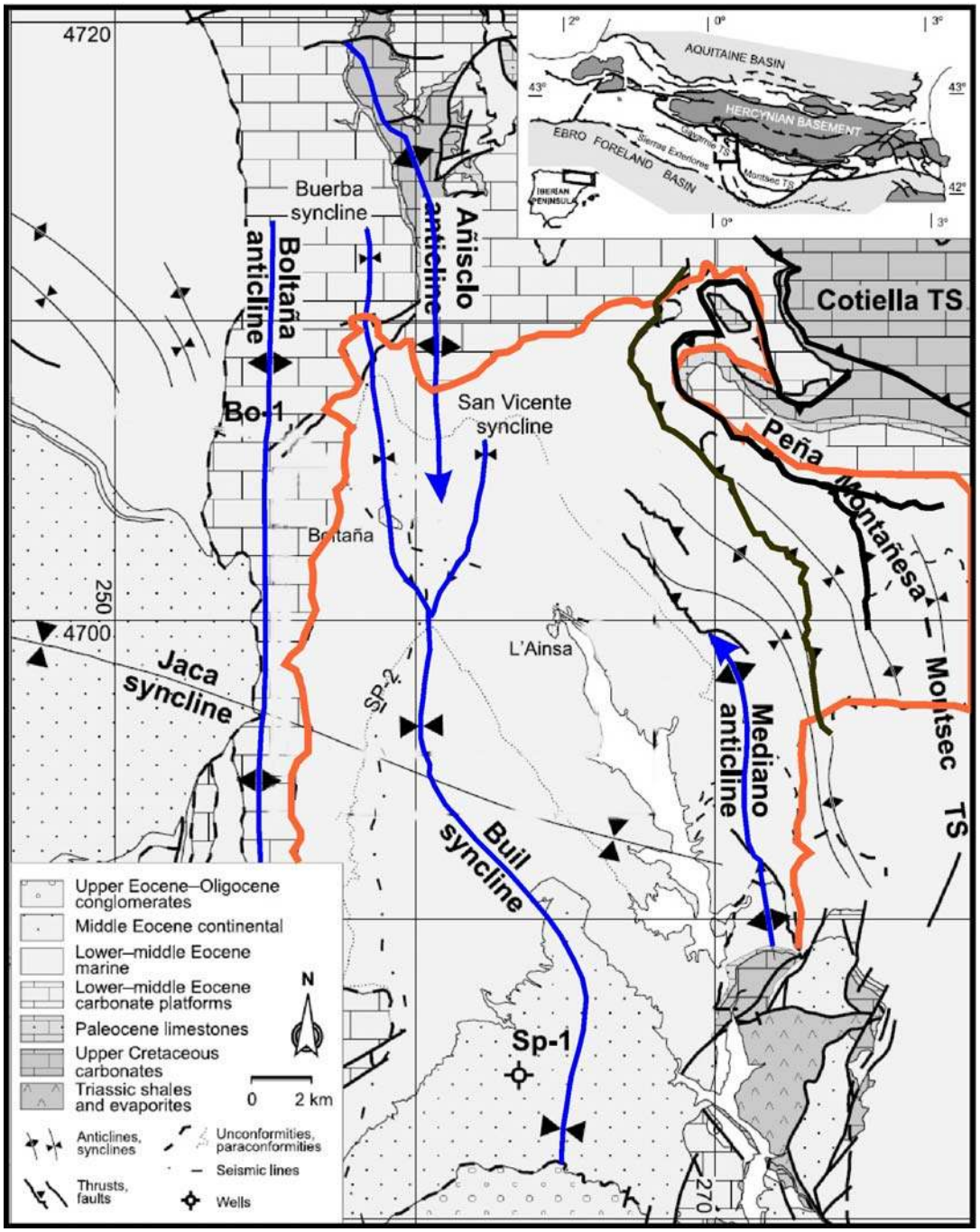


Figure 2.6 Structure map of the Ainsa Basin (Fernandez *et al*., 2004) showing the major structure in the basin. The strikes anticlinal and synclinal axial tracers at Ainsa Basin (N-S) differ from the regional South Pyrenean structure (E-W) shown in Figures 2.3, 2.4 and 2.5.

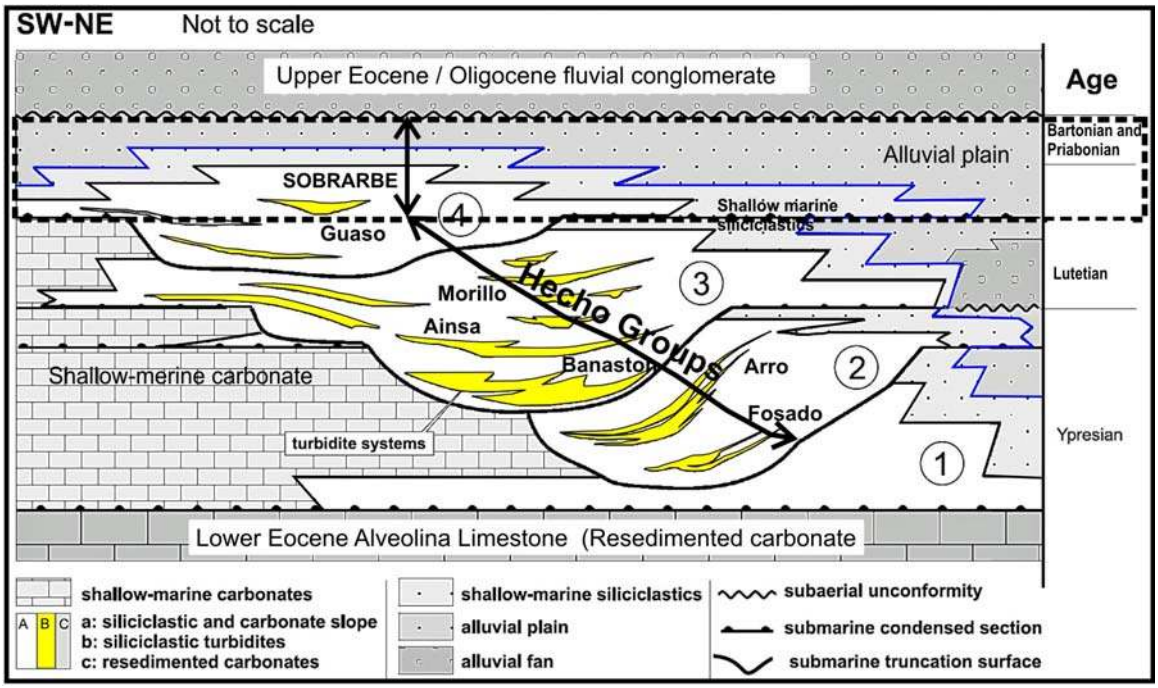


Figure 2.7 Ainsa Basin stratigraphic succession composed of seven formations of deep marine deposits from Fosado (older) to Sobrarbe (younger). This schematic diagram shows the unconformity-bounded units (number 1 to 4 in this figures) described by Mutti *et al*. (1985). The Sobrarbe Formation overlies the Guaso Formation and is indicated by the black box. Modified from Pickering and Corregidor (2005) and Fernandez *et al*. (2004).

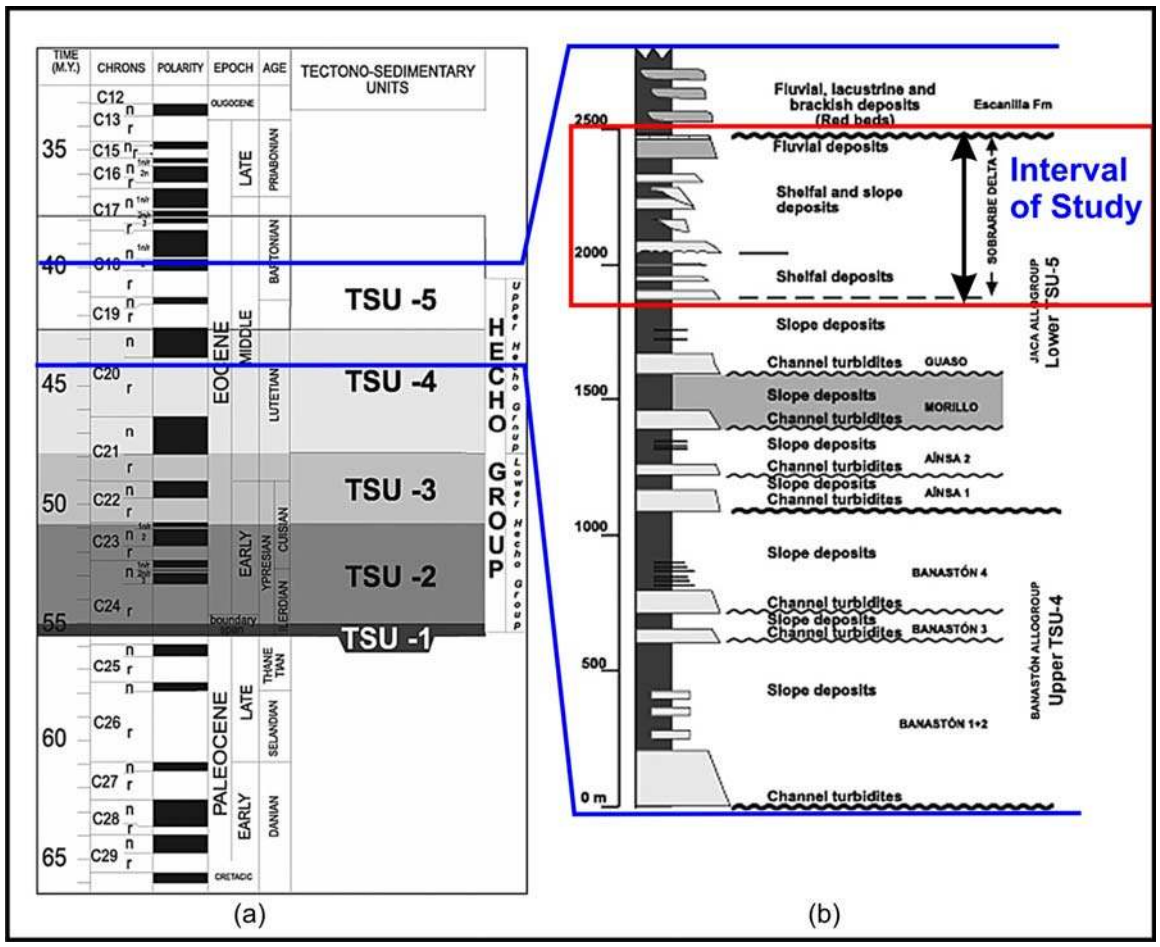


Figure 2.8 Chronostratigraphic chart of Eocene South-Pyrenean Foreland Basin. (A) Chronostratigraphic chart that divides the base of Tectono Sedimentary Unit by Labourdette *et al*., (2008) (modified from Remacha, 2003). (B) Stratigraphic column from the Santa Maria de Buil area that represents the stratigraphic succession from Banaston to Escanilla Formation (Labourdette *et al*., 2008). The research area focuses on the Sobrarbre Formation.

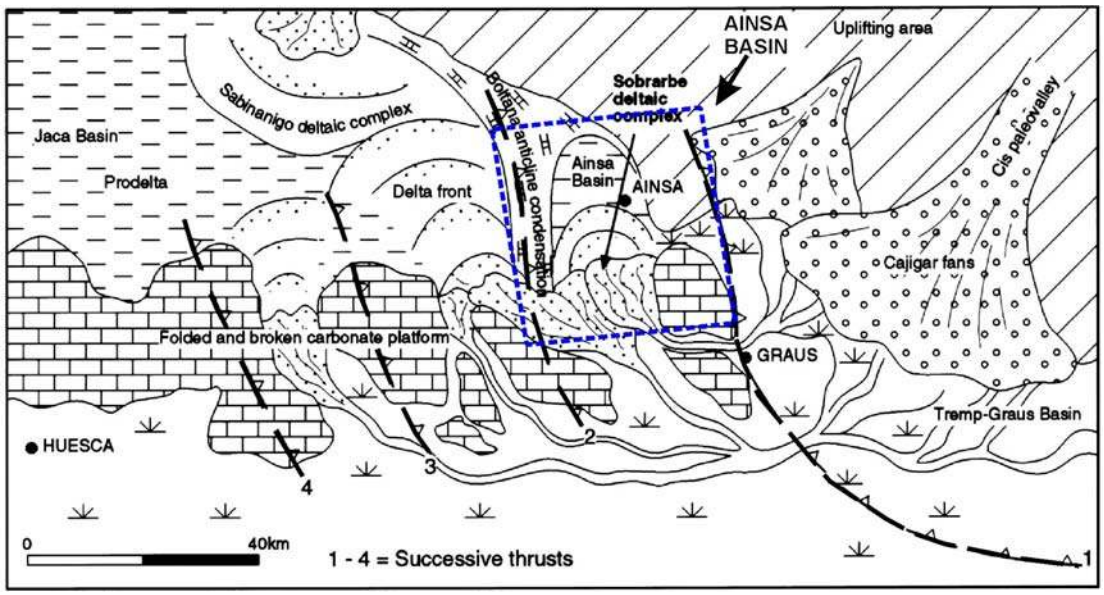


Figure 2.9 Paleo-geographic map of the Ainsa Basin during Late Lutetian. This map shows the Sobrarbe Formation deposition as a fluvial-deltaic system linked to a deepwater basin setting to the north (Dreyer *et al*., 1999).

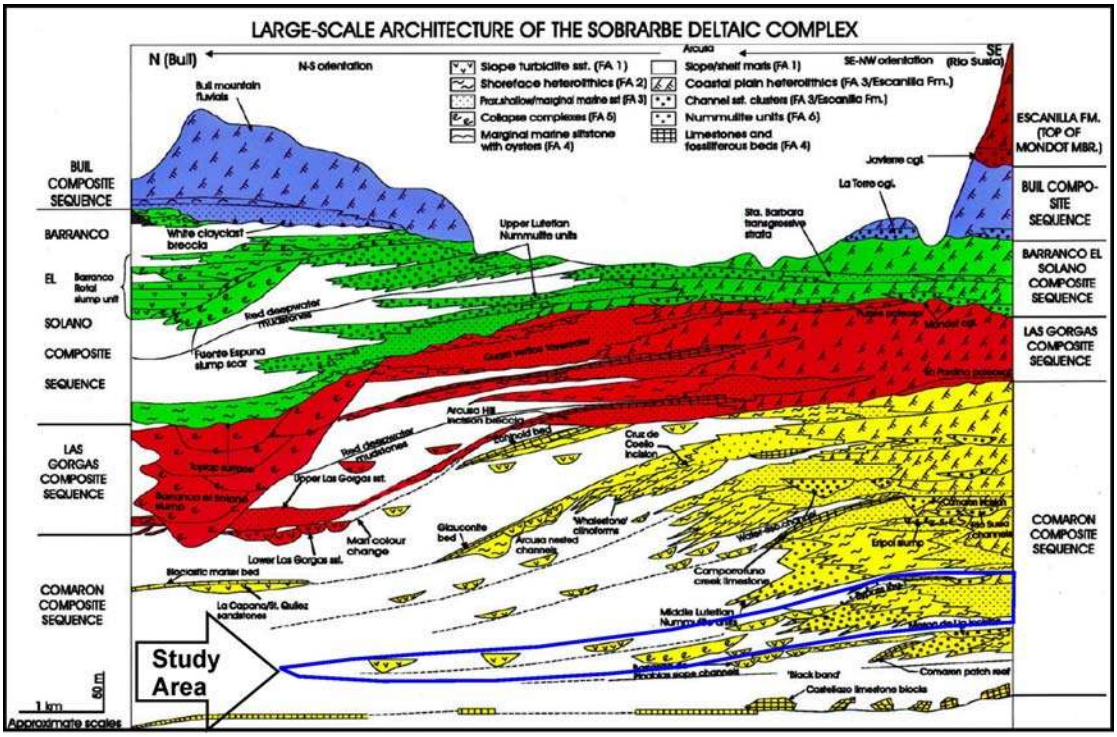


Figure 2.10 Stratigraphic cross section of the Sobrarbe Formation (Dreyer *et al.*, 1999). Dreyer *et al.* (1999) divided the Sobrarbe into four composite sequences. This Study focuses on Parasequence 2 of the Comaron Composite Sequence

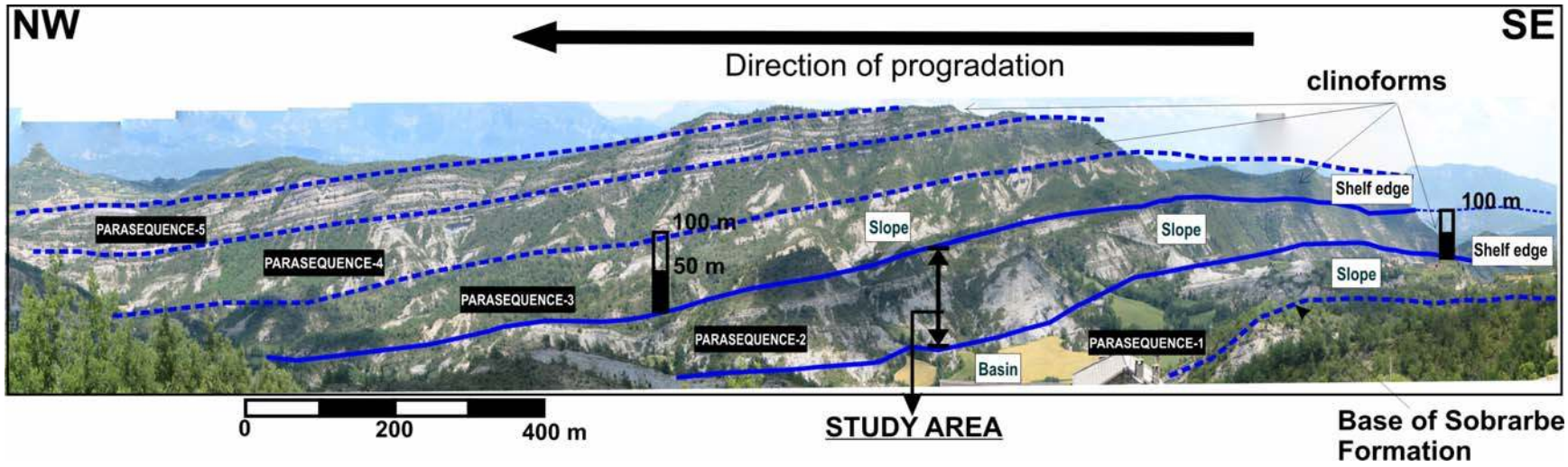


Figure 2.11 Photographs of the Sobrarbe Formation cropping out along at the western part of Santa Maria de Buil syncline. The outcrops reveal a progradational pattern that exposes continuous shelf-slope-basin strata. Parasequence 2 is the most continuous and best exposed parasequence, and it is the focus of study in this research.

19

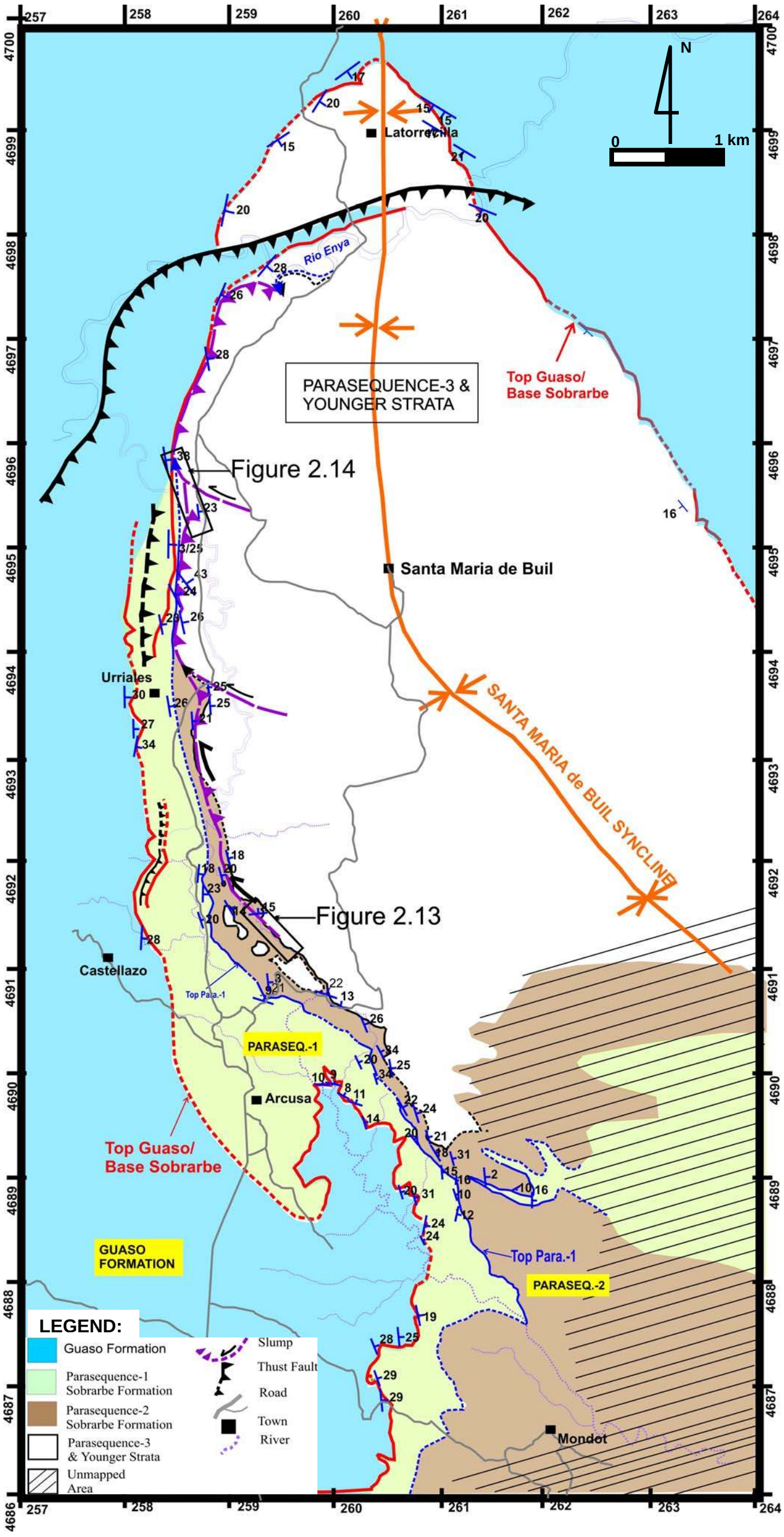


Figure 2.12 Geological Map of Research Area

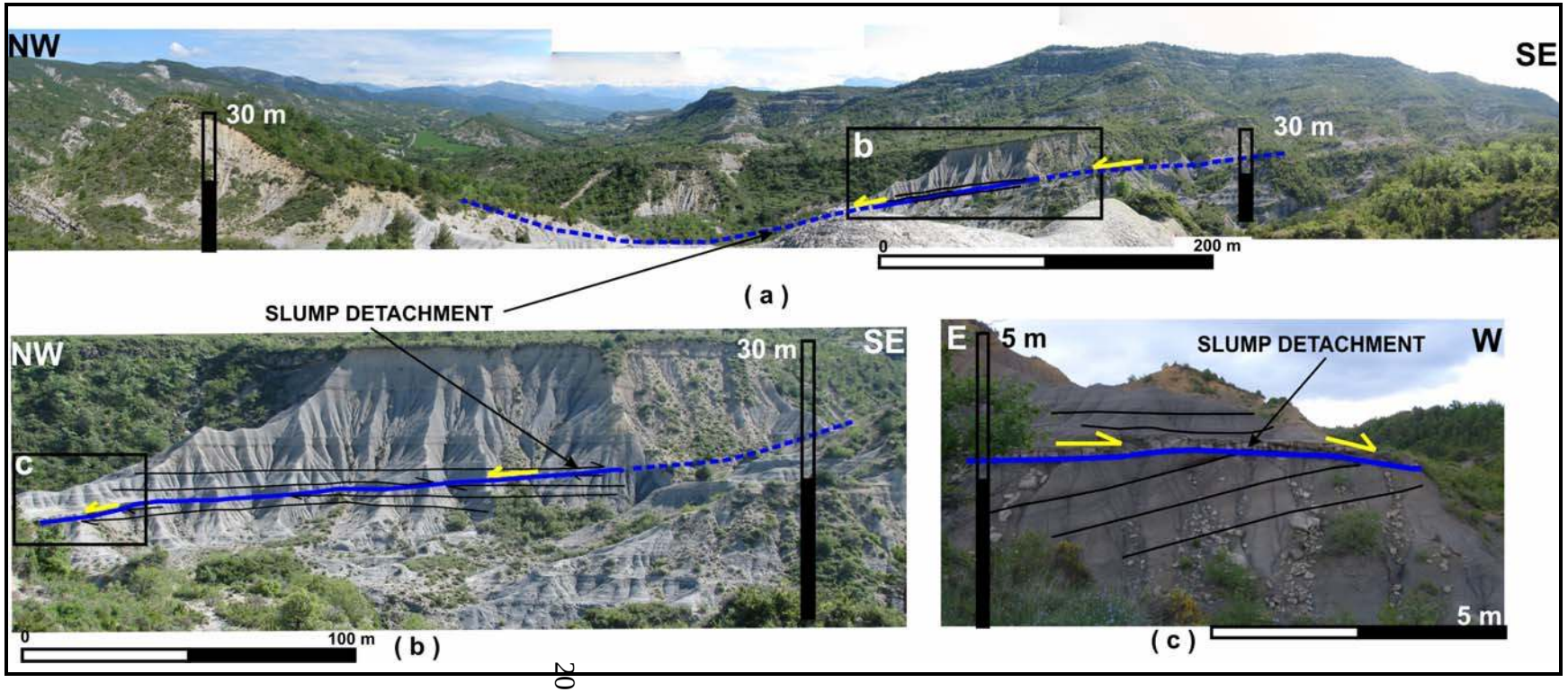


Figure 2.13 Photographs of slumped area that indicated by angular unconformity. Locations of photographs are shown in Figure 2.12.



21

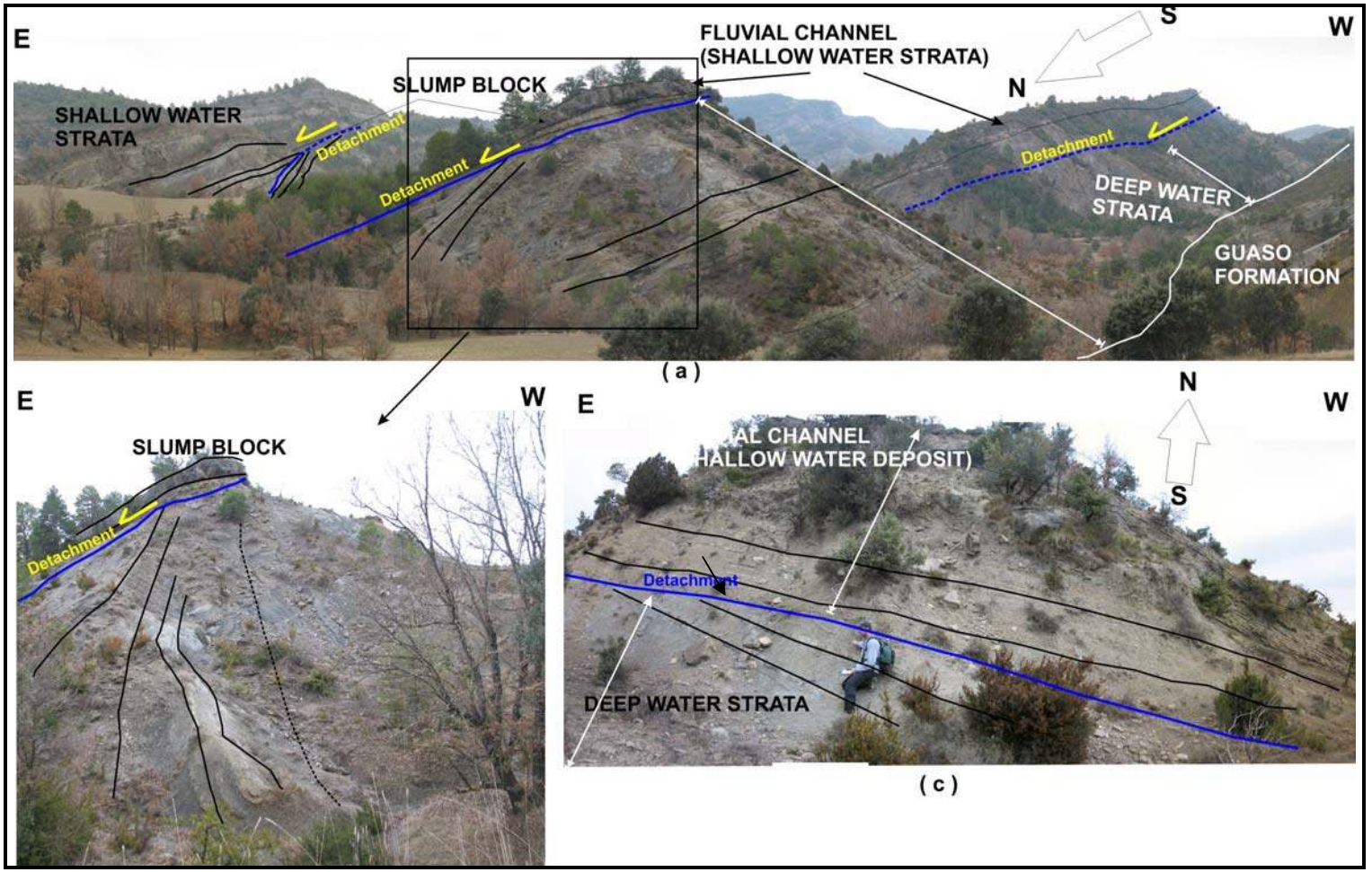


Figure 2.14 Photographs of slumped area showing shallow water strata (fluvial channel deposits) above dipping beds of deepwater strata of the Sobrarbe Formation (angular unconformity)

# CHAPTER 3
# SEDIMENT GRAVITY FLOW PROCESS AND FACIES

This chapter provides an overview of deepwater sediment gravity flow processes as well as description and interpretation of facies observed in the study area.

## 3.1. Deepwater Sediment Delivery Process

The Sobrarbe Formation was deposited across a linked river-delta-slope system. This thesis focuses on the sedimentology of slope strata for one parasequence. This section provides an overview of depositional processes of deepwater slope strata with particular emphasis on fluid and sediment gravity flows.

Fluid and sediment gravity flows differ in their flow mechanisms. In a fluid gravity flow, the fluid is moved by gravity which drives the sediment. In contrast, in sediment gravity flows, the sediments are moved by the force of gravity, and the interstitial fluid is carried along with the sediment (Middleton and Hampton, 1973). Sediment gravity flows also tend to entrain ambient fluid along with them. Since both flows are most likely co-genetic, it is very difficult to definitively differentiate the two processes (Middleton and Hampton, 1973). In this chapter, these flows are discussed separately to emphasis the role of fluvial-deltaic processes on slope deposition.

### 3.1.1 Fluid Gravity Flows

A fluid gravity flow is driven by fluidal movement in response to the force of gravity (Middleton and Hampton, 1973). Fluid gravity flows can create laminar flow and turbulent flow. Fluid is the main media that drives sediment movement through suspension and bed load (traction) (Friedman *et al.,* 1992; Boggs, 1995). Sediment in the bed load is transported by traction mechanisms such as rolling, saltating, sliding, and creeping (Friedman *et al.*, 1992; Pye, 1994). Traction is initiated by the movement of the ambient fluid. Overall, the main sediment support mechanism for the suspended fraction of the flow is fluid turbulence, dispersive pressure and possibly hindered settling.

Fluid gravity flows have an important role in initiating submarine flows, particularly in areas where fluvial/delta systems discharge sediment directly at the shelf-

edge. Fluid gravity flows are divided into three types based on density differences between river discharge and ambient sea water. Hyperpycnal flows occur when the river water is denser than the ambient sea water; homopycnal flows occur when there is an equal fluid density of river and sea water; hypopycnal flows occur when the river water is less dense than the sea water that it enters (Figure 3.1) (Reading, 1996). All these flows are responsible as sediment delivery systems into slope basin. Hypopycnal flow commonly constitutes a suspended muddy plume that bypasses the mouth bar basinward (Bhattacharya, 2006). The muddy plume is created from the suspension part of fluvial flow whereas bedload part of the flow forms a mouth bar during flow expansion at river mouth (Bhattacharya, 2006). This plume controls muddier sediment transported the slope basin.

Hyperpycnal flow is one of effective flow for depositing sand-sized particles in linked fluvial deltaic to deepwater setting. Hyperpycnal flow forms when high density suspended materials in river water reach the seashore and create a submarine hyperpycnal plume. The flow commonly forms at the river mouth (medium to small rivers) during flooding or in extreme events such as jokulhaups, dam breaking and lahars (Mulder *et al.,* 2003; Khan *et al.,* 2005). The hyperpycnal deposit (hyperpycnite), which is interpreted to record the waxing then waning energy of the associated flood, is characterized by a coarsening upward unit at the base (waxing period) and fining-up deposits at the top (waning period) (Mulder *et al.,* 2003).

### 3.1.2 Sediment Gravity Flow Processes and Deposits

There is a continuum of sediment gravity flows that ranges in sediment concentration and sediment support mechanisms. From low to high concentration they are: turbidity current, liquefied flow, grain flow and debris flow (Prior and Coleman, 1984) (Figure 3.2). The deposits of each are unique.

#### *a. Turbidity Current*

Turbidity currents have been defined by a number of authors (Sanders, 1965; Middleton and Hampton, 1973; and Lowe, 1982) as flows that are driven by the force of gravity and which entrain and suspend sediment by fluid turbulence. Shanmugam (1997)

stresses this definition by limiting turbidity flows within turbulent sediment support mechanisms only, while other sediment support mechanisms are excluded. Other authors such as Lowe (1982) and Kneller and Buckee (2000) emphasize that other sediment support mechanisms such as hindered settling, dispersive pressure, buoyant lift and fluid turbulence can all operate in turbidity currents. Various interactions of sediment support mechanisms within turbidity currents allow them to entrain and transport a wide range of grain-sizes (silt to granule / pebble). Kneller and Buckee (2000) use these observations to redefine turbidity current as "flow induced by the action of gravity upon a (fluidal) turbid mixture of fluid and (suspended) sediment, by virtue of the density difference between the mixture and the ambient fluid." Turbidity flows are capable of eroding the seafloor at the locus of the flow head and can entrain water at the top of the flow (Figure 3.3). While traveling down the slope, the density of the flow is always changing in response to erosion, deposition and water entrainment. The erosion and deposition rates control flow sustainability. The flow will be sustained when the erosion rate is larger than the deposition rate, and it will die when the erosion rate is smaller than the deposition rate (Pratson *et al*., 2000).

***b. Liquefied Flow***

Liquefied flows are part of the sediment gravity flow continuum (Figure 3.2). The liquefied flow is generated in response to sudden changes of cohesionless sediment from matrix supported to a suspension supported flow. This process causes the sediment to lose shear strength and behave as a highly-viscous fluid that can flow rapidly down a slope (Boggs, 1995). The sudden change from matrix-supported to suspension-supported flow is likely related to slope instability or a spontaneous process, such as earthquakes (Prior and Coleman, 1984; Boggs, 1995). Most authors describe the liquefied flow as essentially the same as the fluidized flow, however Lowe (1976) state that the liquefied flows are more likely to have turbulent process acting within them.

The sediment support mechanism for liquefied flow is dominantly dispersive pressure with a minor amount of fluid turbulence (Lowe, 1976). The flows can be sustained as long as the sediment grains interact. When the grains reestablish grain-to-grain contact; the flow freezes (Boggs, 1995). Sediment deposition within this flow occurs very rapidly, especially when the flow is thick and is composed of fine-grained

sediment. Rapid deposition creates dish structures in response to water escaping from the sediment (Figure 3.2). Both Lowe (1976) and Boggs (1995) imply that this flow type could evolve into turbidity current when the flow accelerates and entrains more water than sediment.

***c. Grain Flow***

Grain flow is part of the sediment gravity flow continuum commonly associated with steep slope conditions (Figure 3.2). This flow is described as sediment movement that involves loose sand grains (cohesionless sediment) supported in the flow by grain-to-grain interaction or dispersive pressure (Prior and Coleman, 1984; Boggs, 1995). This type of flow is initially dominated by traction which evolves into a grain flow when the shear strength of sediment becomes less than gravity force.

Lowe (1976) suggests that a pure single grain flow can produce deposits of not more than a few centimeters. The deposit is characterized by reverse grading from fine to coarse grain-size because the finer grains are filtered first during the flow (Figure 3.2). Boggs (1995) concluded that grain flows happen very quickly, and they end by sudden freezing in response to slope angle changes.

***d. Debris Flow***

Debris flow is one of two end members of the sediment gravity flow continuum (Figure 3.2). These flows have been described by many authors who are divided into two groups based on their definition of debris flow. The first group stresses the importance of the sediment-fluid composition to define the flow (Middleton and Hampton, 1973 and Mohrig *et al.*, 1998). Middleton and Hampton (1973) defines debris flow as “a flow in the form of sluggish down-slope movements that consists of mixture solid grains (sand grains, boulders), clay minerals and water in response to the pull of gravity.” Mohrig *et al.* (1998) defines debris flow as “a gravity-driven flow of mixtures of solids and fluids for which the volume concentration of each phase is of the same order of magnitude.” The second group defines the flow based on flow rheology. Prior and Coleman (1984) define a debris flow as “a mixture of interstitial fluid and fine sediment that has a finite yield strength.” Boggs (1995) describes debris flow as a Bingham plastic fluid and emphasizes that flow will initiate if the gravity force overcomes the yield strength. Shanmugam (2000) describes debris flows as a “sediment gravity flow with plastic

rheology and a laminar state from which deposition occurs through frictional freezing." In summary, debris flows are flows driven by gravity that have relatively high sediment concentration and which behave as Bingham plastic within a laminar state. The Bingham plastic results from cohesive clay in the fluid-grain mixture and creates the yield/matrix strength which operates the sediment support mechanism.

A detailed description of a debris flow's anatomy was published by Pratson *et al.* (2000) through numerical and mathematical modeling. This model encapsulates the fundamental physics of debris flows from observed and interpreted sedimentology and stratigraphy of field and laboratory data. Pratson *et al.* (2000) describe a debris flow as consisting of a plug-flow (upper part) and a shear-flow region (lower part) (Figure 3.4). The vertical velocity profile in a debris flow progressively increases upward in the shear region as a result of laminar flow in the base of the flows. In this zone, shear stress exceeds shear strength. In contrast, the vertical velocity profile in the plug region is uniform; in this zone shear strength exceeds shear stress (Figure 3.4). In hydroplaning conditions, such as those described by Mohrig *et al.* (1988), the debris flow consists only of a plug layer due to the presence of an interface of a thin water layer between the base of the flow and the bed that dismisses the basal friction. The thin water layer is the result of incomplete ambient water displacement by the flow (Mohrig *et al.*, 1998).

Debris flow sustainability is a function of the force of gravity and depends on the flow shear strength, density and slope steepness. A higher initial flow density and steeper slope will result in higher momentum of the flow that will, in turn, create a longer sustained debris flow. The flow will eventually die or stop when the frictional force becomes larger than the gravity force (Pratson *et al.*, 2000). Alternatively, Mohrig *et al.* (1998) create hydroplaning debris flow in physical experiments. They conclude that hydroplaning debris flows are capable of being transported far into the basin, beyond that of non-hydroplaning flow.

### 3.1.3 Facies Models for Sediment Gravity Flows

Numerous authors have proposed facies models for sediment gravity-flow deposits. Gressly (1938) defines sedimentary facies as "the sum of all primary lithological and paleontological characteristics of a body of rock which differentiate it

from adjacent bodies of rock, both laterally and vertically." Moreover, facies terms can be modified into specific rock characteristic interests such as lithofacies (physical make-up of rock), ichnofacies (trace fossil content) and biofacies (flora and fauna content). In this research, the facies concept has an important role in interpreting the stratigraphic record.

Application of the facies concept to deepwater interpretation was established in 1959 (see summary in Middleton and Hampton, 1973). Since then, several authors have published facies classification schemes for sediment gravity-flow deposits. These schemes are especially powerful because they can be used to predict facies changes from the proximal to the distal part of sediment gravity-flow deposits. The four most commonly cited facies schemes are Bouma (1962), Lowe (1982), Mutti and Nomark (1991) and Kneller (1995).

The Bouma Facies Model is based on field observations, and it defines a single turbidite depositional sequence as one flow event that is waning and depletive (Figure 3.5). Bouma proposed a vertical profile (later known as the Bouma Sequence) and map (later known as depositional cone) to illustrate how turbidity-current deposits vary through time and space. The proximal part of a turbidite is dominated by coarse-grained deposits, whereas the distal deposits are relatively fine grained. A vertical facies succession in a turbidite follows the same pattern (Figure 3.5) as proximal to distal facies changes thereby conforming to Walter's Law of the Correlation of Facies (Figure 3.5 a).

Lowe's (1982) facies model describes sediment gravity flow deposits on the basis of interpreted bed aggradational rate. This model divides facies into three grain size populations: (1) pebble-to-cobble-size clast, (2) coarse-grained sand to small-pebble-size clast, (3) clay, silt, fine to medium grained sand. This model emphasizes that flows laterally evolve from cohesive flow to grain flow to turbulent flow. Corresponding to this flow evolution, deposition occurs by frictional freezing, traction, and suspension deposition respectively, Lowe concludes that distinct sediment-support mechanisms operate within different grain-size populations. A summary of Lowe's flow evolution and depositional processes is shown on his facies scheme (Figure 3.6).

Mutti and Nomark's (1991) model describes facies distribution as a function of spatial flow evolution. Flow initiation is controlled by both slope failure and the direct

discharge of river flood to the basin (Mutti and Nomark, 1991). Mutti *et al.* (1999) describe sediment-gravity flows as deriving from river hyperpycnal flow and deepwater processes, and sediment liquefaction flow in fluvial drainage as being initially formed by slides during flooding. The sediment liquefaction flow then evolves to form a heavy hyperpycnal flow upon arriving in sea water (F3 to F5 of Figure 3.7). It then evolves into submarine granular flow at the proximal, and continues to evolve by generating bipartite current: debris flow and turbidity current. Deposition of debris flow is caused by loss of pore pressure due to water-escaping, triggering the flow to freeze. The finer grains within the turbidity current will overtake the debris flow, and will be deposited further in the basin. Mutti *et al.* (1999) interpret this process to result in spatially reduced grain-size population due to waning flow. Mutti *et al.*'s model, as well as Lowe's, also divides grain size in their facies classification into (A) boulder to small pebble-size clast, (B) small pebbles to coarse sand, (C) medium to fine sand, (D) fine sand to mud. Overall, Mutti *et al.*'s model divides sediment gravity flows into nine facies that are summarized along with process and sediment support mechanisms in Figure 3.8 (Mutti and Nomark, 1991; Mutti *et al.*, 1999).

Kneller (1995) published an acceleration matrix which uses flow non-uniformity (accumulative and depletive) and flow unsteadiness (waxing and waning) to classify turbidite facies (Figure 3.9, 3.10). The matrix describes how turbidity currents spatially and temporally evolve. Kneller further describes the behavior of facies as they encounter topographic obstacles that could create flow deflection and flow stratification.

Kneller and McCafferey (2003) added to the above concept by describing how facies change down the physiographic profile (Figure 3.11) which is interpreted to result from the longitudinal velocity profile of turbidity current. Longitudinal velocity structure of the current is created by flow unsteadiness, and longitudinal density structure in the flow is produced by differences in flow concentration. This model (Figure 3.11) relates sediment deposition to loss of competence and capacity, both of which are governed by flow velocity and sediment concentration. Kneller and McCafferey (2003) also introduces facies distributions based on depletive (non-uniform) flow and waning (unsteady) flow (Figure 3.11). In a depletive flow scenario (Figure 3.11A), a single competent flow begins with bypass (erosion) and is followed by deposition when the

flow no longer has the capacity to carry sediment. This results in massive and non-graded structureless sand deposits (case-A). The following bypassing current of the same flow then erodes the upper part of the massive structureless sand deposits. Since the flow continues to be depletive, the flow is not able to keep the eroded material suspended within the flow and creates a traction carpet deposit at the more distal position (case-B). The next stage of deposition is related to a reduction of flow competency which initiates the deposition of coarser-grained sediment. This deposit will have a non-erosion diffuse boundary with an underlying capacity-driven deposit. The final stages of deposition will look similar to the classic Bouma sequence which indicates a waning process. In contrast to the waning (unsteady) flow depositional process (Figure 3.11B), the massive structureless beds are deposited in response to reduced flow competency. The structureless bed will be capped by an erosional feature due to bypass. The traction carpet deposit can be found at the base of this bed as a product of the erosional process at the proximal position. Overall, the deposit will have a fining upward profile.

## 3.2 Facies Types of Parasequence-2 of the Sobrarbe Formation

Ten facies are defined in this study. The facies are defined based on grain size, sedimentary structures, thickness, associated clasts, and density of bioturbation. Table 3.1 provides a summary of facies descriptions and related hydrodynamic interpretations.

### 3.2.1 Facies 1: Conglomeratic Sandstone

*Description*

Facies 1 is thick bedded, matrix-supported conglomerate (Figure 3.12). The conglomerate is dominated by poorly-sorted pebble- to cobble-sized sand-fill mollusk clasts and bio-clasts that are randomly oriented in the bed (Figure 3.12). The bioclasts consist of mollusks, bivalve and nummulite fragments. The conglomerate matrix is composed of silty sandstone dominated by very-fine grained sand (Figure 3.12b). This facies contains 95% sandstone. The beds have planar, conformable lower contact.

*Interpretation*

Poorly sorted grains, a significant proportion of clay and silt, and random orientation of clast (Figure 3.12 and Table 3.1) provide information about the

depositional process associated with this facies. This facies is interpreted to result from frictional freezing of a cohesive flow. The matrix supported sedimentary structure of this facies suggests that they result from debris flow. Furthermore, clay and silt content within the matrix indicates that related flows behave as Bingham plastic fluid during facies sedimentation. Frictional or cohesive freezing mechanisms control rapid sedimentation of the Bingham plastic fluid flow, and this result in the production of poorly sorted clast-rich deposits. Facies 1 is equal to facies F1 of Lowe's scheme (1982), and facies F1 of Mutti's scheme.

### 3.2.2 Facies 2: Bioturbated Structureless Silty-Sandstone with Bio-clast

*Description*

Facies 2 is a structureless silty sandstone (Figure 3.13, Table 3.1). Part of this facies (60-70%) is composed of structureless sandstone that contains few bio-clasts and the other part (30-40%) is composed of bioturbated structureless beds with lesser bio-clast. The sandstone is dominated by very-fine grained sand which has a "fish scale" look when weathered due to the presence of silt in the matrix. The bed thickness ranges from 50 cm to 3 m. The structureless beds with bioclast contain about 10% various bio-clasts such as mollusk fragments, bivalve fragments and nummulites fragments. Bioclasts size ranges from 2 mm to 5 cm. The clasts are poorly sorted, distributed randomly and are not in contact with each other (matrix supported). The beds have gradual top and flat base. The bioturbated structureless beds contain various borrows (Figure 3.13 b, c, and d). Some deposits are highly bioturbated with large and small trace fossils, but other deposits show very little borrowing.

*Interpretation*

The tabular bedded, structureless, with and without floating poorly sorted clasts and a silty matrix in this facies suggests that the depositional process is controlled by a moving rheology flow (turbidity current) and debris flow. The thick bedded structureless sands without bio-clast are interpreted to result from suspension sedimentation. The matrix supported clasts results from rapid deposition due to decreasing flow capacity of debris flow (probably from a waning evolution of debris flow) or rapid suspension sedimentation of a turbidity current wherein the floating bio-clast is transported by

traction at the base of the flow. The low amount of bioturbation in this facies implies that sedimentation happened very rapidly. Facies 2 is interpreted as equal to facies S1-S2 of Lowe's scheme (1982), and facies F2-F3 of Mutti's scheme.

### 3.2.3 Facies 3: Shale-clast Conglomerates

*Description*

Facies 3 is thin- to thick-bedded (5-40 cm), grain-supported shale clast conglomerate (Figure 3.14 and Table 3.1). The clasts consist of more than 50% shale and siltstone clasts, 30-40% mixed bio-clasts (nummulites, mollusk and bi-valves fragments) and silica minerals. The grain size ranges from granule to pebble and is poorly sorted. Most of the clasts are imbricated. The grain size of the matrix ranges from very fine- to fine-grained sand. Clays and silt-sized grains are found in less than 2% of sediments. Beds of this facies are commonly lenticular and limited in correlation length because they are top truncated and often fill erosive depressions. This facies is only found at the base of the channel elements and within the base of channel stories. Facies 3 beds have an erosional upper and lower bounding strata.

*Interpretation*

The grain supported and imbricate fabric, very fine- to fine-sand grain-size matrix and the large grain size of clast, are interpreted to result from shear flow at the base deposition from bed load sediments at the base of turbidity currents (Table 3.1 and Figure 3.14). This facies is produced from early deposition that only involves the coarser grains and leaves the finer grain entrained in bypassing flows (lag deposits). The erosional surface at the bottom and truncated surface at the tops of the beds provide additional evidence that this facies is associated with bypass flow(Figure 3.14). Facies 3 is equal to facies R3 of Lowe's scheme (1982), and facies F2-F3 of Mutti's scheme.

### 3.2.4 Facies 4: Clast Rich Sandstone Facies

*Description*

Facies 4 is thinly- to thickly bedded (10 cm to1.5 m) low angle, large-scale cross stratificated sandstone (Figure 3.15 and Table 3.1). This facies commonly contains imbricated litho- and bio-clasts (pebble to fined sand) and are normally graded shale clast

at the base of the beds whereas the upper parts of beds are commonly structureless. The litho-clasts are composed of mudstone clasts, quartzite and other silica-clasts, and the bio-clasts are composed of nummulite shells, bi-valves and mollusk fragments. The modal grain size ranges from fine sand to pebble (with a total of 98% sandstone). The beds are characterized by an erosional base and commonly truncated tops (Figure 3.15). Flute and groove are commonly found at the base of Facies 4 beds.

*Interpretation*

Facies 4 is interpreted to result from a combination of suspended and bed load sedimentation from a turbidity current. The larger grain sizes such as litho-clasts and bio-clasts (granule to pebble size) with imbricated fabric are deposited under traction mechanisms at the base of turbidity flow. The very coarse- to fine-grained sand parts of the facies are produced from suspension of turbidity flow. Beds of this facies could be deposited from a single turbidity flow containing a wide range of grain sizes from fine sand to pebble size. However they could also have been produced by separate turbidity flows wherein larger clasts are produced from an earlier bypass flow and this could be followed by a later flow which deposits finer grained sediment. This facies records significant bypass sediment since most of the beds have erotional bases that produce amalgamated beds (Figure 3.15). Facies 4 is equal to Bouma's facies scheme (Facies Ta), S1 of Lowe facies (1982), and F5 facies of Mutti's facies scheme (1999).

### 3.2.5 Facies 5: Structureless Normally Graded Sandstone Facies

*Description*

Facies 5 is composed of thinly to thickly bedded structureless and normally graded sandstone (Figure 3.16 and Table 3.1). The grain size is coarse- to fine-grained sand. Silt and clay size deposits are only found at bed boundaries (Figure 3.16). This facies is composed of 98% sandstone. The bed thickness ranges from 5 cm to 2 meters. Upper and lower bed surfaces are commonly planar; however some lower boundary surface are weakly erosional, and upper surface are eroded (Figure 3.16). Bioturbation, litho-clasts and bio-clast are not found in this facies.

*Interpretation*

Structureless, normally- and un-graded strata of this facies is interpreted to result from rapid deposition of suspended sediments from turbidity current (Table 3.1 and Figure 3.16). The absence of bioturbation also suggests that deposition happened relatively fast, thus preventing a population of living organisms from living within the sediment. This facies is equal to Bouma's facies scheme (Facies Ta); Ta of Lowe facies (1982) and F8 facies of Mutti's (1999) schemes.

### 3.2.6 Facies 6: Structureless Very Fine- to Fine-Grained Sandstone

*Description*

Facies 6 is composed of thick, tabular structureless beds of very fine- to fine-grained sand (Figure 3.17 and Table 3.1). The beds are normally composed of graded and ungraded grain size, with thicknesses ranging from 50 cm to 1.5 m. This facies is dominated by fine- to very fine-sand and a small amount of silt-size grain associated with bed boundaries. The basal beds boundaries are flat to slightly erosional. The upper boundaries are flat to scoured. There is a very small amount of bioturbations in the lower parts of the stacked beds, and there is an increase in borrows density toward the top of the beds.

*Interpretation*

This facies resulted from rapid sedimentation of suspended material from turbidity current. This facies also records a high rate of sedimentation evidenced via thick bedded deposits and the lack of internal sedimentary structures (Figure 3.17). The little amount of bioturbation in the beds also indicates rapid sedimentation that limits the population of organisms within the facies. Facies 6 is equal to facies Ta of Bouma's scheme (1962), facies F5 of Mutti's scheme, and facies Ta of Lowe's scheme (1982).

### 3.2.7 Facies 7: Parallel to Cross Laminated Sandstone

*Description*

Facies 7 is thin- to thick- bedded, parallel to cross laminated sandstone (Figure 3.18 and Table 3.1). The beds range from 10 cm to 50 cm thick and are commonly intercalated with structureless sandstone beds. The grain size ranges from fine- to coarse-

grained sand (containing a total of 98% sandstone). This facies has a flat base and top beds. Burrow account for less then 5% of the sedimentary structure in this facies.

*Interpretation*

Facies 7 is interpreted to result from low suspended fall out rate and tractive deposition from turbidity currents. The intercalation of this facies with thick structureless sand indicates rapid sedimentation related to waning flows. Minimum bioturbation in this facies is a result of rapid sedimentation which does not allow living organisms to live long in the sandstone bed. This facies records a minor bypass of sediment since no clay-size grains are found in Facies 7 (Figure 3.18). Facies 7 is equal to Tb or Tc of the Bouma's facies scheme (1962) and F9 of Mutti's facies (1999).

### 3.2.8 Facies 8: Intercalated Mudstone and Very Fine Sandstone

*Description*

Facies 8 is structureless, parallel laminated to wavy laminated siltstone, shale and very fine sandstone (< 10%) (Figure 3.19 and Table 3.1). This facies is dominated by thin to moderately thick and tabular beds of structureless siltstone. Bed thicknesses range from 2 cm to 30 cm. Some of the siltstone and shale show relatively darker colors compared to others. The shale and sandstone are intercalated within the siltstone. The top and base of Facies 8 beds are characterized by flat and sharp contacts. Burrowing is common in this facies.

*Interpretation*

Facies 8 is interpreted to result from alternating traction deposition from varying turbidity currents and pelagic and hemi pelagic deposition. Parallel to wavy laminated structure sediment equal to Tc and Td Bouma sequences and F9 of Mutti's facies model (1999) (Table 3.1 and Figure 3.19). The presence of darker color in siltstone beds indicates a different organic content that was deposited from hemi-pelagic deposition. Facies 8 is equal to Tc or Td of the Bouma's facies scheme (1962) and F9 of Mutti's facies (1999).

### 3.2.9 Facies 9: Dark Gray to Black Laminated and Structureless Mudstone

*Description*

Facies 9 is composed of black to dark gray silty-mudstone (Figure 2.20 and Table 3.1). The primary sedimentary structure is laminated to structureless bed. Bed's thicknesses range from 5 to 30 cm (Figure 3.20a and c). The modal grain size is clay and very minor silt-size grains. No sand-size grain deposits are found within this facies (0% sandstone). The beds contain sharp flat contacts on the top and base (no erosion features). The color of this interval changes gradually within each bed (Figure 3.20a). Some of the beds are entirely black in color with no gradation. This facies is often heavily weathered. Hard red iron rich nodules are occasionally found within the weathered darker intervals of this facies. Bioturbation and trace fossils do not exist in this facies.

*Interpretation*

The fine grain-size, parallel laminations and thin bedded deposits are interpreted to result from hindered settling mechanism. The dark gray to black color, the lack of bioturbation or trace fossils and the presence of an iron rich nodule (Figure 3.20 b), suggests that the depositional environment was under anoxic conditions. This coupled with the extensive distribution of this facies across the slope deposition indicates that the controls of deposition were dominated by pelagic and hemi pelagic depositional processes. The darker color indicates the richness of organic content in the beds (Table 3.1 and Figure 3.20). This facies is equal to Te of Bouma sequences and F9 of Mutti's facies model (1999).

### 3.2.10 Facies 10: Contorted Siltstone and Sandstone Beds

*Description*

Facies 10 is composed contorted siltstone and sandstone beds (Figure 3.21 and Table 3.1). The thickness of the folded and contorted bed ranges from 40 cm to 1.5 m. Contorted beds are from Facies 2 and 8 with a total of 70% sandstone. The boundaries of contorted units in this facies are relatively flat at the base and the tops. No erosion surface is found in internal facies. Bioturbation and trace fossils are found in part of the pre-deformation sedimentary structure.

*Interpretation*

Facies 10 results from slumping of unconsolidated siltstone and sandstone that is possibly related to rapid sedimentation of overlying bed (Figure 3.21). Overall this facies expresses post-depositional deformations and involves older deposits of Facies 2 and 8.

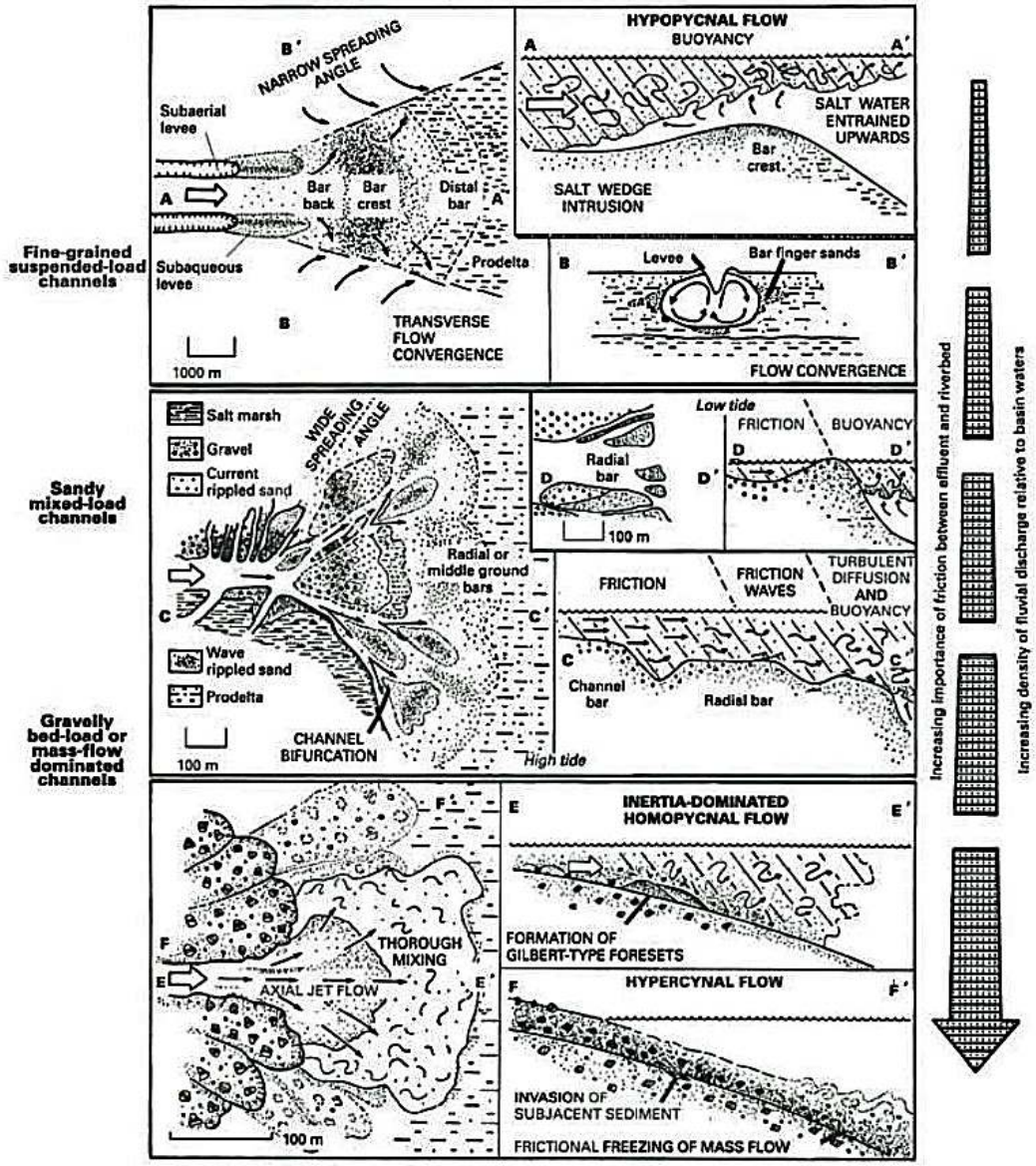


Figure 3.1. Schematic diagram of hypopycnal, homopycnal and hyperpycnal flow in relation to sea water and fluvial interaction. The diagram above shows how the initial grain-size of the suspended materials is a controlling factor in the initiation of flow at the sea shore (Reading, 1996)

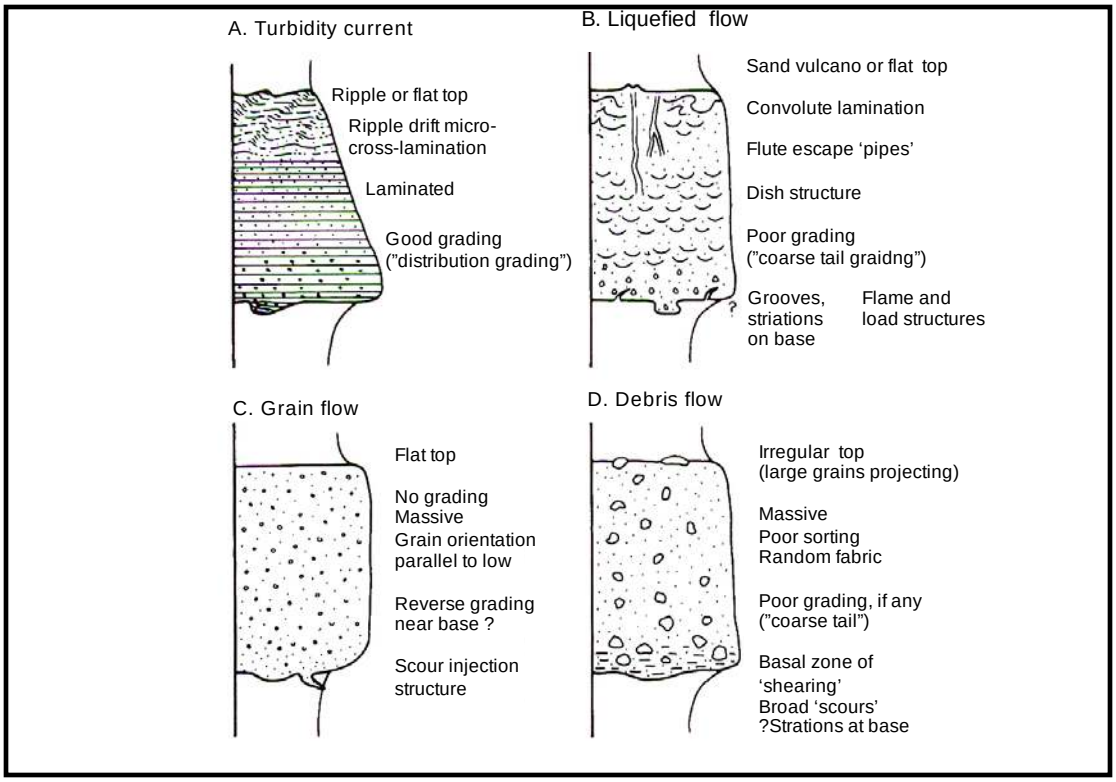


Figure 3.2 : Diagram comparing hypothetical deposits, from the continuum of sediment gravity flow. The continuum is based on flow concentration. Turbidity current has the lowest concentration whereas debris flows have the highest concentration (Middleton and Hampton, 1973)

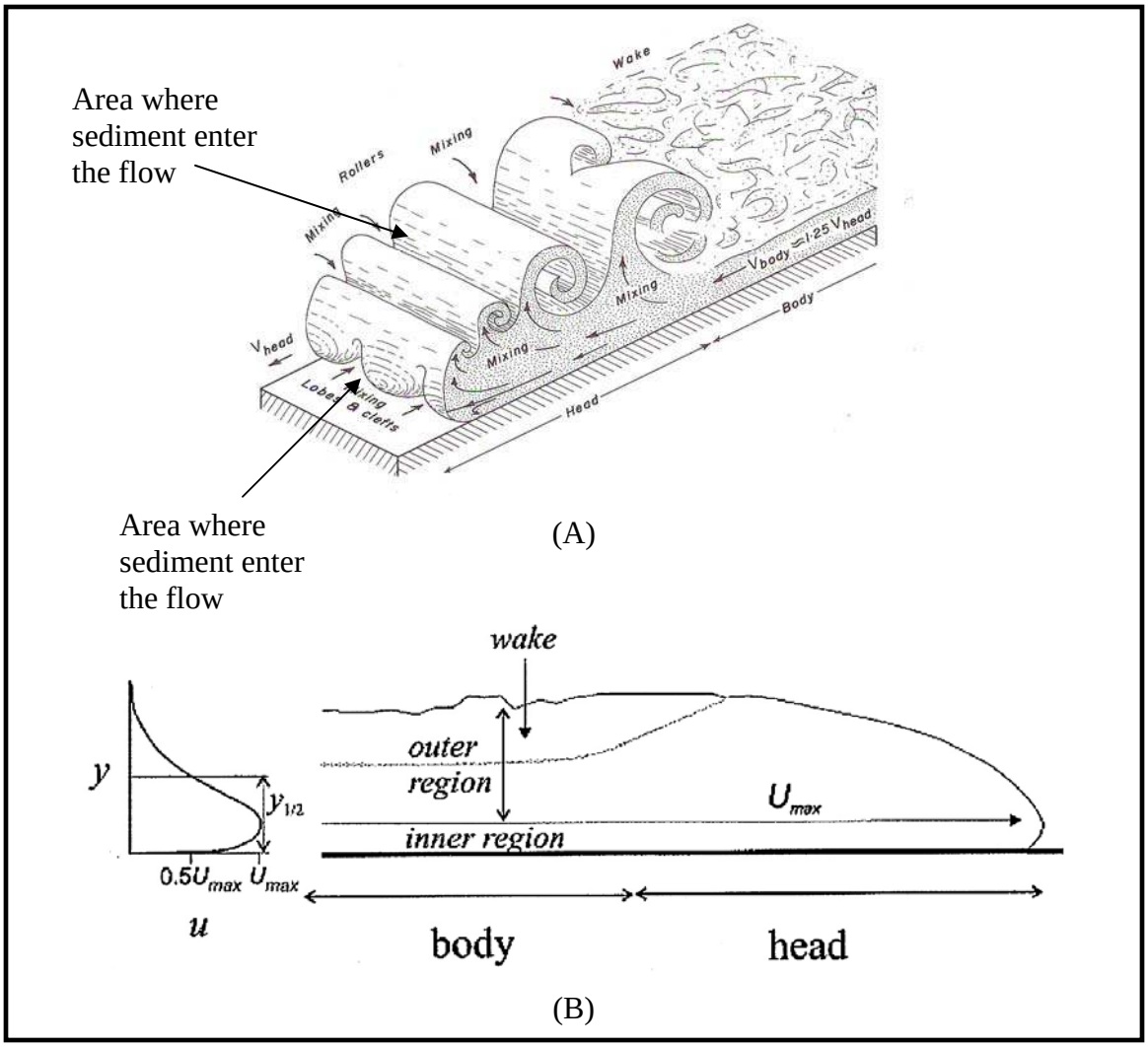


Figure 3.3. (A) A schematic three dimensional diagram illustrating a turbidity current that consists of a body and a head. The mixing zone occurs when water enters the upper part of the head of the flow, and depositional / erosion occurs at the lower part of the flow (after Allen, J.R.L, 1985 in Boggs, 1995); (B) A velocity diagram of a turbidity current shows that the maximum velocity occurs at the flow head, very close to the base, and reduces toward the top of the flow (Kneller and Buckee, 2000).

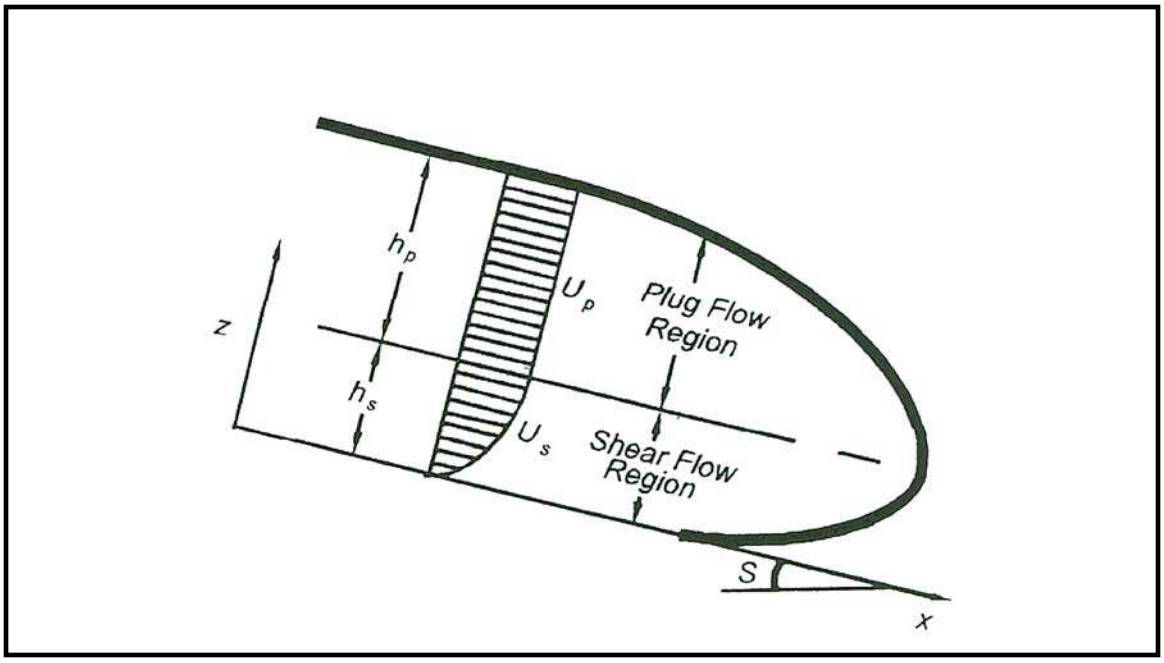


Figure 3.4 : A velocity diagram of debris flow. The diagram illustrates debris flows are composed of plug and shear regions. The plug region has uniform velocity, and the shear region has a decreasing velocity toward the base. Friction is the main control on the velocity profile in the shear region (Pratson *et al.* 2000).

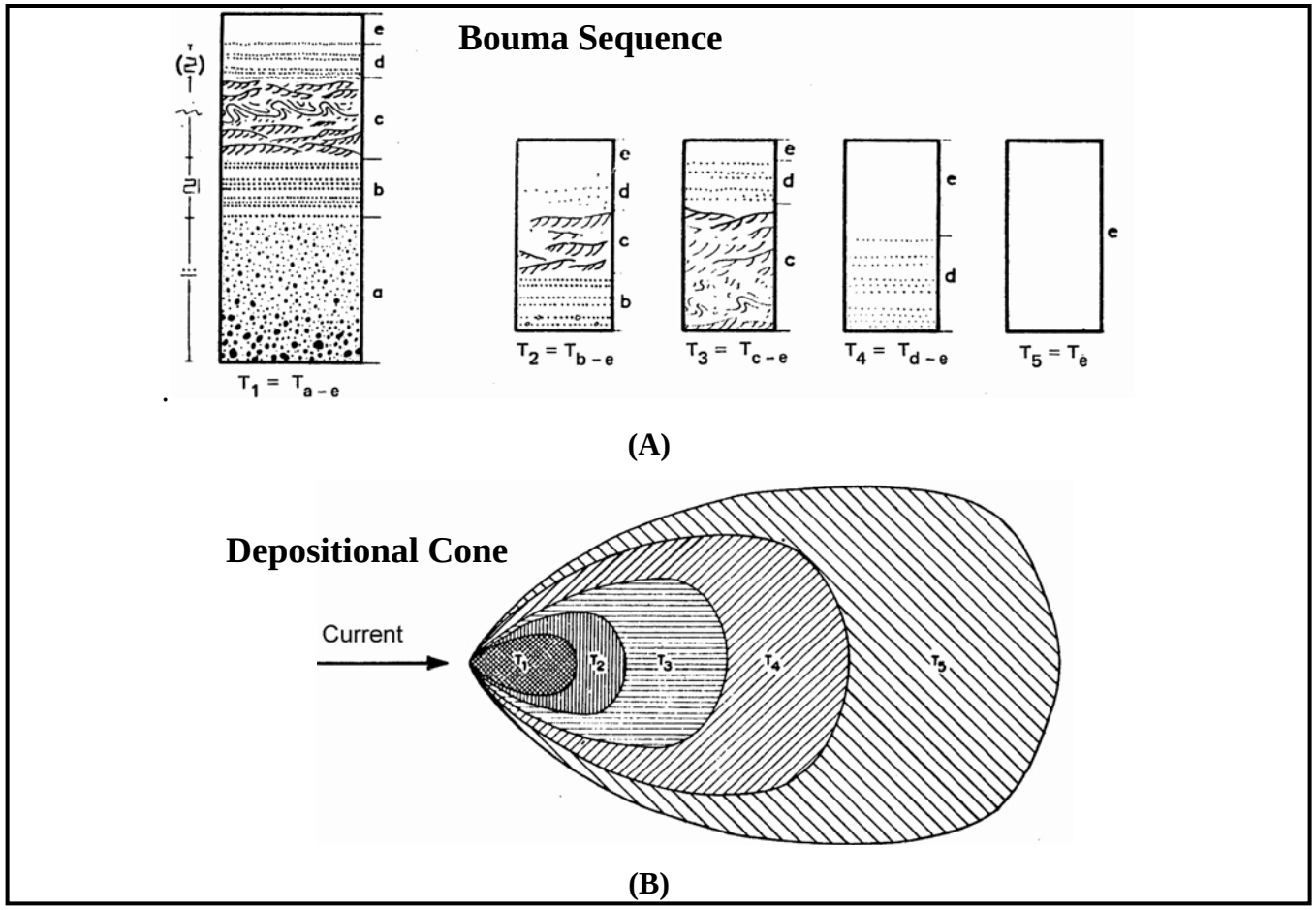


Figure 3.5. The Bouma (1962) sequence describes vertical and lateral distribution of facies in a turbidite deposit. (A) A vertical facies diagram that describes facies association changes from proximal to distal. (B) Map view facies distribution from proximal to distal that presents a waning flow process.

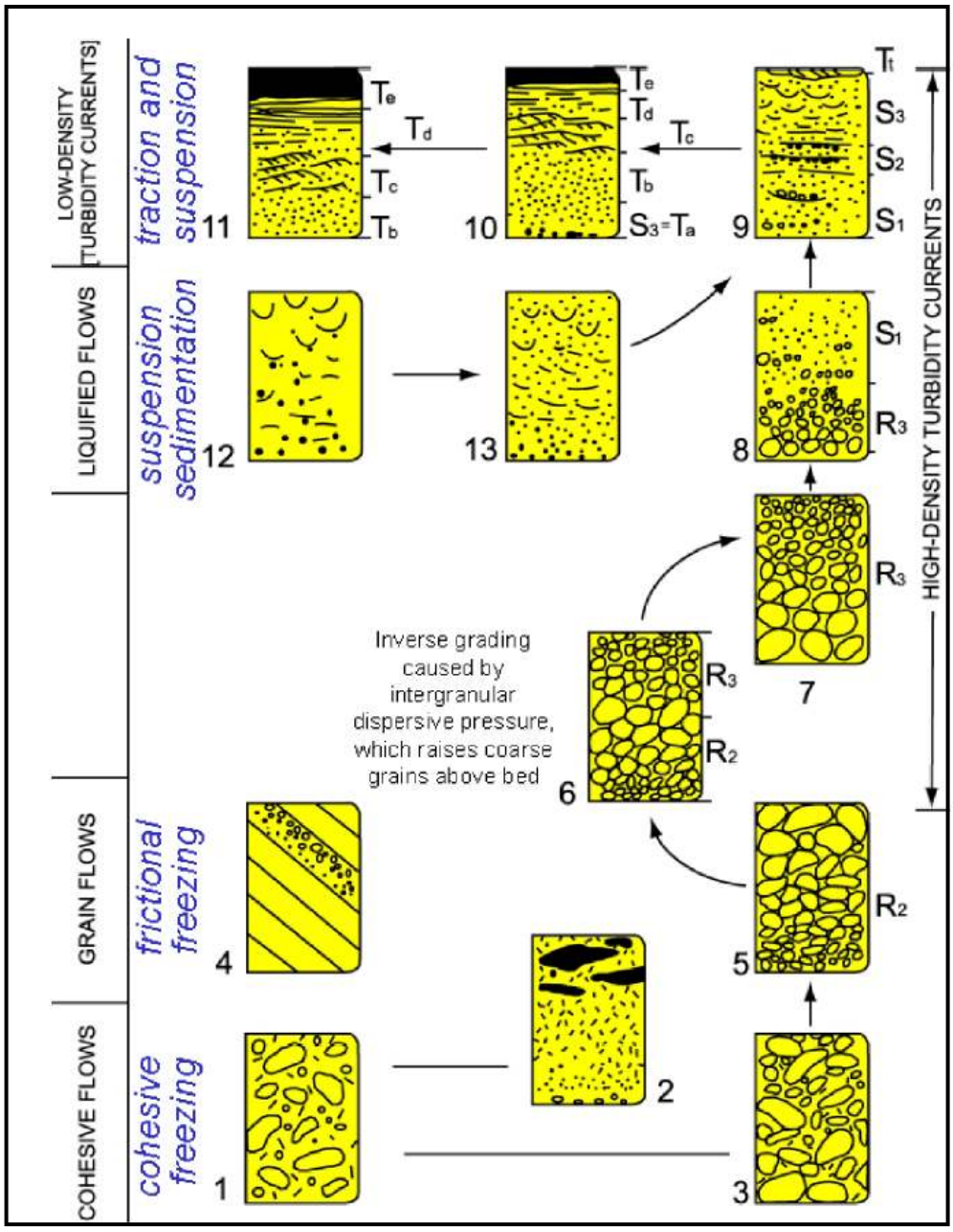


Figure 3.6. Modified Lowe (1982) scheme (after Pyles, 2007) describing facies distribution from proximal to distal deposition as a function of flow evolution and grain size. The flow initiates as a cohesive flow and continually evolves into grain flow, liquefied flow and low-density flow. The schemes describe various depositional facies within each flow process related to three groups of grain size: pebble-to cobble size clast (R), coarse-grained sand to small pebble size clast (S), and clay to medium-grained sand.

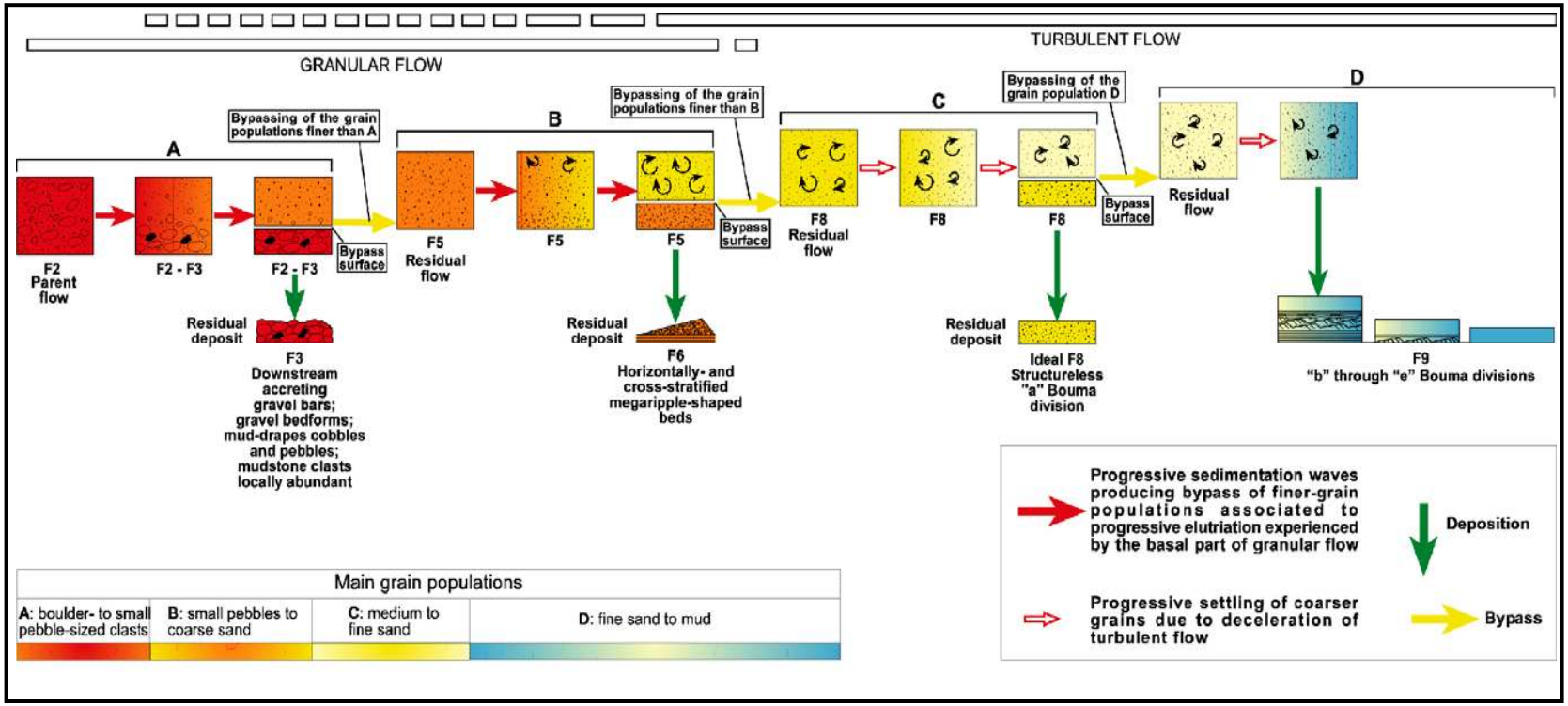


Figure 3.7 Mutti *et al.* (1999) schematic diagram of facies distribution across slope deposition. The diagram describes the flow evolution from granular flow into turbulence flow which indicates an overall waning process. The facies distribution is a function of grain size (like Lowe's scheme), wherein larger grain sizes are deposited in the proximal slope and smaller grain sizes are deposited near the distal slope.

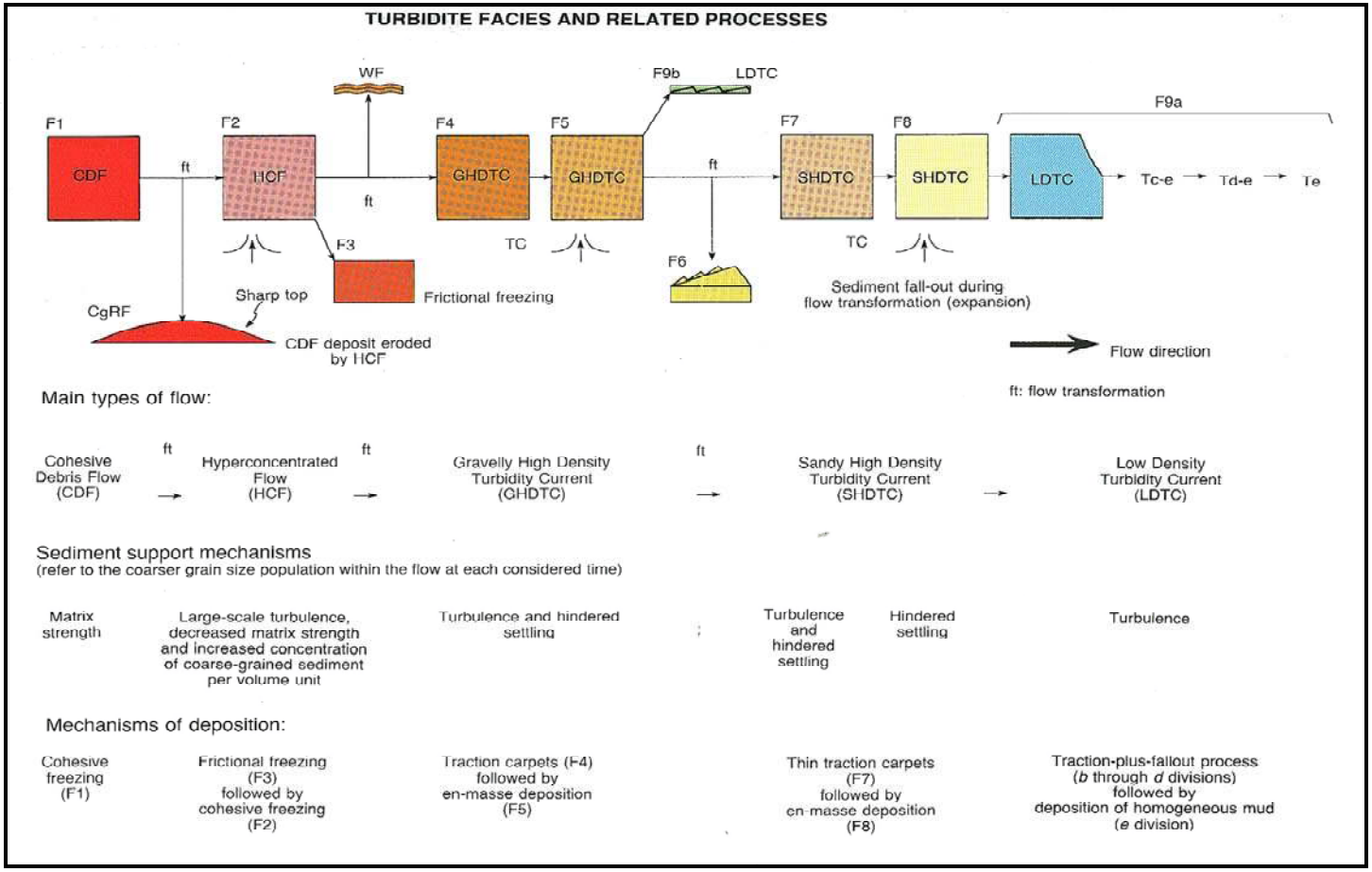


Figure 3.8 Summary of Mutti and Nomark's (1991) facies scheme describing facies distribution in relation to flow evolution that initiates from cohesive debris flow to low density turbidity currents. This scheme also describes various sediment support mechanisms that control different depositional facies from proximal to distal. The facies are divided into nine groups (F1 to F9) mainly based on grain size and particular sediment structure as indicated in the diagram above.

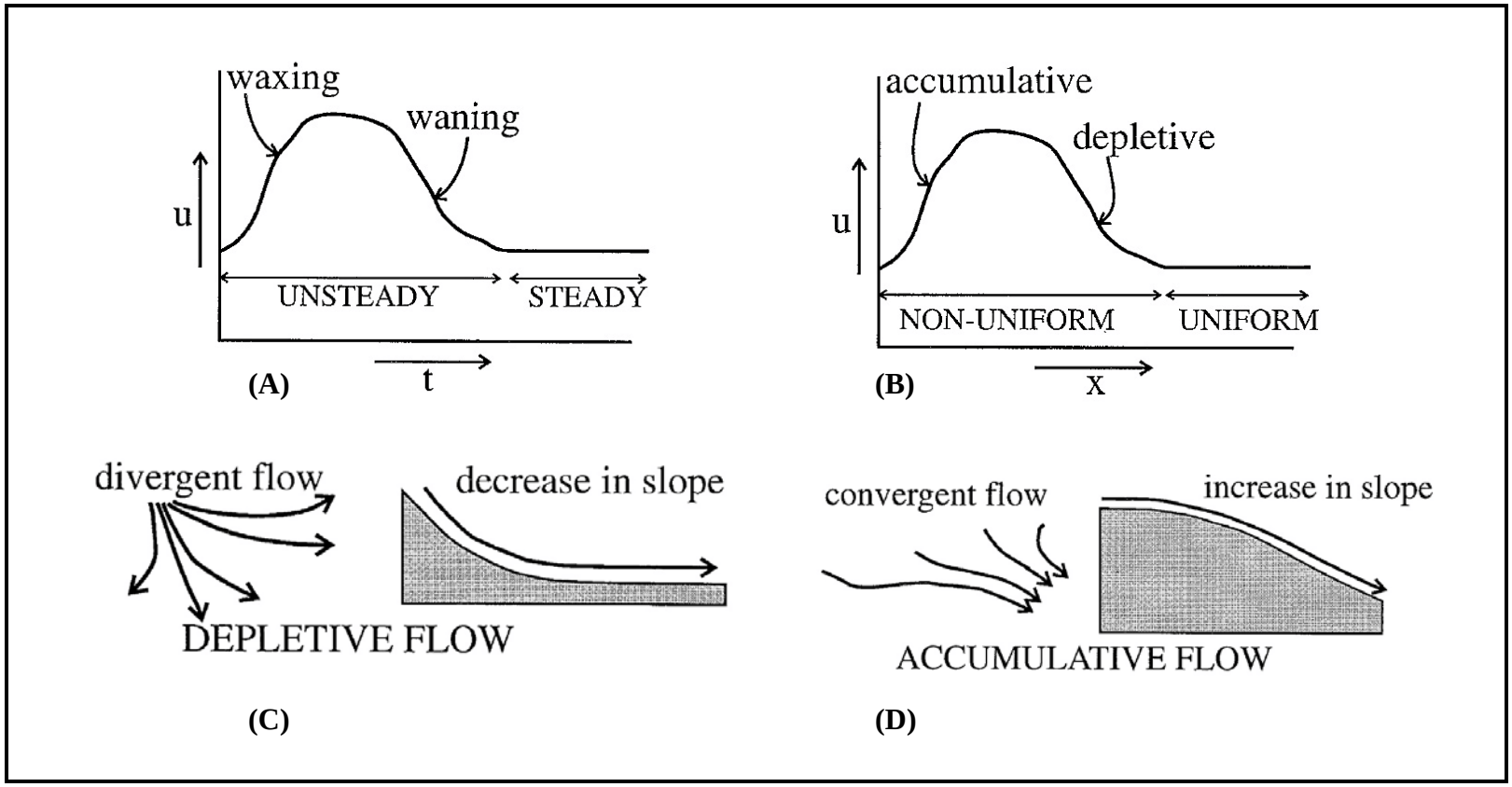


Figure 3.9 Kneller's (1995) flow steadiness and flow uniformity concept diagram. (A) Flow steadiness is measured by using velocity changes through time. Waxing flow is described as an increase in flow velocity through time, and a waning flow indicates a decreasing velocity through time. (B) Flow uniformity is measured by velocity changes through distance. Accumulative flow is described as an increasing velocity through distance, and depletive is indicated as decreasing velocity over distance. Diagrams (C) and (D) describe the relationship of flow depletion and accumulation in relation to slope physiography.

46

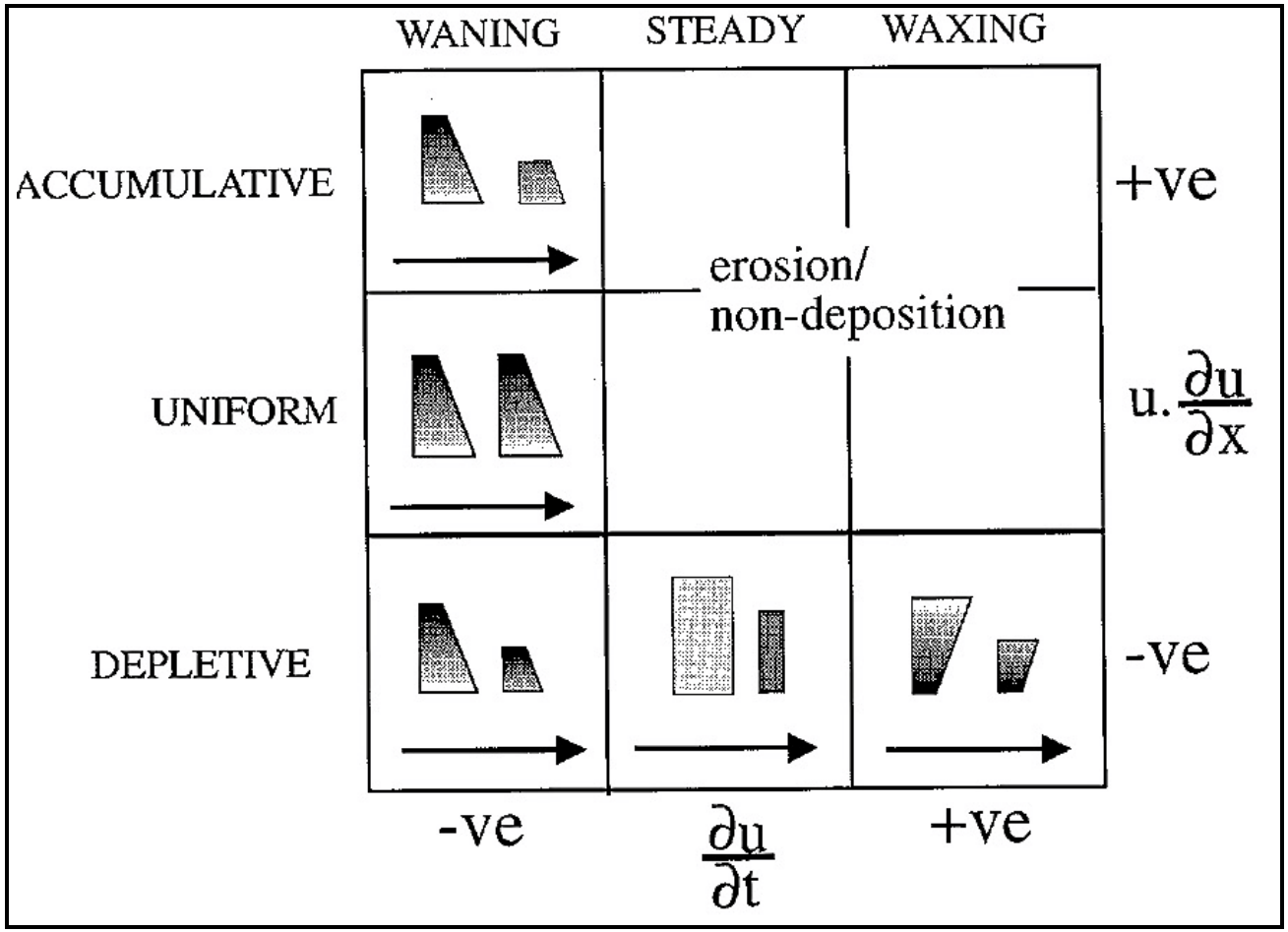


Figure 3.10 Kneller's (1995) acceleration matrix summarizes the interaction of flow velocity changes through time and distance. The matrix describes the effect of flow steadiness and flow uniformity in relation to timing of deposition and non-deposition events. The matrix also describes the proximal to distal changes of facies distribution that are indicated by the arrows within each matrix cluster.

47

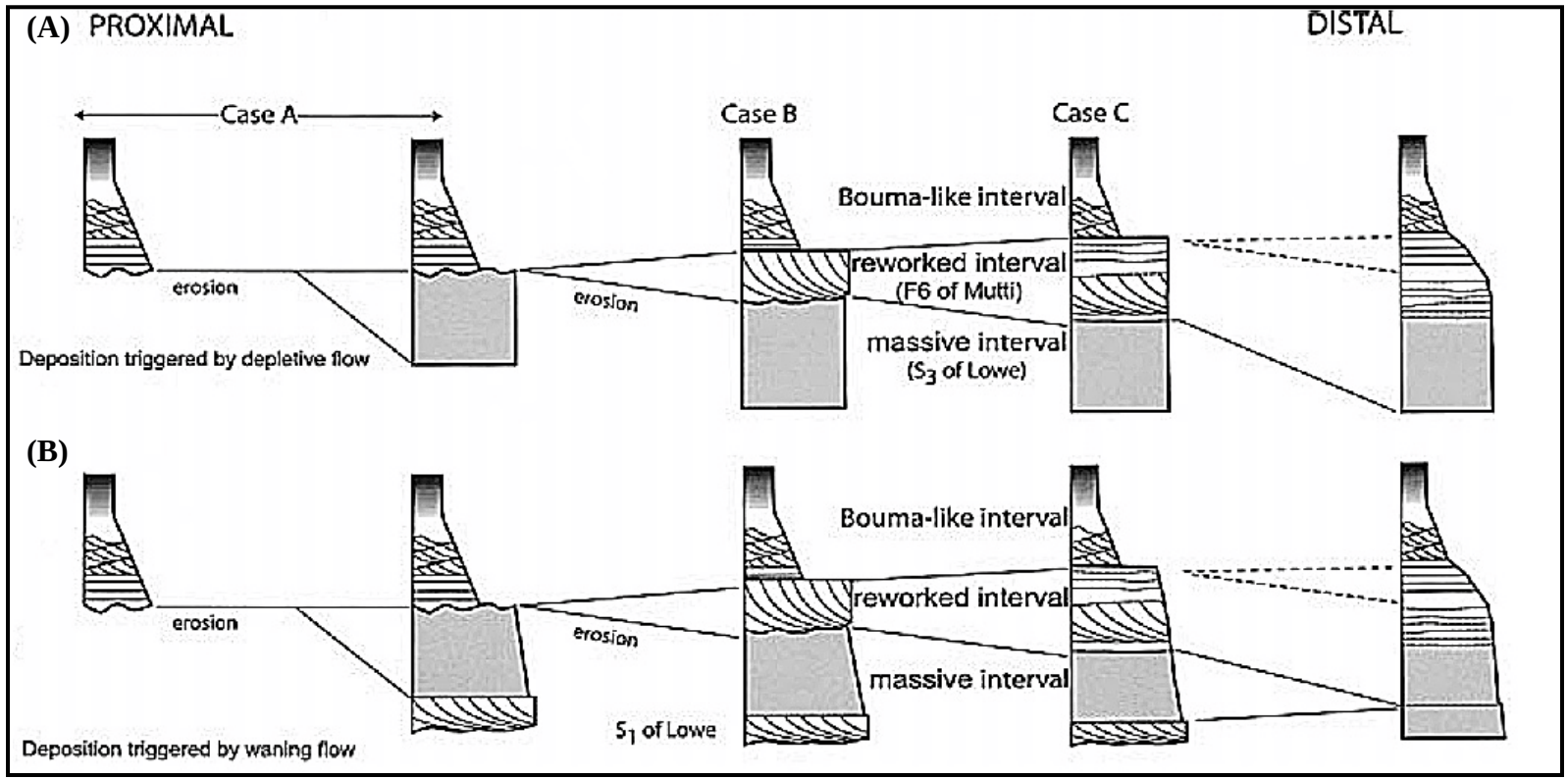


Figure 3.11 The facies distribution model by Kneller and McCafferey. (2003) describes two possible facies distribution end members formed from one event. The waxing flow indicates a massive and non-erosive base of massive sand from lower proximal to distal. The waning flow indicates erosive base facies that are associated with reworked intervals followed by a related depletive flow deposition. Both processes produce almost similar vertical facies at the distal position.

48

Table 3.1 Summary of description and interpretation of Parasequence-2 of the Sobrarbe Formation.

| Facies | Facies Name | Figure | Description | Modal Grain size | Average % Sand | Interpreted Sediment Support mechanism | Interpreted depositional process | Type of flow | Relative bed aggradations rate | Comparison to others studies |
|---|---|---|---|---|---|---|---|---|---|---|
| 1 | Conglomerate Sandstone | Figure 3.12 | Facies 1 is thick bedded, matrix-supported conglomerate. The conglomerate is dominated by poorly-sorted pebble- to cobble-sized sandfilled mollusks clast and bio-clasts that randomly oriented. The conglomerate matrix composed of silty-sandstone dominated by very-fine grained sand. The beds have planar, with a conformable lower contact. | Clast pebble-cobble, matrix very fine grain sand | 95 | Matrix strength | Frictional or cohesive freezing | Debris flow | Medium | Lowe, 1982 (cohesive flow- Facies F1); Mutti et al., 1999 (Facies F1); Gardner et al, 2003 (Facies 1) |
| 2 | Bioturbated Structureless Silty-sandstone with bio-clast | Figure 3.13 | Facies 2 is structureless silty sandstone. About 60-70% of the beds are bioturbated with few bio-clast (mollusk, bi-valve and nummulites fragment) and about 30-40% of the beds do not have bio-clast. The beds has planar contact at the base and gradual contact at the top. Bioturbation is vary, some is highly bioturbate (large and small trace fossils) others show very little borrowing. | Coarse silt to very-fine sand | 90 | Alternatively by separate or alternating fluid turbulence and matrix strength | Combination suspension, tractive and frictional or cohesive freezing | Combination or separate Turbidity and debris flow | Medium | Lowe, 1982 (low density flow- facies S1-S2); Mutti et al., 1999 (Facies F2-F3); Gardner et al, 2003 (Facies 2) |
| 3 | Shale-clast Conglomerate | Figure 3.14 | Facies 3 is thin- to thick-bedded (5 to 40 cm), grain-supported shale clast conglomerate. The conglomerate is dominated pebble to granule of shale and siltstone clast (50%) and bio-clast (30-40%). The matrix compose of silty-sandstone. The bed is lenticular and has an erosional upper and lower bounding surface. | Granule to very fine sand | 80 | Dispersive pressure | Tractive | Turbidity current | Low | Lowe, 1982 (cohesive flow and grain flow, Facies 3 or R3); Mutti et al., 1999 (facies F2-F3); Gardner et al, 2003 (Facies 1) |
| 4 | Clast Rich Sandstone | Figure 3.15 | Facies 4 is thinly- to thickly bedded (10 cm to 1.5 m), low angle to large cross-stratificicated sandstone with normally graded at the base and structureless at the upper part. This facies is dominated by pebble to fine grain sand. The beds contains imbricated litho- and bio-clast at the base of beds. The bed has erosive surface at the base and truncated or flat surface at the top. Flute and grooves structure commonly found at the base of the beds | Pebble to fine sand | 98 | Fluid turbulence, dispersive pressure | Suspension and tractive sedimentation | Turbidity current | High | Bouma, 1962 (facies Ta); Lowe, 1982 (low density flow- Facies S1); Mutti et al., 1999 (facies F5) Gardner et al, 2003 (Facies 12);Plink-Bjorklund et al., 2001(Facies 1.6) |
| 5 | Structureless Normally Graded to Non-Graded Sandstone | Figure 3.16 | Facies 5 is composed of thinly- to thickly bedded (5 cm to 2 m), normally graded and structureless, normally to non-graded sandstone This facies dominated by coarse- to fine-grained sand. Silt and clay size deposit are only found at bed boundaries. The upper and lower bed surface are commonly plane, however some lower boundary are weakly eronsional and upper are eroded. | Coarse to fine sand | 98 | Fluid turbulence | Suspension sedimentation | Turbidity current | High | Bouma, 1962 (facies Ta); Lowe, 1982 (low density flow- Facies Ta); Mutti et al., 1999 (facies F8) Gardner et al, 2003 (facies 9);Plink-Bjorklund et al., 2001(Facies 1.2) |
| 6 | Structureless Very Fine- to Fine Grained Sandstone | Figure 3.17 | Facie 6 is thick (0.5 to 1.5 m), tabular structureless, normally graded sandstone. This facies is dominated by fine- to very fine-sand and small amount of silt-size grain associated with bed boundaries. The basal beds surface is flat to slightly erosional. The upper bed boundaries are flat to truncated. The borrow is increase in density toward the top of beds. | Very fine to fine grain sand | 95 | Fluid turbulence | Suspension and tractive sedimentation | Turbidity current | High | Bouma, 1962 (facies Ta); Lowe, 1982 (low density flow- Facies Ta); Mutti et al., 1999 (facies F5) Gardner et al, 2003 (facies 9); Plink-Bjorklund et al., 2001(Facies 1.4) |
| 7 | Parallel to Cross-laminated Sandstone | Figure 3.18 | Facies 7 is thin- to thick bedded (10 to 50 cm), parallel- to cross-laminated. This facies is dominated by fine- to coarse- grained sand. The bed has a flat base and top. Borrow account for less than 5% in this facies. | Coarse to fine sand | 98 | Fluid turbulence | Suspension and tractive sedimentation | Turbidity current | Medium | Bouma, 1962 (Facies Tb, Tc); Mutti et al., 1999 (Facies F9); Gardner et al, 2003 (Facies 8); Plink-Bjorklund et al., 2001(Facies 1.2) |
| 8 | Intercalated Mudstone and Very Fine Grained Sandstone | Figure 3.19 | Facies 8 is thin- to moderate thick bedded ( 2 - 30 cm), structureless, parallel laminated to wavy laminated siltstone, shale, and very fine sandstone. Shale and very fine sandstone are intercalated within the siltstone beds. The upper and lower surface beds are flat and sharp contacts. Burrow is common in this facies. | Very fine sand to clay | <10 | Hindered settling, turbulence | Suspension sedimentation | Pelagic-hemi pelagic settling from sea water and turbidity current | Low | Bouma, 1962 (facies Tc and Td),Lowe, 1982 (cohesive flow and grain flow Td);Mutti et al., 1999 (Facies F9); Gardner et al, 2003 (facies 13, 14); Plink-Bjorklund et al., 2001(facies 1.5) |
| 9 | Dark Gray to Black Structureless Mudstone | Figure 3.20 | Facies 9 is thin- to moderate thick beds (5 cm-30 cm), structureless to laminated silty mudstone with iron rich nodule. The beds commonly dark gray to black color. The upper and lower boundaries of beds are flat. The beds do not show any bioturbation. | Clay | 0 | Hindered settling | Suspension sedimentation | Pelagic- hemi pelagic settling from sea water | Very low | Bouma, 1962 (Facies Te); Mutti et al., 1999 (Facies F9); Gardner et al, 2003 (Facies 15) |
| 10 | Contorted Siltstone and Sandstone | Figure 3.21 | Facies 10 is composed contorted siltstone and sandstone beds. The thickness of the folded and contorted bed ranges from 50 cm to 1.5 m. The contorted beds are from Facies 2 and 8. The base and top boundaries of this facies are relatively flat. Bioturbation and trace fossils are found in part of the pre-deformation sedimentary structures | Very fine sand to silt | 70 | N/A | N/A | N/A | N/A | Plink-Bjorklund et al., 2001(facies 1.6) |

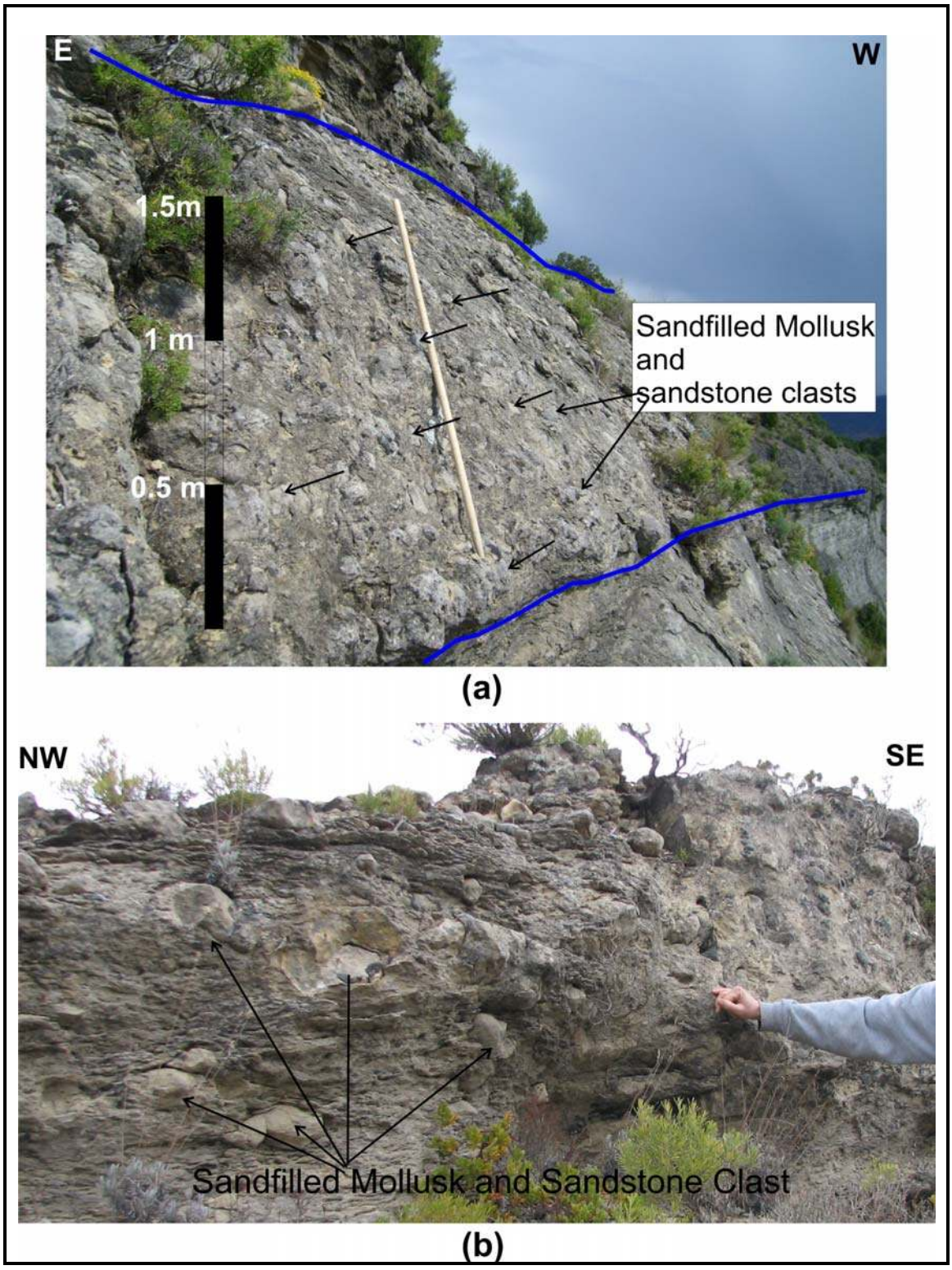


Figure 3.12 Photographs of Facies 1 shows a thick conglomerate bed (a) and are composed of sandfilled mollusk and sandstone clast (b).

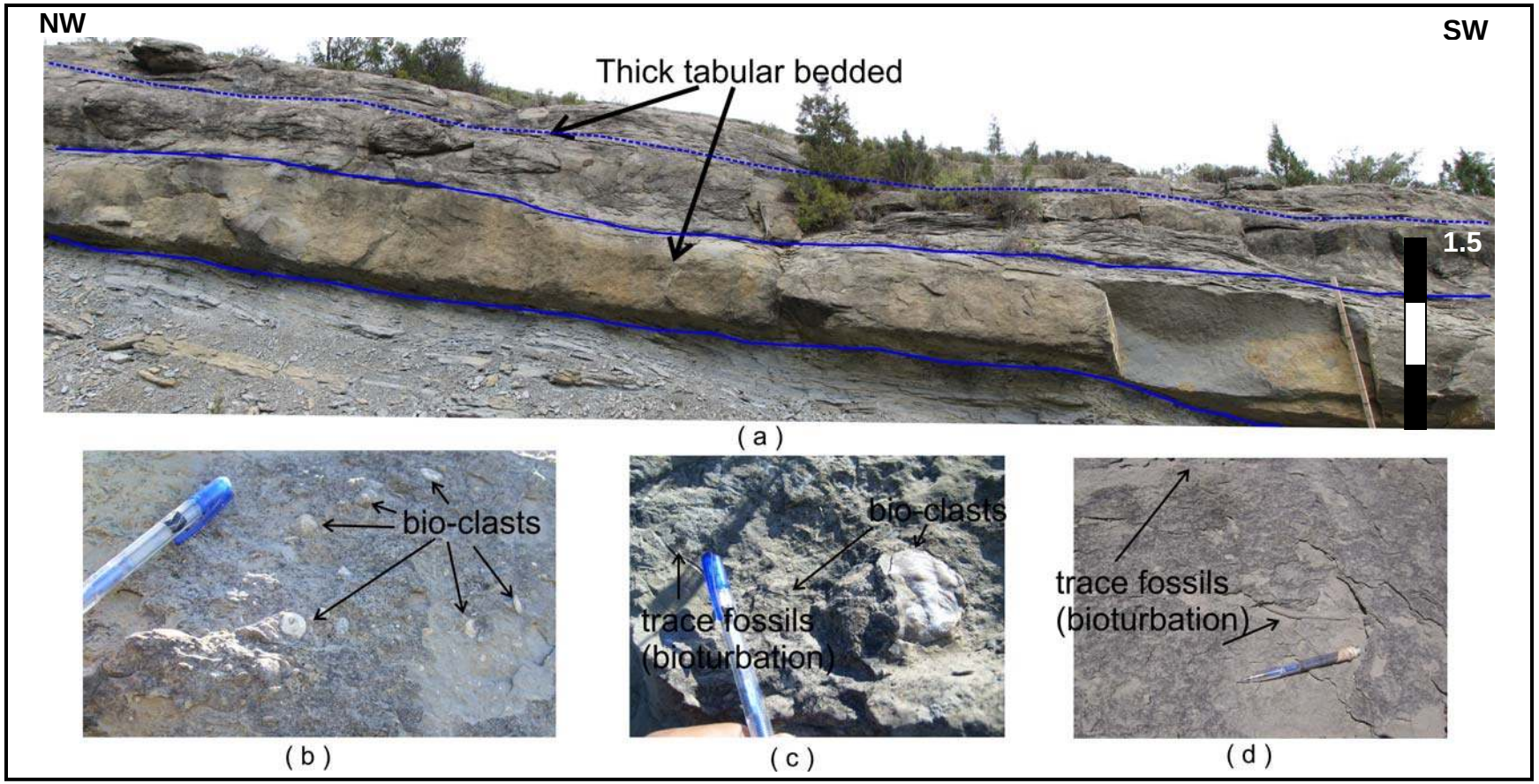


Figure 3.13 Photograph Facies 2 shows thick tabular sandstone beds (a) and bioturbated sandstone (c and d).

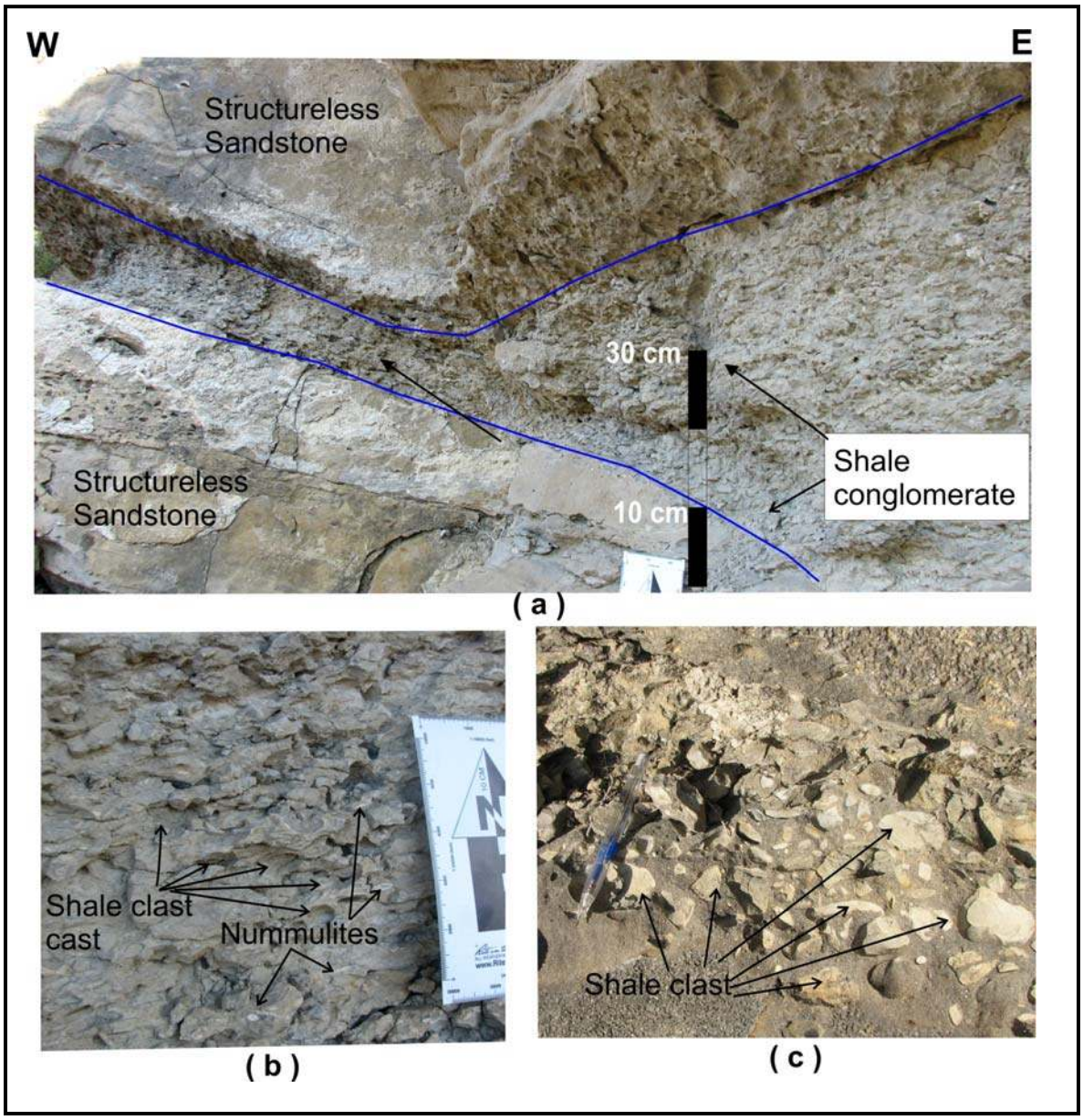


Figure 3.14 Photographs of Facies 3 show a lenticular bed (a) and are composed of shale clast and nummulites fossils (b and c)

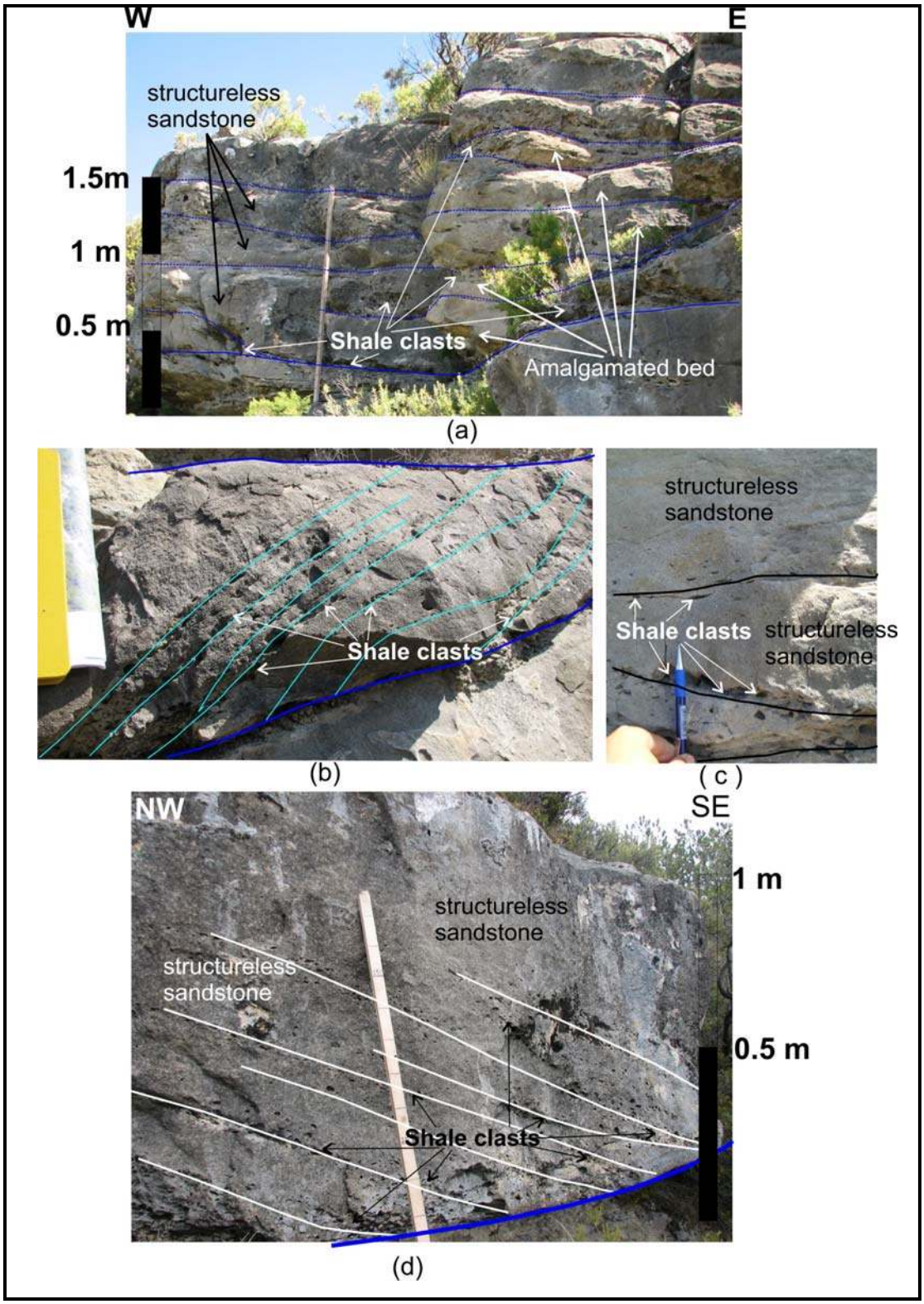


Figure 3.15 Photographs of Facies 4 shows amalgamated beds (a), large scale cross beds and are composed of shale clast at the base (b, c and d)

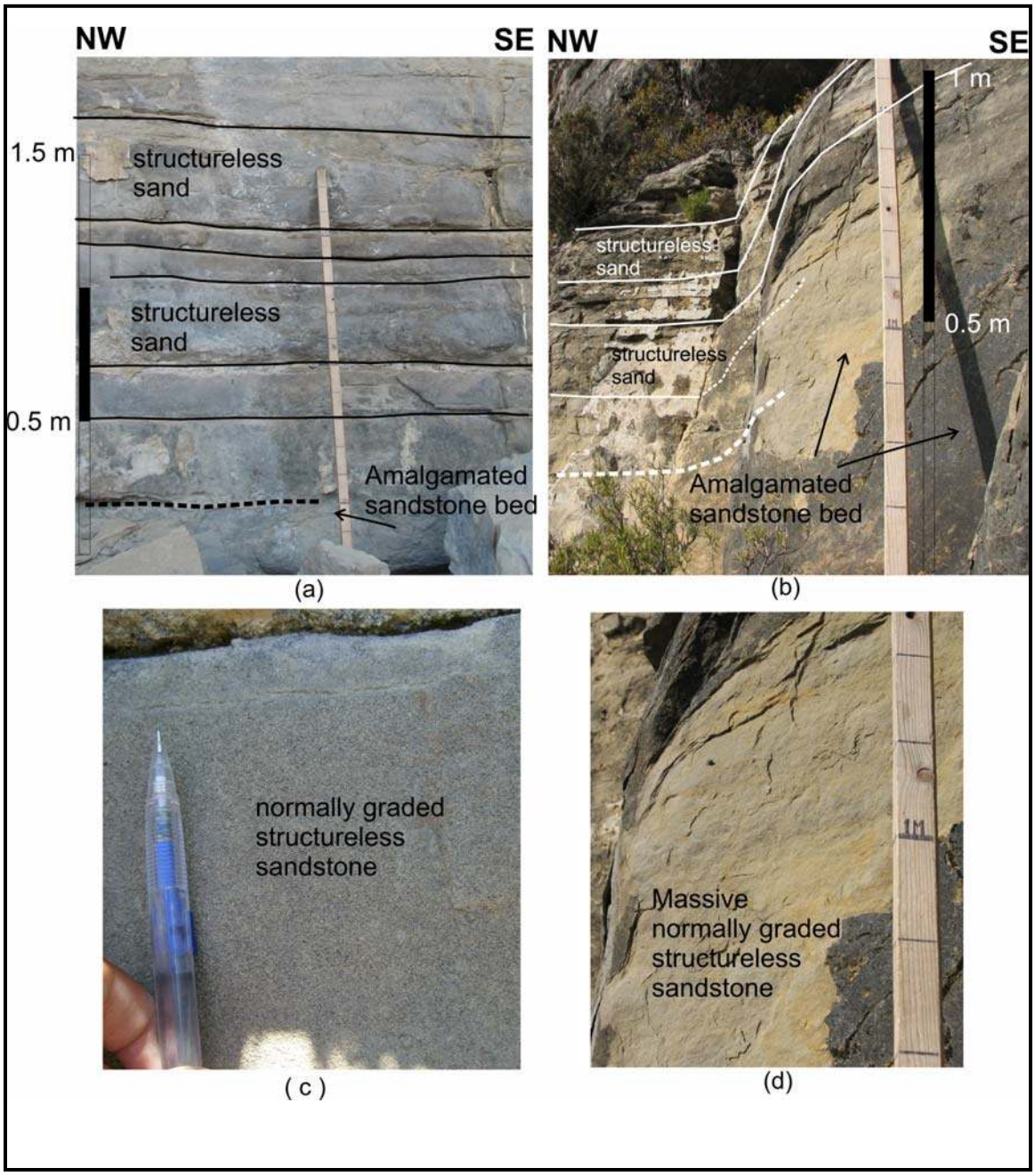


Figure 3.16 Photographs of Facies 5 shows thin to thick bedded structures (a and b) and structureless sandstone (c and d).

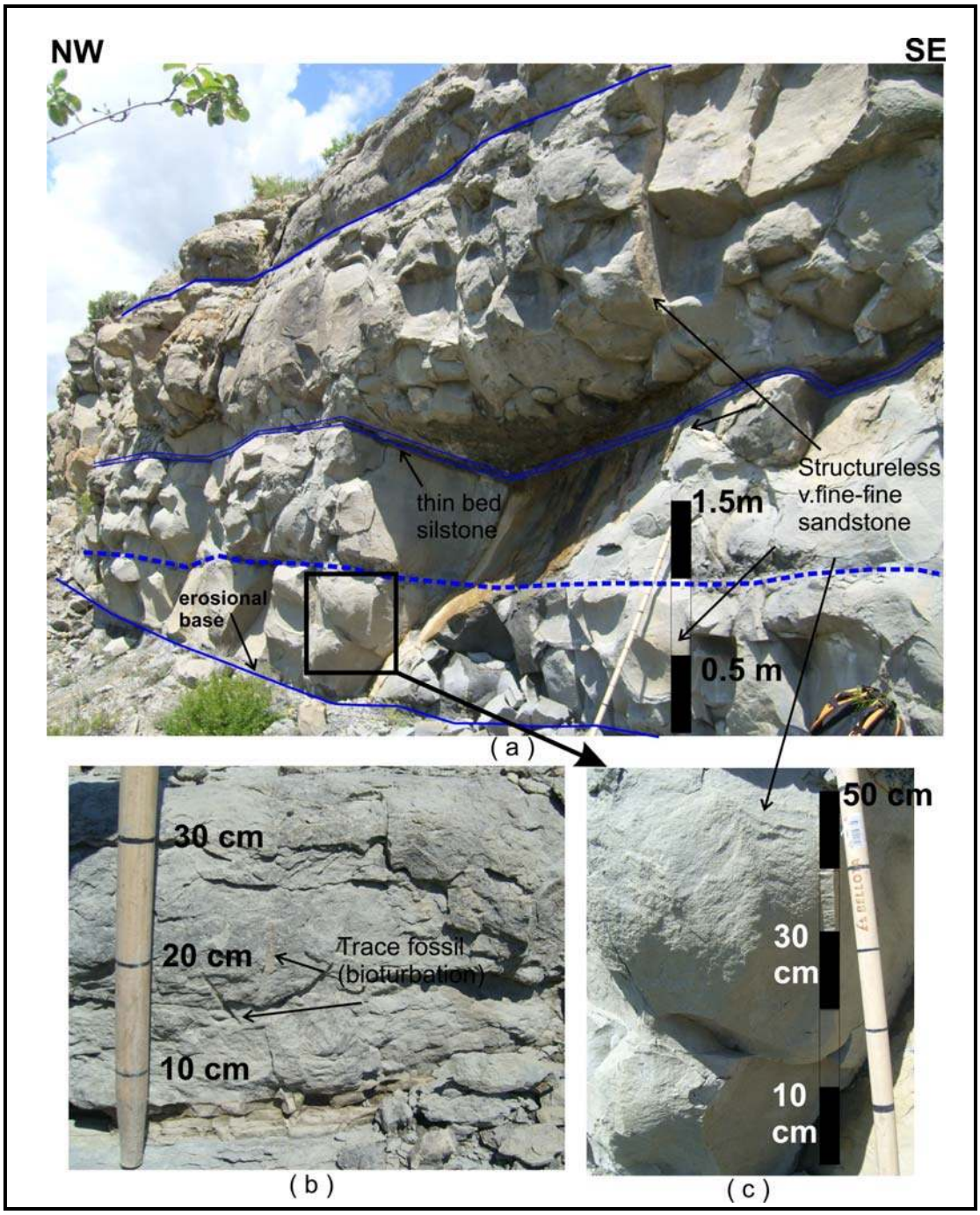


Figure 3.17 Photographs of Facies 6 show thick and tabular beds (a) and structureless sandstone with less bioturbation (b and c).

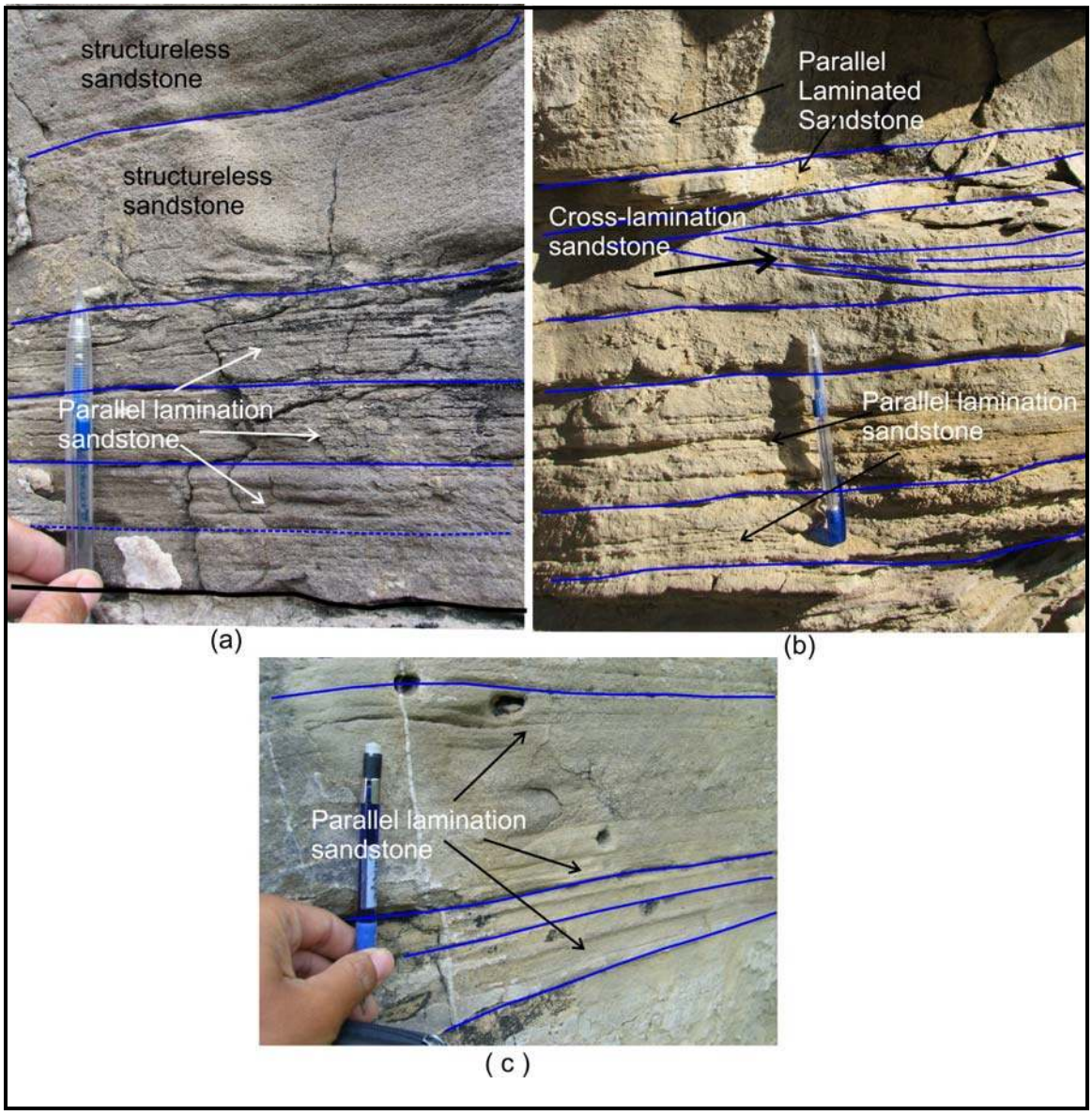


Figure 3.18 Photographs of Facies 7 show parallel laminated beds (a and c) that occasionally intercalated with cross laminated beds (b).

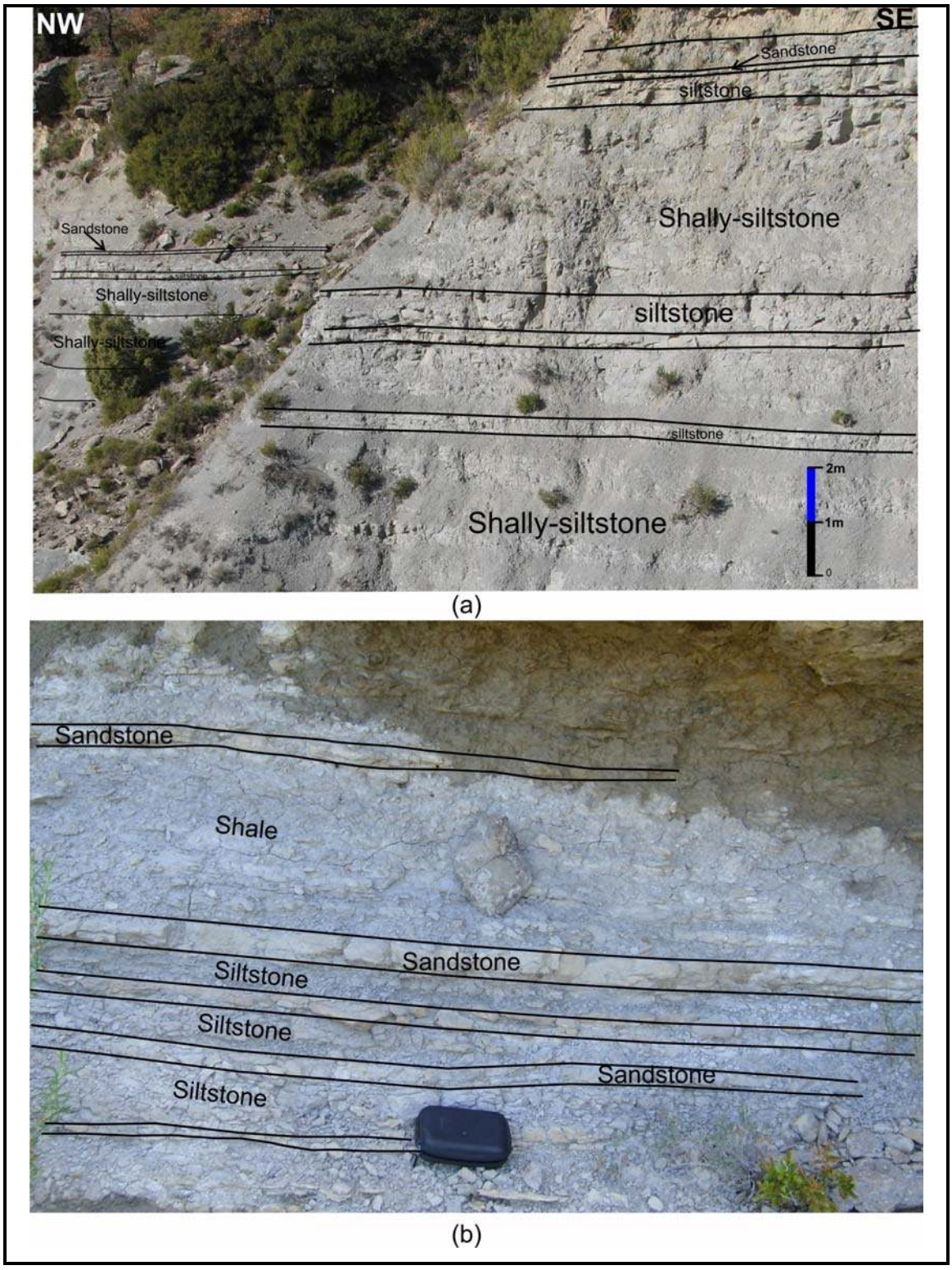


Figure 3.19 Photograph of Facies 8 shows intercalated shaly-siltstone, siltstone and very fine sandstone (a and b).

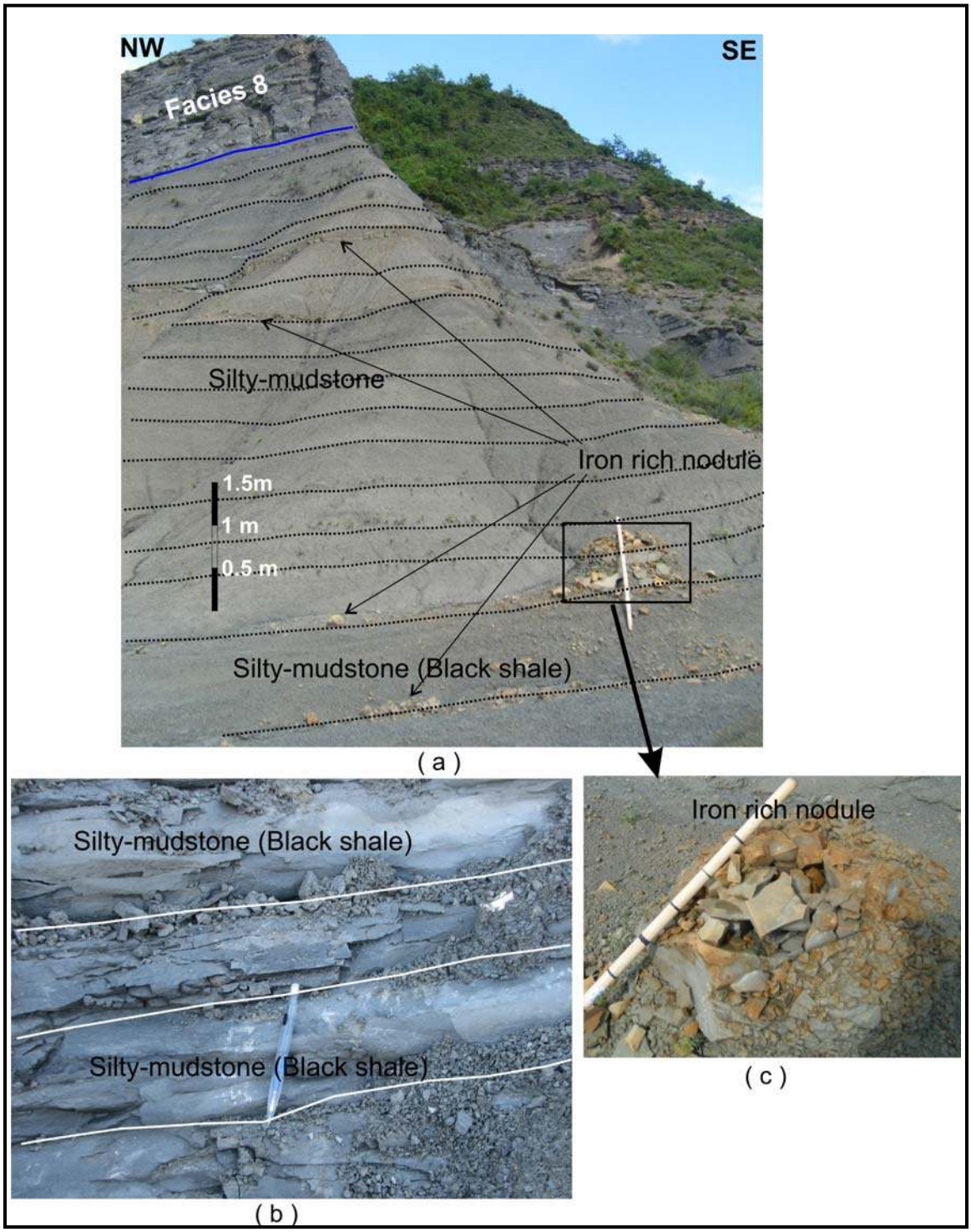


Figure 3.20 Photographs of Facies 9 show black to dark gray intervals of structureless silty-mudstone beds (a and b). The weathered interval of this facies composed of reddish iron rich nodule (a and c).

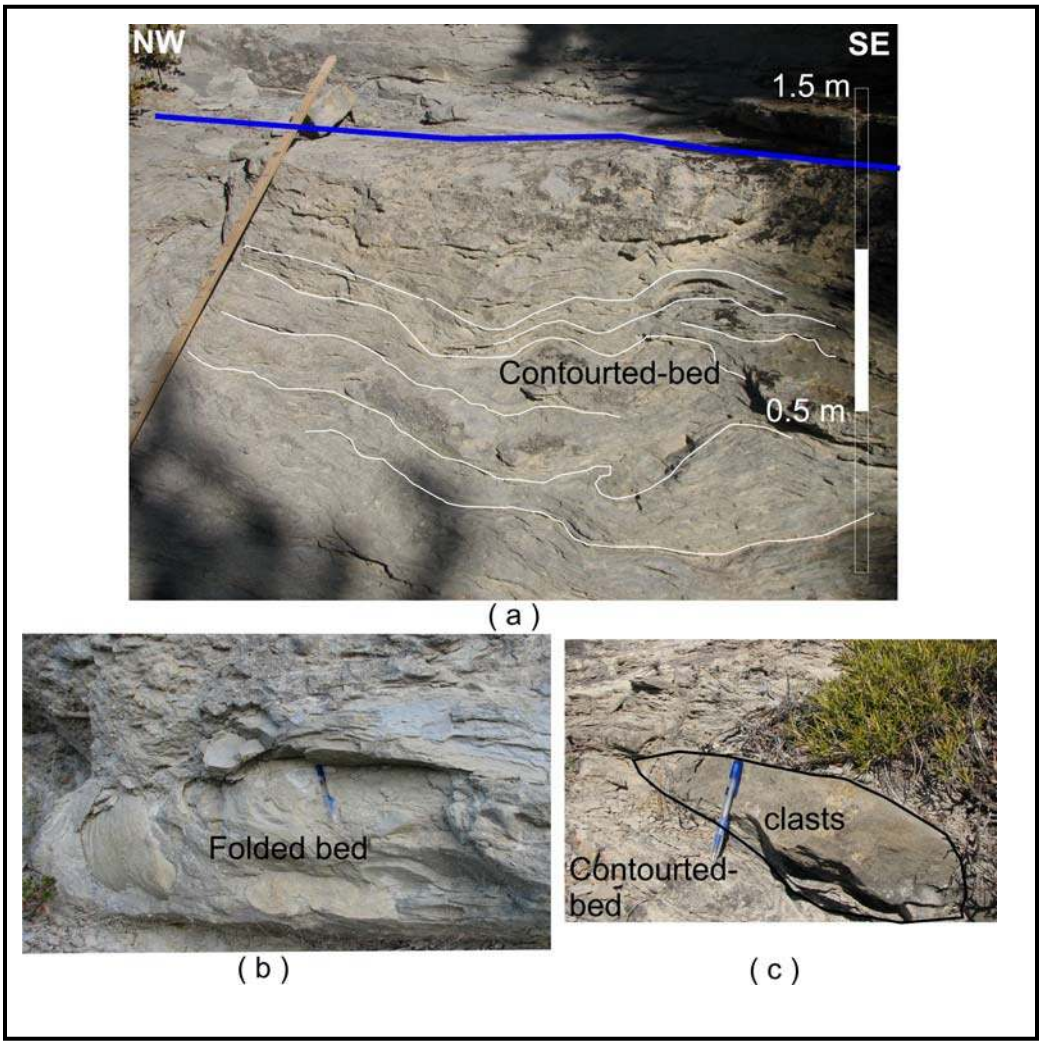


Figure 3.21 Photographs of Facies 10 show contorted beds (a) and folded beds (b). A large sandstone clast was found within the bed a result of soft deformation (c).

# CHAPTER 4
# ARCHITECTURAL ELEMENTS

This chapter provides an overview of architectural element analysis as well as a description of architectural elements, found in this study.

## 4.1 Architectural Element Definition and Scheme

The architectural element concept was introduced by Miall (1985) as a comprehensive and consistent technique in stratigraphic description, compared to previous facies model approaches. Miall defined architectural element as "a lithosome characterized by its geometry, facies composition, (and) scale which represents a particular process or suite of processes occurring within a depositional system" (Miall, 1985). This definition stresses that an architectural element description has to include:

1. Nature of lower and upper bounding surfaces: erosional or gradational; planar; irregular; curved (concave or convex)
2. External geometry: sheet, lens, wedge, scoop, U-shape fill
3. Scale: thickness, lateral extent parallel and perpendicular to flow direction
4. Internal geometry: lithofacies assemblage, vertical sequence, presence of secondary erosion surfaces and their orientations, bed form paleo-flow directions, relationship of internal bedding to bounding surface (parallel, onlap, downlap) (Miall, 1985)

Although this concept originally applied to fluvial deposits, it can also be applied to many studies in deepwater settings, such as Clark and Pickering (1996), Gardner and Borer (2000), Carr and Gardner (2000), Gardner *et al.* (2003) and Pyles (2007). A few authors have introduced the architectural element scheme specifically for deepwater deposits such as Clark *et al*. (1996), Mutti and Nomark (1991) and Pyles (2007). In addition to these schemes, Gardner *et al.* (2003) and Pyles (2007) propose a stratigraphic hierarchy for deepwater deposits. Gardner *et al.* (2003) divides channelize stratigraphy into a hierarchy of channel bodies as follows:

1. Elementary channel fill and lobe (architectural element),
2. Composite channel (architectural complex)

3. Migrating Channel complex or confined channel complex (channel belt; $6^{th}$ – order cycle)
4. Submarine channel fairway (System Tract; $5^{th}$ –order cycle).

Based on observations in the Ross Sandstone, Pyles (2007) proposes a more general sedimentary body hierarchy which emplaces architectural elements into wider ranges of strata temporal packages, as shown in Figure 4.1. This scheme divides the architectural depositional bodies into:

1. Element
2. Complex
3. Complex Set

Pyles's architectural element scheme (2007) is widely applicable to most stratigraphic settings (Figure 4.1). This research utilizes the architectural element scheme proposed by Pyles (2007) because it accommodates the wide range of architecture in many deepwater depositional settings. Moreover, Pyles (2007) re-defined architectural elements into a more specific scale with more practical meaning. He also modified Miall's (1985) architectural element into " a mesoscale lithosome (> 1 m thick, > 20 m wide) characterized by its external shape in depositional-strike view that forms the fundamental building block for larger stratigraphic unit including parasequence, system tracts, and sequences" (Pyles, 2007). Based on this definition, Pyles uses the following criteria to determine stratigraphic hierarchy:

1. Scale: covers mesoscale strata that separates smaller from larger stratigraphic building blocks (Figure 4.1).
2. Geometry: limited to external shape of the deposited strata. The internal shapes of deposits are classified by the lower levels in the stratigraphy hierarchy (Figure 4.1).
3. Observation view: limited to depositional-strike view (normal to paleo-flow) because architectural elements have different external shapes at different angles.
4. Facies: not included to describe the architectural element because facies could change within one element. Moreover, facies is not unique for one particular element.

5. Process or suite of processes: not included for defining architectural elements because this is not unique to one particular element.

### 4.2 Relating Flow Processes to Slope Physiography and Slope Architecture

Recent studies have shown that basin physiography and sediment type control slope architecture. Some authors (Peakall *et al*., 2002; Fildani *et al*., 2006; Posamentier, 2003; Posamentier and Walker, 2006) describe the formation of levees, channels, crevasse splays, sediment waves, channel avulsion and frontal splay/fans in relation to flow stripping, basin physiography and lithology. Flow stripping controls the formation of levees and crevasse splays. The flow-stripping process occurs at the outer bend of a channel when the turbidity current's height exceeds the levee's height. The upper part of the flow that consists of finer suspended sediments spills out of the channel and creates the levee and crevasse splay (Figure 4.2a). This process acts as a sorting mechanism by which sandier sediments are deposited progressively basinward. The frontal splay or lobe occurs when the channel reaches the unconfined area, usually the basin floor. The initial ratio of sand-to-mud within the flow controls flow sustainability and the distance the flow will travel (Posamentier and Walker, 2006). The initial sediment type within the flow is controlled by the type of sediment on the topset of the clinoform (Posamentier and Walker, 2006). The lower sand-to-mud ratio will result in more sustained flows and higher levee crests in the proximal slope, and longer channel distance and muddier crevasse splays at the medial slope (Posamentier and Walker, 2006).

Posamentier and Walker, (2006) described the role of basin physiography and the sand to mud ratio on the formation of submarine channel crevasse splay and frontal splays. A summary of this relationship is shown in Figure 4.2. Frontal splays (lobes) form further basinward when the system has a low-curvature slope and low sand-to-mud ratio (Posamentier and Walker, 2006). In contrast, a frontal splay (slope) will form closer to shelf edge in high-curvature slope and high sand-to-mud ratio. Posamentier and Walker,. (2006) further describe that systems will generate poorly sorted deposits when the slope changes rapidly from steep to a flat basin floor (Figure 4.2 b). In contrast, gentle slope changes produce well-sorted, sand-dominated deposits in the basin.

### 4.3. Architectural Element Distribution across the Physiographic Profile

Few studies focus on describing how architectural elements change down slope to basin profile. Examples include 1) Lewis Shale Formation (Pyles and Slatt, 2007), 2) Clinoforms of Spitsbergen (Plink-Bjorklund *et al*., 2001), and 3) the Brushy Canyon Formation Texas (Gardner and Borer, 2000). The Lewis Shale and the Clinoforms of Spitsbergen both represent linked, prograding shelf-slope-basin systems (Figure 4.3 and Figure 4.4). In contrast the Brushy Canyon formation is aggradational, no sedimentation occurs on the shelf and completely detached from shelf (Figure 4.5).

The Lewis Shale and Spitsbergen studies describe the distribution of architectural elements of prograding (in grade) systems at the shelf edge, slope, and base of slope (basin floor) of the clinoform. The Lewis Shale studies describe delta mouth bars, mudstone sheets, and slumps as the primary architectural elements at the shelf edge; mudstone sheets, levees and non-amalgamated channel elements on the slope; and sandstone sheet, amalgamated channels and fewer mudstone sheet and slump elements at the base of slope (Figure 4.3) (Pyles and Slatt, 2007). The Spitsbergen studies, within two types of shelf margins, describe delta front sheets, mouth bar and distributary channel elements at the shelf edge; sand-rich small channels and small lobes in the middle slope; and sheet-like turbidite beds and channels on the lower slope (Plink-Bjorklund *et al*., 2001 and Plink-Bjorklund and Steel, 2005). The Spitsbergen studies indicate a direct connection of channel bar systems at shelf edges to turbidities at the slope depositional system with fewer slump occurrences (Figure 4.4) (Plink-Bjorklund and Steel, 2005). In contrast, the Brushy Canyon Formation, (Gardner and Borer, 2000) revealed that channels stack more vertically in the slope and were more laterally offset in the basin.

These previous studies demonstrate solid observations for describing architectural elements on proximal, medial and distal slopes, but they lack documentation of how architectural elements, facies, and related lithology change between these areas.

### 4.4. Architectural Elements of Parasequence 2 of Sobrarbe Formation

Parasequence 2 of the Sobrarbe Formation is composed of four types of architectural elements: mouth bar element, channel element, overbank deposit element and mudstone sheet element. A summary of architecture element types of Parasequence 2 is listed in Table 4.1. A geological map shows the location of elements in the research area (Figure 4.6).

#### 4.4.1 Mouth Bar Element

Mouth bar elements are described at two outcrop exposures. One outcrop is oriented parallel to sediment transport direction (Figure 4.7); the other is oriented oblique to sediment transport direction (Figure 4.8). Mouth bar complex are primarily located at the shelf edge and their extend distribution approximately 3 km across the upper slope (Table 4.1). This element has a sigmoid cross-section shape (in dip-parallel view) and contains a series of basinward-dipping thick, massive sandstone beds. In the study area, the beds dip ($1^{o}$ to $9.5^{0}$) toward the basin (Figure 4.7 and 4.8). The upper part of the element is top truncated and the lower surface is flat (Figure 4.7). The mouth bar elements stack to form a complex at the shelf margin. Different mouth bar elements within the complex are separated by erosional surfaces (Figure 4.7). Each of mouth bar element has approximately 1 to 2 km length. The thickness of a single mouth bar element at shelf edge position ranges from 40 to 50 meters. The mouth bar complex in this study area has a total thickness of 75 meters.

Mouth bar elements contain beds that thicken in the landward direction (ranging from 1 to 8 m) and thin to a feather edge in the basinward direction (Figure 4.7 and 4.8). The proximal part of mouth bar contains massive structureless very fine to medium sandstone with floating bio-clasts (Facies 2) and, to a lesser degree, moderate thick sandstone conglomerate (Facies 1). The overlying strata of top truncated mouth bar element are part of transgresive deposits packages. This packages is composed of thick- to thin-bedded (20-40 cm), structureless, medium-grained sandstone (Facies 5), and parallel to cross laminated medium to coarse sandstone (Facies 7). The medial and distal parts of mouth bar elements contain bedded and bioturbated very fine to fine sandstone with few bio-clast (Facies 2). Vertically the association of individual mouth bar elements

have a fining-upward vertical profile (bell shape). The facies, vertically, also changes from moderate thick of structureless medium sand to thickly bed of very fine- to fine-sandstone with bio-clasts. but overall the mouth bar complex has a coarsening upward vertical profile due to progradation from one element to the next.

Mouth bar elements within this research area are interpreted as delta foreset located in front of the river mouth at the shelf edge. The erosion upper boundary surface of this element is interpreted to reflect erosion during the initial stage of transgression (revinment surface).

### 4.4.2 Channel Element.

The channel element is the most studied element in this research. This element is widely distributed in proximal- to distal-slope strata. Most of the description of channel elements comes from outcrops that are oriented oblique to- or almost parallel to paleo-flow direction. This study, describes three different types of channel elements. They are summarized in Table 4.2.

The three different channel elements are physically differences in term of bedding thickness, grain size distribution, facies, changes from axis to margin, stacking pattern and distribution across the slope physiographic. Although channels are divided into three different types, these channels are part of a continuum.

#### 4.4.2.1 Type I Channel Element.

Type I channel elements are found in proximal- and medial-slope exposures, commonly in association with mouth bar elements. Type I channels occur as isolated individual element or staked into complexes. Type I channel elements have an erosional, concave upward lower bounding surface and flat upper bounding surface. When found in complex, 40% to 60% of the older channel elements in the complex are truncated by the younger channels. Because of this degree of erosion, the margins of Type I channel elements are preferentially preserved (Figure 4.9 and 4.10). Type I channel complexes are formed by a number of amalgamated channels in a narrow geographic area. There is no single master erosional cut that confines all single channels within the complex (Figure 4.9).

The internal strata of Type I channel elements change from axis to margin. The axis often contains thick, amalgamated, blocky and massive beds (0.5 to 1 m in thickness). Beds in the axis are commonly composed of normally graded beds (Facies 4 and Facies 5) with shale conglomerate (Facies 3) at the base of bedding (Figure 4.9 and 4.10). The margin of Type I channels are commonly sigmoid-shaped, with some degree of laterally accreting packages of beds (LAPS) similar to those shown by Abreu *et al.* (2004) (Figure 4.9 and 4.10). The LAPs of Type I of channels are shown the present of small degree of sinuosity also found within the channel. These beds laterally thin and de-amalgamate (10 to 50 cm in thickness) and become finer grained toward the margin of the element (Figure 4.9). Strata located at the channel margin may also contain thin- to moderately-thick bedded sandstone (Facies 5). The transition from axis to margin is transitional the shale-conglomerate beds where (Facies 3) reduce in abundance toward the channel margin. In general, Type I channels have a fining upward to uniform vertical grain size profile in axial positions which reflected a facies changes from Facies 3 to Facies 4 and Facies 5. The margin of Type I channel elements are fining upward bedded to thinly bedded which reflected a changes from Facies (Figure 4.9 and 4.10).

#### 4.4.2.2 Type II Channel Element

The type II channel elements are described at a number of outcrops mostly in the medial slope and distal slope position. Type II channel elements occur as isolated individual element or staked into complexes. Type II channels are described from a number of nicely exposed channel outcrops that are oriented perpendicular to paleo-flow direction. Type II channels have an erosional, concave-upward lower bounding surface and a flat top (Figure 4.11, 4.12 and 4.13). Like Type I channel elements, Type II channels stack vertically and laterally to build complexes. However, lateral offset is greater than in Type I channel and as a result, older channels in type II channel complexes are better preserved. Erosion from successive channels removes 20% to 30% of the older element. With less intensive channel amalgamation, Type II channels commonly preserve one side of channel margin and almost all of the channel axis body (Figure 4.11). Type II channel elements are associated with overbank elements and mudstone sheet elements. Mostly, however, Type II, are associated with mudstone sheets.

The internal strata of Type II channel elements also demonstrate axis to margin changes. Axes commonly contain massive, amalgamated beds (1 to 2.5 m) of coarse- to fine-grained sandstone with few nummulites fragments at the base (Facies 5 and Facies 4). These beds thin and de-amalgamate towards the margin of the channel. Vertically, the axis is composed of few normally graded beds which changes from Facie 4 to Facies 5. Most beds are structureless and have a “blocky” vertical grain size profile (Facies 5), and the margin shows a fining upward profile of succession thin beds (Facie 5 and Facies 7) (Figure 4.11). Overall, Type II channel element is capped by thin parallel bedded sandstone.

Type II channel elements differ from Type I channels in the following ways. First, Type II channel elements contain massive to thick bedded sand at the axis (Facies 5 and Facies 4). The bedding surface of channel axes are commonly difficult to distinguish and no shale-clast conglomerate is found (Figure 4.11, 4.12 and 4.13). In contrast, Type I channel elements have high percentage of chale-clast conglomerates (Table 4.2). Second, the channel axis of Type II channel elements commonly has a uniform grain size bed and an overall “blocky” vertical profile. In contrast, Type I channel elements decrease in grain size upward. Third, while Type II channel elements have axis to margin changes, they are not as notable as those in Type I channels. Fourth, Type II channels do not have any lateral accretion packages (LAPs) which are common in Type I channels.

#### 4.4.2.3 Type III Channel Element.

Type III channel elements are only found in distal slope exposures. Type III channel elements are also found to stack in complexes. Type III channel elements are the thickest channels ( 8 to 9 m) found the parasequence. Similar to Type I and II channel elements, Type III channel elements have concave-upward lower bounding surface and flat at top. The bases of Type III channel elements are erosional into older strata. Within complexes, Type III channel elements most commonly stack laterally with little vertical offset between adjacent channels. Overall, 40% to 50% of individual channels in the complex are removed by erosion (Figure 4.14). Type III channels complexes downcut into mudstone sheet elements at the most distal slope profile with no master cut that confined the complex.

Type III channels have little axis to margin changes in facies. The only documented change is a slight thinning of bedding towards the margin. Both the channel axes and margins are composed of thick bedded ( axis beds: 1 to 2 m and margin beds: 0.5 to 1.5 m) structureless very fine- to fine-grained sandstone (Facies 6) and are occasionally inter-bedded with very thin siltstone beds (Facies 8) (< 1 cm thick) (Figure 4.14). These beds lap out directly into the margin of the channel with little change in thickness and grain size. Vertically, the channel axis and margin commonly contain a thick uniform very fine sandstone bed (Facies 6) and few normally graded beds. Toward the channel tops, type III channel is capped by moderate thick parallel bedded bioturbated and structureless very fine sandstone (Facies 6). Both axis and margin strata have a "blocky" uniform grain size profile.

Type III channel elements differ from Type I and Type II channels in the following ways (Table 4.2). First, Type III channel elements contain structureless thick bedded very fine to fine sandstone at the axis and margin (Facies 6). Type III channels have the lowest facies diversity of all channel types. In contrast, Type I and Type II channel elements are composed of coarser sandstone and conglomerates. Second, the channel axis of type III channel commonly contains beds of uniform grain size and few normally graded beds. It has almost the same vertical profile as Type II channels, but is finer grained. In contrast, Type I channel elements decrease in grain size upward. Third, Type III channel elements do not show significant axis to margin changes. In contrast, Type I channel element show significant change from axis to margin, and Type II channels show a decreasing amalgamation to margin.

### 4.4.3 Overbank Element

Overbank elements encompasses all deposits that spill from the channel system, except lobe (frontal splay) elements. These include levees, crevasse splays and sediment waves. Overbank elements are only found in medial to distal slope strata. This element is divided into two types based on their distance to channel elements.

#### 4.4.3.1 Type I Overbank Element

Type I overbank elements are located adjacent to channel elements. These elements are lenticular and “wedge” shaped in cross sectional view (Figure 4.15a). The upper parts of these elements are commonly eroded by adjacent channel elements (Figure 4.15a). The element is composed of intercalated very fine sandstone and siltstone (Facies 8).The internal bedding (30 to 5 cm) laterally thins away from channel element (Figure 4.15a and 4.15b). These elements also show decrease in grain size and increase in bioturbation with distance from the channel element. These observations are interpreted to reflect a genetic relationship between this strata and the adjacent channel. Vertically, this element has a series of cyclical fining-upward successions

The lateral and vertical character of the Type I overbank elements are interpreted as levee deposits. Based on this evidence the first group of overbank deposit elements is interpreted to result from a levee that formed from flow over spill from channel confinement.

#### 4.4.3.2 Type II Overbank Element

Type II overbank element are located away from channels. They have planar bedded, thin to moderate thick ( 10-30 cm), sheet-like bioturbated, very-fine to fine-grained sandstone (Facies 6 and facies 7) and are not intercalated to siltstone or shale (Figure 4.15b and 4.15c). The base of the bed shows limited to no erosion. Although they do not show depositional connection to channel elements, these elements are commonly found close to channel elements (Figure 4.15b and 4.15c). Vertically, this element contains no graded bedding and has a flat top. Type II overbank elements are interpreted as crevasse splay deposits.

### 4.4.4 Mudstone Sheet Element

Mudstone sheet elements are one of the most widely distributed architectural elements in the parasequence. They are found from the shelf edge to distal slope basin. They occupy at least 30% of the parasequence volume (Figure 4.16). Mudstone sheet elements are characterized as extremely continuous, planar, thinly to moderate thickly bedded (10 cm – 50 cm) and are composed of intercalated siltstone and shale (Facies 8

and Facies 9) (Figure 4.16). Overall the elements show an extended and widely sheet-like geometry. The most dominant mudstone sheet element is located in the medial and distal slope. Mudstone sheet elements are distinctively dark gray to black in color or light gray to light brown in color which is related to organic content. Vertically, mudstone sheet elements have uniform grain size profile.

Mudstone sheet elements are interpreted to reflect deposition of hypopycnal plumes formed in front of the delta at the proximal slope. The mudstone sheet mainly results from hindered settling sedimentation. In examples when this element is dark gray to black, this element is interpreted to record hemi pelagic and pelagic suspension

Table 4.1 Summary of Architecture Elements described in Parasequence 2 of the Sobrarbe Formation

| Architectural Element | External Shape | Physiographic Position | Dominant Facies Content | Element Thickness | Lateral Dimension | Vertical Grainsize Profile | Common Grainsize | Associated Element |
|---|---|---|---|---|---|---|---|---|
| **Mouth Bar Element** | Sigmoid (Parallel to paleo flow) | Shelf edge to medial slope | Facies-1, Facies-2 and partially Facies 5 and Facies 7 | Element: 40-50 m Complex: 60-75 m | Element Length: 1 to 2 km | Complex: coarsening upward; Element: fining upward | Very fine to fine sandstone; few medium sand and granule to cobble size | Type I and Type II Channel Element |
| **Channel Element** | Concave-upward lower bounding surface, flat top | Proximal to distal slope | Facies-3, Facies 4, Facies 5, Facies 6, Facies 7, and Facies 8 | Element : 1.5 to 5 m Complex : 6 to 9 m; | width: 14 to 300 m | Ranges from fining upward to uniform (blocky) | Very fine sand to granule, ocassionaly pebble | Mouth bar element, overbank deposit element and mudstone sheet element |
| **Overbank Deposit Element** | Lenticular, wedging and planar to sheet-like | Medial to distal slope | Facies 8 | Element : 1 to 2 m | largest measured: < 60 m | Fining upward | Fine sand to silt | Type II channel element and mudstone sheet element |
| **Mudstone Sheet Element** | Sheet-like | Proximal to distal slope | Facies 8 and Facies 9 | Element :2 to 4 m Complex: 5 to 8 m | - | Uniform | Clay to silt with few very fine sand | Type II and Type III channel element and overbank deposits |

Table 4.2 Table Comparing the Three Types of Channel Elements within Parasequence 2 of the Sobrarbe Formation

| Channel Type | Facies Content | Physiographic Position | Present Conglomerate | Axis to Margin Changes | Bed Thickness (m) | Dominant Vertical Profile | Stacking Pattern | Common Grainsize |
|---|---|---|---|---|---|---|---|---|
| **Type I Channel Element** | Facies 3, 4, 7 and 5 | Proximal Slope | Yes | Changes in bed amalgamation, thickness, facies and grainsize | Axis: 0.5 to 1 m Margin : 10 to 50 cm | Mostly Fining Upward | Vertically | Pebble to medium sand |
| **Type II Channel Element** | Facies 4, 5, 7 and few Facies 8 | Medial to Distal Slope | No | Changes in bed amalgamation, thickness and grainsize | Axis: 1 to 2.5 m Margin : 10 to 50 cm | Mostly Uniform and few fining upward | Vertically, lateraly | Medium to fine sand |
| **Type III Channel Element** | Facies 6 and Facie 8 | Distal Slope | No | Changes in bed thickness | Axis: 1 to 2 m Margin : 0.5 to 1.5 m cm | Mostly Uniform and few fining upward | Laterally and vertically | Very fine to fine sand |

71

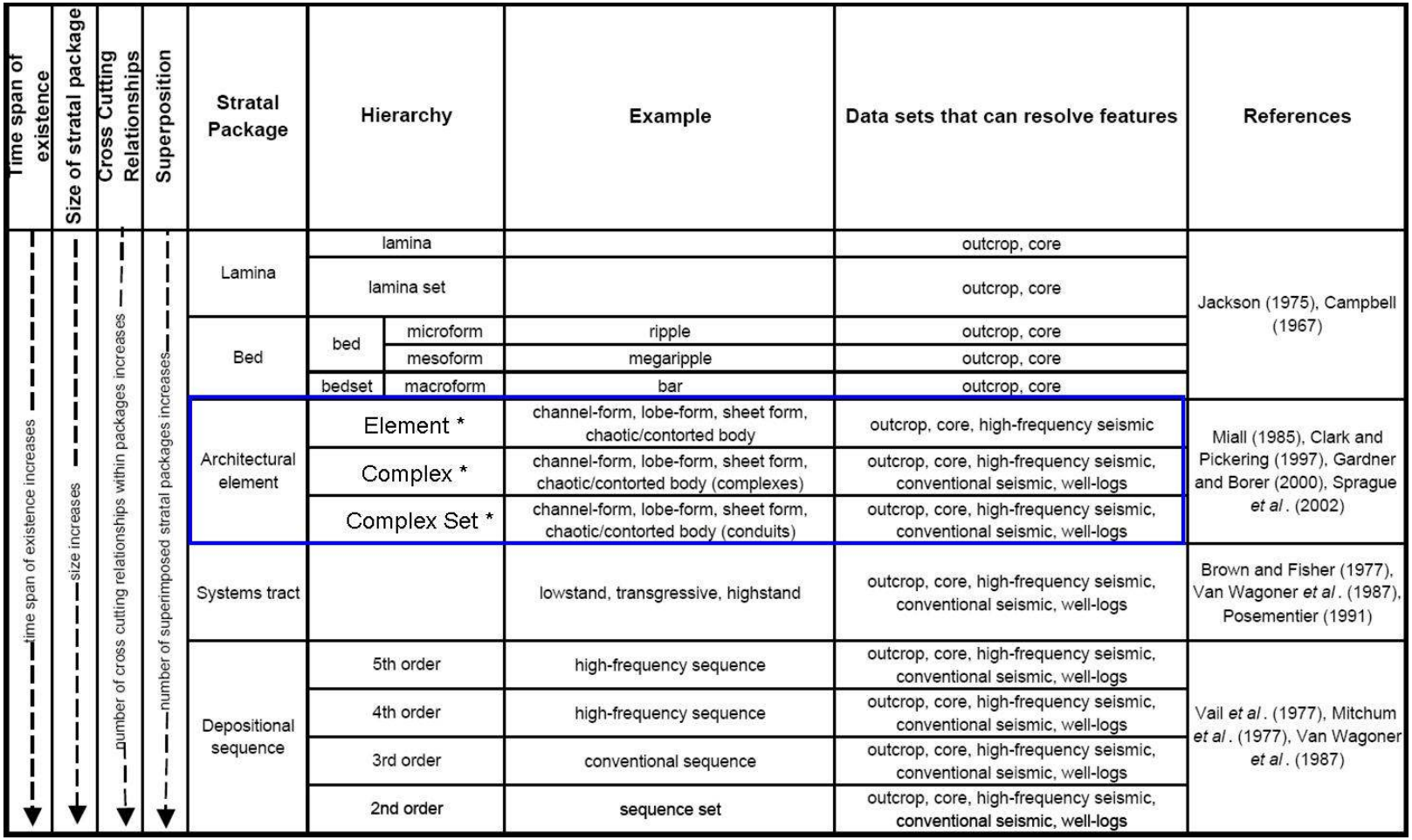


| Stratal Package | Hierarchy | | Example | Data sets that can resolve features | References |
|---|---|---|---|---|---|
| Lamina | lamina | | | outcrop, core | Jackson (1975), Campbell (1967) |
| | lamina set | | | outcrop, core | |
| Bed | bed | microform | ripple | outcrop, core | |
| | | mesoform | megaripple | outcrop, core | |
| | bedset | macroform | bar | outcrop, core | |
| Architectural element | Element * | | channel-form, lobe-form, sheet form, chaotic/contorted body | outcrop, core, high-frequency seismic | Miall (1985), Clark and Pickering (1997), Gardner and Borer (2000), Sprague *et al*. (2002) |
| | Complex * | | channel-form, lobe-form, sheet form, chaotic/contorted body (complexes) | outcrop, core, high-frequency seismic, conventional seismic, well-logs | |
| | Complex Set * | | channel-form, lobe-form, sheet form, chaotic/contorted body (conduits) | outcrop, core, high-frequency seismic, conventional seismic, well-logs | |
| Systems tract | | | lowstand, transgressive, highstand | outcrop, core, high-frequency seismic, conventional seismic, well-logs | Brown and Fisher (1977), Van Wagoner *et al*. (1987), Posementier (1991) |
| Depositional sequence | 5th order | | high-frequency sequence | outcrop, core, high-frequency seismic, conventional seismic, well-logs | Vail *et al*. (1977), Mitchum *et al*. (1977), Van Wagoner *et al*. (1987) |
| | 4th order | | high-frequency sequence | outcrop, core, high-frequency seismic, conventional seismic, well-logs | |
| | 3rd order | | conventional sequence | outcrop, core, high-frequency seismic, conventional seismic, well-logs | |
| | 2nd order | | sequence set | outcrop, core, high-frequency seismic, conventional seismic, well-logs | |

Figure 4.1 The temporal and spatial hierarchy of deepwater architectural element (modified after Pyles, 2007).

72

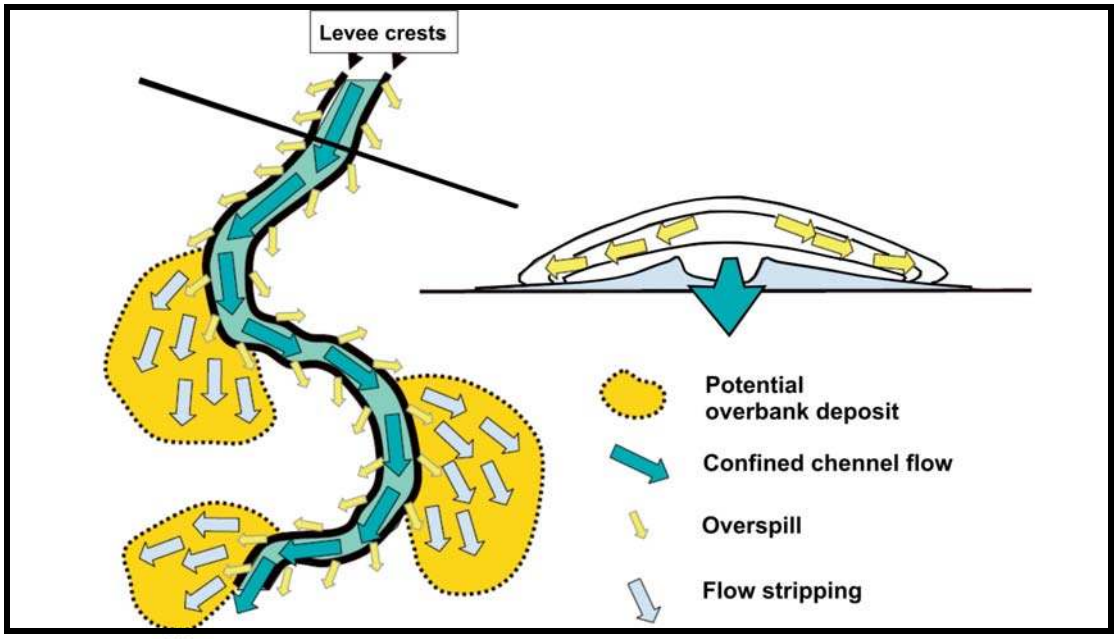


(a)

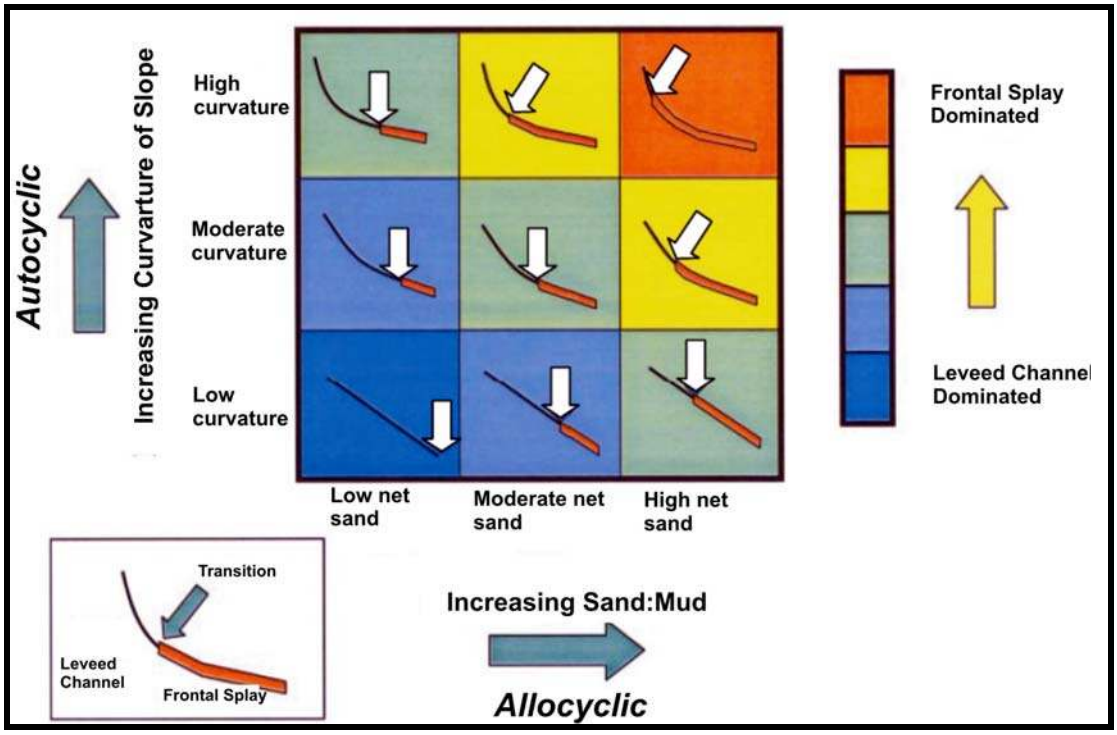


(b)

Figure 4.2 The relationship between flow stripping and slope profile. (a) The crevasse splays and levees form as products of flow stripping. (b) The effect of sand to mud ratio within the flow results in a different physiographic and location of the transition from confined channel to unconfined deposition (frontal splay) on the slope (Posamentier and Walker, 2006).

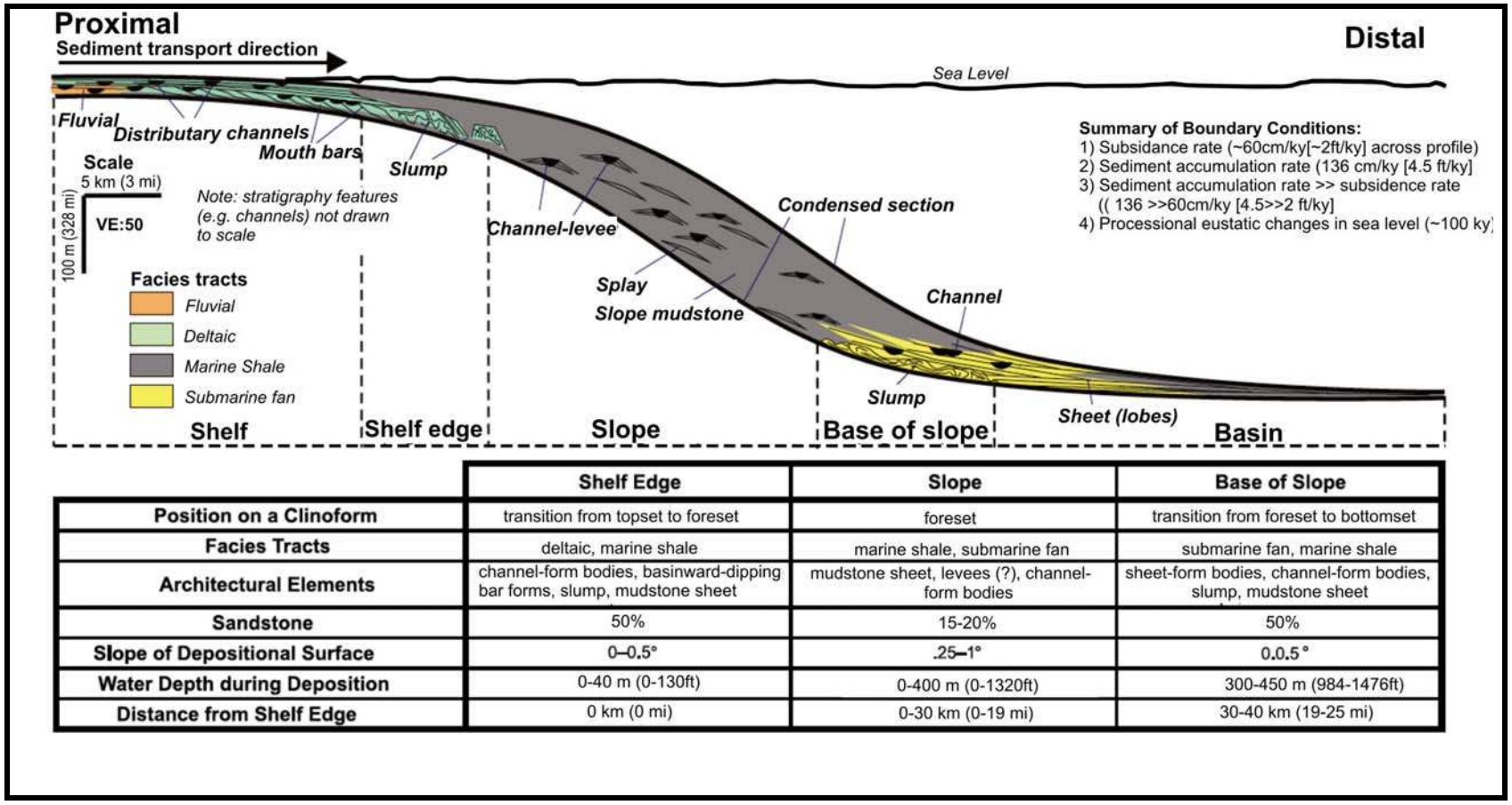


| | Shelf Edge | Slope | Base of Slope |
|---|---|---|---|
| **Position on a Clinoform** | transition from topset to foreset | foreset | transition from foreset to bottomset |
| **Facies Tracts** | deltaic, marine shale | marine shale, submarine fan | submarine fan, marine shale |
| **Architectural Elements** | channel-form bodies, basinward-dipping bar forms, slump, mudstone sheet | mudstone sheet, levees (?), channel-form bodies | sheet-form bodies, channel-form bodies, slump, mudstone sheet |
| **Sandstone** | 50% | 15-20% | 50% |
| **Slope of Depositional Surface** | 0–0.5° | .25–1° | 0.0.5 ° |
| **Water Depth during Deposition** | 0-40 m (0-130ft) | 0-400 m (0-1320ft) | 300-450 m (984-1476ft) |
| **Distance from Shelf Edge** | 0 km (0 mi) | 0-30 km (0-19 mi) | 30-40 km (19-25 mi) |

Figure 4.3 Proximal to distal changes in stratigraphy of the Lewis Shale Formation (Pyles and Slatt, 2007).

74

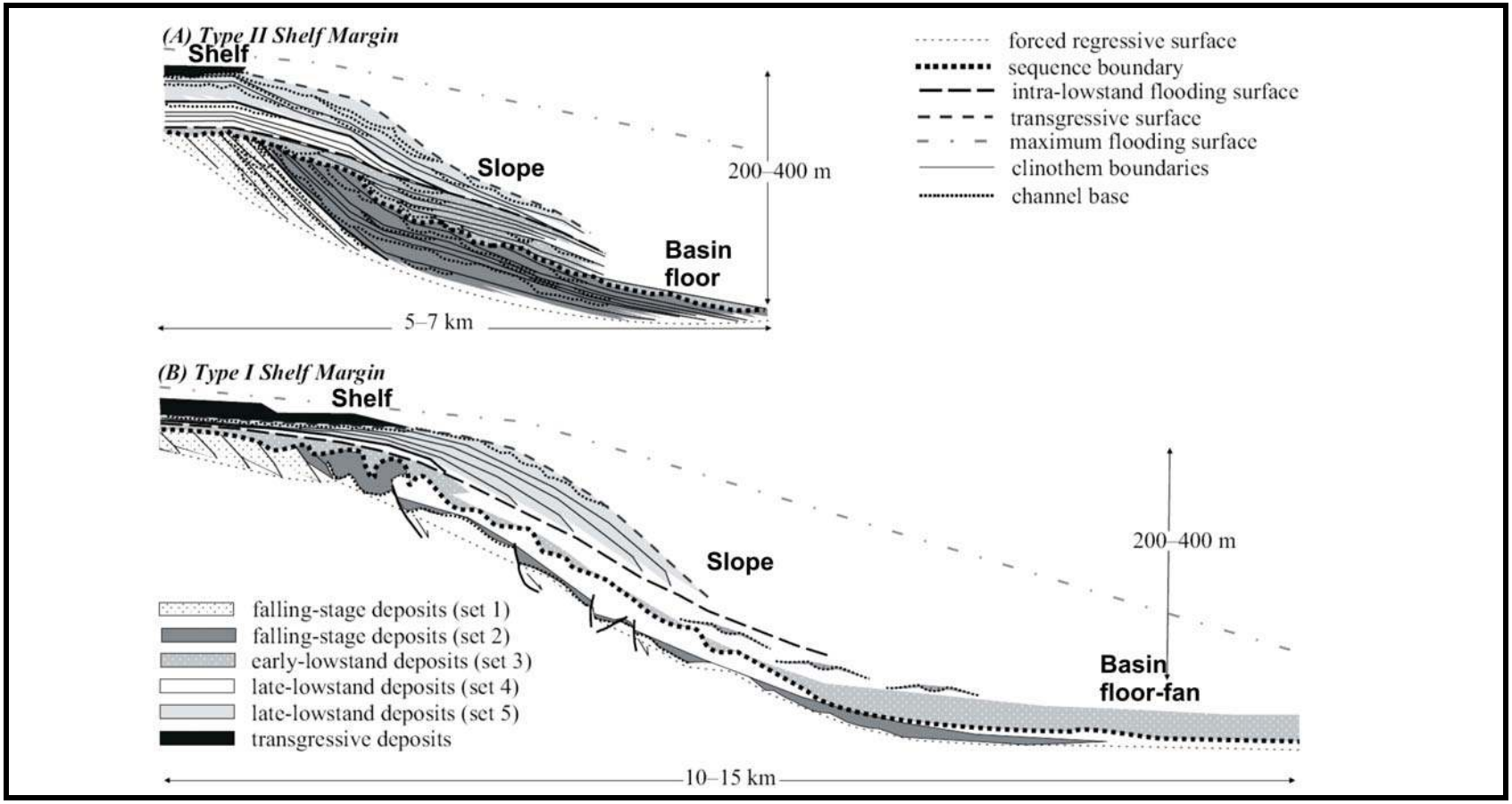


Figure 4.4 Stratigraphic architecture of the Spitsbergen Clinoform. The schematic diagram shows two different architecture element distributions that relate to the type of shelf margin. Stratigraphic architecture within type 1 shelf margin is distributed in relative short distance. This system does not develop basin-floor elements (A). In contrast, an stratigraphic architecture within type 2 shelf margin has more extended distribution with the presence of basin-floor elements (B) (Plink-Bjorklud and Steel, 2005).

75

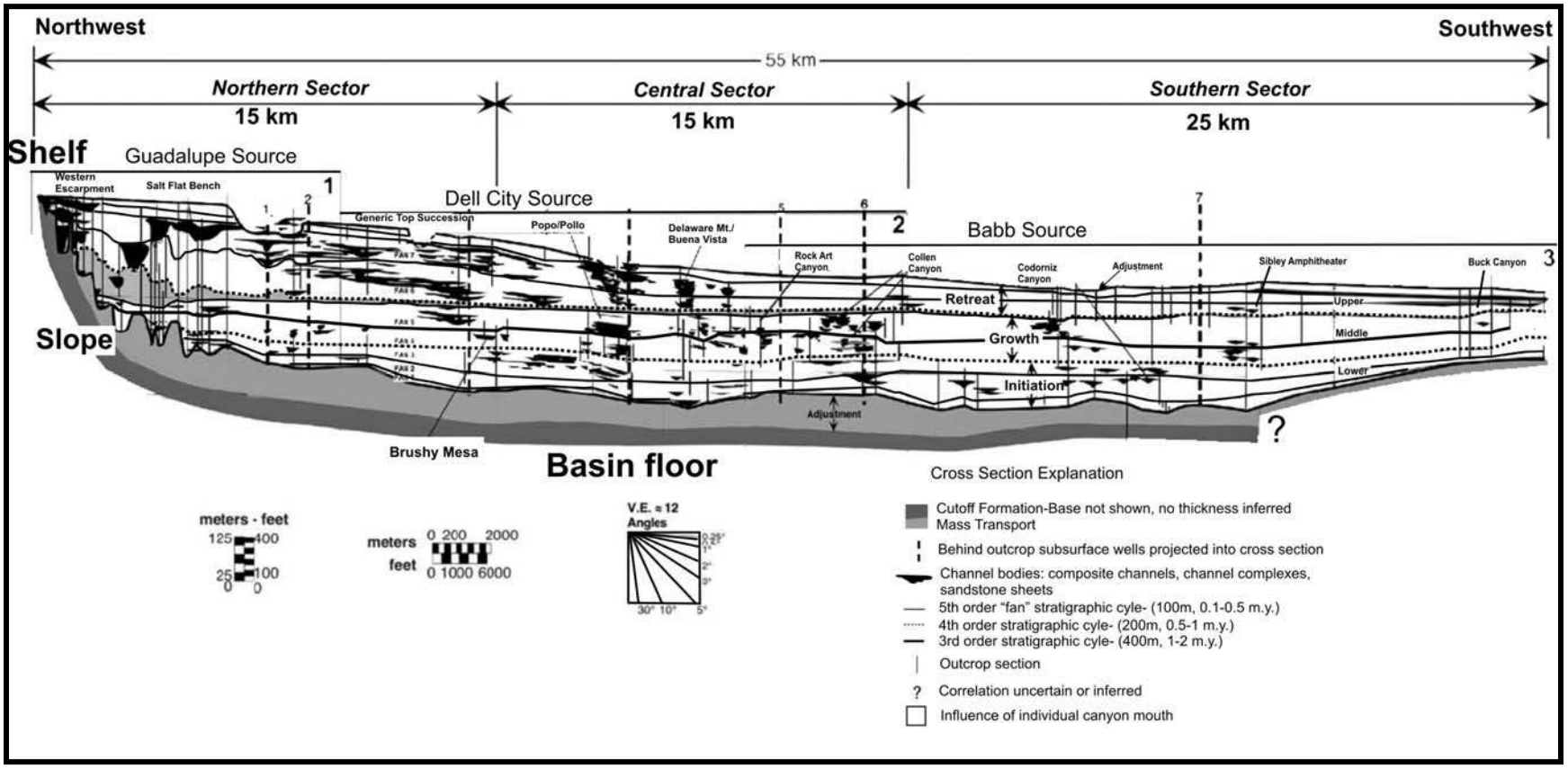


Figure 4.5 Stratigraphic architecture of the Brushy Canyon Formation (Gardner and Borer, 2000). Note that unlike the Lewis Shale and Spitsbergen system, the deepwater stratigraphy are detached from the shelf deposits.

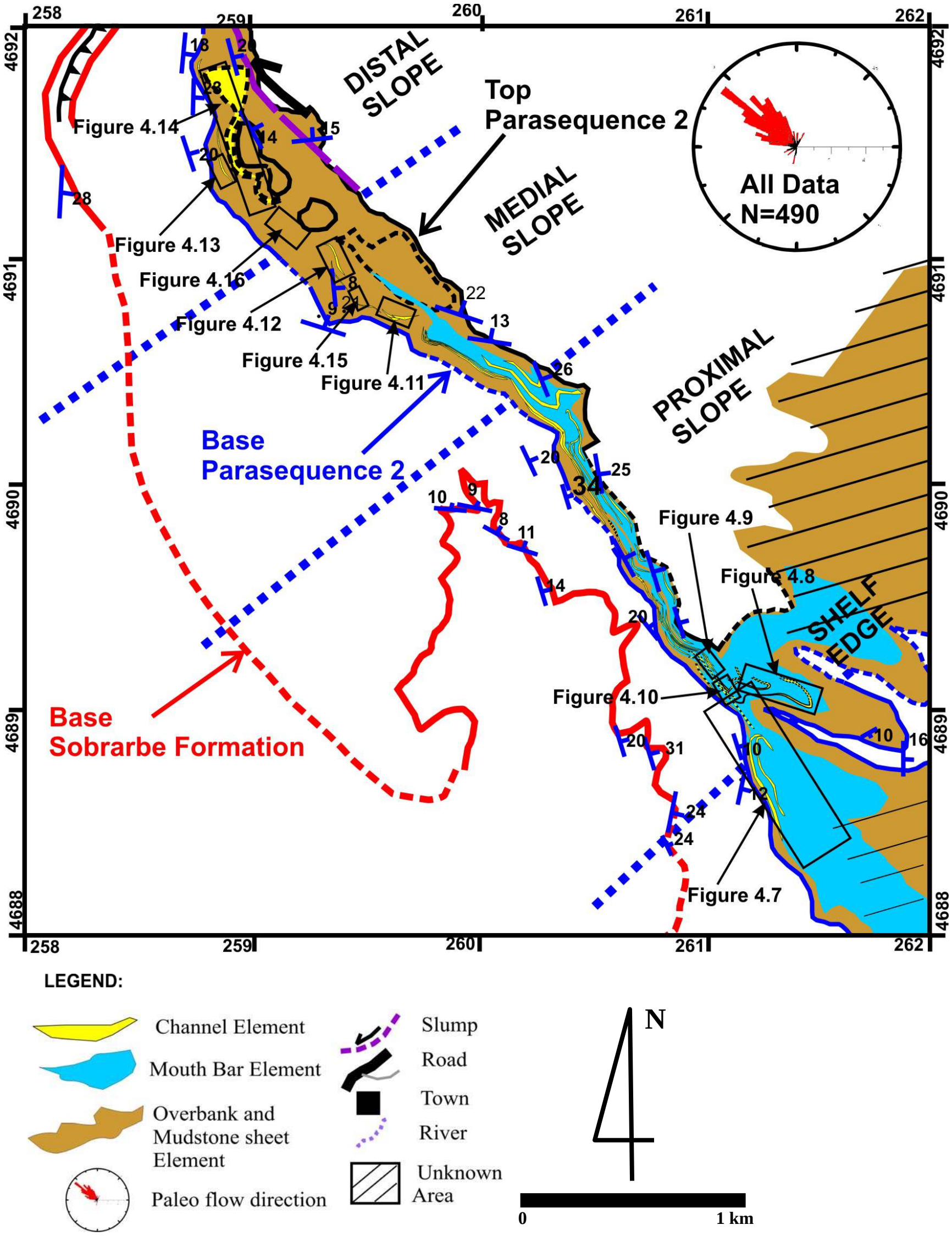


Figure 4.6 Geologic map of research area showing the distribution of architectural element in Parasequence 2 of the Sobrarbe Formation (brown color). The channel element, drawn in yellow, is distributed from south to north.

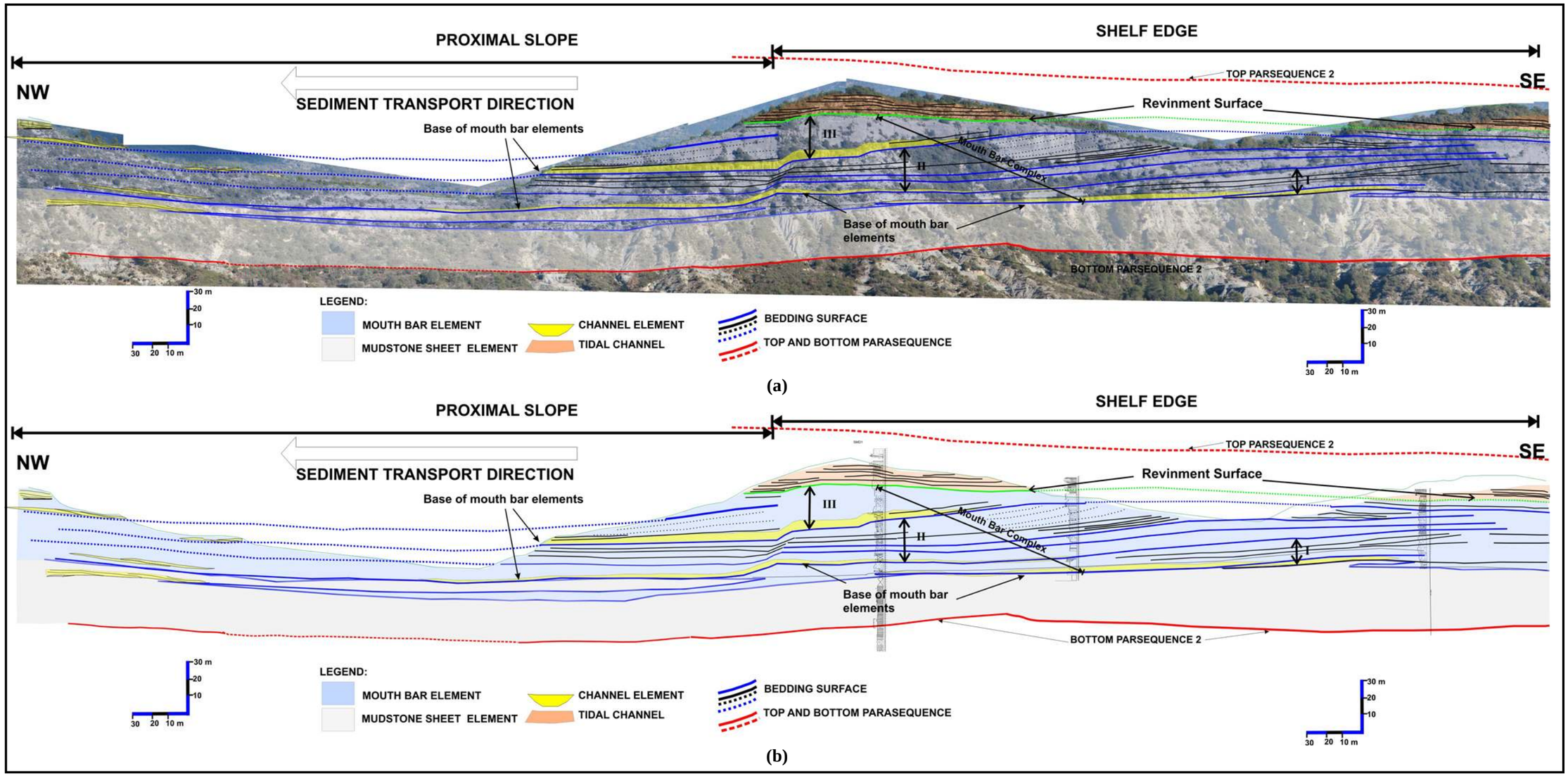


Figure 4.7 Photopanel of mouth bar elements exposed almost parallel to paleo-flow direction. The photograph shows a series of basinward-dipping beds that create a sigmoid shape. The mouth bar elements have a planar, flat base and truncated top. Three different elements are interpreted here. Each is bounded by an erosional surface. These surface correlate landward to bypass surface. The three elements stack to form a mouth bar complex. Location shown in Figure 4.6.

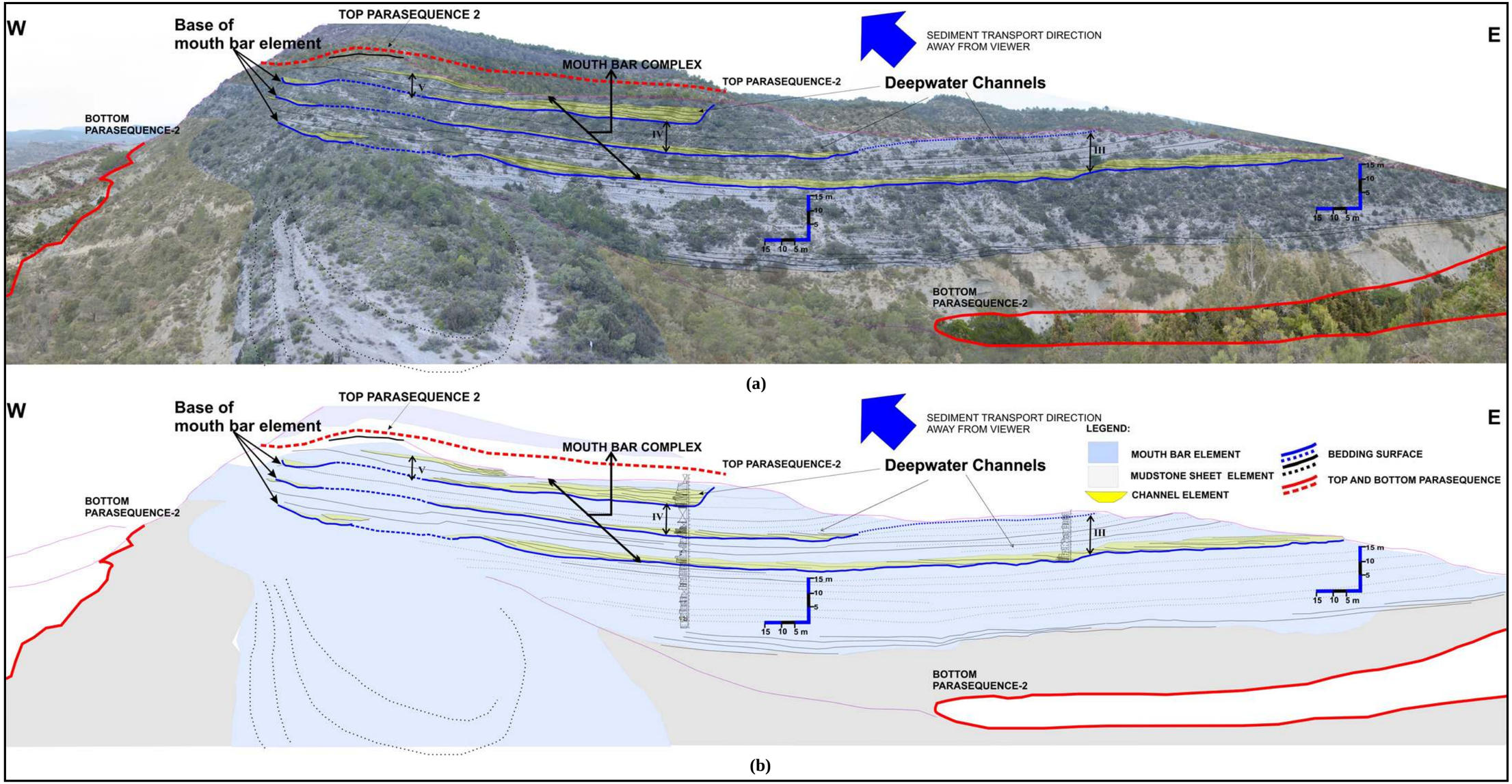


Figure 4.8 Photopanel shows depositional strike view of mouth bar complex (A= photopanel with interpretation ; B= interpretation results). The same erosional surfaces that separate the three different elements are shown in Figure 4.7. Location shown in Figure 4.6.

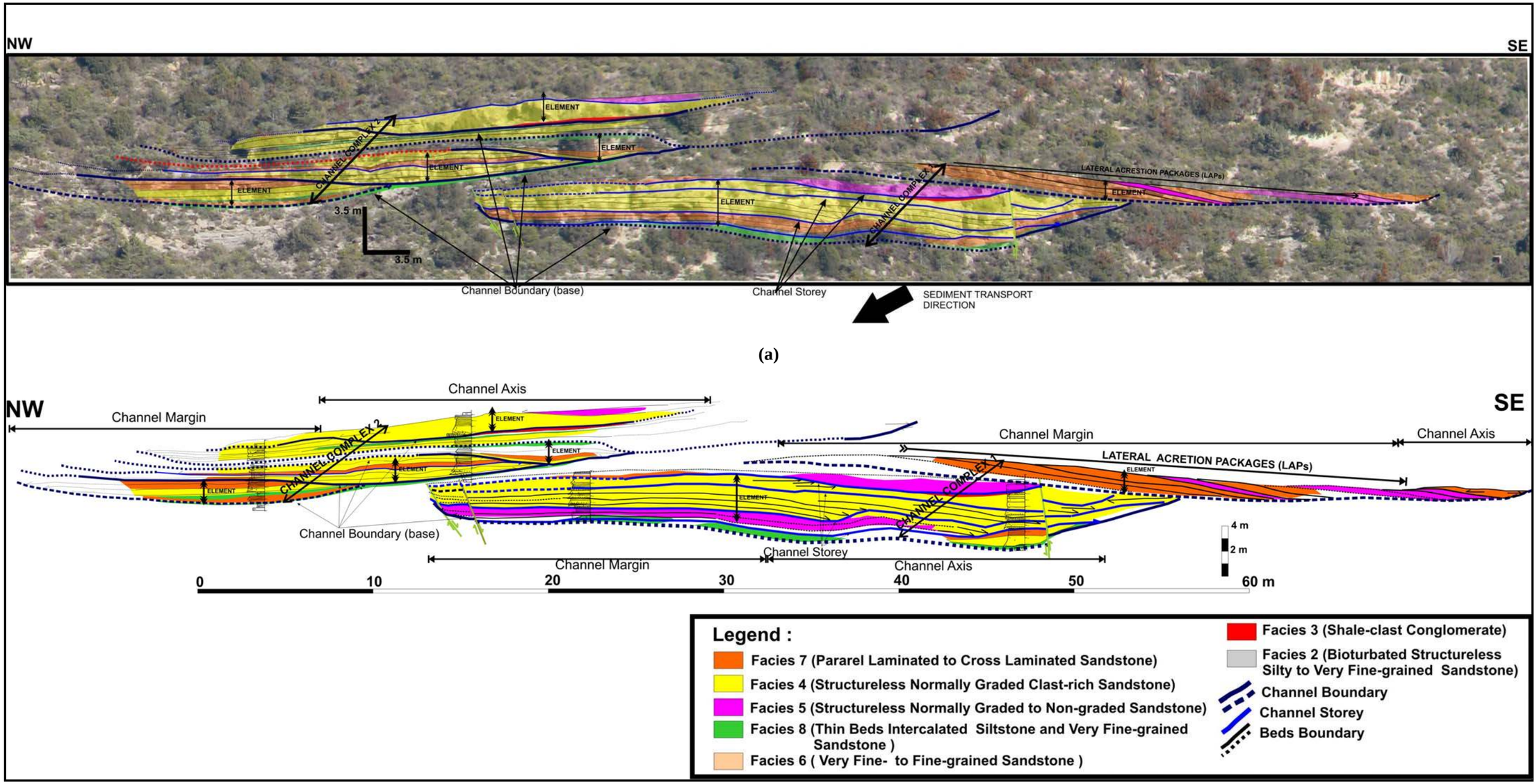


Figure 4.9 Photopanel showing Type I channels. They stack both by lateral and vertical stacking. The complexes do not have a single master erosion surface that confined them. Location shown in Figure 4.6.

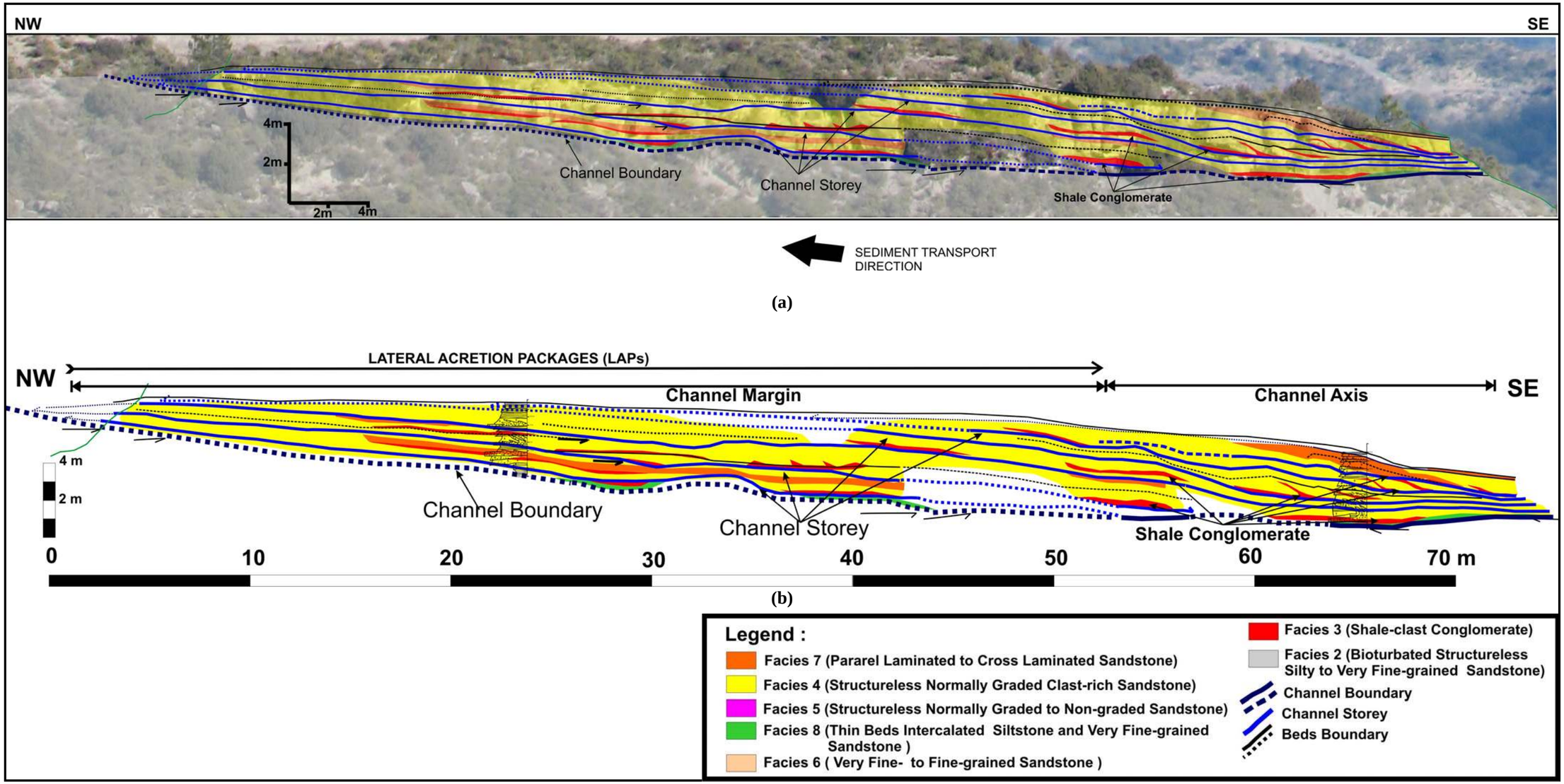


Figure 4.10 Photopanel showing a single Type I channel. Most surfaces within the channel form sigmoid-shape LAPs. Interpretation shows preserved channel margin body. The channel shows the presence of shale-conglomerate at the base of the channel or stories. Laterally, the shale conglomerate is reduced toward channel margin. Location shown in Figure 4.6

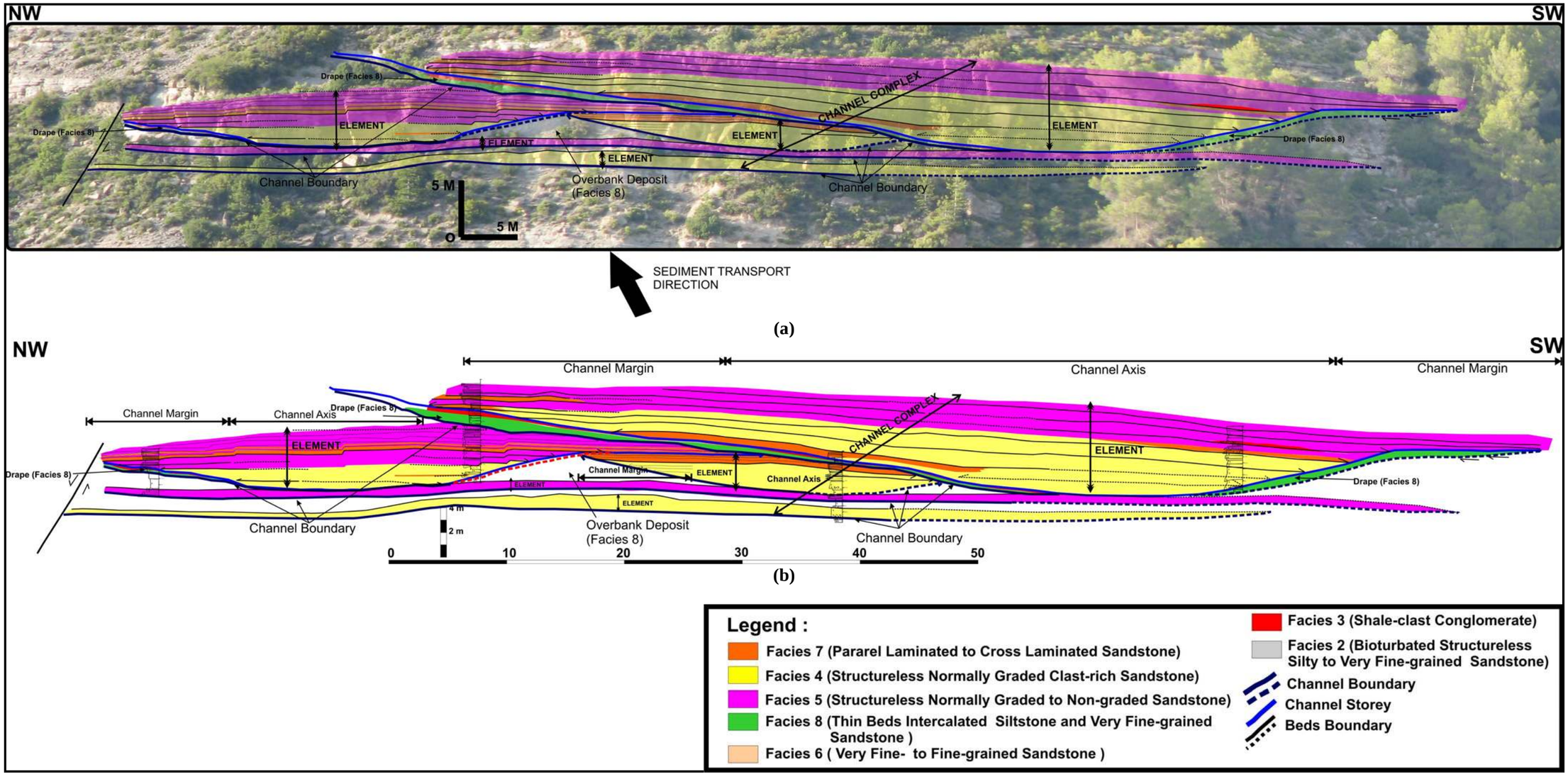


Figure 4.11 Photopanel of Type II channel elements which stack laterally and vertically to build a complex. Most of the channel axis and some channel margin are well preserved. The channel amalgamation is less than type I channels. Type II channel axis is characterized by thick and massive beds and changes into moderate thick and thinly bedded toward channel margin. Type II channels rarely has shale clast conglomerates. The upper part of the channel fill contains intercalated thin-bedded sandstone and siltstone. Location shown in Figure 4.6.

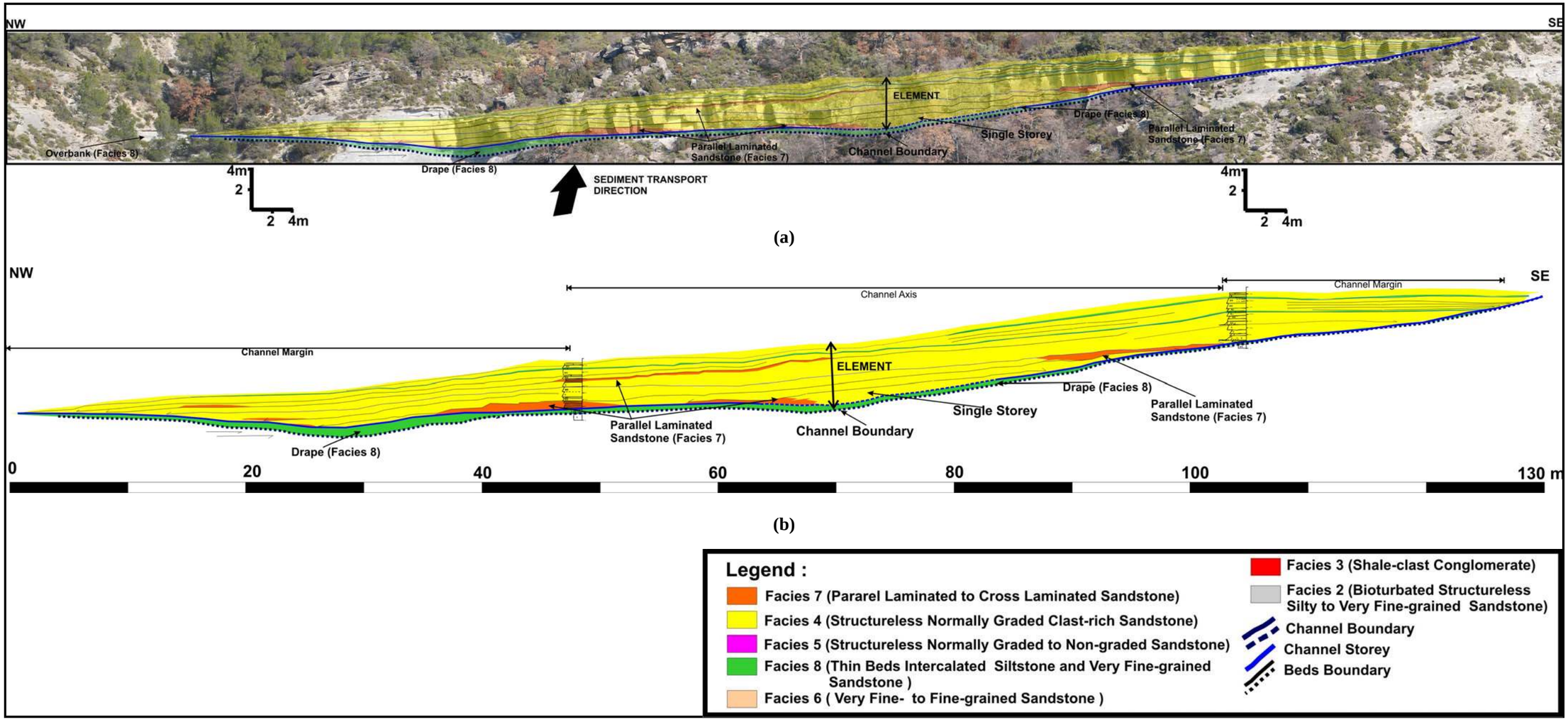


Figure 4.12 Interpreted photopanel of a single Type II channel. The channel has a concave upward lower bounding surface and flat upper bounding surface. The channel axis has thick amalgamated beds. The beds thin and de-amalgamate toward the margin. Shale conglomerates are not found within this channel body. Location shown in Figure 4.6.

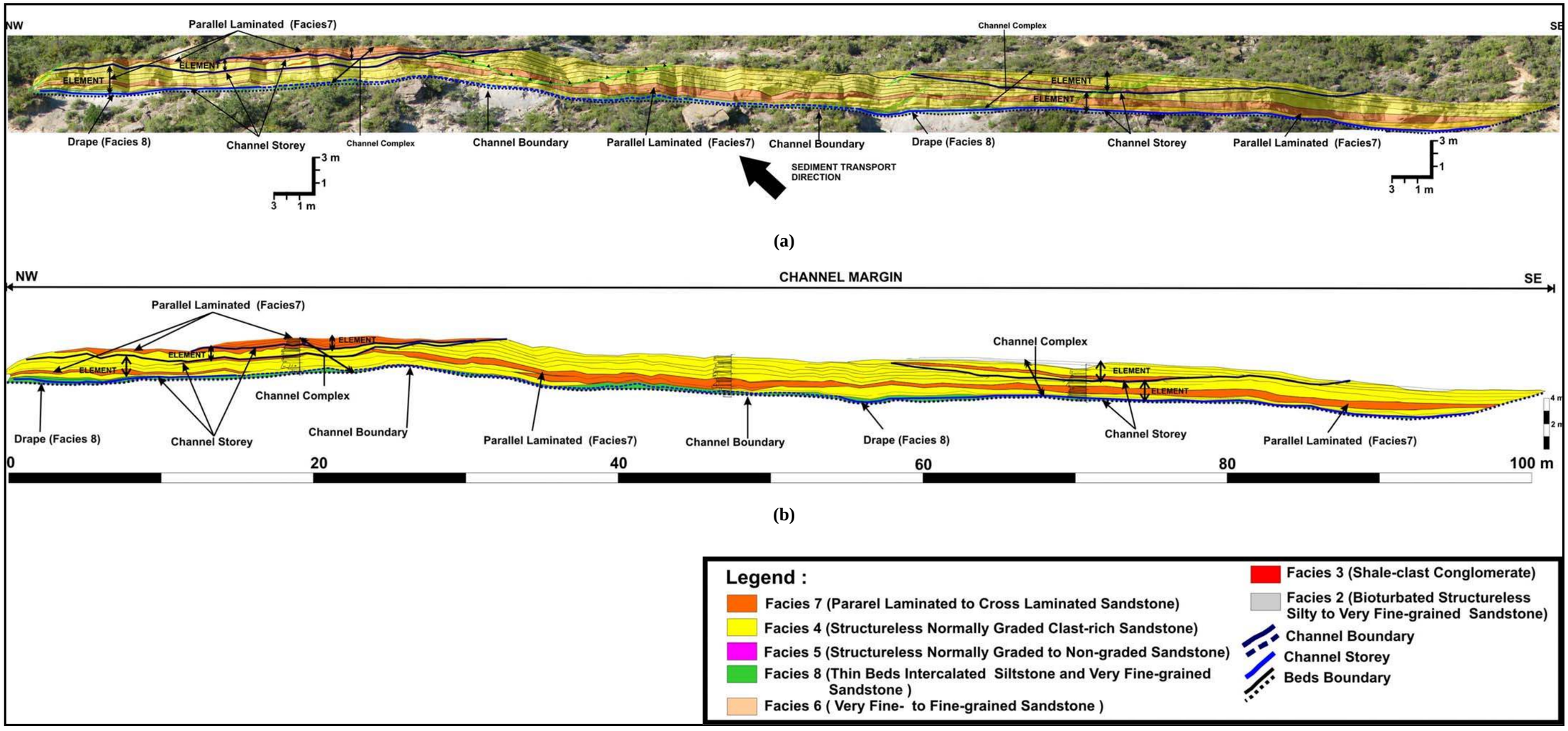


Figure 4.13 Interpreted photo panel of a partial type II channel complex. Because the outcrops of this channel body are almost parallel to paleo-flow direction. The outcrop is interpreted to show only the margins of channels. All the internal channel strata are dominated by thin to moderate thick beds and is commonly composed parallel laminated sedimentary structures. Location shown in Figure 4.6

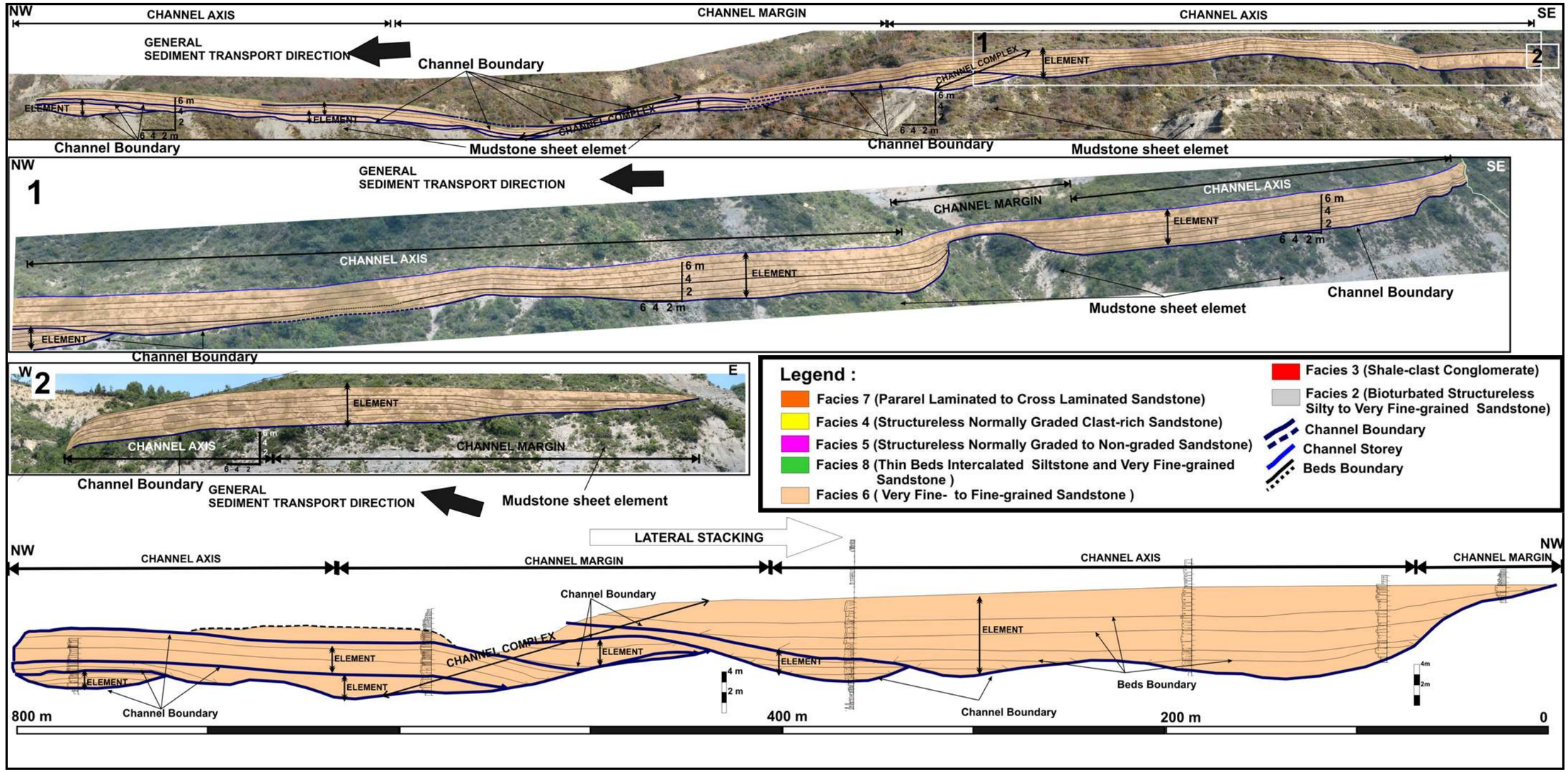


Figure 4.14 Interpreted photopanel of type III channels. They laterally stack to build a complex. The complex shows preserved channel axis and partial channel margins. Type III channels are composed of thick and tabular beds of very fine- to fined grained sandstone. The channel axis to margin change is only indicated by slightly reduced bedding thickness. The vertical bedding succession is occasionally separated by thin siltstone especially toward the top and margin of the channel. Location shown in Figure 4.6.

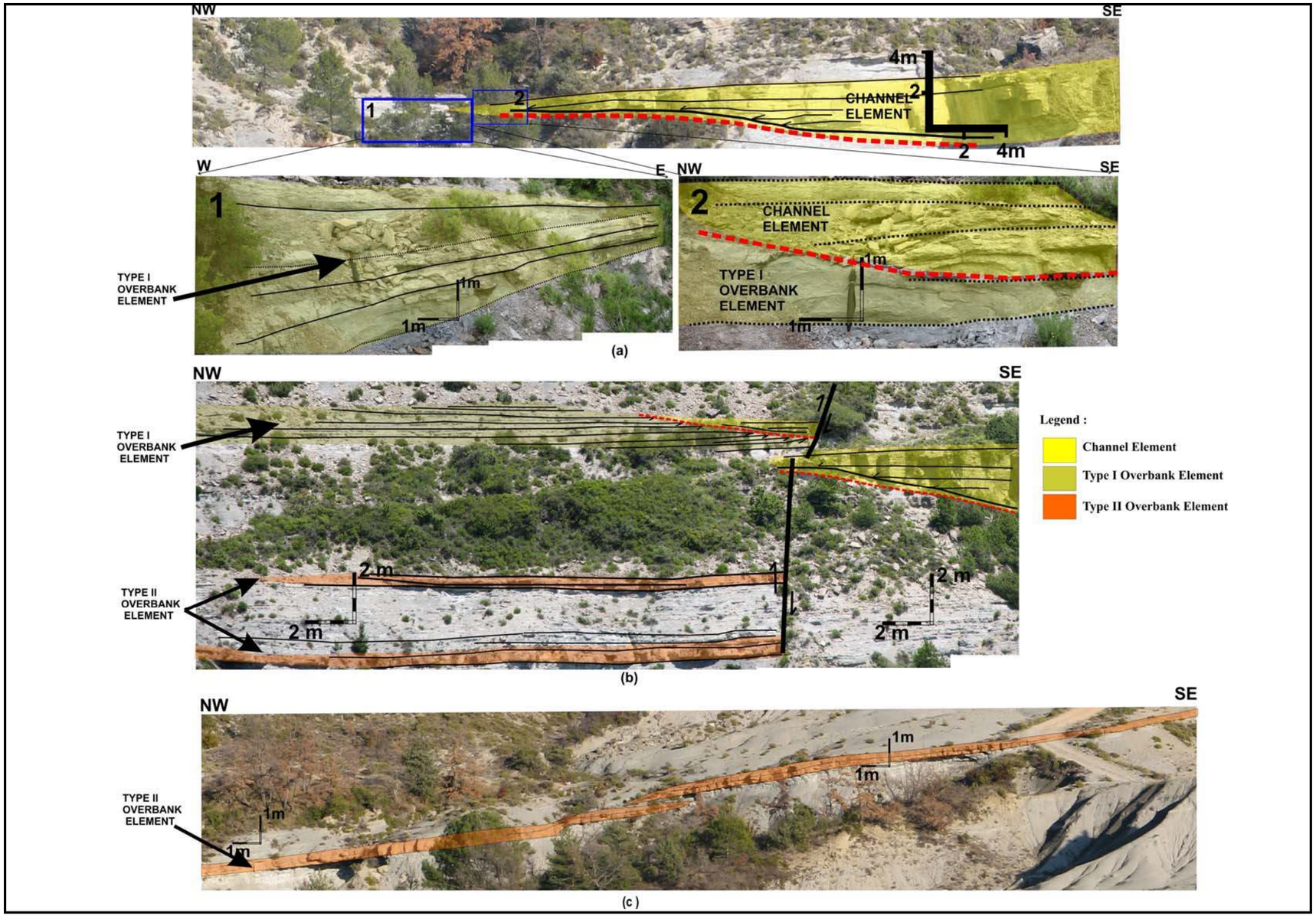


Figure 4.15 Overbank element photographs showing lenticular, wedging deposits that are laterally adjacent to channel elements (a and b) and sheet-like and thin bedded deposits (b and c). Location shown in Figure 4.6.

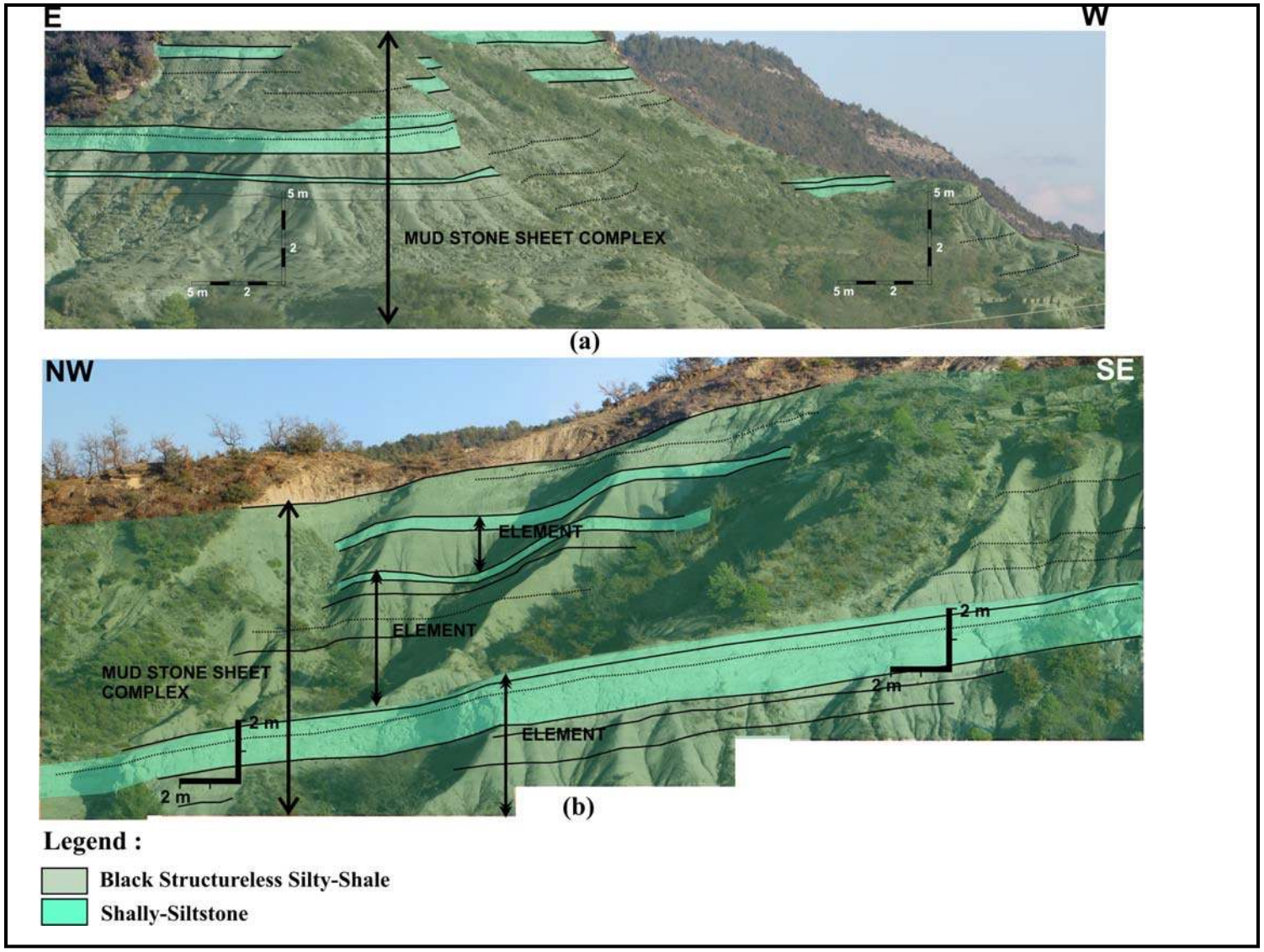


Figure 4.16 Photographs of mudstone sheet elements showing siltstone and shale intercalation at medial (a) to distal slope (b). The element is dominated by dark gray to black mudstone. Location shown in Figure 4.6.

# CHAPTER 5
# CHANGES IN STRATIGRAPHIC ARCHITECTURE FROM THE SHELF-EDGE TO THE DISTAL SLOPE

This chapter provides a detailed discussion of proximal to distal changes in stratigraphic architecture in Parasequence 2. This chapter is divided into three main sub-chapters that each begin with a brief review of related methodology and research, and each are followed by description and interpretation of stratigraphic changes, and a synthesize of the stratigraphic framework.

## 5.1 Methodology

Various methods were used interpret channel geometry, parasequence thickness, net-to-gross ratio and the geological map and regional stratigraphic cross-section. These methods are described below.

### 5.1.1 Geological Map and Regional Section

A regional 2D cross section through the parasequence is constructed by using measured sections, photo panels and the geologic map (Figure 5.1). The datum for this cross section is a black, organic-rich shale that forms the boundary between the Guaso and the Sobrarbe Formation. Measured sections and architectural elements are accurately positioned on the stratigraphic cross section (Figure 5.2).

### 5.1.2 Channel Geometry

Channel geometry calculations used in this study include: (1) Channel preserved width which is perpendicular to paleocurrent direction, (2) aspect ratio, and (3) asymmetry. The calculations use the following measurements: (1) channel thickness, (2) paleocurrent direction, (3) cliff-face/outcrop orientation, (4) location of channel axis, and (5) location of channel margin (Figure 5.3).

Channel width is calculated by using a combination of Pythagorean's theorem and trigonometric functions (Equation 5.1, 5.2; Figure 5.3).

Equation 5.1

$$W=\sqrt{((X1-X2)^2 + (Y1-Y2)^2)}$$

Equation 5.2

$$W'= Sin(Ø - ß) \times W$$

Legend:
W : Channel apparent width (m)
W' : Channel true width (m)
X1,Y1: Lat., Lon. position of channel margin 1 (m,m)
X2,Y2: Lat., Lon. position of channel margin 2 (m,m)
X3,Y3: Lat., Lon. position of channel axis (m,m)


: North direction
Ø : Cliff face orientation
ß : Paleocurrent orientation

Channel aspect ratio is calculated by using Equation 5.3:

Equation 5.3

$$AR = W'/ T$$

Legend:
AR: Aspect Ratio (dimension-less)
W' : Channel true width (m)
T : Channel thickness (m)

Channel asymmetry is calculated by using Equation 5.4-5.8 (from Pyles, 2008). In sequence, channel asymmetry is calculated as follows:

Equation 5.4

$$W1=\sqrt{((X1-X3)^2 + (Y1-Y3)^2)}$$

Equation 5.5

$$W2=\sqrt{((X2-X3)^2 + (Y2-Y3)^2)}$$

Equation 5.6

$$W1'= Sin(Ø - ß) \times W1$$

Equation 5.7

$$W2'= Sin(Ø - ß) \times W2$$

Equation 5.8

$$AS = Wmax / Wmin$$

Legend
W1: apparent axis-to-margin distance 1 (m)
W2: apparent axis-to-margin distance 2 (m)
W1': true axis-to-margin distance 1 (m)
W2': true axis-to-margin distance 2 (m)
X1,Y1: GPS position of channel margin 1 (m,m)
X2,Y2: GPS position of channel margin 2 (m,m)
X3,Y3: GPS position of channel axis (m,m)
Ø : Cliff face orientation (degree)
ß : Paleocurrent orientation (degree)
AS: Channel Asymmetry (dimension-less)
Wmax: Largest value of W1 and W2
Wmin: Smallest value of W1 and W2

### 5.1.3 Parasequence Thickness

Parasequence thickness is calculated by combining Pythagorean's Theorem and trigonometric functions. The calculation uses latitude, longitude, elevation (x, y, z), and strike and dip data of bedding at the base and top of the parasequence (Figure 5.4). The calculation methods are described sequentially as follows:

Equation 5.9

$$\text{Øavg} = \text{ArcTan}((\text{Sin Ø1} + \text{Sin Ø2}) / (\text{Cos Ø1} + \text{Cos Ø2}))$$

Equation 5.10

$$H = \sqrt{((X1-X2)^2) + ((Y1-Y2)^2)}$$

Equation 5.11

$$\Delta V = (V1-V2)$$

Equation 5.12

$$R = \sqrt{(H^2) + (\Delta V^2)}$$

Equation 5.13

$$\mu = \text{Arctan}(\Delta V / H)$$

Equation 5.14

$$T = \text{Sin}(\text{Øavg} + \mu)R$$

where ß1 = ß2

Øavg : Average dip of Ø1 and Ø2
Ø1 : Dip of the bed at the top of the parasequence
Ø2 : Dip of the bed at the bottom of the parasequence
ß1 : Strike of the bed at the top of the parasequence
ß2 : Strike of the bed at the bottom of the parasequence
H : Horizontal distance between the top and base of the parasequence (m)
ΔV : Elevation differences between the top and base of the parasequence (m)
V1 : Elevation at the top of the parasequence (m)
V2 : Elevation at the bottom of the parasequence (m).
μ : Angle between horizontal position to hypotenuse line (figure 5.4)
T : Thickness of parsequence

### 5.1.4 Net-to-Gross Ratio

Net-to-gross ratio is calculated by dividing the thickness of sand in a measured section (net) by the total interval thickness (gross). The net thickness is defined by using grainsize very fine sand. The beds with very fine sand and above are grouped into net thickness. This cutoff will be different compare to subsurface cutoff that utilize porosity and permeability data to calculate the net-to-gross ratio. The measured section is recorded

with scale 1 cm = 1 m actual measurement. With this scale, the beds with less then 10 cm thick are mostly not recorded.

### 5.2 Proximal to Distal Changes in Stratigraphic Architecture

Multiple changes in stratigraphic architecture are documented along slope physiographic of research area. The startigraphic changes analysis and observation are mainly focus on several stratigraphic aspects. They are: (1) paleo flow direction, (2) architectural elements, (3) channel geometry, (4) facies, and (5) grain size and net-to-gross ratio. In this study, the slope physiography is divided into three equal area (proximal, medial and distal slope) for statistical analysis and trend analysis purposes as shown in Figure 5.1 and 5.2.

#### 5.2.1 Changes in Paleo Flow Direction

Paleo flow directions are measured from the flute, grooves, ripples and channel-margin orientations. 487 paleocurrents were measured in this study. These data are presented in rose diagrams on the geologic map (Figure 5.5) and a cross plot (Figure 5.6).

The average of all paleocurrent data collected on slope strata of Parasequence 2 is $282^0$ (Figure 5.5). For purpose of statistical comparison, the slope was divided into three areas of equal length: proximal, medial slope and distal slope. Each zone has a distinctive average and variance in paleocurrent directions are (Figure 5.5 and 5.6). Since paleocurrent data are collected form channels, paleocurrent variance is interpreted to be a proxy for channel sinuosity. Areas with low paleocurrent diversity (proximal and distal slope) are interpreted to be areas with relatively straight channels. In contrast, areas with high paleocurrent diversity (middle slope) are interpreted to reflect areas with high channel sinuosity.

#### 5.2.2 Changes in Architectural Elements

Architectural elements within Parasequence 2 of the Sobrarbe Formation are mapped from the shelf edge to the base of slope (Figure 5.5 and 4.6). The architectural elements vary by physiographic position. At the shelf edge, the parasequence is composed of mouth bars, channel and mudstone sheets (Figure 5.2 and 5.7). Mouth bars

occupy approximately 60% of shelf edge strata. The elements consist of multiple stacked mouth bar elements which stack basinward to build a mouth bar complex. Channel elements are found at the boundaries between mouth bar elements (channels occupy less than 10% of shelf edge strata). Mudstone sheets occur stratigraphicaly below the mouth bars. Mudstone sheet elements occupy approximately 30% of shelf edge strata.

Proximal slope strata are composed of mouth bar elements, channel elements and mudstone sheets (Figure 5.2 and 5.7). At this location only the distal toes of mouth bar are exposed. The toe of mouth bar elements decrease in thickness toward medial slope. Mouth bar elements occupy approximately 45 % of proximal slope strata. Channel elements are associated with mouth bar elements. Channel element stack laterally and vertically to form channel complexes. Channel elements occupy approximately 30% of proximal slope strata (Figure 5.7 and 5.8). Most of channels in the proximal slope are Type I channel elements. Mudstone sheet elements are positioned at the lower and upper part of the parasequence. Mudstone sheets occupy about 30% of proximal slope strata.

Medial slope strata are composed of mouth bar elements, channels elements, overbank elements and mudstone sheet elements (Figure 5.2 and 5.9). The distal most toe of mouth bar elements are located at this position and they are partitioned to upper part of the parasequence (Figure 5.9 and 5.10). The mouth bar element occupies about 25% of medial slope strata, channel elements and associated with mouth bar element and overbank elements. They occupy about 30% medial slope strata. Channels stack vertically and laterally to build channel complexes (Figure 5.9 and 5.10). At this location, channels have greater lateral stacking than observed in proximal slope strata. Type II channels are most common in medial slope strata. Overbank elements are difficult to map in medial slope strata due to vegetation. These elements commonly occur close to channel elements in the medial slope strata (Figure 4.14). The overbank element occupies about 5% of medial slope strata. Mudstone sheet elements occupy approximately 45% of medial slope strata.

Distal slope strata are composed of channel elements, overbank elements and mudstone sheet elements (Figure 5.2 and 5.11). They stack laterally to build complexes. Channel elements are associated with overbank elements and mudstone sheets (Figure 5.2 and 5.11). Channel elements occupy about 28% of distal slope strata. At this location,

most channel elements are Type III channels with few examples of Type II channels element. Type II channel elements are commonly found in the proximal part of the distal slope and are formed as thinly to moderately thick (2- 4.5 m) individual channel (Figure 4.12, 4.13 and 5.11). The overbank element commonly occurs adjacent to channel elements. When not adjacent to channels, the overbank element is not easily mapped. The overbank elements occupy approximately 10% of distal slope strata. Mudstone sheet elements occupy approximately 60% of distal slope strata (Figure 5.2 and 5.11).

Figure 5.12 summarizes proximal to distal changes in stratigraphic architecture. The chart shows that mudstone sheet elements increase basinward at the expense mouth bars. Overbank strata are only located in medial and distal slope strata and channels are roughly uniform in proportion across the slope. Figure 5.12 show the proximal to distal slope changes in channel architecture. Lateral offset between channel elements increase basinward. Associated with these changes is a basinward decreasing in vertical offset between channels. Type I channel elements are most common in the proximal slope. Type II channels are most common in medial slope, and Type III channel are most common in the distal slope.

### 5.2.3 Changes in Channel Geometry

Channel geometry changes from the proximal to distal slope. Because most of the exposures are oriented parallel to paleo flow direction, the geometry of several channels in the parasequence can not be measured. Table 5.1 contains the data collected in this analysis.

Four channel geometry variables are used in this analysis. They are channel thickness, width, aspect ratio and asymmetry. The analysis reveals the following trends. First channel thickness increases from the proximal to the distal slope (Figure 5.14). Second, channel width increases from the proximal to the distal slope (Figure 5.15). Based on these first two trends, channel size increases from the proximal to the distal slope. Third, aspect ratio increases basinward (Figure 5.16). The average aspect ratio increases by the factor of four from the proximal to the distal slope. Fourth, there is no measureable change in channel asymmetry from proximal to distal slope (Figure 5.17).

### 5.2.4 Changes in Facies

Data used to define proximal to distal facies patterns are from measured sections and photopanel interpretations. Six regional measured sections spanning the shelf edge to distal slope document vertical facies information for the entire the parasequence. Lateral facies information is gathered from photo panel documentation of facies in several selected channel elements spanning upper slope to lower slope.

The facies distribution chart shown in Figure 5.18 show that the numbers of facies decrease from the shelf edge to distal slope. Figure 5.19 only shows extra channel facies. This chart shows the same overall decrease in the number of facies from the proximal to distal slope. When only observing strata outside of channels, bioturbated structureless silty-sandstone with bio-clast (Facies 2), which is only associated with mouth bar elements decrease to zero within 3 km of the shelf edge (Figure 5.19). The other non-channel fill facies, such as intercalated mudstone and very fine sandstone facies (Facies 8) and dark gray to black structureless mudstone facies (Facies 9), increase basinward (Figure 5.8). The diversity of facies in extra channel strata decrease basinward. Sandstone conglomerates (Facies 1), structureless normally graded to non-graded sandstone (Facies 5), shale-clast conglomerate (Facies 3), clast rich sandstone (Facies 4), structureless very fine to fine grain sandstone (Facies 6) and parallel to cross-lamination sandstone (Facies 7) decrease from proximal to distal slope (Figure 5.20).

In summary there is a basinward decrease in facies diversity for channel and extra-channel strata (Figure 5.18, 5.19 and 5.20). Associated with this decrease is an overall decrease in grain size. All coarser facies (Such as Facies 1, 3, 4, 5, 6 and 7) are deposited within channel elements.

### 5.2.5 Changes in Grain Size and Net-to-Gross

Grain size and net-to-gross ratio are calculated from measured sections. Grain size data was measured using a hand-held Wentworth grainsize chart. For purpose of this study, grain size populations are divided into silt- to clay-, very-fine sand and fine- sand to granule. Net-to-gross ratio is calculated for each measured section by separating the proportion of sand and coarser sediment from the total thickness of the measured interval (Figure 5.21b).

Figure 5.21 shows the decrease in coarse-grained facies in proportion down the slope. The coarsest grainsize population shows the largest basinward changes from 28% to < 5%. Associated with this pattern is an over all decrease in net-to-gross from 0.81 to 0.05.

Table 5.1 Geometry of from proximal to distal slope channels.

| | Channel | Thickness (m) | Width (m) | Aspect Ratio | Asymmetry | Distance to Shelf Edge (m) |
|---|---|---|---|---|---|---|
| Proximal Slope | 4B_shelfedge | 2 | 16 | 11 | 2 | 350 |
| | 3_shelfedge | 4 | 25 | 6 | 1 | 550 |
| | 4_shelfedge | 2 | 32 | 18 | 1 | 570 |
| | 8_shelfedge | 4 | 66 | 19 | 1 | 840 |
| | 9_shelfedge | 3 | 67 | 27 | 1 | 850 |
| | 16_shelfedge | 2 | 22 | 13 | 2 | 1110 |
| | y_waterfall | 4 | 21 | 6 | 2 | 1430 |
| | 1_waterfall | 6 | 63 | 11 | 1 | 1760 |
| | 2_waterfall | 7 | | | | 1780 |
| Medial Slope | HorgeA_2 | 3 | 28 | 9 | 2 | 2440 |
| | HorgeA_1 | 2 | 46 | 23 | 3 | 2480 |
| | HorgeB_3 | 7 | 116 | 17 | 2 | 2600 |
| | HorgeB_2 | 2 | 21 | 11 | 1 | 2610 |
| | HorgeB_1 | 5 | 45 | 9 | 1 | 2630 |
| | HorgeC_1 | 2 | 98 | 38 | 1 | 2760 |
| | HorgeC_2 | 5 | 70 | 31 | 1 | 3000 |
| Distal Slope | HorgeC_7 (type III) | 8 | 250 | 31 | | 3770 |
| | HorgeC_8 (type III) | 4 | 300 | 75 | | 4500 |

Table 5.2 Geometry of proximal to distal slope channels

| Variable | Mean | Standard Deviation | Variance | Number of Samples |
|---|---|---|---|---|
| **Thickness** | | | | |
| Proximal | 3.5 | 1.82 | 1.354 | 9 |
| Medial | 3.85 | 1.827 | 1.35 | 7 |
| Distal | 6 | 2 | 1.41 | 3 |
| | | | | |
| **Width** | | | | |
| Proximal | 38.8 | 20.9 | 4.6 | 9 |
| Medial | 60.59 | 32.8 | 5.7 | 7 |
| Distal | 275 | 25 | 5 | 3 |
| | | | | |
| **Aspect Ratio** | | | | |
| Proximal | 13.66 | 6.61 | 2.6 | 9 |
| Medial | 19.48 | 10.7 | 3.3 | 7 |
| Distal | 53.125 | 21.875 | 4.67 | 3 |
| | | | | |
| **Asymmetry** | | | | |
| Proximal | 1.52 | 0.3 | 0.55 | 9 |
| Medial<br>Distal | 1.51 | 0.54 | 0.73 | 7 |

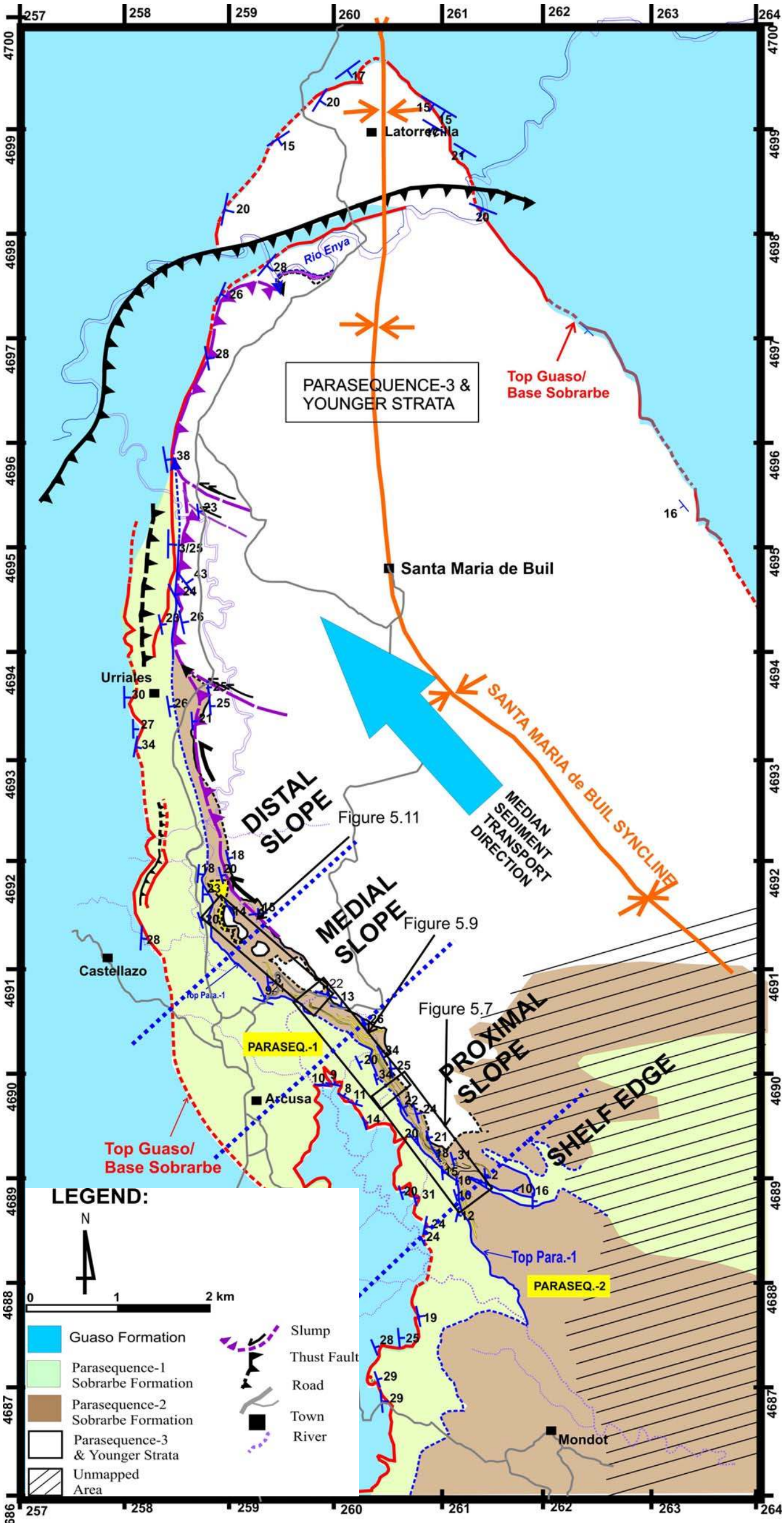


Figure 5.1 Geologic map of the study Area**.** The slope is divided into three of equal area in order statistically evaluate proximal to distal changes in slope architecture

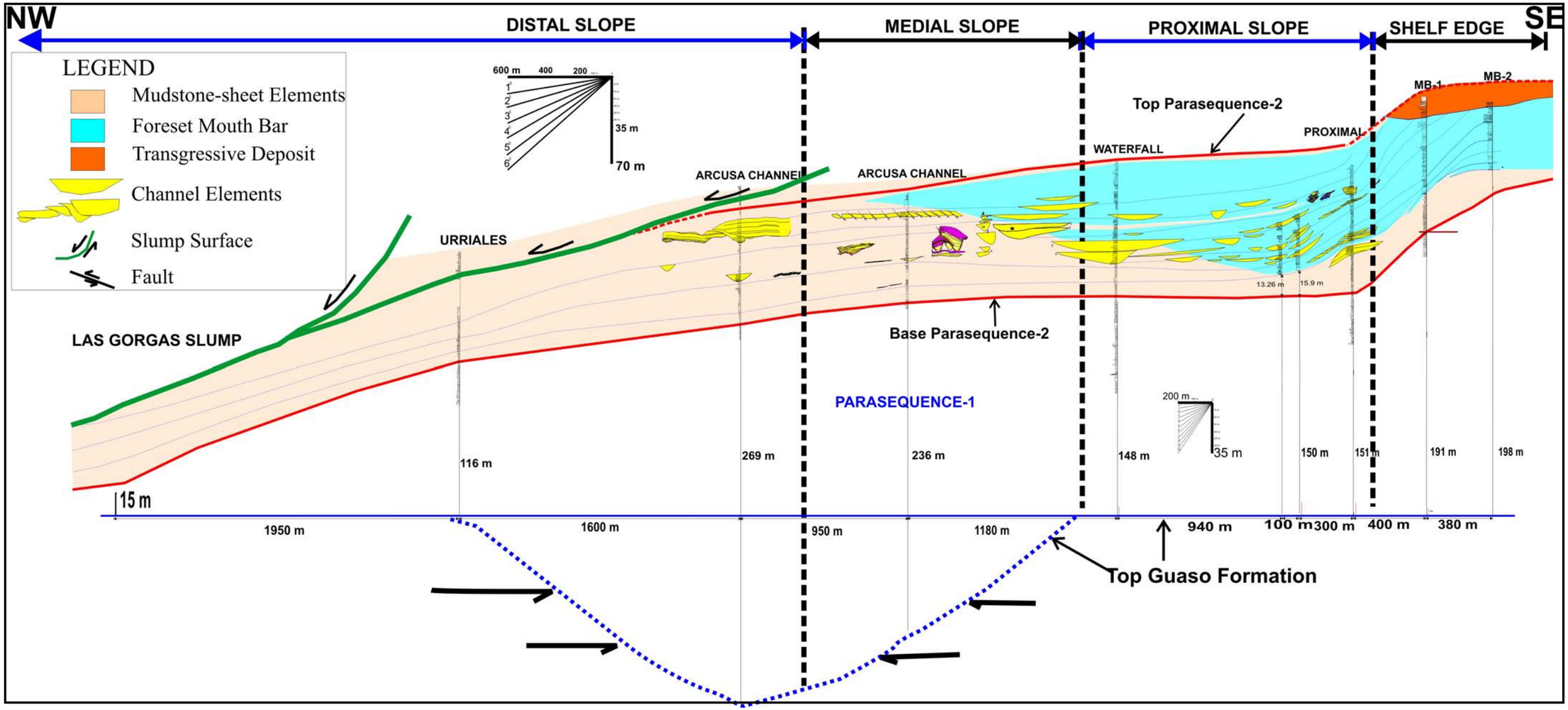


Figure 5.2 Cross section showing the stratigraphy of the Parasequence 2 Sobrarbe Formation. This cross section presents the distribution of architecture elements from the shelf edge to distal slope within Parasequence 2.

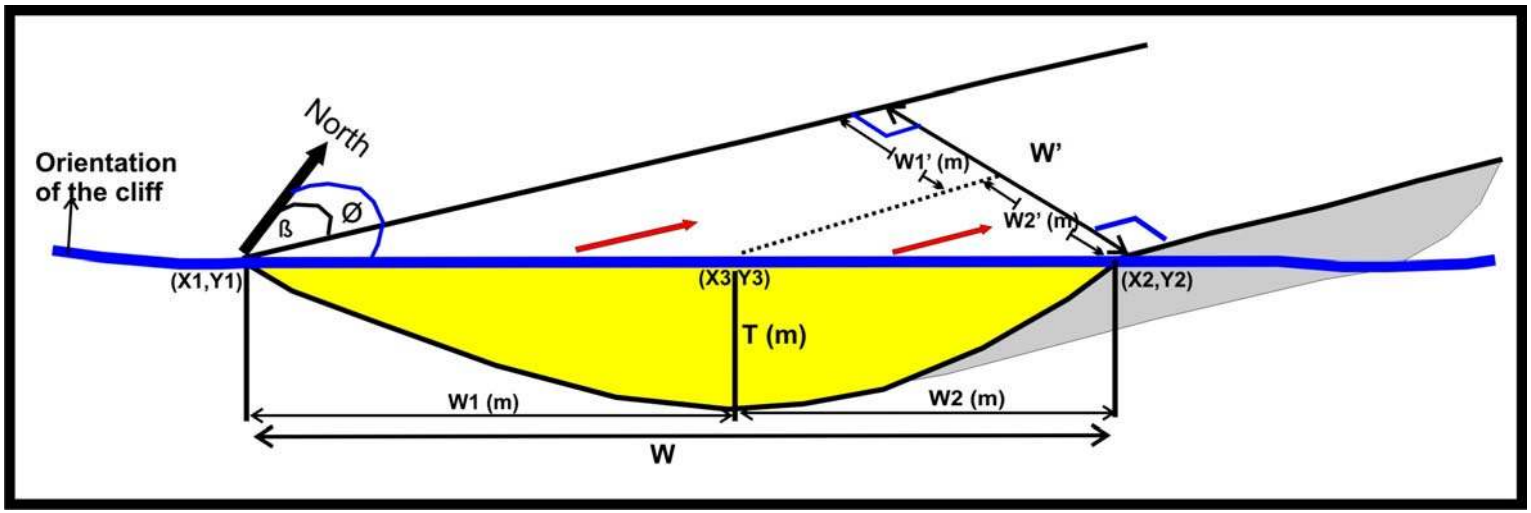


Figure 5. 3 Diagram showing how channel geometry is calculated.

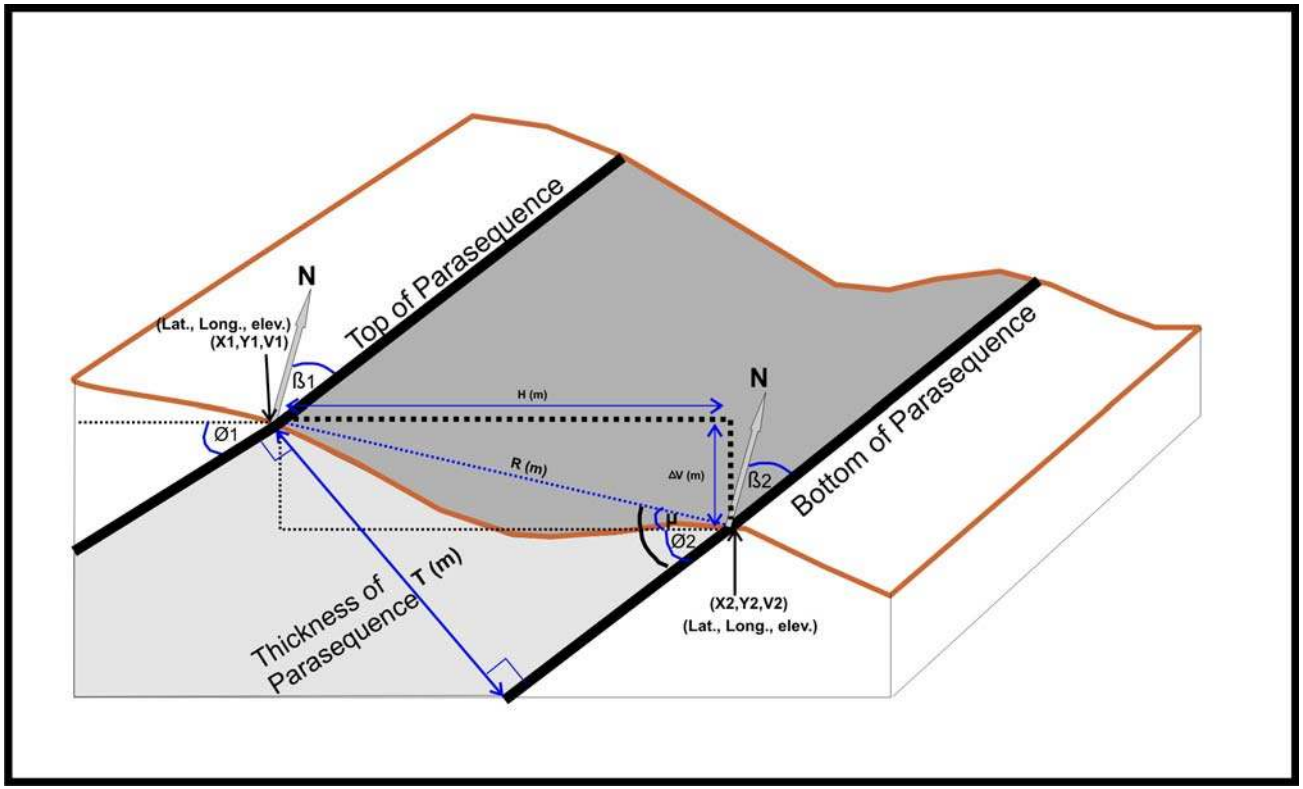


Figure 5.4 Block diagram illustrating the methods for calculating parasequence thickness. The thickness calculation utilizes data that are measured where the top and bottom of the parasequence forms a straight-line parallel to the dip of the bedding (See equations 5.9-5.14 for explanation of variables).

101

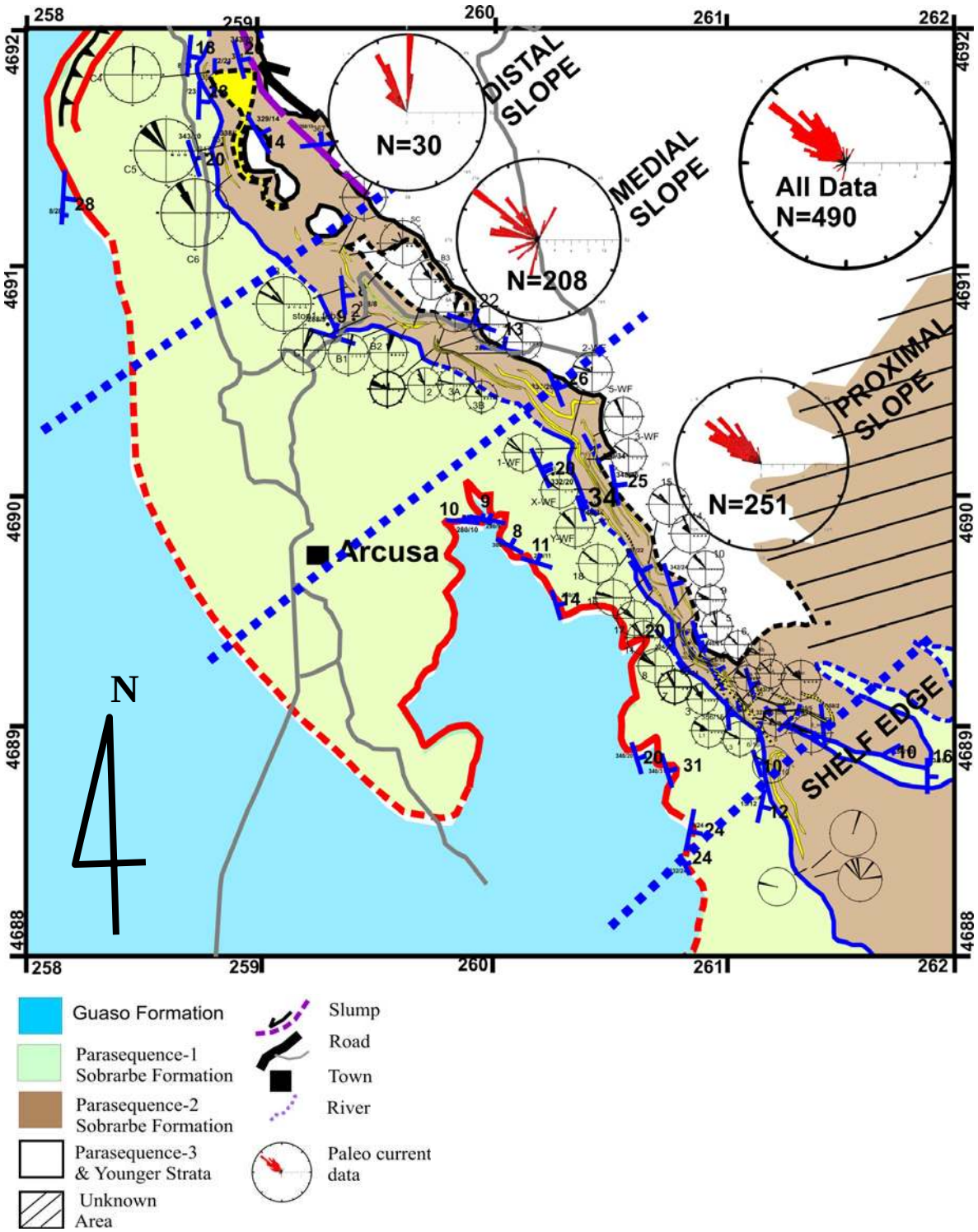


Figure 5.5 Geologic map showing paleocurrents collected in this study. The average modal paleo current is southeast to northwest. The study area is divided into three zones: proximal slope, medial slope and distal slope. Paleo-current is distinctive in each zone.

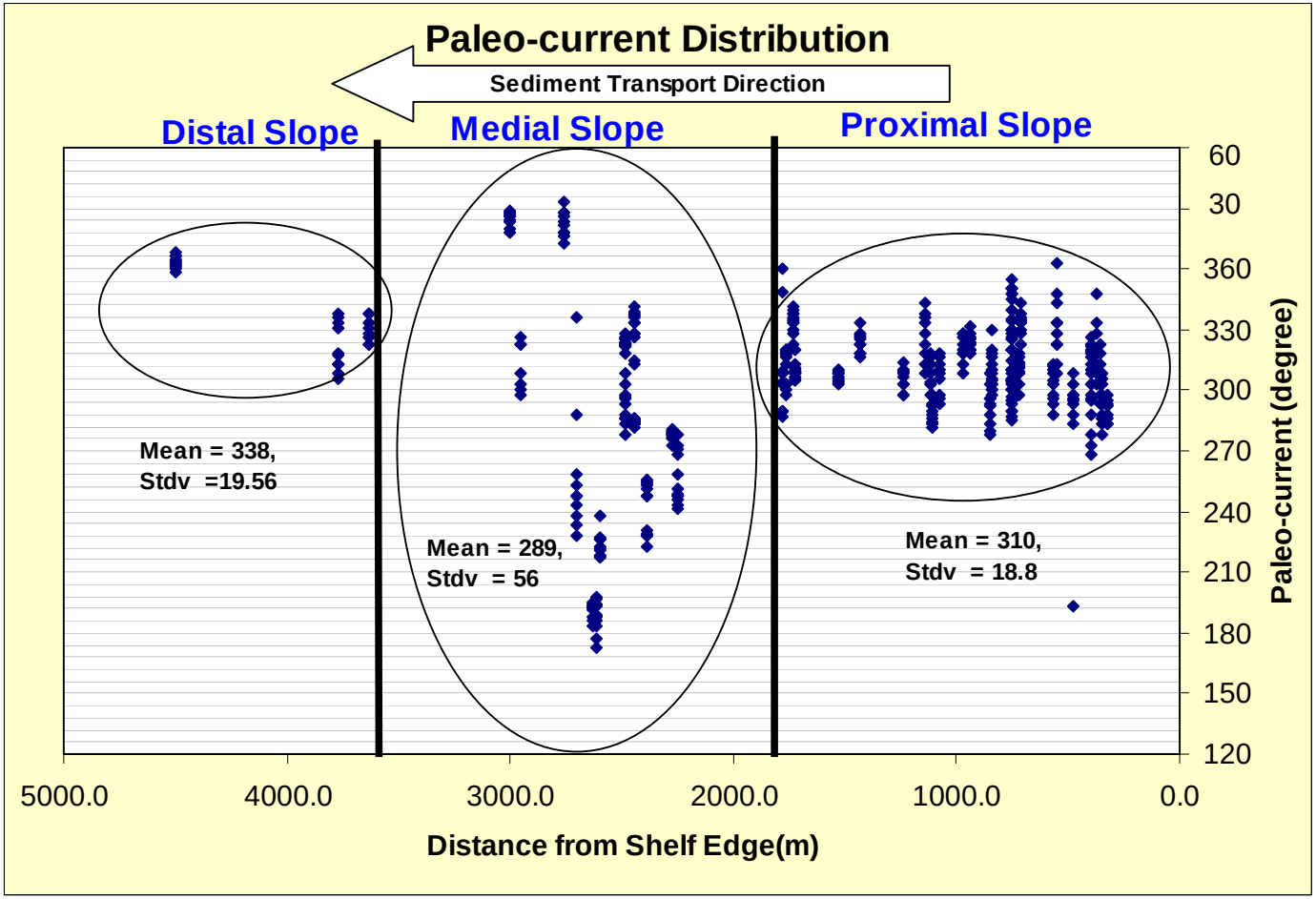


Figure 5.6 Cross plot showing paleocurrent data scaled to distance from shelf edge (see Figure 5.4 for location). The study area is divided into three zones of equal length (proximal slope, medial slope and distal slope). Each zone has a different paleocurrent signature. The proximal and distal slope has low paleocurrent diversity paleocurrent and medial slope has high paleocurrent diversity.

103

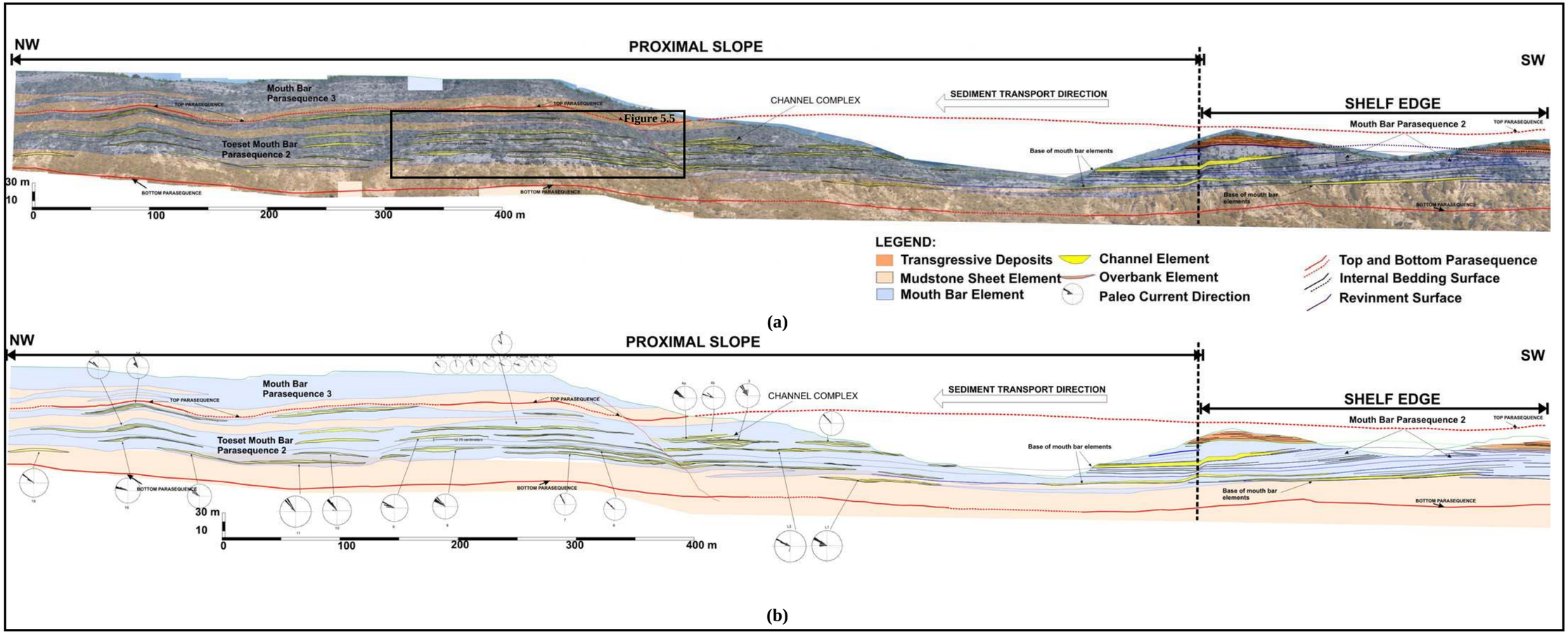


Figure 5.7 Photopanel and interpretations of shelf edge and proximal slope strata. Location of photopanel shown in Figure 5.1

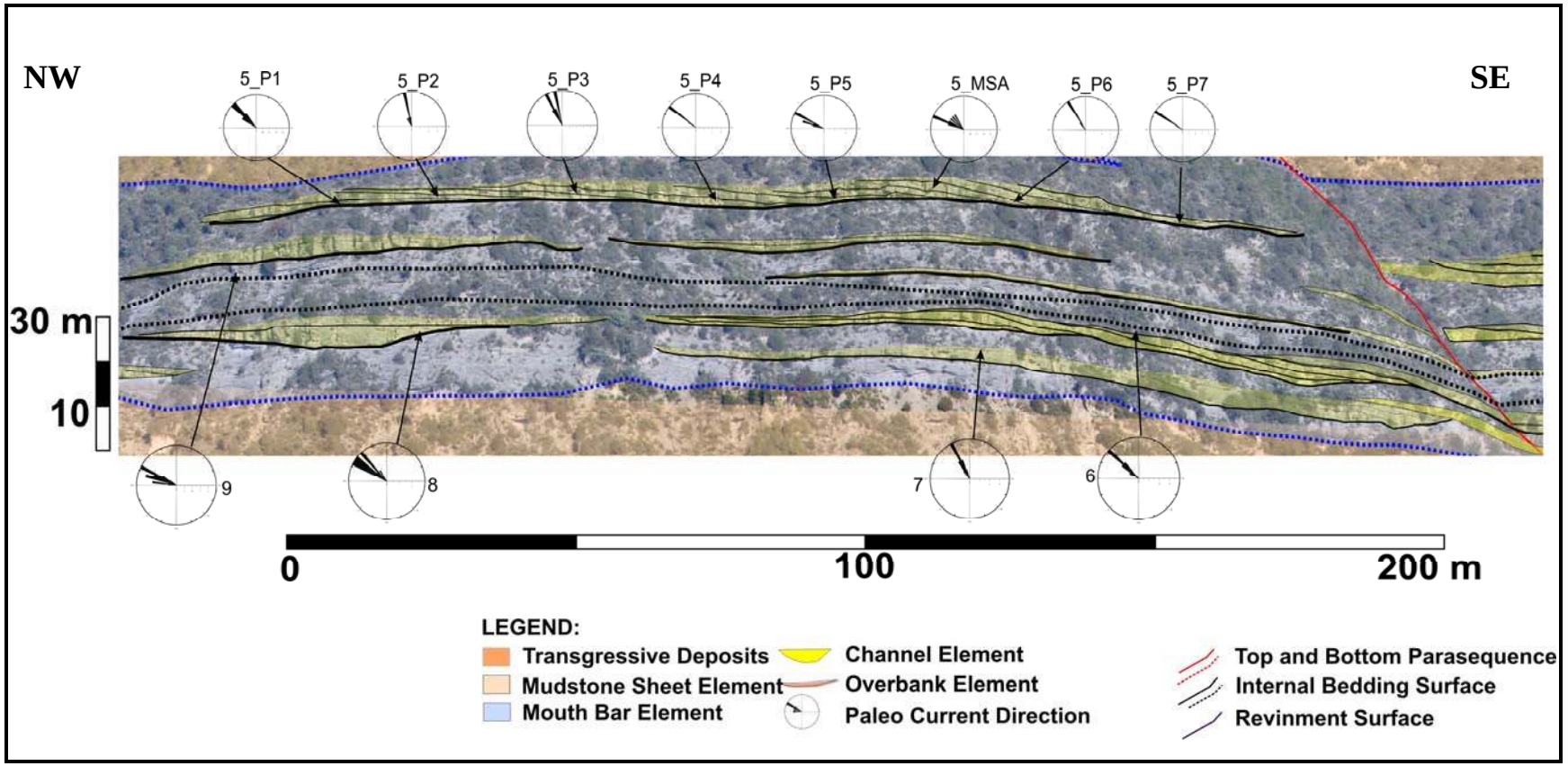


Figure 5.8 Photopanel of proximal slope strata showing Type I channel elements, mouth bar element and mudstone sheet.

105

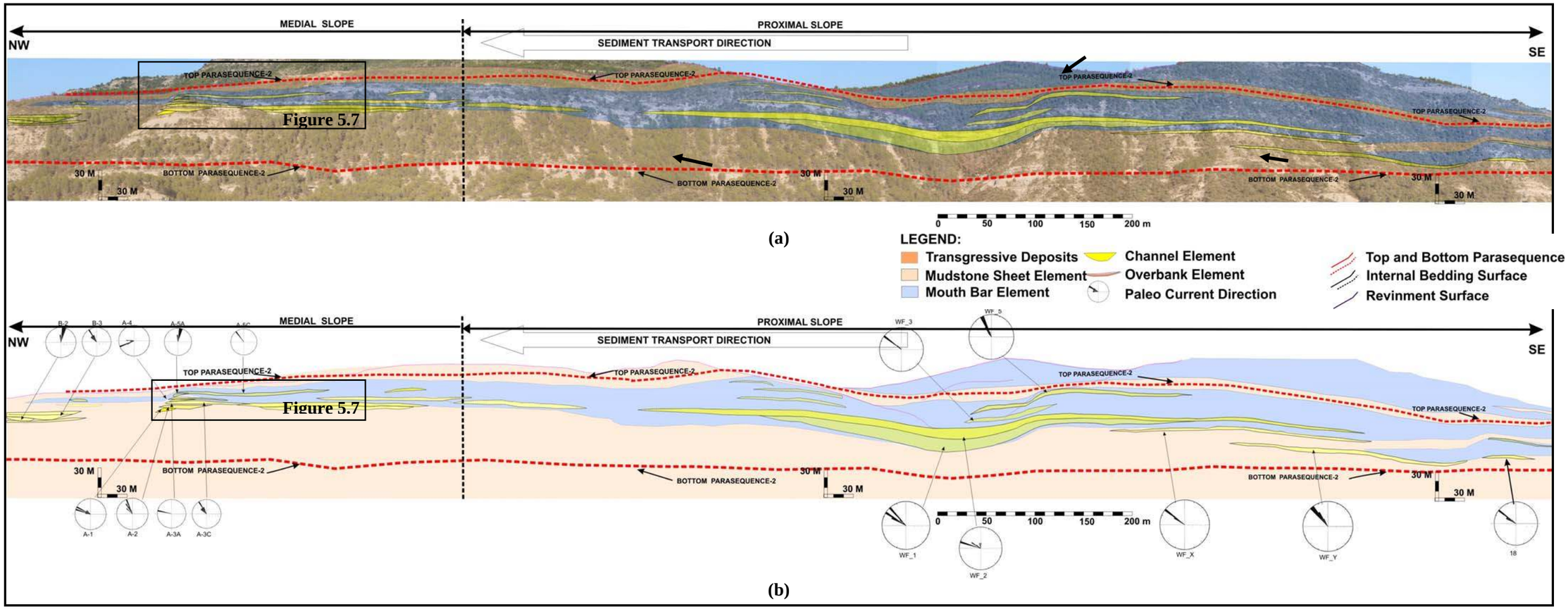


Figure 5.9 Photopanel and interpretation of slope strata. At this position, the distal toe of mouth bar elements laterally thin. Mudstone sheet elements increase basinward. Channel elements are most commonly Type II channels.

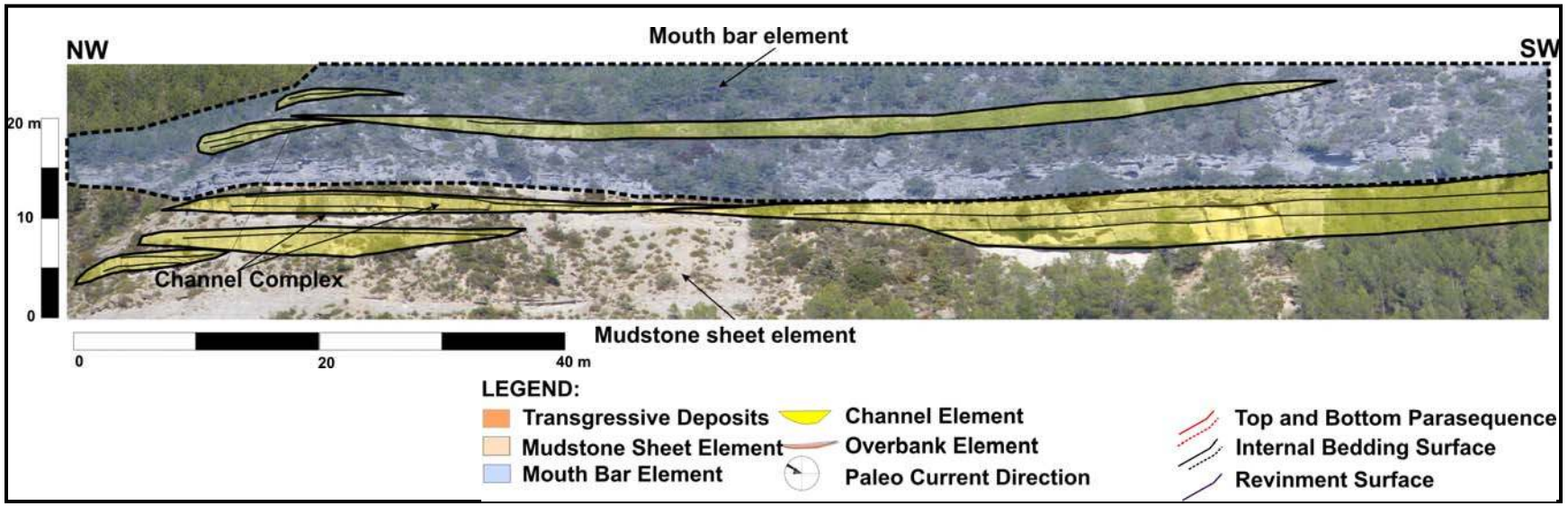


Figure 5.10 Photopanel interpretation of a channel complex in medial slope strata. Channels stack laterally and vertically to build a complex.

107

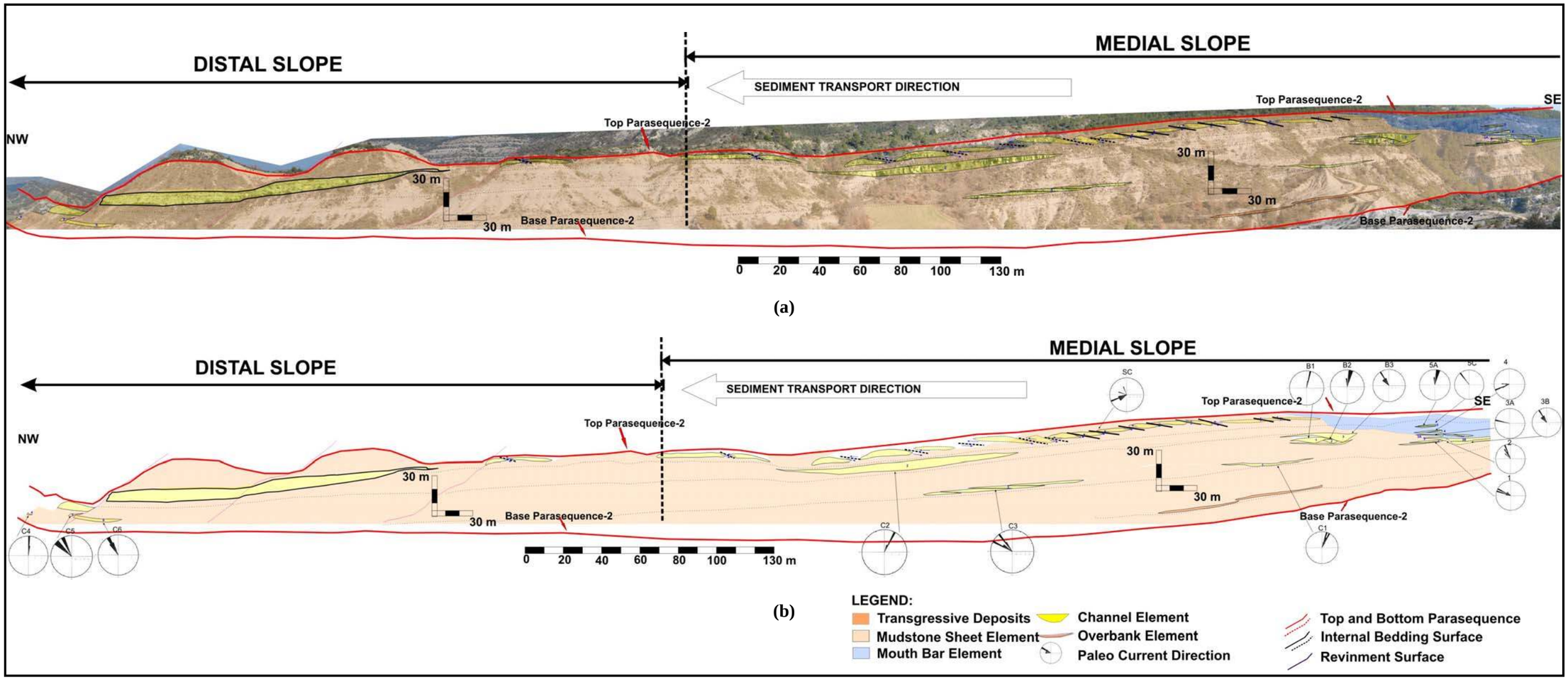


Figure 5.11 Photopanel interpretation of distal slope strata. Mudstone sheets are the most common element at this location. The most common type of channel is Type III channels. They stack laterally to build the largest channel complex in the slope. Most of the channel elements in this position occur within mudstones sheet elements.

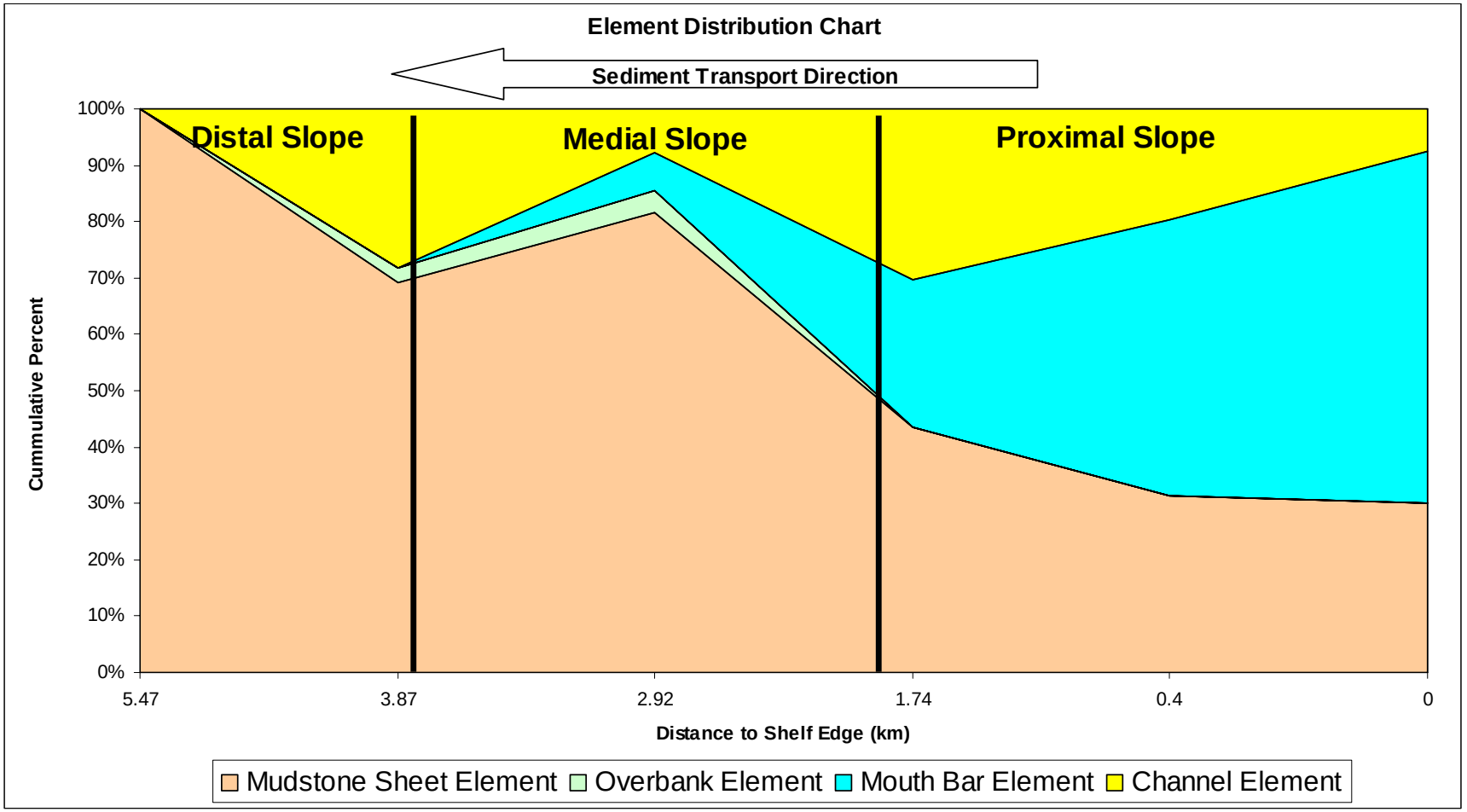


Figure 5.12 Chart of element distribution from proximal to distal slope

109

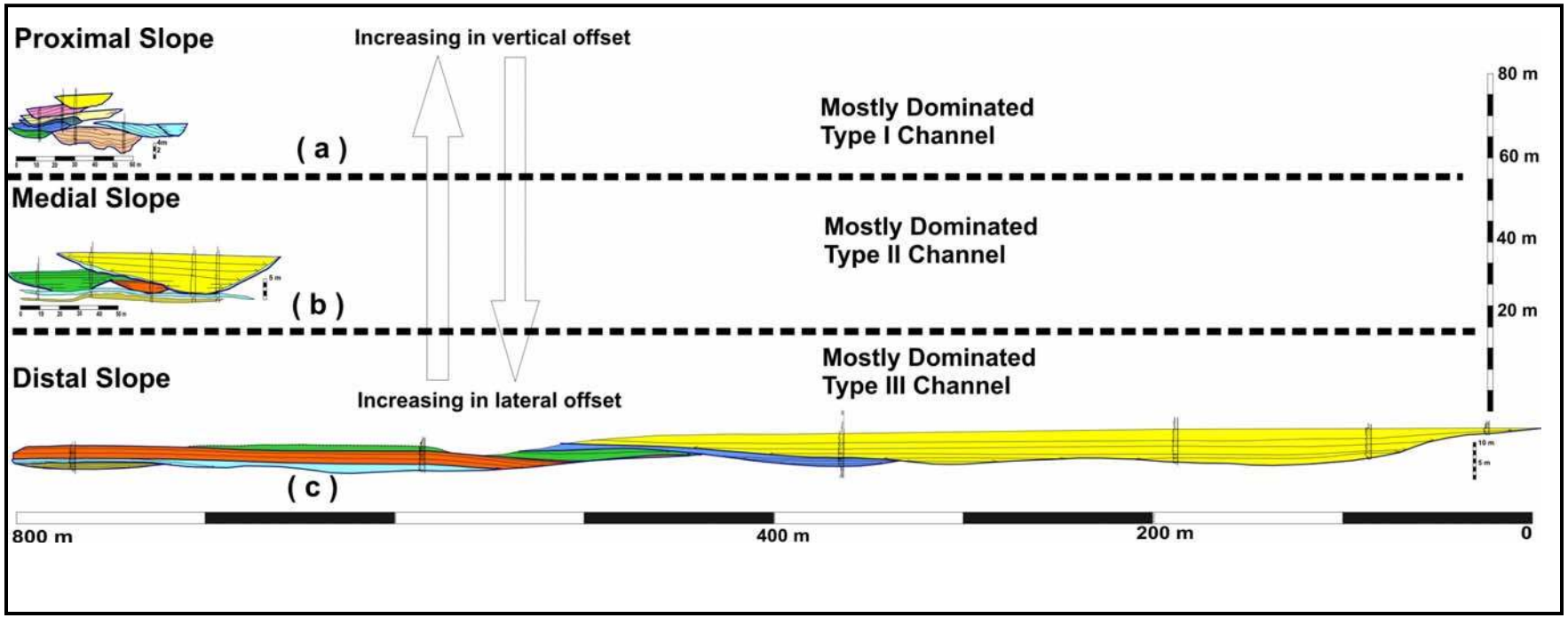


Figure 5.13 Schematic diagram of channel evolution from proximal to distal slope basin. The channel evolution is characterize by large number of evenly distributed of lateral amalgamated channel elements at the proximal (a), which become fewer in number, less laterally amalgamated and more focused at medial (b) and thicker, more focused and less amalgamated toward the distal slope (c).

110

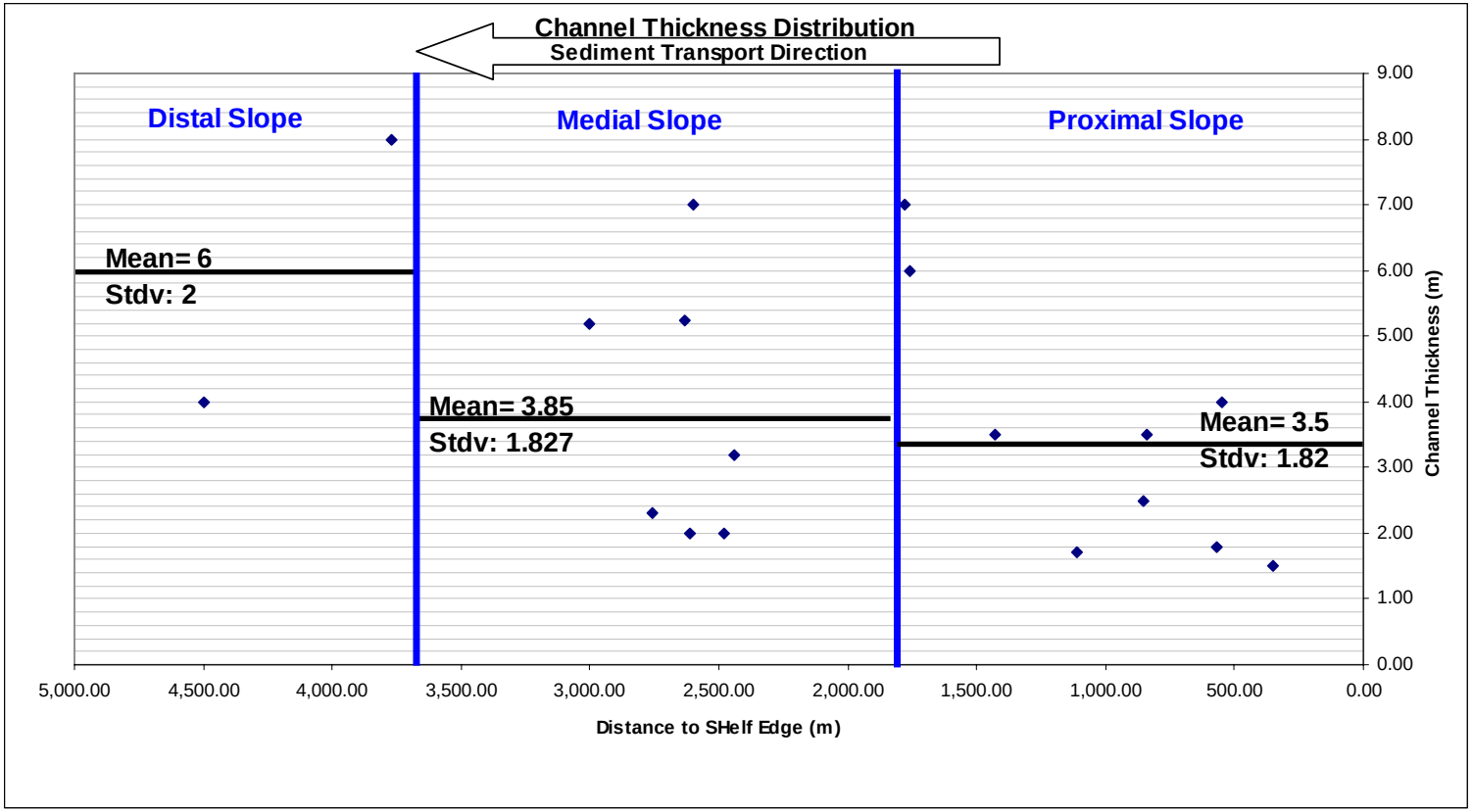


Figure 5.14 Channel thickness distribution from proximal to distal slope. The thickness is measured from preserved channels. These data covered both truncated and non-truncated channel thickness. The crossplot shows that channel mean thickness generally increases basinward, but it also increases in variance.

111

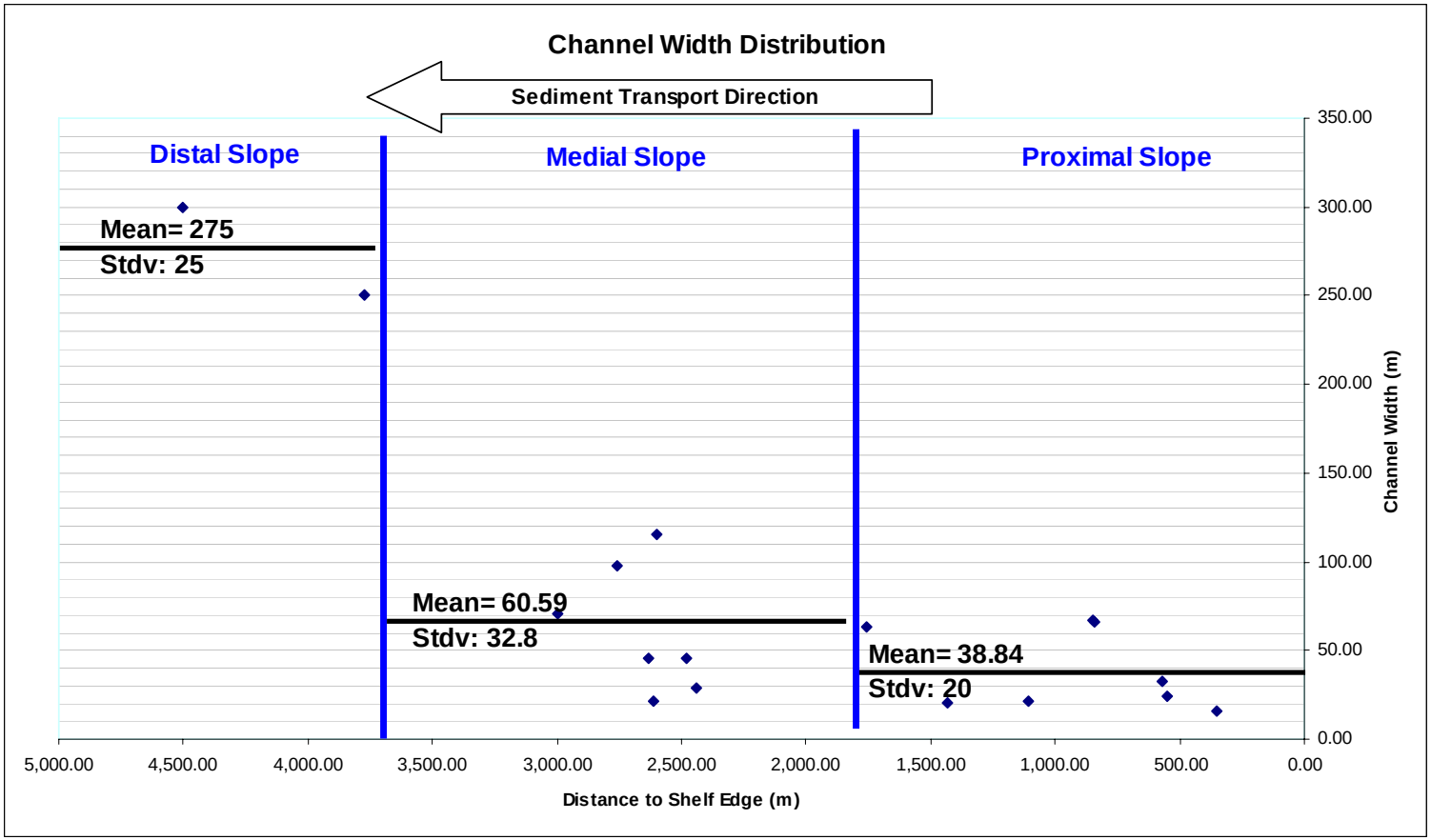


Figure 5.15 Channel width distributions from proximal to distal slope, including truncated and non truncated channels. The distal channel widths are calculated from two incomplete channel outcrops which only preserved approximately half of the channel body. The distal channel widths obtain by assuming the channel is perfectly symmetry. All these channel width data are corrected for paleocurrent orientation. The cross plot shows that mean channel width generally increases basinward.

112

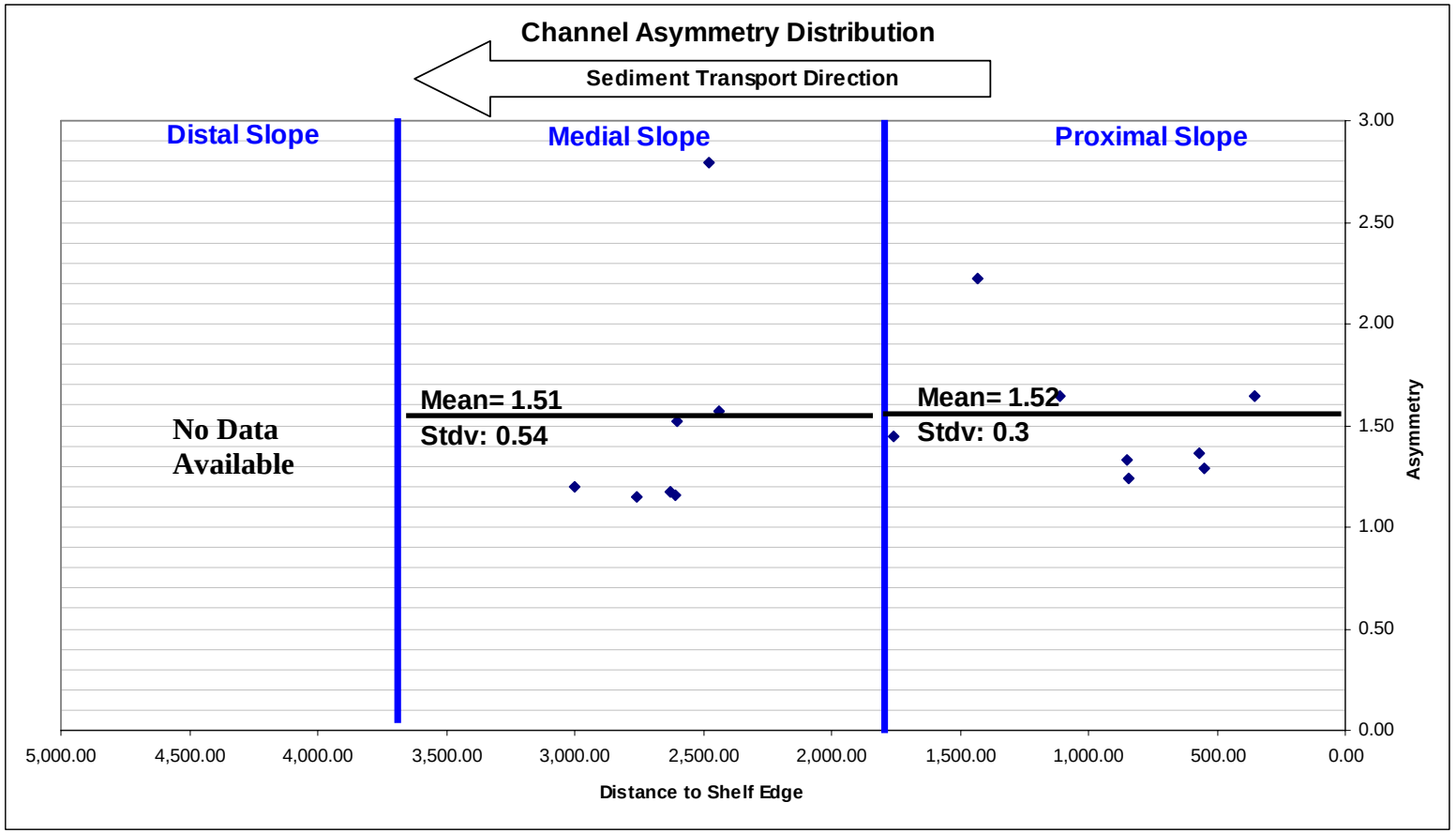


Figure 5.16 Channel asymmetry distribution from proximal to distal showing increase in variance but no significant change from the averages values.

113

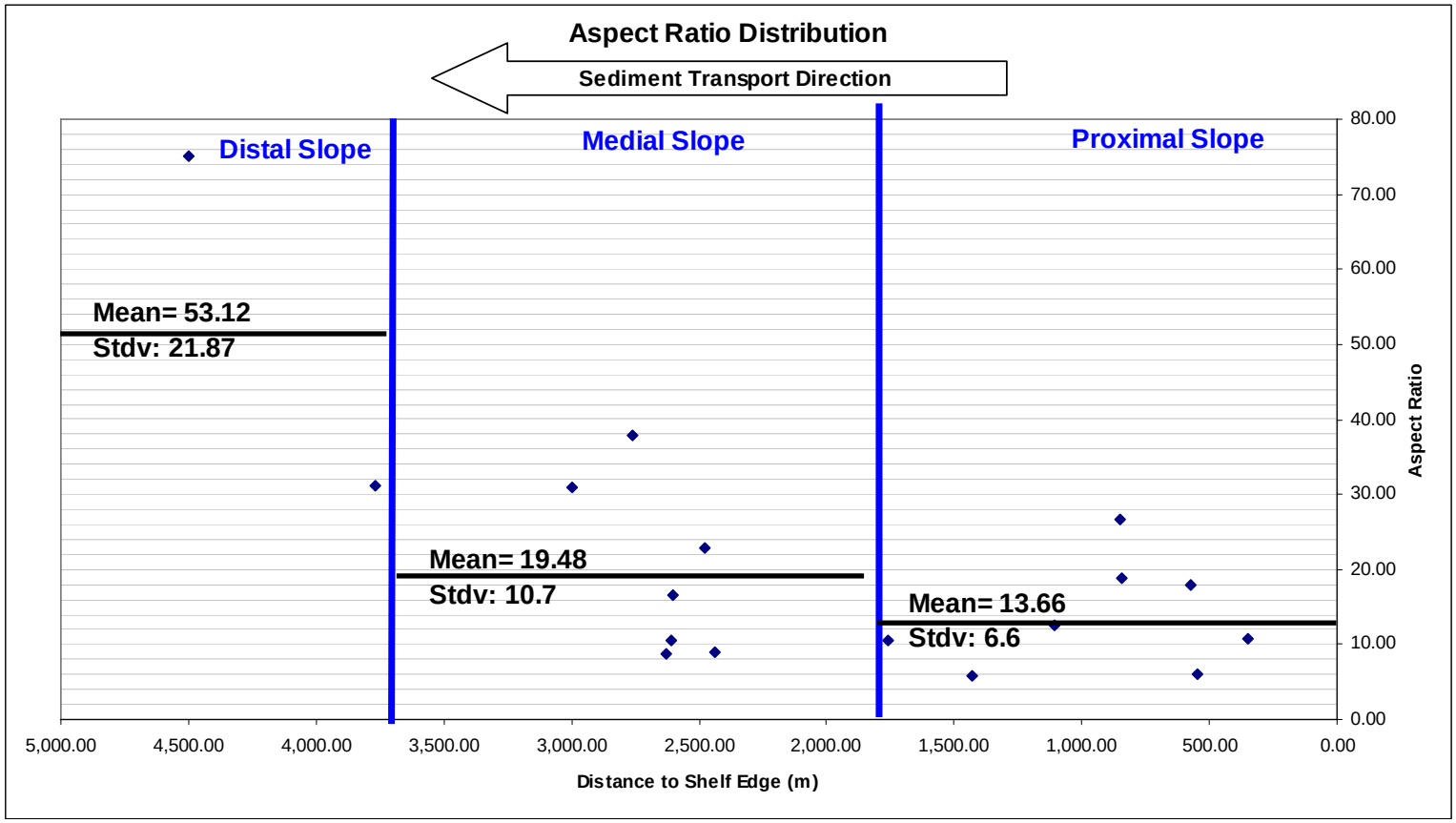


Figure 5.17 Channel mean aspect ratio distribution showing an overall increase from proximal to distal slope. The variance also increases basinward.

114

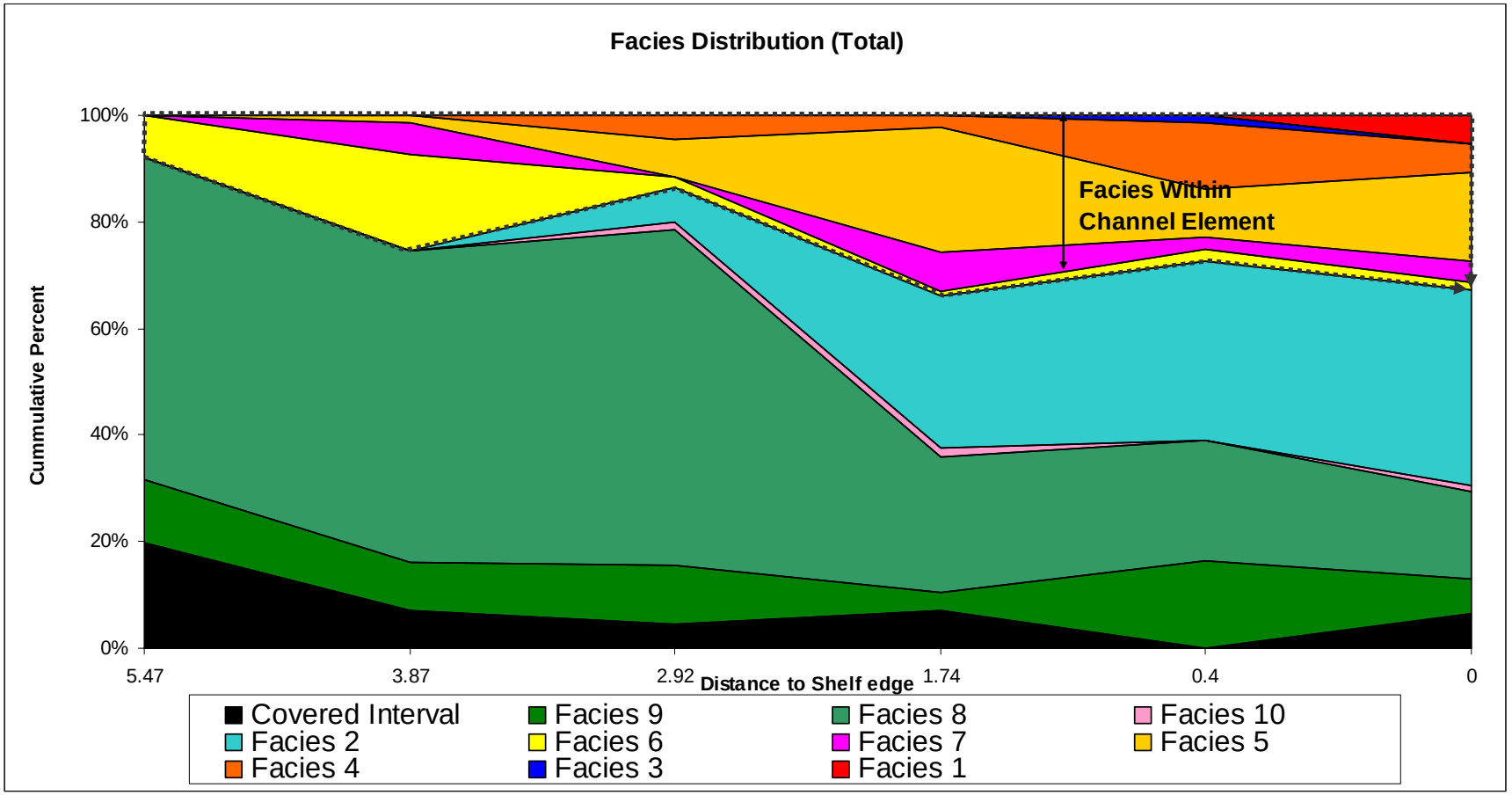


Figure 5.18 Chart showing facies distribution using six continuous measured sections of the Parasequence 2 Sobrarbe Formation. The diagram reveals that coarser facies reduces in proportion basinward.

115

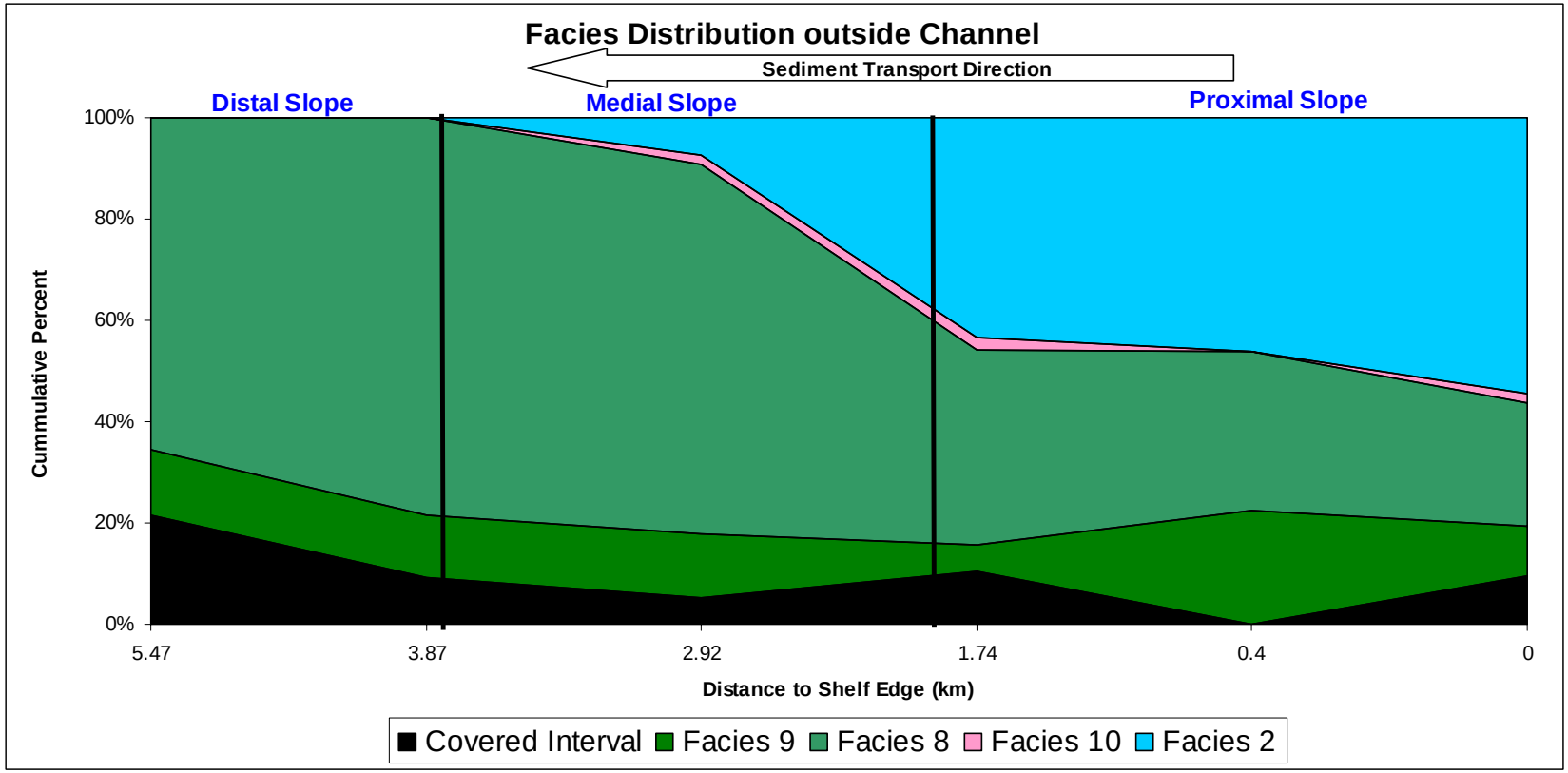


Figure 5.19 Chart showing facies distribution of sediment outside channel elements indicating a general trend of a decrease in facies diversity and grainsize basinward.

116

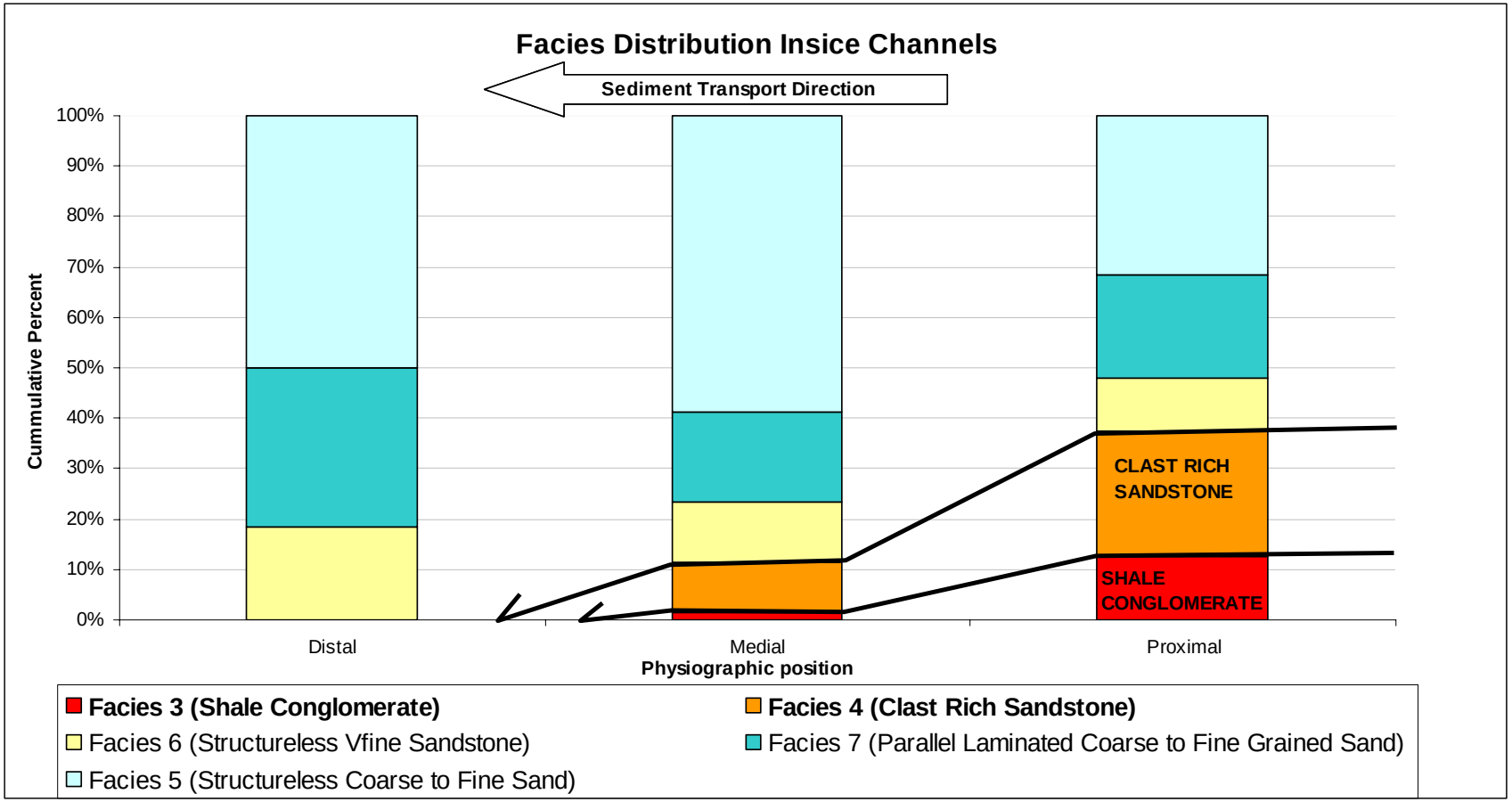


Figure 5.20 Chart showing facies distribution within channel elements. Facies proportion is calculated from measured sections through channel elements at representative positions from proximal to distal slope. The facies distribution trend shows a decrease in coarser facies basinward.

117

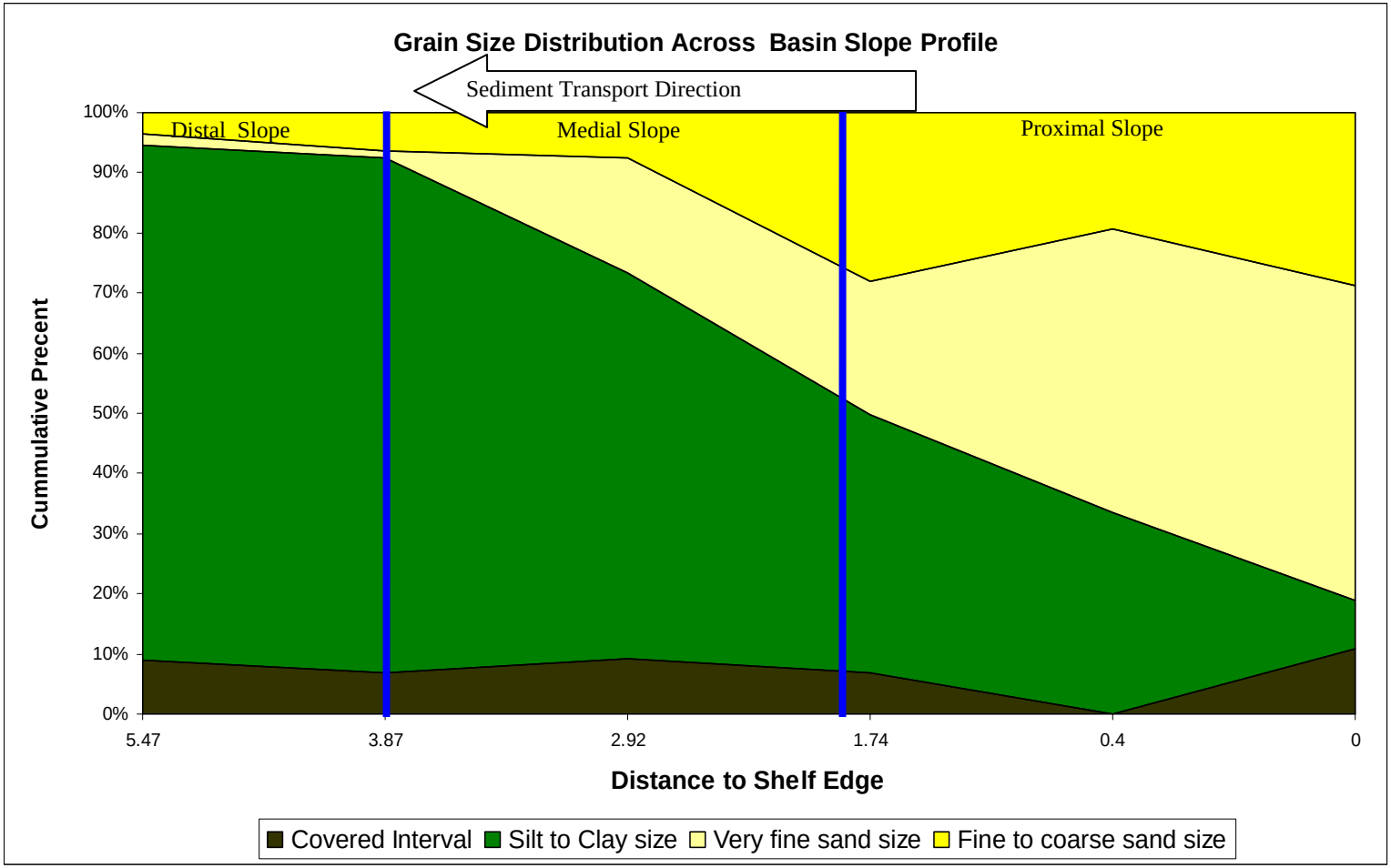


Figure 5.21 Grain size distribution chart shown basinward decrease in coarse sediment.

118

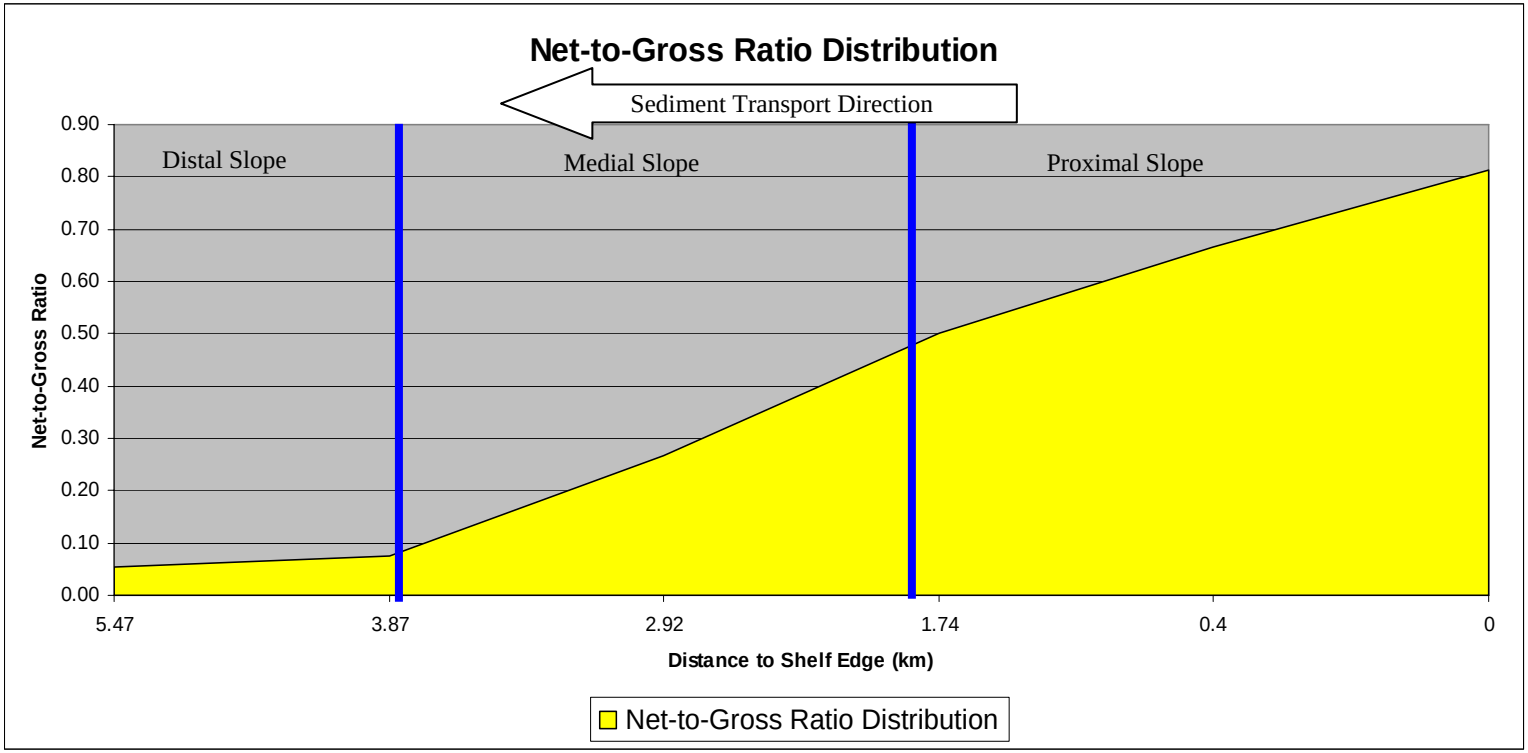


Figure 5.22 Net-to-gross ratio distribution is reduced basinward within 5 to 6 km.

119

# CHAPTER 6
# DISCUSSION

This chapter unifies information presented in the previous chapters to propose a stratigraphic model and process-related concepts.

## 6.1 Basic Summary of Observation

The data shown in Chapter 5 reveals a number of proximal to distal change in stratigraphy. These changes are summarized below in the block diagram in Figure 6.1.

1. Paleo flow diversity, which is interpreted to reflect sinuosity is low in the upper slope, high in the middle and low in the distal slope.
2. Distribution of architectural elements changes basinward. Proximal slope, strata contain mouth bar elements, channel elements and mudstone sheets. Medial slope, strata contain mouth bar elements, channel elements, overbank elements and mudstone sheet elements. Distal slope, strata contain channel elements, overbank elements and mudstone sheet elements.
3. Channel type changes across the slope. The upper slope contains mostly Type I channels. The medial slope contains mostly Type II channels. The distal slope contains mostly Type III channels.
4. Channel geometry changes basinward. Channel thickness, width, and aspect ratio increase from proximal to distal slope. Channel asymmetry is uniform over the same distance.
5. Facies diversity in the Parasequence, extra channel strata, and channel strata decrease from the proximal to distal slope.
6. Grain size distribution decrease gradually from the proximal to distal slope.
7. Net-to-gross ratio decreases from proximal to distal slope.

### 6.2 Channel Formation related to Deltaic Process

Channel elements in the proximal slope are associated with erosional surfaces between mouth bar elements (Figure 6.2). Channels therefore laterally correlate to sharp, erosional surfaces at the shelf edge within mouth bar complexes. These sharp erosional surfaces separate distinctive mouth bar elements (Figure 6.2, 6.3, 6.4, 6.5 and Figure 4.7). Immediately overlying these surfaces on the mouth bars are conglomerates (Facies 1 and 2), the coarsest facies documented in this study (Figure 6.2, 6.3, 6.4, 6.5 and 4.7). Above this thick conglomerate, the mouth bar element internally fines upward. Vertical decrease in erosion and grain size is interpreted to reflect an overall decrease in energy through time. The maximum energy is associated with erosion at the base of the element.

The unique association between mouth bar elements and deepwater channel elements are interpreted to reflect a genetic linkage between mouth bar erosion/ bypass and slope channel initiation. The relationship between proximal slope channels and mouth bars are described in a three stage model (Figure 6.4). At Time I the delta system has an established direction of progradation. Mollusks are living in a shallow water inter-distributary environment. At Time II, the distributary channel avulsed to the lower area of the delta, the inter-distributary. The avulsion is interpreted occurred during river floods that produce a dense hyperpycnal flows that locally flushed the mollusks onto the mouth bar and subsequently erodes a slope channel.

At Time III, delta mouth bar deposition resumes and progrades out the proximal slope. This three-stage processes occur multiple times during deposition of parasequence. In bigger scale, the climatic controls also contribute for river flooding cycle. Autocyclic and allocyclic (climate) process therefore govern mouth bar and slope channel formation.

### 6.3 Timing and Sediment Delivery Process of Deepwater Deposition

Timing of shelf and slope deposition is relatively coeval. In previous sub-chapters 6.2, the channel element is correlated to mouth bar elements reflecting a coeval connection of the fluvial and deepwater depositional systems. At the shelf edge, the mouth bars stack in both an aggradational and progradational pattern (Figure 6.2, 6.4, and 6.6). The same aggradational pattern occurs between parasequences within Sobrarbe Formation (Figure 6.7). Align with this observation, the Sobrarbe Formation does not

have any large erosional unconformities (sequence boundary) anywhere that temporally separates slope and basin deposition, with exception of inter mouth bar erosional surface.

Therefore, the physical correlation of deltaic deposition and slope deposition reveals that slope and shelf deposition was coeval. The inter- and intra-parasequence stacking pattern is both aggradational and progradational. This relationship suggests that deepwater strata were deposited during a rising relative sea level or still stand relative sea level (high stand).

### 6.4 Down Slope Changes in Flow Characteristics in Slope Channels

A number of observations suggest that there are down profile changes in flow characteristic in deepwater channels.

1. Grain size distribution within parasequence decreases basin ward.
2. Bedding thickness within channel elements thickens basinward.
3. Overall facies diversity within the parasequence is decrease basin wards
4. Lateral accretions packages (LAPS) within channel element decrease significantly basinward.
5. Number of intra-channel erosion or channel storey boundaries decreases basinward
6. Channel axis to margin changes also decrease basinward.

These observations are used to interpret the following change in turbidity current flow characteristics.

A. Overall the flow is decreasing in turbulent kinetic energy in basinward. This interpretation is supported by a basinward decrease of inter-channel erosional surface / LAPs. Associated with the basinward decrease in turbulence kinetic energy, is increasing deposition of sand grade sediment. This interpretation is supported by increasing bed thickness basin ward.
B. The continuous decrease in grain size, flow erosional capability, coarser facies in beds and increase in net deposition of sand grades sediment in a basinward direction, indicate that the flow is continuously depletive from proximal to distal.

C. The proximal to distal decrease in grain size of the turbidity currents is controlled by the following processes.
    - On the proximal slope, the flows contain a range of grain sizes from pebble to silt-size grains. At this position, most of coarser grain (Pebble to coarse sand size) are deposited due to a rapid reduction in flow competency and also flow capacity.
    - On the medial slope, the flow still contains the medium to silt size grains. At this position some of silt size grains are deposited from dilute tops of flows as overbank strata, enhanced by flow stripping at the bends of sinuous channels. This is the location where paleocurrent diversity (sinuosity) is greatest. The deposition of overbank silt occurs by flow stripping where the finer upper part of turbulent cloud spills at the bend. The medium grain sediment remains within the channel and is deposited in this position as result continuous energy flow depletion (decreasing in flow competency).
    - On the distal slope, the turbidity currents only have fine to very fine sand grain within the flow, and this is deposited as part of last stages of flow depletion. At this position the flows do not have sufficient turbulence kinetic energy to entrain anything large than silt.

Depletive flow is therefore interpreted to govern the partitioning of grain size across the profile. In summary the flows laterally indicate a continuous depletive from proximal to distal slope. At the same time, the general vertical fining upward successions indicate that the flow is waning through the time.

### 6.5 Controls of Channel Sinuosity

Paleocurrent diversity, which is interpreted to reflect sinuosity, is lowest at the upper slope, high in the middle slope and low in the distal slope. This section uses observations and data from Chapter 5 to interpret possible controls on this change in sinuosity.

The change in sinuosity described above and shown in Figure 5.5 and Figure 6.1 are associated with distinctive changes. First the lithology of the substrate adjacent to

channels changes from sand in the upper slope to silt and clay in the middle slope. These changes coincide with the increasing in sinuosity (Table 6.1). Cohesive substrata (silt and clay) are more difficult to erode compared to less cohesive sandier substrata (e.g. mouth bar facies). This factor prohibits the flow from forming a straight channel within the mudstone sheet element. Other explanation to channel sinuosity is that the deepwater channel sinuosity formed as controls stable channel levee formation. The stable levee is formed from cohesive sediment that deposited from the flow. This is a similar conclusion to that drawn by an analysis of an integrated Beacon channel sinuosity data set by Pyles (2008). The lithology of the substrate may therefore be a first order control on sinuosity.

Secondly, the slope angle is highest ($2\text{-}9^0$) where the channel is straight, low ($0.5\text{-}1^0$) at area where channel sinuous and moderate ($1 – 2.5^0$) when the channels are straight again. These results exactly match with those describe by Clark *et al.*, (1992) and Babonneau, *et al.*, (2002), where one slope angle was interpreted as the first order control of sinuosity (Figure 6.9). Thirdly a deep structure underlies the parasequence exactly where the increase in sinuosity occurs. This structure may have caused the channel to become more sinuous at this position. However, this does not explain why they straighten out in the distal slope. In summary sinuosity may be governed by lithology of the substrate and angle of slope.

## 6.6 Comparison of Parasequence 2 of the Sobrarbe Formation to Other Deepwater System

The study in Parasequence 2 slope system reveals an important characteristic of hyperpycnal dominated deepwater slope deposits. This study records prograding linked shelf to basin system with relative short slope (5-7 km long). Deepwater channels are interpreted to be formed and filled by hyperpycnal process (Figure 6.7).

In contrast to this study, the Brushy Canyon Formation shows a detached system whereby the deepwater channel elements does not physically correlate to coeval delta. This system is covers very large area (40-60 km long). The deepwater channel system and fan system are large compared to the Parasequence 2. The Brushy Canyon shows a gradual increase in grain size and net-to-gross ratio from proximal to distal slope

(Gardner and Borer, 2000 and Carr and Gardner, 2000). This is opposite to the Sobrarbe Formation system.

Other slope prograding system, such as Lewis Shale of Wyoming and Clinoform Spitsbergen, are also different to the stratigraphy model of this study. First, the Lewis Shale of Wyoming system is dominated by collapse triggered turbidity currents (Pyles and Slatt, 2006). Also the slope of this study is 40 km from shelf to basin floor setting. Pyles and Slatt show that this system increase in net-to-gross ratio from proximal to distal slope. Second, the clinoform Spitsbergen is divided into two type deepwater system. The first system is formed by a relative sea level drop where as the deepwater channel and fan developed during early low stand. It is spread out along 15 km from proximal to distal slope (Plink-Bjoklund *et al.*,2001 and Plink-Bjoklund and Steel, 2005). The second is formed during highstand system where the deepwater channel linked to shelfedge delta. This system only spread out 6 km long from delta to distal slope that almost similar to this study Plink-Bjoklund *et al.*,2001 and Plink-Bjoklund and Steel, 2005).

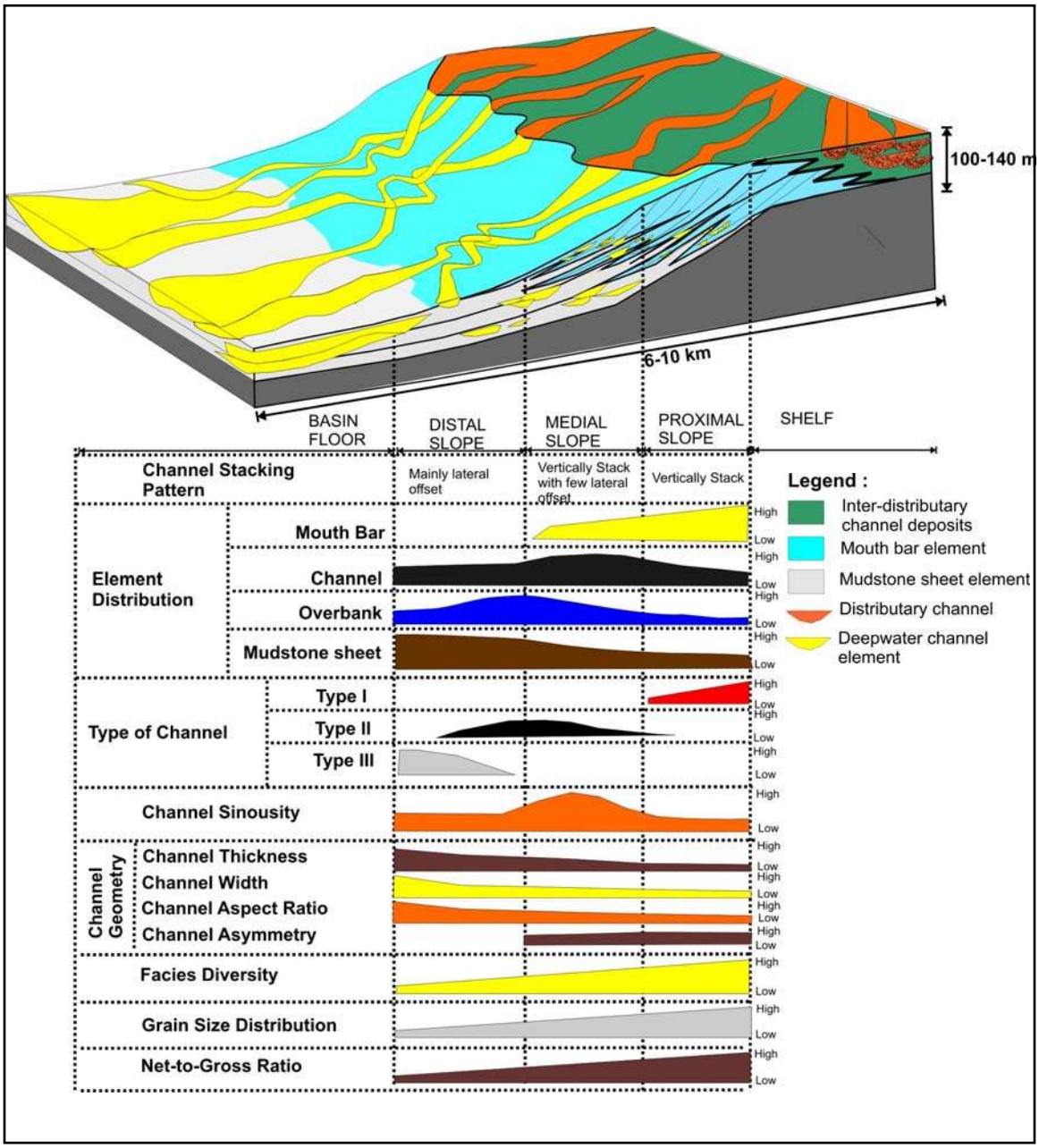


Figure 6.1 Block diagram of proximal to distal changes in stratigraphy in Parasequence 2 of the Sobrarbe Formation.

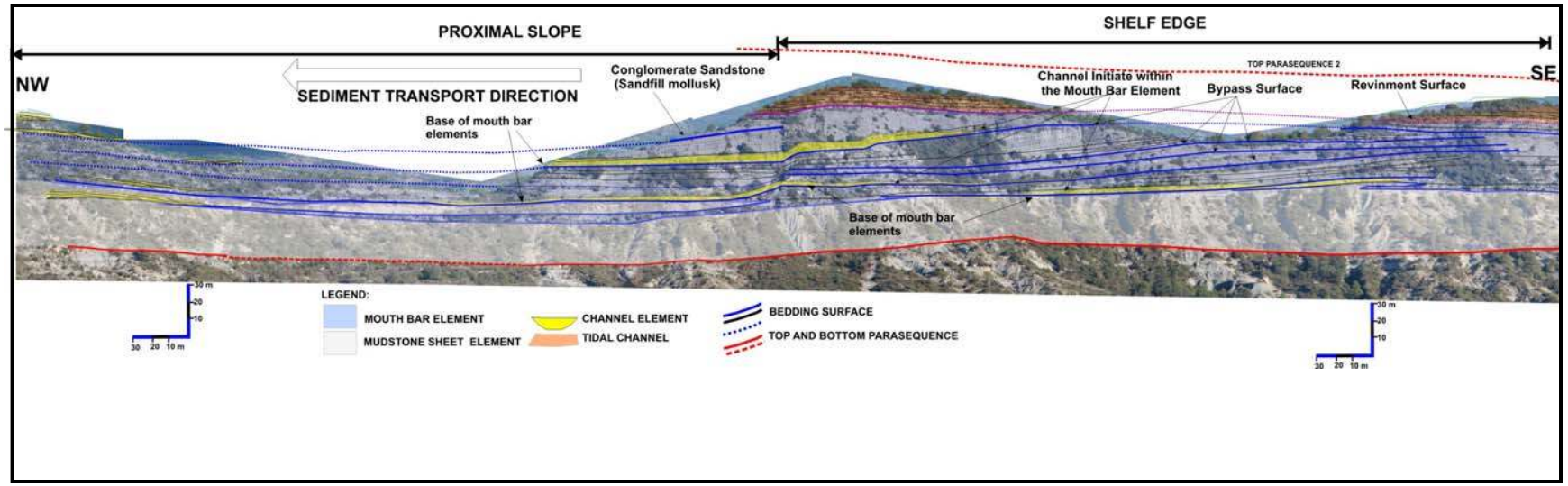


Figure 6.2 Photopanel interpretations showing the physical correlation between channel elements and mouth bar elements.

127

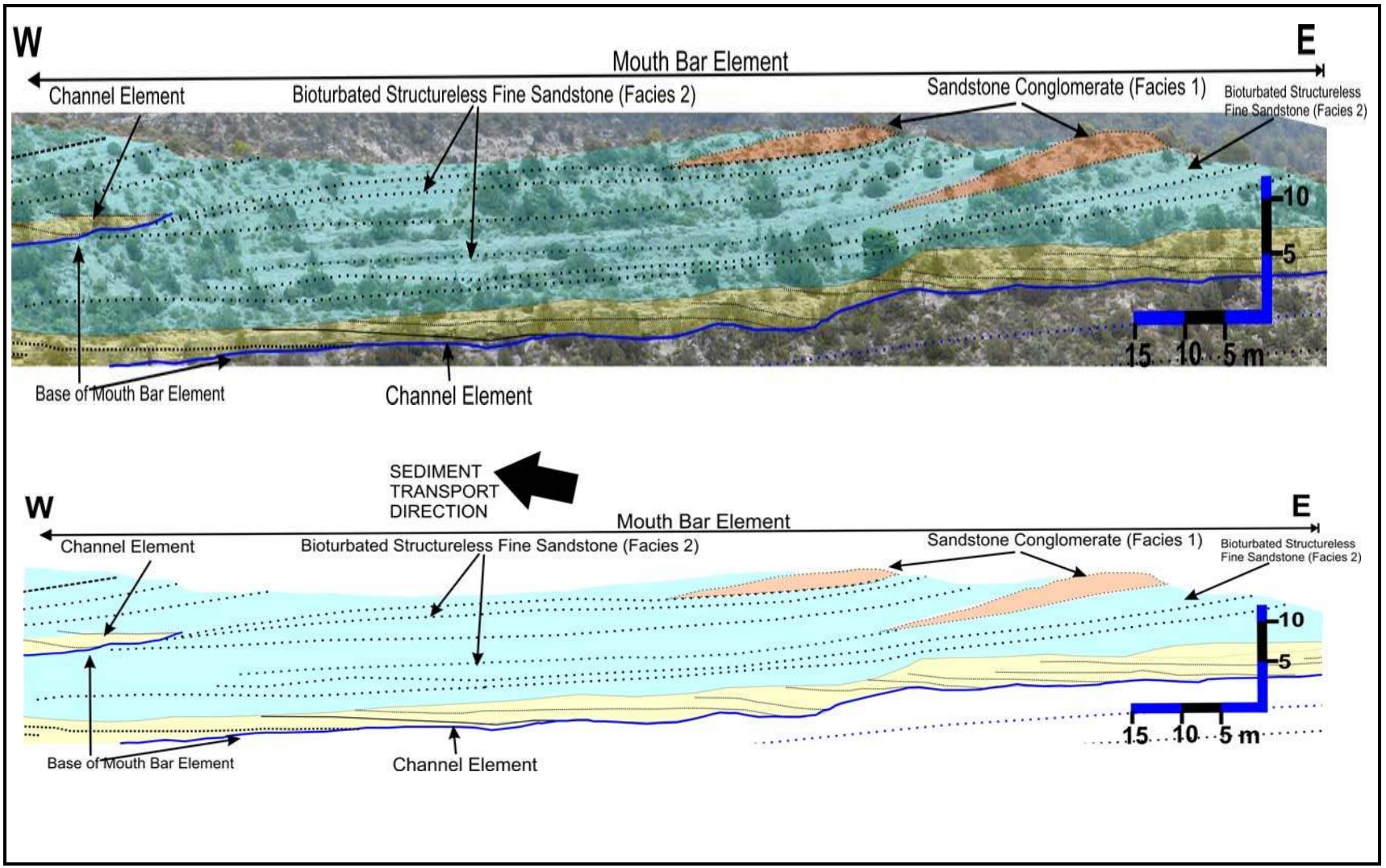


Figure 6.3 Photopanel interpretations showing how channels correlate to bypass surface.

128

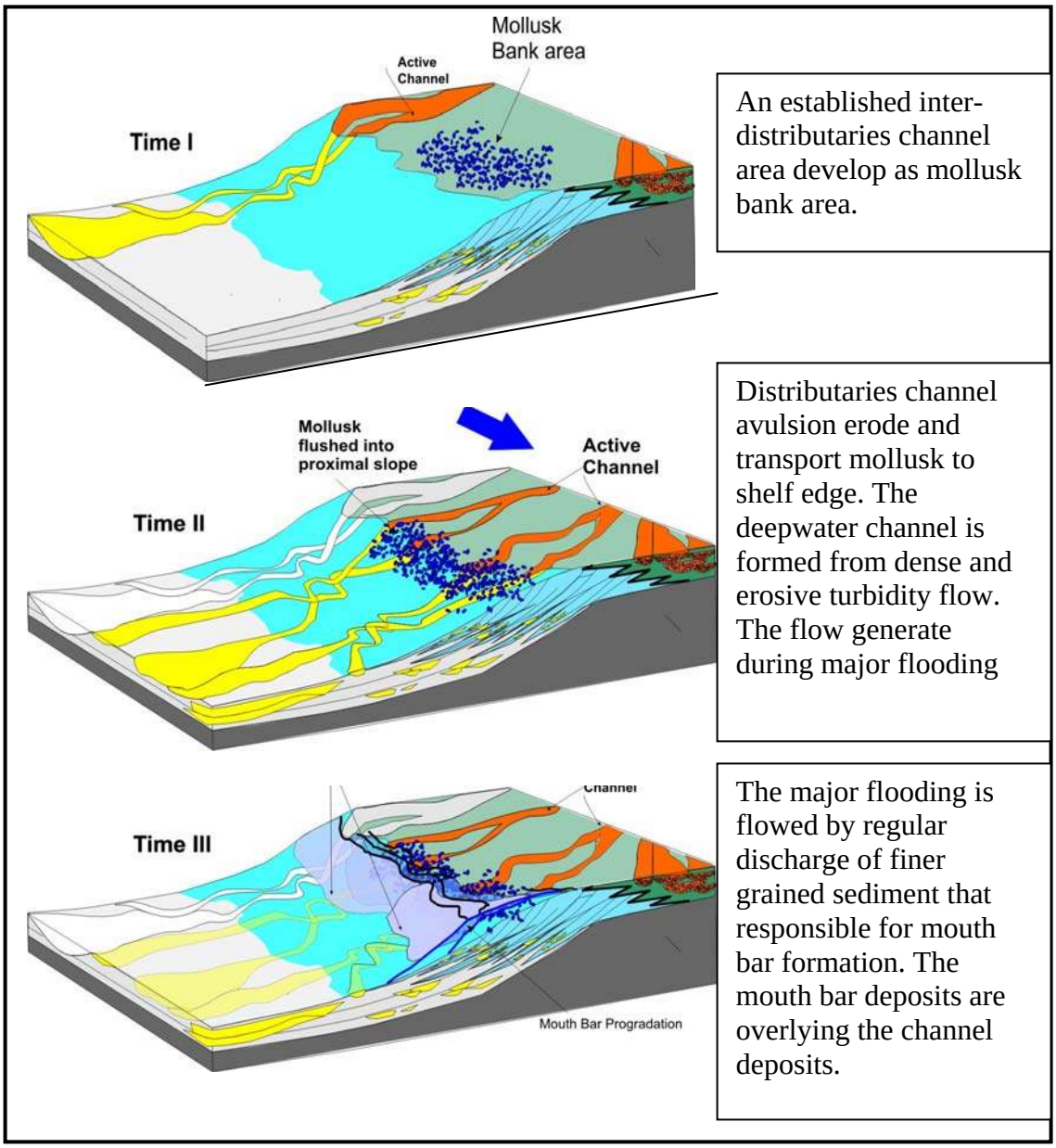


Figure 6.4 Block diagram illustrating a 3-stages model by which deltaic processes are related to slope channels. Time I illustrates an established inter-distributaries area develops as mollusk bank area. Time II, the distributary channel avulses and erodes and flushes mollusk banks on the upper slope. This new system also create deepwater channel that produced by erosion from dense turbidity currents flow during major flooding. At time III , mouth bars are deposited above deepwater channels.

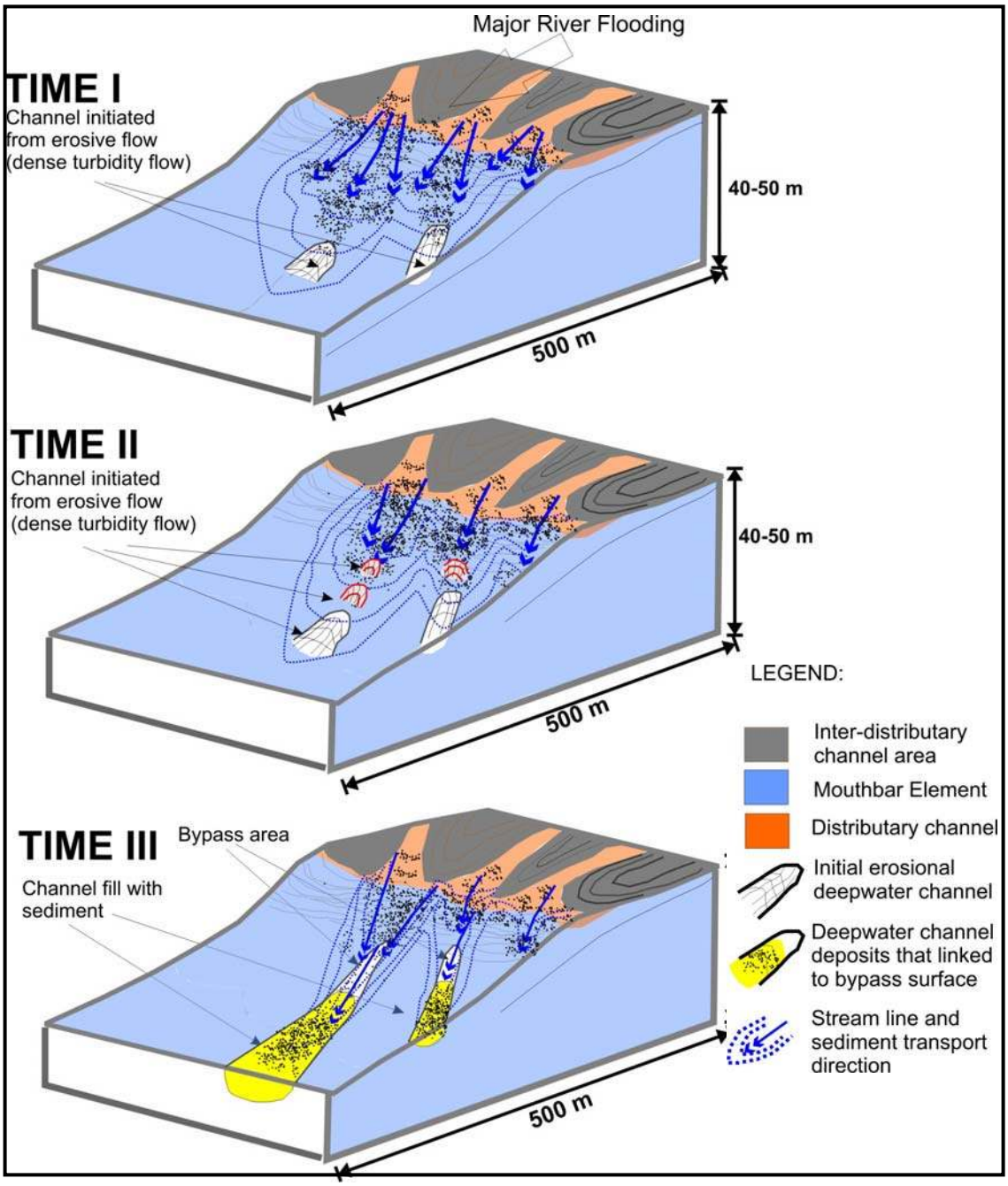


Figure 6.5 Block diagram illustrated the 3-stages model for deepwater channel initiation at the proximal slope.

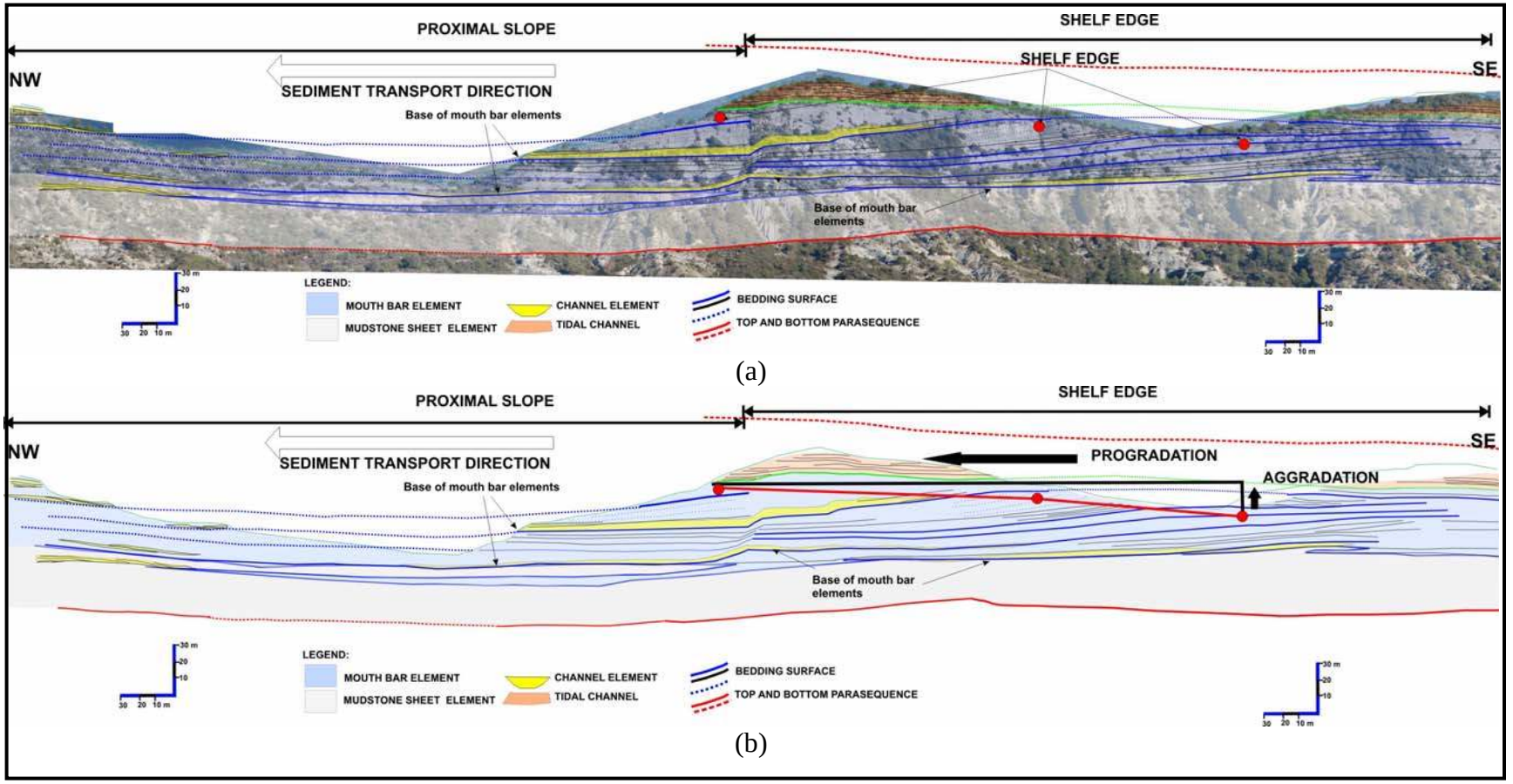


Figure 6.6 Photopanel interpretations of Parasequence 2 on the shelf edge area showing a progradation and aggradations of mouth bar elements.

131

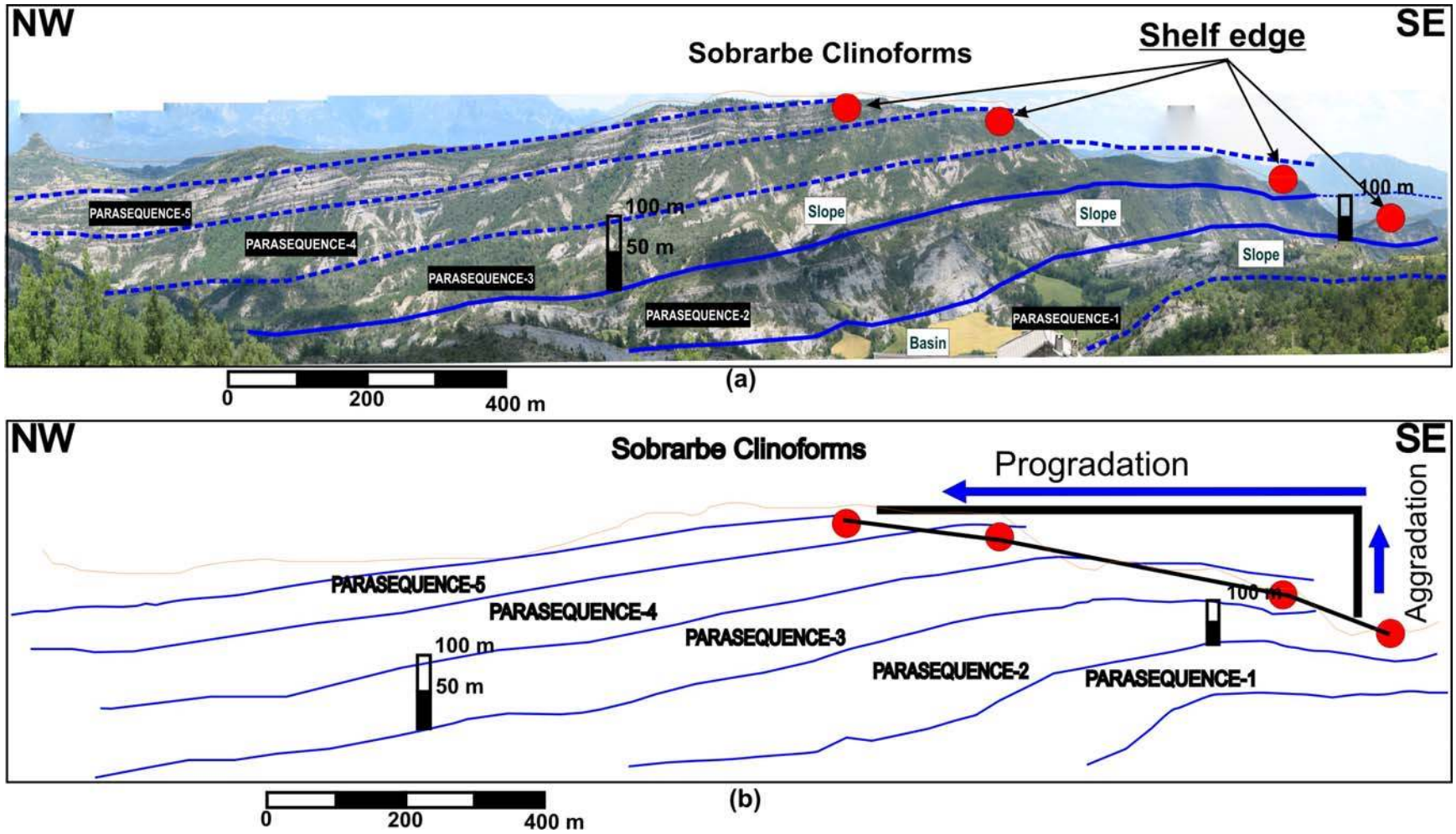


Figure 6.7 Photopanel interpretations of the Sobrarbe Formation that reveal the aggradational and progradational stacking pattern of parasequences in the Sobrarbe Formation.

132

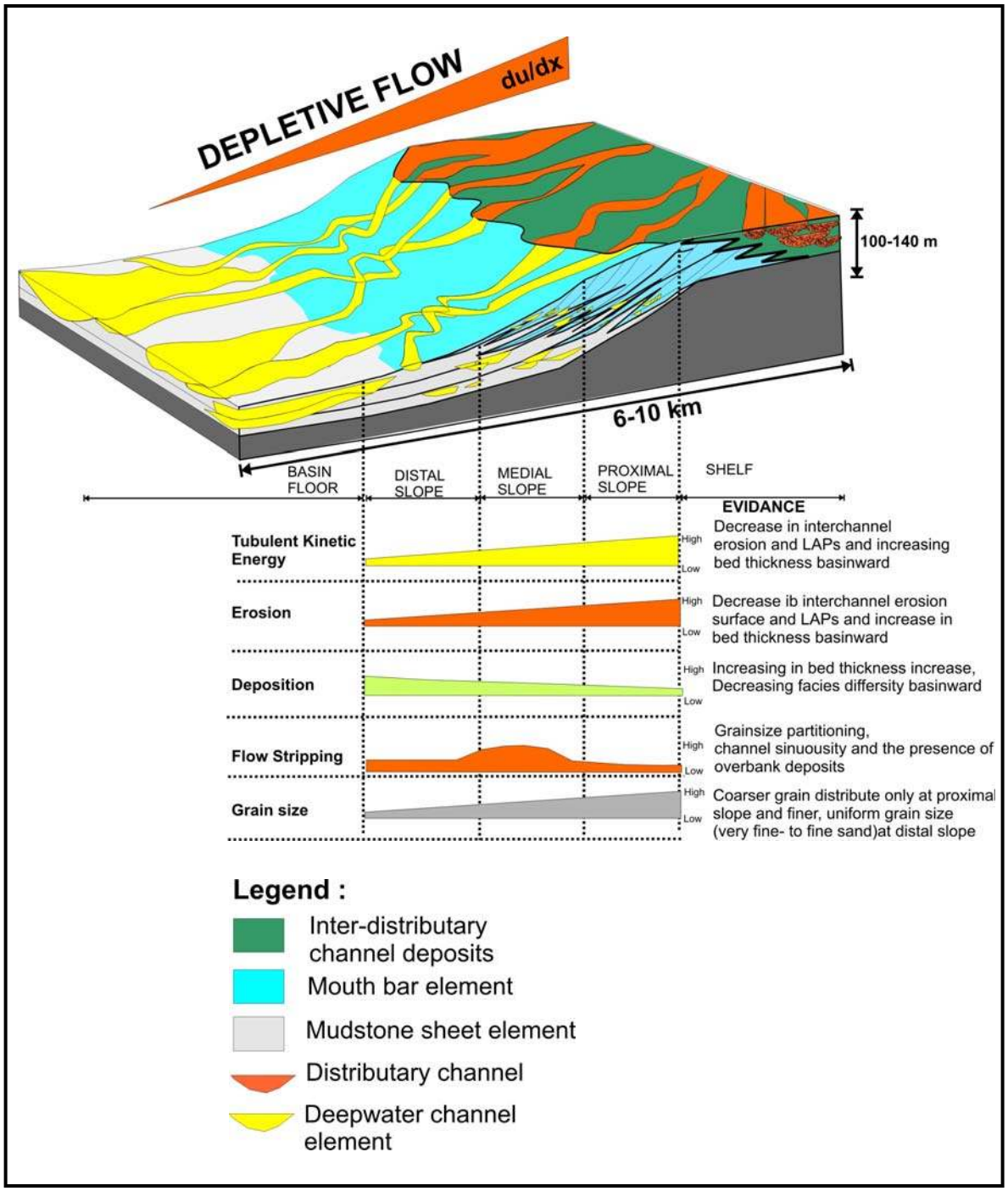


Figure 6.8 Schematic diagram showing changes in flow characteristics.

Table 6.1 Table relating sinuosity to lithology of substrate and slope angle

| **Position in slope physiographic** | **Sinuosity** | **Lithology of Substrate** | **Approximate of Slope Angle (degree)** | **Structure** |
|---|---|---|---|---|
| **Proximal** | Low | Sand | 2 to 9 | No structure |
| **Medial** | High | Sand and Silt | 0.5 to 1 | Possible deep structure |
| **Distal** | Low | Silt | 1 to 2.5 | Possible deep structure |

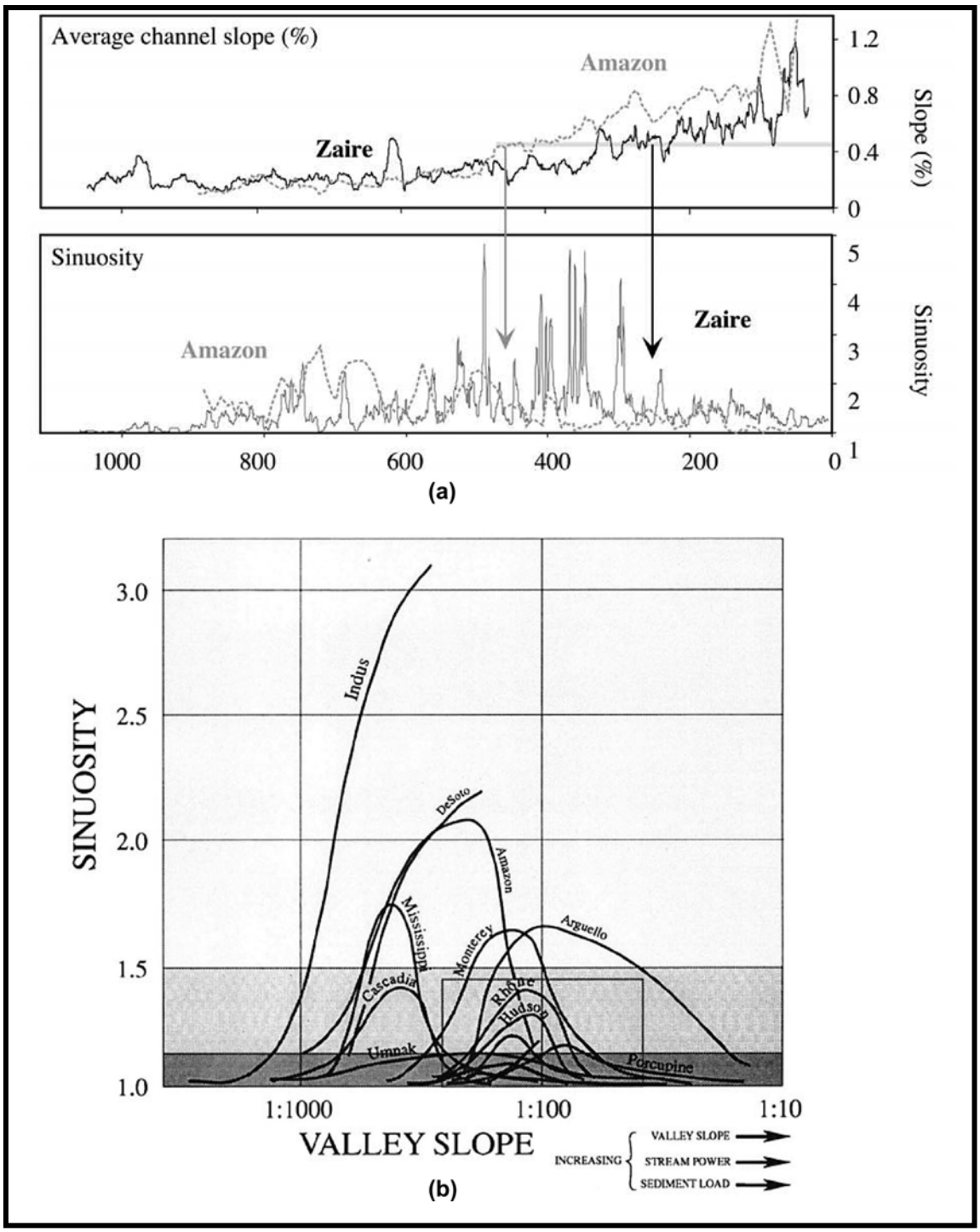


Figure 6.9 Crossplot showing the relationship between slope angle and sinuosity. This data are from Babonneau, *et al.*, (2002) (a) and Clark *et al.*, (1992) (b).

# CHAPTER 7
# THESIS CONCLUSION AND APPLICATION

This chapter presents the conclusions of this research and their applications in petroleum exploration purposes.

## 7.1 Application of Parasequence 2 Sobrarbe Formation Stratigraphy Model to Petroleum Exploration

The continuous stratigraphic record of Parasequence 2 of the Sobrarbe Formation provides information about the reservoir-scale stratigraphic architecture from the proximal to distal slope. This study reveals detailed vertical and lateral changes in architecture elements, facies, grain size and net-to-gross ratio of the entire parasequence, as summarized in Figure 5.9 and 6.1. Some possible application and related limitation are explained in following paragraphs.

A new deepwater stratigraphic model of prograding system is introduced based on this field study. This model is applicable as prediction tool for reservoir scale analog to subsurface study of slope prograding system. Subsurface studies such as Western Siberia Basin, Northwest Slope of Australia, North Slope of Alaska, and Sakhalin Island of Russia are relevant in application of this model. The model created form the Sobrarbe Formation contributes to reduce uncertainty of reservoir prediction in the slope setting of prograding system. An example where this stratigraphic model and data can be used is shown from the Western Siberian Basin (Figure 7.1). The stratigraphy of this basin was constructed from log correlation. There is no detailed control over how the stratigraphy changes from proximal to distal slope basin. Based on the constructed model of the Sobrarbe Formation, the unpredicted area could be resolved by applying an analog model between those areas.

Although this stratigraphy information provide a good data analog, the limitation of this model need to be considered. First, the model is only applicable for slope prograding systems during high stand  Second, the model is only applied to prograding systemsthat are related to hyperpycnal flow (non collapse triggered turbidity current or non slope failure dominated).

## 7.2 Conclusion

This study documents continuous reservoir-scale changes in stratigraphic architecture from the proximal to distal slope. Prior to this study, only two outcrop studies recording large and small scale deepwater stratigraphic architecture within prograding systems existed (Pyles and Slatt, 2007, and Plink-Bjorklund *et al*., 2005). The result of this study significantly contributes data relating to proximal to distal slope changes than these earlier studies. The new finding and key concepts introduced in this study are summarized below.

1. The Parasequence 2 Sobrarbe Formation is composed of four types of architecture elements: mouth bar elements, channel elements, overbank deposits and mudstone elements.
2. The distribution of architectural elements changes basinward. Proximal slope strata contain mouth bar elements, channel elements and mudstone sheets. Medial slope, strata contain mouth bar elements, channel elements, overbank elements and mudstone sheet elements. Distal slope, strata contain channel elements, overbank elements and mudstone sheet elements.
3. Paleo flow diversity which is interpreted to reflect sinuosity is low in the upper slope, high in the middle and low in the distal slope.
4. There are three channel type founded in the parasequence. Type I channel is characterize by multi-storey channel, significantly amalgamated (mainly preserved channel margin), vertically stacking and compose of moderate to thick bedded of pebble to coarse sandstone deposits with fining upward grain size vertical profile. Type II channel is characterize by a single storey channel, amalgamated (preserved the most channel axis and margin), vertically stacking with few lateral offset and composed of thickly amalgamated beds of medium to fine grained sandstone with mostly uniform grain size vertical profile. Type III channel is characterize by a single storey channel, amalgamated (preserved the most channel axis and margin), mostly lateral offset and composed of thickly beds of medium fine- to very fine grained sandstone with mostly uniform grain size vertical profile.

5. Channel type changes across the slope. The upper slope contains mostly Type I channels. The medial slope contains mostly Type II channels. The distal slope contains mostly Type III channels.
6. Channel geometry changes basinward. Channel thickness, width, and aspect ratio increase from the proximal to distal slope. Channel asymmetry is uniform over the same distance.
7. Facies diversity in the Parasequence, extra channel strata, and channel strata decrease from the proximal to distal slope.
8. Grain size distribution decreases gradually from the proximal to distal slope.
9. Net-to-gross ratio decreases from proximal to distal slope.
10. Slope channel initiation is related to processes active on the delta (avulsion/hyperpycnal flow).
11. The slope and shelf/deltaic deposition system are coeval.
12. Sinuosity of slope channels is controlled by lithology of the substrate and slope gradient.
13. The Parasequence 2 of the Sobrarbe Formation is an excellent reservoir analog for prograding systems such as West Siberian Basin.

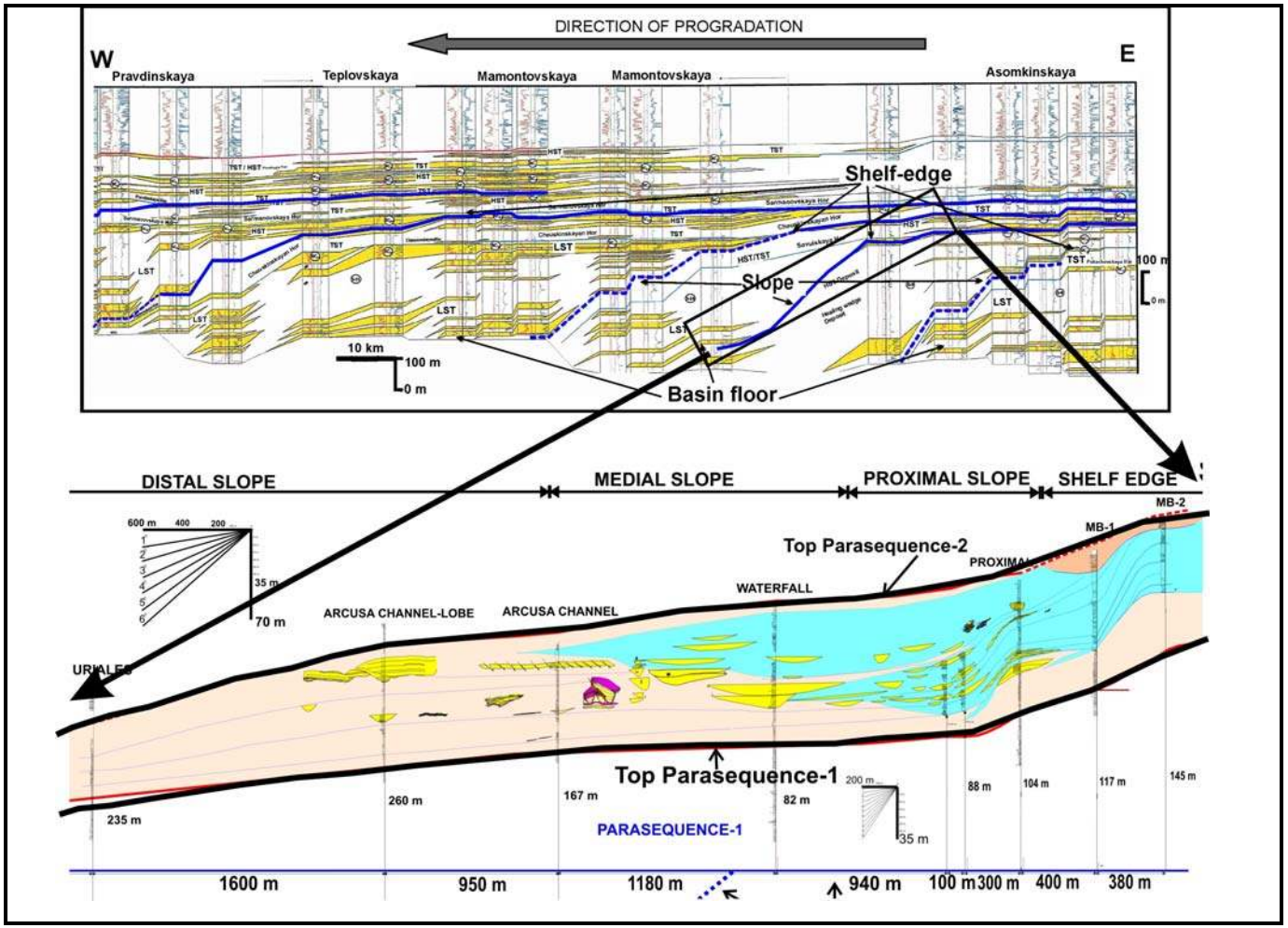


Figure 7.1 Schematic diagram shows a comparison between the Sobrarbe Formation Parasequence 2 and the Western Siberian Basin. This comparison shows how the depositional trends in stratigraphy derived from this outcrops study could be used to predict facies trends in this subsurface reservoir.

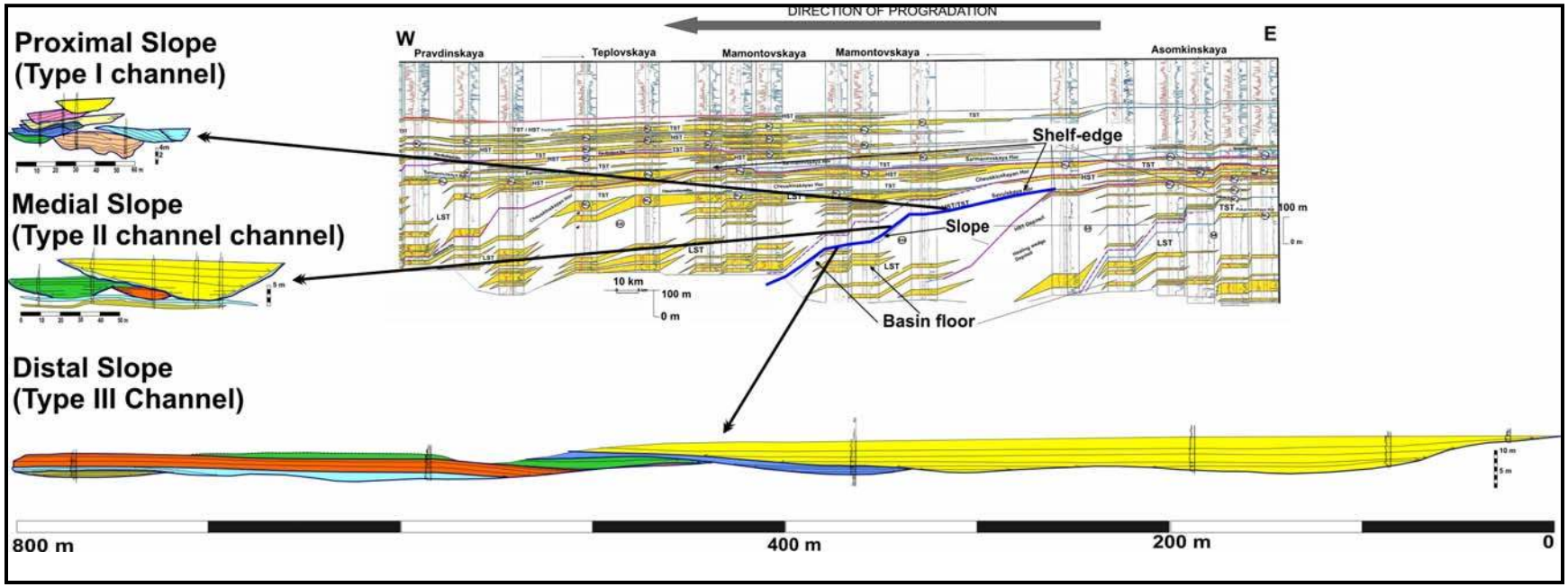


Figure 7.2 Schematic diagram of channel element changes, including vertical log prediction, applied to predict the channel geometry and from vertical log profile at various locations along the physiographic slope.

# REFERENCE CITED

Abreu V., M. Sullivan, C. Pirmez, and D. Mohrig., 2002, Lateral accretion package (LAPs): an important reservoir element in deep water sinous channel: Marine and Petroleum Geology, v. 20, p. 631-648.

Babonneau, N., B. Savoye, M. Cremer, and B. Klein, 2002, Morphology and architecture of the present canyon and channel system of the Zaire deep-sea fan : Marine and Petroleum Geology, v. 19, p. 445-467.

Berggren, W.A., D.V. Kent, M. Aubry, and J. Hardenbol, 1995, Geochronology, time scale and global stratigraphic correlation: Special Publication-Society for Sedimentay Geology, v.54

Bhattacharya, J.P., 2006, Facies Model Revisited: Deltas : SEPM Special Publication v. 84, p. 237-293.

Boggs, S.Jr., 1995, Principle of Sedimentary and Stratigraphy 2nd Edition, Prentice Hall, Englewood New Jersey.

Bouma A.H, 1962, Sedimentology of Sum flysch Deposits: Aggresive Approach to Facies Iterpretation, Elsevial Amasterdam, p 168.

Brown, L. F., J. M. Benson, G. J. Brink, S. Doherty, A. Jollands, E. H. A. Jungslager, J. H. G. Keenan, A. Muntingh, and N. J. S. Van Wyk, 1995, Sequence stratigraphy in offshore African Divergent Margin, Pletmos Basin: AAPG Special Study Geology, v. 41, p. 19-82.

Carr, M., and M.H. Gardner, 2000, Potrait of a basin-floor fan for sandy deepwater systems, Permian lower Brushy Canyon Formation, west texas, in A.H. Bouma and C.G. Stone, eds., Fine-grained turbidites systems: AAPG Memoir 72/SEPM Special Publication 68, p.215-232.

Choukroune, P., 1992, Tectonic evolution of the Pyrenees: Annual Revues of Earth and Planetary Science, v.20, p. 134-158.

Clark, J. D., N.H. Kenyon, and K. T. Pickering, 1992, Quantitative analysis of submarine channels: Implications for the classification of submarine fans: Geology, v. 20, p. 633-636.

Clark, J. D. and K. T. Pickering, 1996, Architectural elements and growth patterns of submarine channels: application to hydrocarbon exploration: AAPG Bulletin, v. 80, p. 194-221.

Clark, J. D. and Pickering, K. T., 1996, Submarine channels process and architecture: Vallis Press, London, p.13-15.

Donovan, A. D., 2003, Clinoform control on submarine fan development within depositional sequence: Geological Society of America, v.35(6), p. 625

Dreyer, T., J. Corregidor, P. Arbues, and C. Puigdefabregas, 1999, Architecture of tectonically influenced Sobrabre deltaic complex in the Ainsa Basin, northern Spain: Sedimentary Geology, v. 127, p. 127-169.

Erskine, R.D. and P.R. Vail, 1988, Seismic stratigraphy of the Exmouth Plateau (*in* Atrlas of seismic stratigraphy, Bally): AAPG Studies in Geology 27, v. 2, p. 163-173.

Fischer, M., 1984a, Thrust tectonic in the northern Pyrenees: Journal of Structural Geology, v. 6, p. 721-726.

Farrel, S. G., G.D. Williams, and C.D. Atkinson, 1987, Constrains on the age of movement of the Montesech and Cotiella Thrusts, south central Pyrenees, Spain: Jounal of Geological Society, London, v. 144, p. 907-914.

Fernandez, O., Munoz, J.A., Arbues, P., Falivene, O., and Marzo, M., 2004, Three-Dimensional Reconstruction of Geological Surfaces: An Example of Growth Strata and Turbidite systems from the Ainsa Basin (Pyrenees, Spain): AAPG Bulletin, Vol. 88, No. 8, p. 1049-1068.

Fildani, A., W. R. Normark, S. Kostic, and G. Parker, 2006, Channel formation by flow stripping: large-scale scour features along the Monterey Easet Channel and their relation to sediment waves: Journal Compilation International Association of Sedimentologists. p.1-23.

Friedman, G.M., J.E. Sanders, and D. C. Kopaska-Merkel, 1992, Principle of sedimentary deposits: stratigraphy and sedimentology: New York

Gardner, M. H. and J. M. Borer, 2000, Submarine channel architecture along a slope to basin profile, Brushy Canyon Formation, West Texas *in* A.H. Bouma and C.G. Stone, eds., Fine-grained turbidite systems: SEPM Special Publication 68, p. 195-214.

Gardner, M. H., J. M. Borer, J. J. Mellick, N. Mavilla, M. Dechesne, and R. N. Wagerle, 2003, Stratigraphic process-response model for submarine channels and related features from studies of Permian Brushy Canyon outcrops, West Texas: Marine and Petroleum Geology, v. 20, p. 757-787.

Gradstein, F.M., and OGG, J.G., 2004, Geological time scale: Lethaia, v. 37, p. 127-222.

Gressly, A., 1938, Observation Geologiques sur le Jura Sloleurois: Nouveaux memoires de la Societe Helveteque des Sciences Naturelles. Neuchatel, v.2, p. 349.

Kneller, B., 1995, Beyond the turbidite paradigm: physical models for deposition of turbidites and their implication for reservoir prediction: Geological Society Special Publication, no. 94, p. 31-49.

Kneller, B.C., and Buckee, C., 2000, The Structure and Fluid Mechanics of Turbidity Currents: A Review of Some Recent Studies and Their Geological Implications: Sedimentology, no 47, p. 62-94.

Kneller, B., and W. D. McCafferey, 2003, The interpretation vertical sequence in turbidite beds: the influence of longitudinal flow structure: SEPM Journal Sedimentary Research, v. 73, no. 5, p. 706-713.

Khan, S.M., J. Imran., S.Bradford, and J.P.M. Syvitski, 2005, Numerical modeling of hyperpycnal plume (*in* Mediterranean prodelta system): Merine Geology, v. 223,p. 193-211

Labourdette, R., P. Cremeyrolle, and E. Remacha, 2008, Characterization of dynamic flow patterns in turbidite reservoirs using 3D outcrops analogues: Example of the Eocene Morillo turbidite system (south-central Pyrenees, Spain) : Marine and Petroleum Geology v. 25, p. 255-270.

Le Pichon, X., J. Bonnin, and I.C. Sibuet, 1970, La faille transformante liee a l'ouverture du Golfe de Gascogne: Comptes Rendus Academie de Science de Paris, v.1941-4.

Lowe, D.R., 1976, Subaqueous liquefied and fluidized sediment flows and their deposits: Sedimentology, v. 23, p. 285-308.

Lowe, D.R., 1982, Sediment Gravity Flows II: Depositional Models with Special Reference to the Deposits of High-Density Turbidity Currents, Journal of Sedimentary Petrology, V. 52, No.1, p. 279-297.

Mayall, M., E. Jones, and M. Casey, 2005, Turbidite channel reservoir-key element in facies prediction and effective development: Marine and Petroleum Geology, v. 23, p. 821-841.

Mial, A.D., 1985, Architec tural-element analysis: a new method of facies analysis applied to fluvial deposits: Earth-Science Review, v 22, p. 261-308

Middleton, G.V., and M.A. Hampton, 1973, Sediment gravity flows: mechanisms of flow and deposition, in Turbidites and deepwater sedimentation: Pacific Section SEPM, short course notes, p. 1-38.

Mohrig D., K. X. Whipple, M. Hondzo, C. Ellis, and G. Parker, 1998, Hydroplaning of subaqueous debris flows, GSA Bulletin, v. 110 no. 3, p. 387-394.

Mulder, T. and Syvitski, J.P.M., 1995. Turbidity Currents Generated at River Mouths during Exceptional Discharge to the World Oceans: Journal of Geology, v. 103, p. 285-299.

Mulder, T., J.P.M. Syvitski, S. Migeon, J. Faugeres, and B. Savoye, 2003, Marine hyperpycnal flows: initiation, behavior amd related deposits. A review : Marine and Petroleum Geology, v. 20, p. 861-882.

Munoz, J. A., A. Martinez, and J. Verges, 1986, Thrust Sequence in the eastern Spanish Pyrenees: Journal of Structural Geology, v. 8, p. 399-405.

Mutti, E., and W. R. Nomark, 1991, An integrated approach to study of turbidite system: seismic facies and sedimentary processes of submarine fans and turbidite systems: Speinger-Verflag, New York, p. 75-101.

Mutti, E., 1992, Turbidite sandstone: Agip, San Donato Milanese, Parma, p.236

Mutti, E., M. Siguret, and M Sgavetti, 1988, Sedimentation and deformation in the Tertiary sequence of the Southern Pyrenees: Field Trip Guide 7, AAPG Mediterranean Basins Conference, Nice, Frence.

Mutti, E., Titteri, R., Remacha, E., Mavilla, N., Angella, S., and Fava, L., 1999, An Introduction to the Analysis of Ancient Turbidite Basins from an Outcrop Perspective, AAPG course notes, p. 121-211.

Peakall, J.B. McCaffrey, and B. Kneller, 2002, A process model for the evolution, morphology, and architecture of sinuous sub marine channels: Journal of Sedimentary Research, v. 70, p. 434-448.

Pickering, K.T., and Corregidor, J., 2005, Mass-Transport Complexes (MTCs) and Tectonic Control on Basin-Floor Submarine Fans, Middle Eocene, South Spanish Pyrenees, Journal of Sedimentary Research, Vol. 75, p. 761-783.

Pinous, O. V., M. A. Levchuk, and D. L. Sahagian, 2001, Regional synthesis of the productive neocomian complex of West Siberia: sequence stratigraphy framework: AAPG Bulletion, v. 85, p. 1713-1730.

Plink-Bjoklund, P., D. Mellere, and R. J. Steel, 2001, Turbidite variability and architecture of sand-prone, deep-water slopes: eocene clinoforms in the Central Basin, Spitsbergen: Journal of Sedimentary Research, v. 71, no. 6, p. 895-912.

Plink-Bjoklund, P. and R. J. Steel, 2005, Delta on falling-stage and lowstand shelf margins, the eocene central basin of spitbergen: importance of sediment supply: SEPM Special Publication no. 83, p. 179-206.

Porebski, S. J. and R. J. Steel, 200 Shelf-margin deltas: their stratigraphic significance and relation to deepwater sands: Earth Science Review, v. 62, p.283-326.

Posamentier, H. W, 2003, Depositional elements associated with a basin floor channels-levee system: case study from the Gulf of Mexico: Marine and Petroleum Geology, v. 20, p. 677-690.

Posamentier, H. W., and R. G. Walker, 2006, Facies model revisited: deep-water turbidiete and submarine fans: SEPM Special Publication, no. 84, p. 397-520.

Pratson, L. F., J. Imran, G. Parker, J. P. M. Syvitski, and E. Hutton, 2000, Debris flow vs. tubidity currents: a modeling comparison of their dynamics and deposits: SEPM Special Publication, no. 68, p. 57-72.

Prior, D. B. and J. M. Coleman, 1984, Submarine slope instability: slope instability: British Library Cataloguing in Publication Data.

Puigdefabregas, C., J.A. Munoz, and Mariano Marzo, 1986, Thrust belt development in the eastern Pyrenees and related depositional sequences in the southern foreland basin (*in* Foreland basins): Special Publications of the International Association of Sedimentologists, v. 8, p.229-246.

Puigdefabregas, C., and Souquet, P., 1986, Tecto-Sedimentary Cycles and Depositional Sequences of the Mesozoic and Tertiary from the Pyrenees, Tectonophysics 129, pp. 173-203.

Pye, K., 1994, Sediment Transport and Depositional Proccesses, Blackwell Scientific Publications, Edinburg.

Pyles, D.R., D.C. Jennette, M. Tomasso, R.T. Beaubouef, and C. Rossen, in press, Concepts Learned from a 3D Outcrop of a Sinous Slope Channel Complex: Beacon Channel Complex, Brushy Canyon Formation, West Texas: Journal of Sedimentary Research.

Pyles, D.R., and J. Clark, 2007, Preliminary Study of Sobrarbe Formation, unpublished work.

Pyles, D.R., 2007, Architectural elements in a ponded submarine fan, carboniferous Ross Sandstone, Western Ireland: AAPG Studies in Geology, v. 56.

Pyles, D.R. and Slatt, R.M., 2006. Stratigraphy of the Lewis Shale, Wyoming, USA: Application to Understanding Shelf Edge to Base-of-slope Changes in Stratigraphic Architecture of Prograding Basin Margins *in* Nilsen, T.H., Shew, R.D., Steffens, G.S., and Studlick, J.R.J. (Ed.s), Atlas of Deep-Water Outcrops, American Association of Petroleum Geologists Studies in Geology v. 56., p. 1-19.

Reading, H.G., 1996, Sedimentary environtments; process, facies and stratigraphy: Blackwell Science, Oxford, United Kingdom.

Ross, W. C., B. A. Halliwell, J. A. May, D. E. Watts, and J. P. M. Syvitski, 1994, Slope readjustment: a new model for the development of submarine fans and aprons: Geologi, v. 22, p. 511-514.

Sanders, J.E., 1965, Primary sedomentary structures formed by turbidity currents and related resedimentation mechanisms (*in* Primary sedimentary structures and their hydrodynamic interpretation): Special Publication-Society of Economic Paleontologists and Mineralogists v.1965, p. 192-219

Shanmugam, G., 1997, The Bouma Sequence and the Turbidite Mind Set, Earth Science Review 997, p. 1-28

Shanmugam, G., 2000, 50 years of the turbidite paradigm (1950s-1990s); deepwater procces and facies models; a critical prespectie (*in* Deep-water sedimentary systems; new models for the 21st century): Marine and Petroleum Geology, v.17, p. 285-342.

Soto, R., A.M. Casas, F. Strorti, and C. Faccenna, 2002, Role of lateral thickness variations on the development of oblique structures at the western end of the South Pyrenean Central Unit : Tectonophysics v. 350, p. 215-235.